

# Abstract

Title of dissertation: Formation of Magnetized Prestellar Cores  
in Turbulent Giant Molecular Clouds

Che-Yu Chen, Doctor of Philosophy, 2015

Dissertation directed by: Professor Eve C. Ostriker  
Department of Astronomy

The main goal of this thesis research is developing a theory to describe the early stages of star formation within magnetized, turbulent molecular clouds, which is a fundamental problem in astrophysics. In giant molecular clouds, supersonic turbulence creates shocks and compresses material to generate overdense structures that can later collapse gravitationally, while the intrinsic magnetic fields in the clouds limit the compression in turbulent shocks and provide support to prestellar cores against self-gravity. Previous numerical simulations had shown promising results that prestellar cores with realistic physical properties can form in shocked regions with the presence of magnetic fields and ambipolar diffusion, but left a big gap in understanding the fundamental mechanism driving prestellar core formation in turbulent, magnetized environments, especially the longstanding puzzle of how these dense, self-gravitating cores form in the diffuse, thermally-supported, and highly magnetized clouds. In this thesis, we firstly adopted both analytic and numerical methods to investigate a one-dimensional C-type shock created by turbulence-

accelerated ambipolar diffusion, and we discovered a transient stage that can theoretically generate overdense regions with relatively low magnetic pressure. We then turned to fully three-dimensional MHD simulations with supersonic convergent flows, and quantitatively studied the physical properties of cores formed in the shock-compressed regions, together with the detailed flows leading to core formation. These cores have similar masses and sizes as the observed ones, and form within a timescale comparable to the observed core lifetime. However, we found that ambipolar diffusion may not be a crucial mechanism for cores to lose magnetic support, because gas in overdense regions preferably flows along the magnetic field lines. We therefore extended the parameter space of our simulations to further examine the anisotropic core formation model. Our results suggest that while prestellar cores are seeded by perturbations from local turbulence, they are built up by collecting surrounding materials anisotropically along the magnetic field lines. To conclude, though turbulence-enhanced ambipolar diffusion can highly reduce the level of magnetization within shock-compressed dense regions, anisotropic contraction may be the key mechanism driving prestellar core formation within turbulent, magnetized giant molecular clouds. This mechanism leads to cores with masses and sizes that are in good agreement with observed prestellar cores.

**Formation of Magnetized Prestellar Cores  
in Turbulent Giant Molecular Clouds**

by

Che-Yu Chen

Dissertation submitted to the Faculty of the Graduate School of the  
University of Maryland, College Park in partial fulfillment  
of the requirements for the degree of  
Doctor of Philosophy  
2015

Advisory Committee:  
Professor Eve C. Ostriker, Chair/Advisor  
Professor Lee Mundy  
Professor Massimo Ricotti  
Professor Andrew Harris  
Professor William Dorland

© Copyright by  
Che-Yu Chen  
2015

## Preface

This thesis contains research that has already been published. Chapter 2 entitled “Ambipolar Diffusion in Action: Transient C Shock Structure and Prestellar Core Formation” has been published in the *Astrophysical Journal* (Chen, C.-Y. & Ostriker, E. C. 2012, *ApJ*, 744, 124). Chapter 3 entitled “Formation of Magnetized Prestellar Cores with Ambipolar Diffusion and Turbulence” has been published in the *Astrophysical Journal* (Chen, C.-Y. & Ostriker, E. C. 2014, *ApJ*, 785, 69). Chapter 4 entitled “Anisotropic Formation of Magnetized Cores in Turbulent Cloud” has been submitted to the *Astrophysical Journal* (Chen, C.-Y. & Ostriker, E. C. 2015). Simulations presented in Chapters 3–5 were performed on the HPCC *deephought* cluster administrated by the OIT at the University of Maryland, the *yorp* cluster in the Department of the Astronomy, as well as the *Tiger* cluster at Princeton University. This work was supported by grant NNX10AF60G from NASA ATP, and by grant NNX13AO52H supporting C.-Y. C. under the NASA Earth and Space Science Fellowship Program

## Acknowledgments

I still remember that summer seven years ago. As a shy, young girl speaking fluent English, I traveled from the other side of the planet to pursue my astronomy dream. I was so excited about my new life at Maryland, yet scared of all these challenges in front of me. Looking back, I feel so lucky to have all the help and support during the highs and lows in my graduate student life, and I am so grateful to all the people who have made this thesis possible.

First and foremost, I want to thank my advisor, Professor Eve Ostriker, who took me in since my first year in graduate school. She is always kind, encouraging, and patient, but she also never hesitates to point out any flaws in my argument. Without her, I would never have accomplished so many things in my graduate school years and grown up to become a confident researcher. She is not only my thesis advisor, but also my role model in seeking an academic career.

I also want to thank Professor Lee Mundy, my research committee member since my second-year project, who also accepted me as his step-student and took care of me during conferences when Eve was not around. He has provided numerous observational insights that are extremely helpful for me to develop this thesis work. I would also like to thank Professor Massimo Ricotti for serving on my thesis committee for so many years, and Professor William Dorland for agreeing to be the Dean's Representative on my committee. I also owe my gratitude to Professor Andrew Harris for spending his invaluable time preparing a lot of reference letters for me when I was applying for postdoc positions.

My fellow astronomy graduate students, thank you all for making my graduate school experience so joyful that I will cherish forever. I want to thank Hannah Krug for introducing me Maryland basketball, which has become an inevitable part of my life. I also want to thank my dear friend and closest collaborator Shaye Storm, who has provided me numerous support on both research work and daily life. To my dear classmates/officemates/intramural teammates Alex McCormick, Kari Helgason, Jithin George, and Holly Sheets, thank you for all the homework discussions, hallway chatting, and volleyball/soccer time we shared together. I also want to express my appreciation to Hao Gong, who helped me get start with my project in my early years of graduate school.

I would also like to acknowledge the support from the Astronomy department, and thank all the faculty and staff members for creating such a friendly, pressure-less environment for graduate students. I want to mention my special thanks to Professor Cole Miller, who has been a mentor for me whenever I have doubts in my career choice.

I am so grateful to have parents who always support me and believe in me. I am also very lucky to have a sister who is always there for me whenever I need someone to talk to. I also want to thank my dear husband Joseph, who has been my motivation to stand up and face challenges ever since we met. To my dear baby girl Lyra, though you cry and interrupt me from working every 40 minutes, you are still my little princess.

It is impossible to include everyone that I have received help from, and I apologize to those I have left out. Thank you all for being in my life!

# Table of Contents

List of Figures	viii
1 Introduction	1
1.1 Giant Molecular Clouds and Star-forming Regions . . . . .	3
1.2 Prestellar Core Properties in Observations . . . . .	6
1.3 The Importance of Supersonic Turbulence and Convergent Flows . . . . .	9
1.4 The Magnetic Field and Ambipolar Diffusion . . . . .	10
1.5 Theories of Prestellar Cores . . . . .	13
1.6 Thesis Outline . . . . .	16
2 Ambipolar Diffusion in Action: Transient C shock Structure and Prestellar Core Formation	18
2.1 Introduction . . . . .	19
2.2 Dynamical Equations and Model Parameters . . . . .	25
2.2.1 Basic Equations . . . . .	25
2.2.2 Steady State One-dimensional Shock Equations . . . . .	26
2.2.3 Governing Ordinary Differential Equation . . . . .	28
2.2.4 Ionization Fraction . . . . .	30
2.2.4.1 Recombination-Ionization Equilibrium . . . . .	30
2.2.4.2 Frozen-in Magnetic Field . . . . .	31
2.2.4.3 Explicit Solution . . . . .	32
2.2.4.4 Comparison of Ionization Treatments . . . . .	32
2.3 Steady C Shock Thickness . . . . .	34
2.3.1 Exact Solution . . . . .	34
2.3.2 Zeroeth-order Approximation . . . . .	36
2.3.3 Magnetic Field Influence . . . . .	39
2.3.4 Numerical Approach . . . . .	41
2.4 C Shock Formation . . . . .	43
2.4.1 Numerical Algorithm for Ambipolar Diffusion . . . . .	43
2.4.2 Convergent Flow Test . . . . .	44
2.4.2.1 Simple Convergent Flow Test . . . . .	44
2.4.2.2 Colliding Clouds . . . . .	46

2.4.2.3	Transient C shock Development . . . . .	49
2.5	Criticality of Clouds . . . . .	51
2.5.1	Mass-to-flux Ratio . . . . .	51
2.5.2	Bonnor-Ebert Sphere . . . . .	53
2.6	Core Forming Process . . . . .	55
2.6.1	Evolution of Overdense Regions . . . . .	55
2.6.2	Time Scale and the Mass-to-flux Ratio . . . . .	58
2.6.3	Simulation Results . . . . .	62
2.7	Summary . . . . .	66
3	Formation of Magnetized Prestellar Cores with Ambipolar Diffusion and Turbulence . . . . .	72
3.1	Introduction . . . . .	73
3.2	Theoretical Analysis . . . . .	80
3.2.1	Oblique MHD Shock . . . . .	80
3.2.2	Gravitational Critical Scales in Spherical Symmetry . . . . .	85
3.3	Numerical Methods and Models . . . . .	88
3.3.1	Simulation Setup and Equations . . . . .	88
3.3.2	Model Parameters . . . . .	90
3.3.3	Analysis of Core Properties . . . . .	94
3.4	Sample Evolution of Structure . . . . .	96
3.5	Survey of Core Properties . . . . .	104
3.5.1	Mass and Size . . . . .	106
3.5.2	Magnetization . . . . .	112
3.6	Anisotropic Core Formation . . . . .	115
3.6.1	Examples of Simulation Evolution . . . . .	115
3.6.2	Theoretical Scalings . . . . .	116
3.7	Summary . . . . .	122
4	Anisotropic Formation of Magnetized Cores in Turbulent Clouds . . . . .	127
4.1	Introduction . . . . .	128
4.2	Anisotropic Core Formation: Review . . . . .	131
4.3	Numerical Methods and Models . . . . .	134
4.4	Post-shock Environment and Structure Formation . . . . .	138
4.4.1	Post-shock Layer . . . . .	138
4.4.2	Structure Formation . . . . .	140
4.5	Statistical Core Properties . . . . .	147
4.6	Comparison to the Perseus Molecular Cloud . . . . .	156
4.6.1	Cloud Environment . . . . .	156
4.6.2	Bonnor-Ebert Mass . . . . .	157
4.6.3	Mass-radius Relation . . . . .	160
4.7	Summary . . . . .	164

5	Summary and Future Work	169
5.1	Summary of Thesis Study . . . . .	169
5.2	Future Work . . . . .	173
5.2.1	From Local to Global Simulations . . . . .	173
5.2.2	Potential Future Projects . . . . .	174
A	Oblique C shocks	177
	Bibliography	185

## List of Figures

1.1	Aquila cloud from <i>Herschel</i> . . . . .	2
1.2	Serpens Main molecular cloud from <i>CARMA</i> . . . . .	7
1.3	Core mass function in Aquila molecular cloud . . . . .	8
1.4	The four stages of star formation . . . . .	14
2.1	Comparison of different C shock solutions . . . . .	33
2.2	C shock structure: exact solution vs. analytic approximations, I . . . . .	37
2.3	C shock structure: exact solution vs. analytic approximations, II . . . . .	38
2.4	Transient C shock and ideal MHD shock structures . . . . .	45
2.5	Shock structure created by clump collision, I . . . . .	47
2.6	Shock structure created by clump collision, II . . . . .	48
2.7	The gas pressure structure created by clump collision . . . . .	49
2.8	Core column density evolution . . . . .	56
2.9	Time evolution of mass-to-flux ratio in transient shock . . . . .	63
3.1	Multiple solutions for oblique shocks . . . . .	81
3.2	The schematic configuration for our simulations . . . . .	90
3.3	Evolution sample of post-shock layer (model A20X10) . . . . .	97
3.4	Evolution sample of post-shock layer (model A5X3) . . . . .	98
3.5	Evolution sample of post-shock layer (model A45ID) . . . . .	99
3.6	The spectrum of gas structures in the post-shock region . . . . .	102
3.7	Core identification from <i>GRID</i> core-finding method . . . . .	105
3.8	Core mass and size distributions . . . . .	106
3.9	Comparison of core properties in different models . . . . .	108
3.10	The core mass-size and density-size plots . . . . .	111
3.11	The core mass-to-flux ratio distribution . . . . .	112
3.12	Core mass-to-flux ratio versus core mass . . . . .	113
3.13	Gas dynamics around a forming core . . . . .	117
3.14	Space-time diagrams around forming cores in different models . . . . .	118
4.1	Illustration of anisotropic core formation . . . . .	132
4.2	The post-shock layer thickness compared with other physical scales . . . . .	139

4.3	Gas structures within post-shock layers in different models . . . . .	141
4.4	Space-time diagrams of gas velocity around forming cores . . . . .	142
4.5	Filamentary structures with different cut-off column densities . . . . .	145
4.6	Time evolution of the column density within post-shock layers . . . . .	146
4.7	Statistical distribution of core mass and size . . . . .	150
4.8	Statistical distribution of core magnetic field and mass-to-flux ratio . . . . .	151
4.9	Core formation efficiency compared with core collapse timescale . . . . .	152
4.10	Summary of simulated core statistical properties . . . . .	154
4.11	Statistical distribution of $M_{\text{core}}/M_{\text{BE}}$ . . . . .	158
4.12	Core mass-to-flux ratio vs. $M_{\text{core}}/M_{\text{BE}}$ . . . . .	160
4.13	The core mass-size relationship . . . . .	161
4.14	Core column density vs. core mass . . . . .	162
4.15	The comparison of core mass-size relationship in different models . . . . .	163
A.1	Oblique C shock structures and compression ratio . . . . .	180
A.2	The transient behavior and time evolution in oblique C shocks . . . . .	184

# Chapter 1: Introduction

Human society has always been fascinated by the night sky. The eagerness to study astronomy begins with the observed stars, which are the birthplace of heavier elements like helium, carbon, and oxygen that build up life on the Earth. The formation process of individual stars is therefore one of the most important topics in astronomy and astrophysics.

Stars form from cold, condensed molecular gas in the interstellar medium (ISM), within which the extensive, coherent volumes with the highest column density and extinction are considered giant molecular clouds (GMCs; see Figure 1.1). In GMCs, supersonic flows randomly compress material to initiate creation of a filamentary network that can be observed in both gas and dust emission (André et al. 2014). Gravity also plays a role in creating filaments with high mass per unit length. Some of the overdense regions will then shrink to form prestellar cores, which can collapse gravitationally to create protostellar systems and later become stars (Shu et al. 1987).

During the star forming process, magnetic fields within GMCs may play crucial roles at all physical scales, and throughout different evolutionary stages. At earlier stages and larger scales, the magnetic field can limit compression in turbulence-



Figure 1.1: A composite 3-color images of the Aquila molecular cloud taken by the ESA *Herschel* Space Observatory with the Spectral and Photometric Imaging Receiver (SPIRE, *red* at 500  $\mu\text{m}$ ) and the Photodetector Array Camera and Spectrometer (PASC, *green* at 160  $\mu\text{m}$  and *blue* at 70  $\mu\text{m}$ ) (André et al. 2010, also see the ESA's Online Showcase of Herschel Images: <http://oshi.esa.int/>).

generated interstellar shocks that create dense clumps and filaments (Mestel & Spitzer 1956). On the other hand, the local magnetic field within collapsing cores can help to remove angular momentum during the disk formation process (Gillis et al. 1979; Mouschovias 1991). Therefore, magnetic effects are considered one of the key dynamical mechanisms affecting star forming process in GMCs, in combination with turbulence and gas gravity (McKee & Ostriker 2007).

## 1.1 Giant Molecular Clouds and Star-forming Regions

The ISM fills the space between stars within galaxies. GMCs, the colder, denser components of the ISM, contain mostly molecular hydrogen ( $\text{H}_2$ ) because of the low penetration ability of dissociating ultraviolet (UV) radiation in high column density regions, although the molecular gas is lightly ionized by cosmic rays. Stars form exclusively within molecular clouds because of the dense, cool environment. It has also been shown in observations that the molecular gas is tightly correlated with star formation, in the form of a power-law between the surface density of star formation rate (SFR) and the total gas content,  $\Sigma_{\text{SFR}} \propto \Sigma_{\text{gas}}^N$  (Kennicutt 1998; Bigiel et al. 2008; Heiderman et al. 2010). The slight ionization of GMCs (ionization fractions  $\sim 10^{-7} - 10^{-4}$ , Draine et al. (1983)), in fact is sufficient for magnetic effects to be important (see Section 1.4).

Spatially, GMCs can spread over tens of parsecs in the interstellar space (Roman-Duval et al. 2010). These clouds have masses  $\sim 10^2 - 10^7 M_\odot$ , with typical particle number density  $\sim 10^2 - 10^3 \text{ cm}^{-3}$  and column density  $\sim 10 - 100 M_\odot \text{ pc}^{-2}$

(see review in Dobbs et al. 2014). Most observations of the physical properties of GMCs have been conducted using carbon monoxide (CO) molecular lines (Lada 1976; Solomon et al. 1987; Fukui et al. 1999; Dame et al. 2001), especially the millimeter rotational line  $J = 1 \rightarrow 0$  because the required minimum local density for excitation is similar to the densities of GMCs. At least on large scales, for whole GMCs, theoretical and observational investigations have indicated that CO can be considered to trace  $\text{H}_2$  using a roughly constant conversion factor (Dickman 1978; Frerking et al. 1982; Shetty et al. 2011; Bolatto et al. 2013). Since  $\text{H}_2$ , the predominant component in GMCs, is not a preferred tracer for ground-based observations because of its lack of a radio spectrum, CO is commonly considered as an indicator of the  $\text{H}_2$  distribution and other GMC properties (Scoville & Solomon 1975; Sanders et al. 1984; Combes 1991; Heyer et al. 1998). Within individual GMCs, the  $^{13}\text{CO}$  isotope traces detailed structure better than  $^{12}\text{CO}$  (e.g. Bally et al. 1987).

Observations have also revealed that the physical environment in GMCs is highly turbulent with large velocity dispersion,  $\sigma_v \sim 1 - 5$  km/s (Larson 1981; Heyer et al. 2009, and references therein), and it has been commonly agreed that these random, supersonic gas motions crucially contribute to star formation within GMCs (Mac Low & Klessen 2004; McKee & Ostriker 2007). Theoretical and observational analysis show that turbulent flows are self-similar and follow specific power spectra  $P_v(k) \propto k^q$  (Brunt & Heyer 2002; Padoan et al. 2006), which have dominant influence on density structures within GMCs that later provide seeds for overdense prestellar clumps to form (Elmegreen 1993; Klessen et al. 2000; Padoan et al. 2001). More detailed connections between supersonic turbulence and star formation are discussed

in Section 1.3.

In addition to  $^{12}\text{CO } J = 1 \rightarrow 0$ , high-density tracers (e.g.  $^{13}\text{CO}$ ,  $\text{C}^{18}\text{O}$ ,  $\text{NH}_3$ , CS, and dust continuum) have revealed internal structures within GMCs at smaller scales, including elongated structures and dense clumps (Myers & Benson 1983; Snell et al. 1984; Bally et al. 1987; Chini et al. 1997; Johnstone & Bally 1999; Hacar et al. 2013). The filamentary network shown in Figure 1.1 is commonly seen in multiple GMCs, and has been considered as a universal feature within star-forming molecular gas (see reviews in André et al. 2014; Molinari et al. 2014). Observations suggest that prestellar cores are preferably distributed along dense filaments (André et al. 2010; Könyves et al. 2010; Hacar & Tafalla 2011), but the evolutionary relationship between filamentary structures and prestellar core formation is yet not well understood.

Physically, the balance between different energy components within GMCs can be estimated using typically observed values. If  $\mathcal{E}_{\text{mag}}$ ,  $\mathcal{E}_{\text{th}}$ ,  $\mathcal{E}_{\text{dyn}}$ , and  $\mathcal{E}_{\text{grav}}$  represent the magnetic, thermal, dynamic, and gravitational energy densities, respectively, then for a GMC (Solomon et al. 1987; Blitz 1993; Dobbs et al. 2014):

$$\mathcal{E}_{\text{mag}} = \frac{B^2}{8\pi} \approx \frac{(10 \mu\text{G})^2}{8\pi} \sim 10^{-11} \text{ erg cm}^{-3}, \quad (1.1)$$

$$\mathcal{E}_{\text{th}} = \frac{1}{2}\rho c_s^2 \approx \frac{1}{2} (10^3 \text{ cm}^{-3} m_{\text{H}}) (0.2 \text{ km/s})^2 \sim 10^{-12} \text{ erg cm}^{-3}, \quad (1.2)$$

$$\mathcal{E}_{\text{dyn}} = \frac{1}{2}\rho v_{\text{turb}}^2 \approx \frac{1}{2} (10^3 \text{ cm}^{-3} m_{\text{H}}) (5 \text{ km/s})^2 \sim 10^{-10} \text{ erg cm}^{-3}, \quad (1.3)$$

$$\mathcal{E}_{\text{grav}} = \frac{3}{5} \frac{GM\rho}{R} \approx \frac{3}{5} \frac{G \cdot 4\pi (10 \text{ pc})^3 / 3 \cdot (10^3 \text{ cm}^{-3} m_{\text{H}})^2}{10 \text{ pc}} \sim 10^{-10} \text{ erg cm}^{-3}. \quad (1.4)$$

This suggests that the turbulent energy and magnetic pressure are the main components supporting GMCs from gravitational collapse.

## 1.2 Prestellar Core Properties in Observations

A local minimum in the cloud's gravitational potential may be considered a prestellar core if it is gravitationally bound but does not yet contain a protostar. Because of their overdensity ( $n \sim 10^4 - 10^5 \text{ cm}^{-3}$ ) and coldness ( $T \sim 10 \text{ K}$ ; see review in Andre et al. 2000), prestellar cores can be identified in GMC observations using optical/infrared absorption, far infrared or sub-millimeter dust continuum emission, or line emission of dense-gas tracers like  $\text{NH}_3$  and  $\text{N}_2\text{H}^+$  (Myers et al. 1983; Jijina et al. 1999; Lee & Myers 1999; Bacmann et al. 2000; Caselli et al. 2002; Ward-Thompson et al. 2002; also see Figure 1.2). Surveys in nearby clouds have provided constraints on physical properties of prestellar cores; in general, core mass and size are in the ranges  $\sim 0.1 - 10 M_\odot$  and  $\sim 0.01 - 1 \text{ pc}$  (Motte et al. 2001; Ikeda et al. 2009; Rathborne et al. 2009; Kirk et al. 2013). Multiple studies have also shown that the density profile of prestellar cores is very similar to that of a Bonnor-Ebert sphere (Alves et al. 2001; Kandori et al. 2005; Kirk et al. 2005), and the internal motion seems to be subsonic (Lee et al. 1999, or see review in di Francesco et al. 2007). In addition, prestellar cores tend to be magnetically supercritical, with normalized mass-to-flux ratios  $\sim 2$  (Falgarone et al. 2008; Troland & Crutcher 2008).

One intriguing feature of prestellar cores is the core mass function (CMF), which shows the statistical distribution of the core counts over a range of masses (Figure 1.3). There have been numerous measurements of the CMF in different GMCs (e.g. Onishi et al. 2002; Enoch et al. 2006; Alves et al. 2007; Nutter & Ward-Thompson 2007), which all show similar shape to the one in Figure 1.3 and the initial

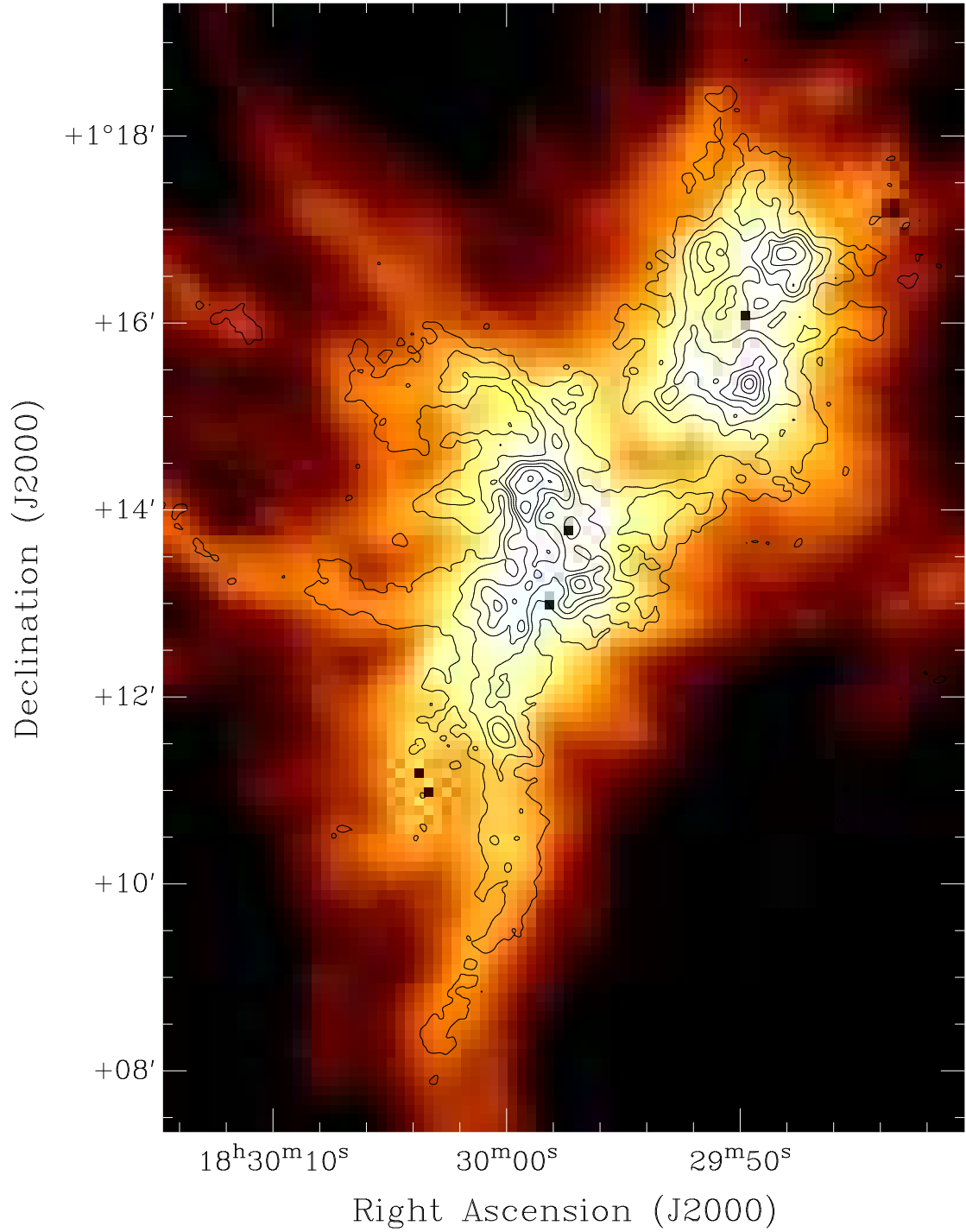


Figure 1.2: The integrated intensity contours of  $\text{N}_2\text{H}^+$  (1 – 0) of the Serpens Main molecular cloud observed by the Combined Array for Research in Millimeter-wave Astronomy (*CARMA*), overlaid on a *Herschel* 250  $\mu\text{m}$  continuum image (Lee et al. 2014). Candidates of prestellar cores can be easily picked by eye from the  $\text{N}_2\text{H}^+$  line emission map.

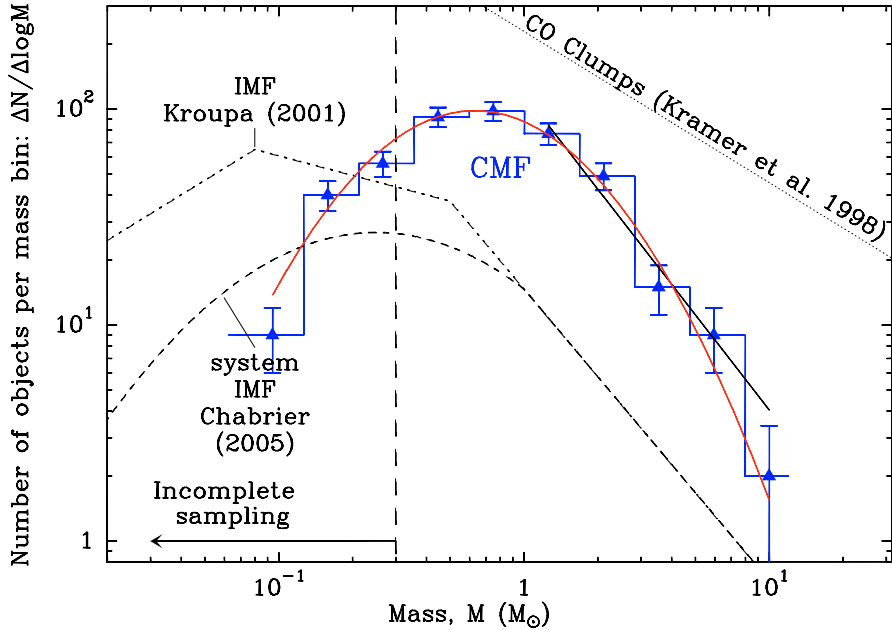


Figure 1.3: The core mass function (CMF) from prestellar cores observed by *Herschel* in the Aquila molecular cloud (Könyves et al. 2010).

stellar mass function (IMF; see e.g. Kroupa 2001; Chabrier 2005). Because of the similarity between stellar IMFs/CMFs across different star-forming regions, it has been suggested that there are universal star formation mechanisms that happen early during the star-forming process leading to this shape (see review in Kroupa et al. 2013). Theoretical efforts have been conducted to study the origin of the IMF/CMF (see reviews McKee & Ostriker 2007 and Offner et al. 2014). Density fluctuation generated by the power spectrum of the multi-scale turbulence within GMCs are believed to play a key role (Federrath et al. 2008; Hennebelle & Chabrier 2008; Hopkins 2012; Krumholz et al. 2012), but later accretion onto individual forming stars may also be important (Bonnell & Bate 2006). However, there still are many uncertainties in understanding of the earliest stage of star formation.

### 1.3 The Importance of Supersonic Turbulence and Convergent Flows

The observed supersonic linewidth in GMCs is a strong indication that the GMCs are highly turbulent (Williams et al. 2000). A power-law relation between the velocity dispersion  $\sigma_v$  (measured by the linewidth of molecular emission lines) and the size of the measured region  $L$  have been reported in many studies, typically  $\sigma_v(L) \propto L^{0.5}$  (Larson 1981; Myers 1983; Solomon et al. 1987; Passot et al. 1988; Heyer & Brunt 2004). The nearly universal size-line relationship across different GMCs in the Milky Way indicates that molecular clouds are gravitationally bound systems with a characteristic surface density; generally, we have  $GM/r \sim \sigma^2$  for gravitationally bound systems, and since  $M \sim \Sigma r^2$  where  $\Sigma$  is the surface density, simple theoretical scaling gives  $\sigma^2 \sim G\Sigma r$ , or  $\sigma \propto \Sigma^{1/2} r^{1/2}$  (see review in Dobbs et al. 2014).

Overdense fragments within GMCs may have formed due to in-cloud shocks and colliding gas flows from cloud-scale turbulence (see reviews in Scalo 1985 and Ballesteros-Paredes et al. 2007). Supersonic turbulence can generate density enhancement, and thus many numerical simulations have been conducted to study the density structure and gravitational instability induced by the supersonic turbulence inside GMCs, with or without magnetic effects (e.g. Vazquez-Semadeni et al. 1995; Klessen 2000; Klessen et al. 2000; Li et al. 2004; Ostriker et al. 2001), which may be directly related to the observed IMF/CMF (e.g. Klessen 2001; Padoan & Nordlund

2002; Jappsen et al. 2005; also see Section 1.2 above).

Supersonic turbulence within GMCs creates a combination of shearing, diverging, and converging effects at all physical scales, but it is those regions with large-scale convergent flows that will compress gas and strongly alter the gravitational stability in the cloud (Mac Low & Klessen 2004). Gong & Ostriker (2011) therefore adopted an idealized model of a local region inside a GMC containing multi-scale turbulence where two large-scale supersonic flows collide. These simulations showed that the convergent flow creates a planar, dense layer bordered by two shock fronts, which provides favorable conditions for the birth of prestellar cores. These simulations had a range of convergent inflow Mach number  $\mathcal{M} = 1.1 - 9$ , and found cores with masses  $0.05 - 50 M_{\odot}$ . However, Gong & Ostriker (2011) only considered hydrodynamic flows, and therefore could not predict the level of magnetization within prestellar cores, which is an important factor determining the ability of the core to collapse and form a protostellar disk (see review in Li et al. 2014).

## 1.4 The Magnetic Field and Ambipolar Diffusion

The existence of magnetic fields in the ISM has been inferred since the discovery of polarized light from distant stars (Hiltner 1949, 1951; Chandrasekhar & Fermi 1953), which reveals the two-dimensional field morphologies within atomic clouds and GMCs (Vrba et al. 1976; Moneti et al. 1984; Heyer et al. 1987; Tamura et al. 1987; Goodman et al. 1990). Though it is hard to detect, the magnetic field strength can be directly measured via Zeeman splitting of molecular lines (Good-

man et al. 1989; Heiles et al. 1993; Crutcher 1999; Bourke et al. 2001). Observations indicate the cloud-scale magnetic field strength is  $\sim 10 \mu\text{G}$ , while it can be slightly stronger ( $\sim 20 - 50 \mu\text{G}$ ) in the filament/core regions (e.g. Troland & Crutcher 2008; Chapman et al. 2011; or see review in Crutcher 2012).

The role played by magnetic fields during star formation within GMCs is a complicated but important topic. At the cloud scale, magnetized shocks have less compression than hydrodynamic shocks (see e.g. Shu 1992), so that turbulence creates less dense structures. Also, because magnetic and gravitational energies both increase as  $R^{-1}$  for a fixed mass and magnetic flux, sufficiently strong magnetic fields may prohibit the formation or collapse of gravitationally bound cores (Mestel & Spitzer 1956; Strittmatter 1966; Mouschovias & Spitzer 1976). Locally within prestellar cores, magnetic braking can be catastrophic and entirely remove the core angular momentum so that no disks will form (Mestel 1985; Mouschovias 1991; Allen et al. 2003; also see review in Li et al. 2014).

To make things even more complicated, the GMCs are lightly ionized, and only the charged particles (ions) are affected by magnetic fields. This suggests that for theoretical modeling, it is necessary to consider non-ideal effects in magneto-hydrodynamics (MHD), which means the material is not perfectly coupled to the magnetic field.

In astrophysics, ambipolar diffusion is “*a slip between neutrals and the charged plasma,*” (Shu 1992) and is the dominant non-ideal MHD process at the density in clouds and cores ( $n \sim 10^3 - 10^7 \text{ cm}^{-3}$ ). In partially ionized systems, ambipolar diffusion allows neutral particles to decouple from the magnetic fields, because

the neutrals experience electromagnetic forces only through collisions with charged species (Shu 1992). Magnetized shocks with active ambipolar diffusion therefore show smooth transition between upstream and downstream conditions as continuous (C-type) shocks (Draine 1980). Because ambipolar drift modifies the dynamical effect of magnetic fields on the material, it has been considered in classical theory as the main mechanism for overdense clumps to lose magnetic support within GMCs. However, more recent simulations have suggested models of prestellar core formation that more realistically take into account the supersonic motions observed in star-forming GMCs (see Section 1.5 below).

The ability of magnetic fields to affect the neutrals in GMCs depends on the drag force and the collision rate between neutrals and ions (Spitzer 1956). The timescale for magnetic diffusion can be estimated from the drift velocity

$$v_{\text{drift}} = \frac{(\nabla \times \mathbf{B}) \times \mathbf{B}}{4\pi\alpha\rho_i\rho_n} \sim \frac{B^2}{L} \frac{1}{4\pi\alpha\rho_i\rho_n}, \quad (1.5)$$

with the collision coefficient  $\alpha = 3.7 \times 10^{13} \text{ cm}^3\text{s}^{-1}\text{g}^{-1}$  (see Equations (27.8) in Shu 1992). The corresponding timescale is therefore

$$t_{\text{drift}} = \frac{L}{v_{\text{drift}}} \sim 4\pi\alpha\rho_i\rho_n \frac{L^2}{B^2}. \quad (1.6)$$

In GMCs,  $\rho_n \sim 10^3 \text{ cm}^{-3} m_{\text{H}}$ ,  $L \sim 20 \text{ pc}$ ,  $B \sim 10 \text{ } \mu\text{G}$ , and  $\rho_i \sim \mu_i \cdot 10^{-7} \rho_n / \mu_n$  with  $\mu_i \approx 30 m_{\text{H}}$ ,  $\mu_n \approx 2.3 m_{\text{H}}$  (see Chapter 2 for detailed discussions); thus  $t_{\text{drift}} \sim 10^9 \text{ yr}$ . The dynamical timescale across the same system is  $t_{\text{dyn}} \sim L/v$ ; for a typical GMC  $v \sim 5 \text{ km/s}$ , which gives  $t_{\text{dyn}} \sim 10^6 \text{ yr}$ . Since it takes longer than a crossing time ( $t_{\text{dyn}}$ ) for the magnetic field to drift relative to the neutrals, the effect of ambipolar diffusion in GMCs most likely to happen in local regions. At

prestellar core scale,  $\rho_{\text{core}} \sim 10^3 \rho_{\text{GMC}}$ ,  $B_{\text{core}} \sim 10 B_{\text{GMC}}$ , and  $L_{\text{core}} \sim 0.001 L_{\text{GMC}}$  (see Section 1.2 above); also, the ionization fraction is dependent on density, as  $n_i/n_n \propto n_n^{-1/2}$  (see Equation 2.28). Therefore  $t_{\text{drift}}|_{\text{core}} \sim 10^6$  yr, which is longer than the typical observed core lifetime (a few  $10^5$  yr; see Chapter 2). This suggests that prestellar cores become supercritical *not* through quasi-static ambipolar diffusion. This leads to the idea of turbulence-accelerated ambipolar diffusion and its application to core formation, or the anisotropic core formation model that material flows along magnetic field lines into cores. We investigate both processes in this thesis work.

## 1.5 Theories of Prestellar Cores

The classical theory of star formation can be summarized in the four-stage picture described in Shu et al. (1987), illustrated in Figure 1.4. The sites of star formation are overdense prestellar cores within GMCs. When these cores are able to overcome both the thermal and magnetic pressure, they will collapse gravitationally, forming a protostellar system. The central protostar will continue accreting from the gaseous envelope and the protostellar disk until a stable state is reached and a new star is born. These stages are interconnected, with one setting the initial conditions for the next one. Therefore, understanding the forming mechanism of prestellar cores within GMCs is a fundamental problem in astrophysics, especially in how do these cores lose magnetic support within the strongly-magnetized ISM to become magnetically supercritical (Mouschovias 1978; Lizano & Shu 1989).

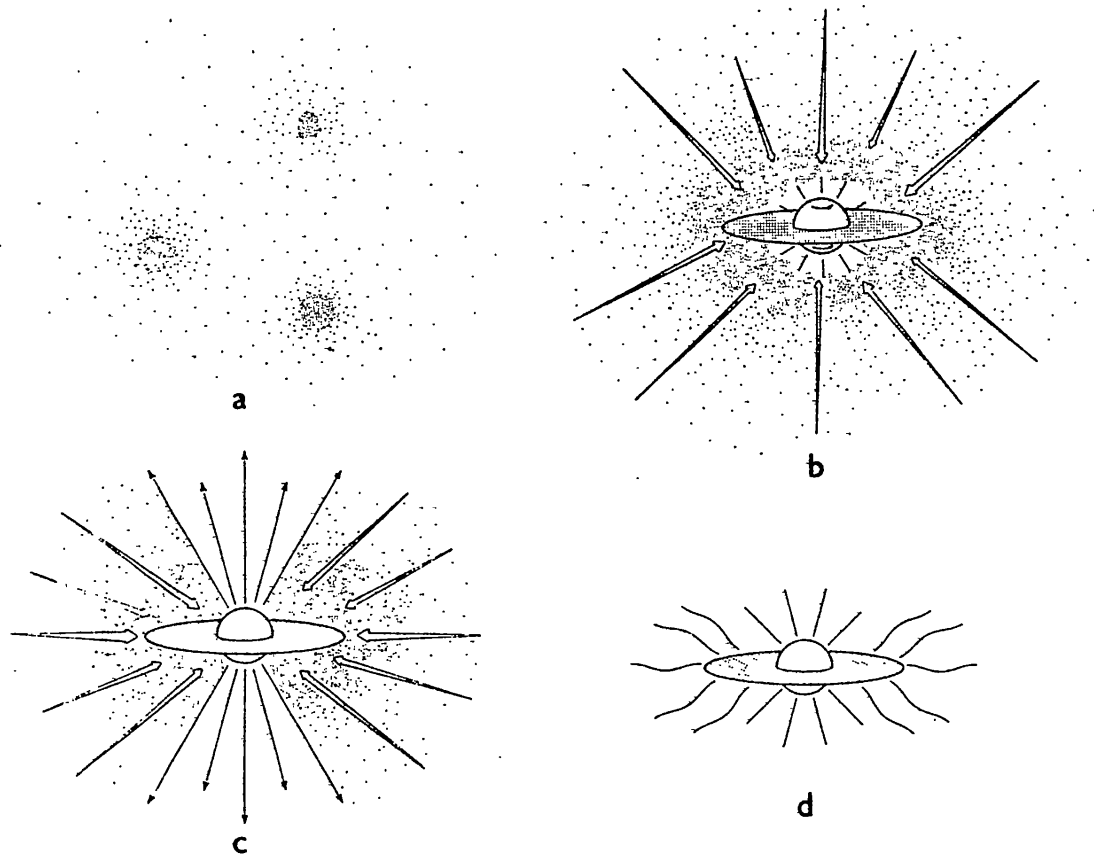


Figure 1.4: The various stages of star formation within GMCs (Shu et al. 1987): (a) Cores form from overdense regions in GMCs, (b) if gravitationally bound, a core will collapse to become a protostar with a disk, (c) the protostar continues to accrete from the disk and ejects material via bipolar winds, and (d) a new born star with a circumstellar disk.

Classical theory of core formation only applies to the scenario in which a dense, magnetized clump has already formed within the cloud, and considers quasi-static ambipolar diffusion as the main mechanism for the cores to lose magnetic support (Nakano 1979; Mouschovias 1979; Mouschovias & Ciolek 1999; Ciolek & Basu 2001). The main difficulty with the classical picture (in addition to the lack of explanation for how dense clumps form within GMCs) is that the timescale for quasi-static ambipolar drift under typical dense core conditions is much longer than the observed prestellar core lifetime (Ward-Thompson et al. 2007; Evans et al. 2009). In contrast to the magnetic-dominated regime, there are alternative models that consider the magnetic effects to play a minor role during the core forming process, as compared to the supersonic turbulence (Mac Low & Klessen 2004; Vázquez-Semadeni et al. 2005).

Similar to the discussion in Section 1.1, we can estimate the balance between the magnetic, thermal, dynamic, and gravitational energy densities within a prestellar core using typically observed values:

$$\mathcal{E}_{\text{mag}} = \frac{B^2}{8\pi} \approx \frac{(50 \mu\text{G})^2}{8\pi} \sim 10^{-10} \text{ erg cm}^{-3}, \quad (1.7)$$

$$\mathcal{E}_{\text{th}} = \frac{1}{2}\rho c_s^2 \approx \frac{1}{2} (10^5 \text{ cm}^{-3} m_{\text{H}}) (0.2 \text{ km/s})^2 \sim 10^{-10} \text{ erg cm}^{-3}, \quad (1.8)$$

$$\mathcal{E}_{\text{dyn}} = \frac{1}{2}\rho v_{\text{internal}}^2 \lesssim P_{\text{th}}, \quad (1.9)$$

$$\mathcal{E}_{\text{grav}} = \frac{3}{5} \frac{GM\rho}{R} \approx \frac{3}{5} \frac{G \cdot 4\pi (0.05 \text{ pc})^3 / 3 \cdot (10^5 \text{ cm}^{-3} m_{\text{H}})^2}{0.05 \text{ pc}} \sim 10^{-10} \text{ erg cm}^{-3}. \quad (1.10)$$

The magnetic pressure can easily become the key support against gravity, because though both  $\mathcal{E}_{\text{th}}$  and  $\mathcal{E}_{\text{dyn}}$  increase with the core density,  $\mathcal{E}_{\text{grav}}$  has a stronger depen-

dence on  $\rho$ .

In fact, it is now generally recognized that turbulence and magnetic fields both play a crucial role during prestellar core formation (McKee & Ostriker 2007). Theoretical studies have shown that large-scale supersonic turbulence can accelerate ambipolar diffusion process within GMCs (Fatuzzo & Adams 2002; Heitsch et al. 2004; Li & Nakamura 2004; Nakamura & Li 2005), and recent MHD simulations including both turbulence and ambipolar diffusion have successfully created prestellar cores with realistic masses, sizes, mass-to-flux ratios, and lifetimes (Kudoh & Basu 2008, 2011; Nakamura & Li 2008). Though the fundamental physics has not been fully explained, turbulence-accelerated, magnetically-regulated processes are considered necessary for understanding prestellar core formation (André et al. 2009; Crutcher 2012). This thesis work aims to investigate the detailed physical mechanism driving turbulence-enhanced ambipolar diffusion, and more generally to characterize the role played by magnetic effects during prestellar core formation.

## 1.6 Thesis Outline

This thesis focuses on the early stages of star formation in magnetized clouds. Chapter 2 presents a combined numerical and analytic investigation of one-dimensional C-type shocks, which allows us to characterize the physics of turbulence-enhanced ambipolar diffusion. In Chapter 3 we demonstrate that solar-mass prestellar cores are able to form in shock-compressed dense regions in GMCs, based on our MHD simulations with supersonic converging flows. The MHD simulations presented here

show that anisotropic gas flow along the magnetic field lines may be the main mechanism driving core formation within post-shock dense layers, and in fact ambipolar diffusion is not a required factor during this process. In Chapter 4, the parameter space of Chapter 3 is extended, to determine how varying magnetic field strength and converging flow velocity affect core properties. This also includes a comparison with observed core properties. I summarize my thesis work in Chapter 5 and describe possible research plans in the future.

# Chapter 2: Ambipolar Diffusion in Action: Transient C shock Structure and Prestellar Core Formation

## Abstract

We analyze the properties of steady and time-dependent C shocks under conditions prevailing in giant molecular clouds. For steady C shocks, we show that ionization equilibrium holds and use numerical integrations to obtain a fitting formula for the shock thickness mediated by ambipolar diffusion,  $L_{\text{shock}} \propto n_0^{-3/4} v_0^{1/2} B_0^{1/2} \chi_{i0}^{-1}$ . Our formula also agrees with an analytic estimate based on ion-neutral momentum exchange. Using time-dependent numerical simulations, we show that C shocks have a transient stage when the neutrals are compressed much more strongly than the magnetic field. The transient stage has a duration set by the neutral-ion collision time,  $t_{\text{AD}} \sim L_{\text{shock}}/v_{\text{drift}} \sim 0.1 - 1$  Myr. This transient creates a strong enhancement in the mass-to-magnetic flux ratio. Under favorable conditions, supercritical prestellar cores may form and collapse promptly as a result of magnetic flux loss during the transient stage of C shocks.

## 2.1 Introduction

Within giant molecular clouds (GMCs), dense gravitationally bound cores form and collapse to create protostars (Shu et al. 1987; McKee & Ostriker 2007; André et al. 2009). Supersonic turbulence is believed to strongly affect the core formation and evolution processes, with post-shock dense regions the most susceptible to collapse (see Gong & Ostriker 2011 and references therein). These processes can be modified significantly by the interstellar magnetic field. Sufficiently strong magnetic fields, if they are well-coupled to the gas, can entirely prevent collapse (Mestel & Spitzer 1956); this can be expressed in terms of a minimum ratio of mass to magnetic flux, or  $\Sigma/B$  (Nakano & Nakamura 1978). However, in a partially-ionized medium, magnetic fields are coupled to the neutrals only through ion-neutral collisions. This ambipolar drift modifies the dynamical effect of magnetic fields on the neutral gas (Mouschovias 1979), in particular altering the character of shocks (Draine & McKee 1993).

In ideal MHD, the fluid and magnetic fields are perfectly coupled by assumption. When flow velocities exceed the relevant signal propagation speeds for a magnetized medium, discontinuities representing shock fronts (jump shock or J-type shock) can form. The compression ratio is parametrized by the particle density, inflow velocity, and magnetic field (e.g. Shu 1992). However, in lightly ionized clouds, velocity differences that would produce a J shock in ideal MHD are small compared to the magnetic signal speed (“Alfvén speed”) in the ionized medium,  $v_{A,i} = B/\sqrt{4\pi\rho_i}$ . Ions and magnetic fields therefore smoothly transition between

upstream and downstream conditions without discontinuities. As a result of the ion-neutral drag forces, the transition in the neutrals is also modified and all physical quantities vary smoothly in the shock region, forming a continuous (C-type) shock (Draine 1980). In a steady C shock, upstream and downstream values of the neutral density, velocity, and magnetic field are the same as for a J shock. Thus, upstream and downstream values of the mass-to-magnetic flux ratio (per unit length parallel to the shock) are the same. Many studies of C shocks have investigated their formation (e.g. Smith & Mac Low 1997), structure (e.g. Mac Low et al. 1995), and stability (e.g. Wardle 1990; Stone 1997), as well as detailed chemical and emission properties (e.g. Draine et al. 1983; Pineau des Forets et al. 1997).

Ambipolar diffusion may play a key role in the star-forming process. In the traditional picture, quasi-static prestellar cores form by gravitationally-driven ambipolar diffusion in magnetically-supported clouds (see review by André et al. (2009)). For a star to form out of gas that is initially strongly magnetized, dense cores must lose magnetic support so that gravitational collapse can take place (Mouschovias 1978; Lizano & Shu 1989). If the magnetic pressure in a gravitationally-confined core exceeds that in its surroundings, the gradient in magnetic pressure makes the magnetic field (and ions) tend to expand. The neutrals will be left behind as a supercritical core as the magnetic field diffuses outward (Nakano 1979). More realistically, Mouschovias (1979) argued that a cloud does not need to lose magnetic flux as a whole to collapse. Rather, ambipolar diffusion redistributes the mass within dense clumps, with the neutrals diffusing inward while the magnetic field threading the outer region is left behind. The duration of the ambipolar diffusion process

can be considerably longer (up to a factor of 10) than the gravitational free-fall timescale  $t_{\text{ff}}$ , although the evolution is more rapid if cores are initially closer to critical (e.g. Mouschovias & Ciolek 1999; Ciolek & Basu 2001).

Observationally, the prestellar core lifetime can be estimated by calculating the ratio of the number of cores with embedded young stellar objects (YSOs) to the number of prestellar cores, which should be comparable to the ratio of protostar lifetime to the prestellar core lifetime (Lee & Myers 1999). Several studies have suggested a prestellar core lifetime of  $\sim 10^6$  yr, or  $(2 - 5)t_{\text{ff}}$  (Ward-Thompson et al. 2007; Evans et al. 2009). This value is much lower than expected from the magnetic-dominated model. In addition, in the turbulence-controlled regime where magnetic field and ambipolar diffusion play minor roles (Mac Low & Klessen 2004), ideal MHD simulations have shown that cores only live for  $(1 - 2)t_{\text{ff}}$  (e.g. Vázquez-Semadeni et al. 2005), after which they either collapse or re-expand. This would not permit an extended period of ambipolar diffusion.

Several studies have suggested that turbulence in GMCs can accelerate ambipolar diffusion and star formation, by introducing large local gradients and nonlinearities. Considering small-scale fluctuations in a background field, Fatuzzo & Adams (2002) analytically showed that turbulence can enhance the ambipolar diffusion rate by a factor of 2 – 3 for typical conditions in GMCs. Heitsch et al. (2004) investigated this problem numerically in a 2.5-dimensional geometry and concluded that the enhanced diffusion rate must be balanced against large-scale compressive flows. Independently, Li & Nakamura (2004) and Nakamura & Li (2005) noted that the failure of the standard theory to predict core formation timescales indicates

that dense clumps may not have formed quasi-statically through ambipolar diffusion. By performing two-dimensional simulations of magnetized sheetlike clouds, they found that with sufficiently strong turbulence, dense filaments can form from magnetic-field-dominated clouds in one turbulence crossing time ( $t \sim 10^6$  yr).

Turbulence-accelerated, magnetically-regulated star formation was studied by Kudoh & Basu (2008) using three-dimensional simulations, including self-gravity and adopting hydrostatic equilibrium in the vertical direction as an initial condition. More recently, Kudoh & Basu (2011) conducted a parameter study of fragmentation in magnetically subcritical clouds regulated by ambipolar diffusion and nonlinear turbulent flows. They concluded that the core formation time is strongly affected by the turbulence speed and the density in compressed region. These and other recent simulations with both strong turbulence and ambipolar diffusion (e.g. Nakamura & Li 2008) are consistent with observations in terms of the core evolution time, the relatively low efficiency of star formation ( $\sim 3 - 6\%$ , see Evans et al. (2009)), and the core structure (subsonic infall motions, see Lee et al. (1999)). However, the fundamental physical process driving core formation via turbulence-enhanced ambipolar diffusion, as well as its dependence on environmental parameters, still remain unclear.

To investigate this problem, we consider the simplest possible time-dependent problem with large spatial gradients: a one-dimensional high-speed converging flow that shocks. In order to clearly distinguish the effect of ambipolar diffusion from other dynamics, we neglect the self-gravity of the gas. We also focus on the simplified case in which the inflow velocity is perpendicular to the magnetic field lines; more

general geometry (i.e., oblique shocks) is discussed in the Appendix A.

When gas is compressed by converging flow, the neutrals are pushed to accumulate downstream. The ion density and magnetic field strength, however, will be only moderately enhanced since the magnetic pressure resists strong compression. These lagging ions exert a drag force on neutrals, reducing the streaming of neutrals into the post-shock region. The momentum exchange between neutrals and ions speeds up ions, increases the compression of the magnetic field, and reduces the post-shock density of the neutrals. Over time, a steady C shock develops. However, at early stages, for an interval comparable to the neutral-ion collision time, the neutrals do not experience drag forces from the ions (Roberge & Ciolek 2007; van Loo et al. 2009; Ashmore et al. 2010). As a consequence, the initial shock for the neutrals is essentially unmagnetized, and the neutrals can be very strongly compressed. If the gravitational collapse timescale is sufficiently short, and a dense enough layer of gas builds up, the magnetically supercritical region may be able to collapse gravitationally before a steady C shock structure forms. The transient ambipolar diffusion process in shocks may help to explain the physics of turbulence-accelerated, magnetically regulated star formation.

In this chapter, we first revisit the steady-state structure of C-type shocks in conditions appropriate for GMCs, in particular allowing for varying ionization fraction. By fitting the results of steady one-dimensional solutions, we obtain an expression for the C shock thickness as a function of the upstream density, the velocity, the magnetic field, and the ionization fraction. These C shock thicknesses are comparable to, or exceed, the size of observed cores. We then consider time-

dependent shocks, which we follow by implementing ambipolar diffusion in the MHD code, *Athena*. Our simulations suggest that under some circumstances, transient C shocks make it possible for a magnetically subcritical cloud to form supercritical dense cores, which would then be able to collapse promptly. We show more generally that the mass-to-flux ratio is significantly increased by ambipolar diffusion in transient post-shock regions, compared to the value that would hold under ideal MHD or in a steady C shock.

This chapter is organized as follows. The model and the governing equations are described in Section 2.2. In Section 2.3 we investigate the structure of steady C shocks, and obtain (analytically and numerically) an explicit formula for the dependence of shock thickness on environmental parameters. In Section 2.4 the time-dependent numerical method is described, and we show that in the transient early development of C shocks, the post-shock ratio of density to magnetic field is very large. In Section 2.5, we discuss mass-to-flux ratios of shocked gas, which we use to quantify the effect of ambipolar diffusion. A parameter study of the duration and effect of transient C shocks is presented in Section 2.6. We summarize our conclusions in Section 2.7.

## 2.2 Dynamical Equations and Model Parameters

### 2.2.1 Basic Equations

For a partially ionized medium with a drag force  $\mathbf{f}_d$  between ions and neutrals, the neutral fluid equations are

$$\frac{\partial \rho_n}{\partial t} + \nabla \cdot (\rho_n \mathbf{v}_n) = 0, \quad (2.1)$$

$$\rho_n \left[ \frac{\partial \mathbf{v}_n}{\partial t} + (\mathbf{v}_n \cdot \nabla) \mathbf{v}_n \right] + \nabla P_n = \mathbf{f}_d, \quad (2.2)$$

which represent conservation laws of mass and momentum, respectively. The corresponding momentum equation for the ionized fluid and magnetic induction equation are

$$\rho_i \left[ \frac{\partial \mathbf{v}_i}{\partial t} + (\mathbf{v}_i \cdot \nabla) \mathbf{v}_i \right] + \nabla P_i - \frac{1}{4\pi} (\nabla \times \mathbf{B}) \times \mathbf{B} = -\mathbf{f}_d, \quad (2.3)$$

$$\frac{\partial \mathbf{B}}{\partial t} + \nabla \times (\mathbf{B} \times \mathbf{v}_i) = 0. \quad (2.4)$$

We discuss the ion density evolution below; this must take into account ionization and recombination.

The ion-neutral drag force per unit volume is

$$\mathbf{f}_d = \alpha \rho_n \rho_i (\mathbf{v}_i - \mathbf{v}_n), \quad (2.5)$$

where  $|\mathbf{v}_i - \mathbf{v}_n|$  is the slip speed, and  $\alpha = \langle \sigma v_{\text{rel}} \rangle / (\mu_n + \mu_i)$  is the collision coefficient with the collisional cross-section  $\sigma$ . The mean neutral and ion molecular weight  $\mu_n$  and  $\mu_i$  are applied here so the number density is  $n_n = \rho_n / \mu_n$ ,  $n_i = \rho_i / \mu_i$ . For simplicity, we shall assume an isothermal equation of state,  $P_n = c_{sn}^2 \rho_n$ ,  $P_i = c_{si}^2 \rho_i$ , and  $c_s^2 = P / \rho = kT / \mu$ .

## 2.2.2 Steady State One-dimensional Shock Equations

We now consider one-dimensional solutions that are steady,  $\partial/\partial t = 0$ , in the shock frame. We assume the magnetic field is parallel to the shock front. The  $x$  coordinate is taken to be perpendicular to  $\mathbf{B}$  and the shock front. We define the compression ratio of neutral density induced by the shock:

$$\rho_n \equiv \rho_{n,0} r_n, \quad (2.6)$$

where  $r_n \rightarrow 1$  upstream, and  $r_n \rightarrow \text{const.}$  downstream. Since  $\rho_n v_n = \text{const.}$  from Equation (2.1),  $v_n = v_{n,0}/r_n$ , where  $v_{n,0}$  is the neutral speed far upstream.

Since magnetic flux is conserved,  $v_i B = \text{const.}$  in the gas. Far upstream,  $B \rightarrow B_0 = \text{const.}$ ,  $v_i \rightarrow v_{i,0} = \text{const.}$ . We define the compression ratio for magnetic field such that

$$B \equiv r_B B_0, \quad (2.7)$$

and  $v_i = v_{i,0}/r_B$  with  $r_B \rightarrow 1$  upstream and  $r_B \rightarrow \text{const.}$  downstream.

For regions far from the shock there is no structure in the fluid,  $\partial v/\partial x \rightarrow 0$ ,  $\partial \rho/\partial x \rightarrow 0$ ,  $\partial B/\partial x \rightarrow 0$ . For Equations (2.2) and (2.3), this means  $v_i = v_n$  far upstream and downstream. Therefore  $v_{n,0} = v_{i,0} \equiv v_0$  far upstream, and  $r_n = r_B \equiv r_f$  far downstream. The velocities of neutrals and ions are therefore given in terms of the upstream shock-frame speed  $v_0$  and the compression ratios at any  $x$  as

$$v_n = \frac{v_0}{r_n} \quad (2.8)$$

and

$$v_i = \frac{v_0}{r_B}. \quad (2.9)$$

To simplify the equations, we define an ion compression ratio

$$\rho_i \equiv \rho_{i,0} r_i, \quad (2.10)$$

where  $\rho_{i,0}$  is the upstream ion density, and  $r_i \rightarrow 1$  upstream,  $r_i \rightarrow \text{const.}$  (not necessarily equal to  $r_f$ ) downstream, similar to  $r_n$  and  $r_B$ .

The momentum equations can now be expressed in dimensionless form as

$$\mathcal{M}^2 \frac{\partial}{\partial x} \left( \frac{1}{r_n} \right) + \frac{\partial}{\partial x} (r_n) = \frac{\alpha \rho_{i,0}}{v_0} \mathcal{M}^2 r_n r_i \left( \frac{1}{r_B} - \frac{1}{r_n} \right), \quad (2.11)$$

$$\frac{\rho_{i,0}}{\rho_0} \mathcal{M}^2 \frac{r_i}{r_B} \frac{\partial}{\partial x} \left( \frac{1}{r_B} \right) + \frac{\rho_{i,0} \mu_n}{\rho_0 \mu_i} \frac{\partial}{\partial x} (r_i) + \frac{1}{\beta} \frac{\partial}{\partial x} (r_B^2) = -\frac{\alpha \rho_{i,0}}{v_0} \mathcal{M}^2 r_n r_i \left( \frac{1}{r_B} - \frac{1}{r_n} \right), \quad (2.12)$$

in which  $\mathcal{M}$  and  $\beta$  are two dimensionless parameters defined as

$$\mathcal{M}^2 \equiv \left( \frac{v_0}{c_s} \right)^2, \quad \frac{1}{\beta} \equiv \frac{B_0^2}{8\pi \rho_0 c_s^2} = \frac{1}{2} \left( \frac{v_{A,0}}{c_s} \right)^2, \quad (2.13)$$

that is, upstream values of the square of Mach number and (half of) the square of the Alfvén Mach number of neutrals, respectively. In Equations (2.11)–(2.13) and subsequently, we use the shorthand notation  $c_{sn} \rightarrow c_s$ ,  $\rho_{n,0} \rightarrow \rho_0 \equiv \mu_n n_0$ , and  $v_{An,0} \rightarrow v_{A,0}$ . The drag force terms on the right-hand sides of Equations (2.11) and (2.12) have equal magnitudes and opposite signs. Note that although Equations (2.11) and (2.12) represent the case with magnetic field parallel to the shock front, the results for the case with more general geometry are qualitatively similar (see Appendix A for detailed discussion).

### 2.2.3 Governing Ordinary Differential Equation

Typically, we have  $\mu_i/\mu_n \approx 30/2.3 \approx 13$ , and

$$\alpha = \frac{\langle \sigma v_{\text{rel}} \rangle}{\mu_i + \mu_n} \approx \frac{2 \times 10^{-9} \text{ cm}^3 \text{ s}^{-1}}{32.3 m_{\text{H}}} = 3.7 \times 10^{13} \text{ cm}^3 \text{ s}^{-1} \text{ g}^{-1} \quad (2.14)$$

(Draine et al. 1983). The Mach number  $\mathcal{M}$  is generally at least  $\sim 10$ , the plasma parameter is uncertain, but presumably  $\beta \sim 0.01 - 1$ , and since we are considering lightly ionized fluid,  $x_{i,0} \equiv n_{i,0}/n_0$  is a very small number,  $\sim 10^{-6}$  (here,  $n_0 = \rho_0/(2.3m_{\text{H}})$ ). The compression ratios  $r_n$ ,  $r_B$ , and  $r_i$  are dimensionless and are maximal downstream, with typical values  $\sim 10$ . Therefore, the last term on the left-hand side in Equation (2.12) dominates over the other two terms.

Retaining only the largest terms in the ion momentum equation yields

$$\frac{dr_B^2}{dx} = -\beta \frac{\alpha \rho_{i,0}}{v_0} \mathcal{M}^2 r_n r_i \left( \frac{1}{r_B} - \frac{1}{r_n} \right). \quad (2.15)$$

Using this result, the neutral momentum equation can be written as

$$\frac{d}{dx} \left( \frac{\mathcal{M}^2}{r_n} \right) + \frac{d}{dx} (r_n) = -\frac{1}{\beta} \frac{d}{dx} (r_B^2), \quad (2.16)$$

or

$$\frac{\mathcal{M}^2}{r_n} + r_n + \frac{r_B^2}{\beta} = \text{const.} = \mathcal{M}^2 + 1 + \frac{1}{\beta}, \quad (2.17)$$

an expression of conservation of momentum of the magnetized medium. On the right-hand side of Equation (2.17), we have used  $r_n = 1 = r_B$  upstream. Equations (2.15) and (2.16) represent the ‘‘strong coupling’’ approximation, in which the full magnetic force on the ions is conveyed to the neutrals, i.e.,

$$\mathbf{f}_d = \alpha \rho_i \rho_n (\mathbf{v}_i - \mathbf{v}_n) = \frac{(\nabla \times \mathbf{B}) \times \mathbf{B}}{4\pi} \quad (2.18)$$

(Shu 1992, Equation (27.8)).

We can solve Equation (2.17) to obtain

$$r_B = \left[ 1 + \beta (r_n - 1) \left( \frac{\mathcal{M}^2}{r_n} - 1 \right) \right]^{1/2}; \quad (2.19)$$

once  $r_n(x)$  is known, this gives  $r_B(x)$ . The compression ratio  $r_f$  for both neutrals and magnetic field lines in the post-shock region is obtained by setting  $r_B = r_f = r_n$  in Equation (2.19), yielding

$$r_f = \frac{2\beta\mathcal{M}^2}{1 + \beta + [(1 + \beta)^2 + 4\beta\mathcal{M}^2]^{1/2}}. \quad (2.20)$$

Note that if  $\beta\mathcal{M}^2 \gg 1$ , for a strong shock,

$$r_f \approx \sqrt{\beta}\mathcal{M} = \sqrt{2} \frac{v_0}{v_{A,0}}. \quad (2.21)$$

In dimensional form, this is

$$r_f \approx 9.8 \left( \frac{n_0}{100\text{cm}^{-3}} \right)^{1/2} \left( \frac{v_0}{\text{km/s}} \right) \left( \frac{B_0}{\mu\text{G}} \right)^{-1}. \quad (2.22)$$

Note that for oblique C shocks,  $r_B \neq r_f$  in the post-shock region, and they both depend on the angle  $\theta$  between  $\mathbf{B}$  and  $\mathbf{v}$ . Appendix A provides expressions for generalized  $r_f(\theta)$  with Equation (A.20) and  $r_{B,f}(\theta)$  with Equation (A.19).

Combining Equations (2.19) and (2.15), we obtain an ODE for  $r_n$ . The governing equation is

$$\frac{dr_n}{dx} = \frac{-Dr_n r_i}{1 - \frac{\mathcal{M}^2}{r_n^2}} \left[ \frac{1}{r_n} - \frac{1}{\sqrt{1 + \beta (r_n - 1) \left( \frac{\mathcal{M}^2}{r_n} - 1 \right)}} \right], \quad (2.23)$$

where

$$D \equiv \frac{\alpha\rho_{i,0}}{v_0} \mathcal{M}^2 = \frac{\alpha\mu_i}{c_s^2} x_{i,0} n_0 v_0. \quad (2.24)$$

If we use  $c_s = 0.2 \text{ km/s } (T/10\text{K})^{1/2}$ ,

$$D = 150 \text{ pc}^{-1} \left( \frac{n_0}{100 \text{ cm}^{-3}} \right) \left( \frac{v_0}{\text{km/s}} \right) \left( \frac{x_{i,0}}{10^{-6}} \right) \left( \frac{T}{10\text{K}} \right)^{-1}. \quad (2.25)$$

## 2.2.4 Ionization Fraction

To solve the ODE in Equation (2.23), we need a relation between  $r_n$  and  $r_i$ . In the dense interstellar medium, the main source of neutral ionization is cosmic rays, while ions may recombine in the gas phase, or on dust grains. The evolution of ion number density can be written as

$$\frac{dn_i}{dt} = \zeta_{\text{CR}} n_n - \alpha_{\text{gas}} n_i^2 - \alpha_{\text{grain}} n_i n_n. \quad (2.26)$$

Comparing the orders of magnitude of the three coefficients,  $\zeta_{\text{CR}} \sim 10^{-17} - 10^{-16} \text{ s}^{-1}$  for cosmic ray ionization (Shu 1992; Draine et al. 1983),  $\alpha_{\text{gas}} \sim 10^{-7} - 10^{-5} \text{ cm}^3 \text{ s}^{-1}$  (Tielens 2005, Table 4.11), and  $\alpha_{\text{grain}} \sim 10^{-15} \text{ cm}^3 \text{ s}^{-1}$  when  $T \sim 10 \text{ K}$  (Weingartner & Draine 2001). In moderate-density clouds  $n_i/n_n \sim 10^{-5} - 10^{-7}$  and  $n_n \sim 10^2 - 10^3 \text{ cm}^{-3}$ , so we can drop the grain surface recombination term. The ion balance equation becomes

$$\frac{\partial n_i}{\partial t} + \nabla \cdot (n_i \mathbf{v}_i) \approx \zeta_{\text{CR}} n_n - \alpha_{\text{gas}} n_i^2. \quad (2.27)$$

### 2.2.4.1 Recombination-Ionization Equilibrium

In solving Equation (2.27), one possible approximation is to assume ionization-recombination equilibrium everywhere. In this case,  $\zeta_{\text{CR}} n_n \approx \alpha_{\text{gas}} n_i^2$ , so that

$$n_i = \sqrt{\frac{\zeta_{\text{CR}}}{\alpha_{\text{gas}}}} n_n^{1/2} \equiv 10^{-6} \chi_{i0} n_n^{1/2}, \quad (2.28)$$

for

$$\chi_{i0} \equiv 10^6 \times \sqrt{\frac{\zeta_{\text{CR}}}{\alpha_{\text{gas}}}}, \quad (2.29)$$

where the coefficient  $\chi_{i0} \sim 1 - 20$  (McKee et al. 2010).

If we adopt Equation (2.28), then  $r_i = r_n^{1/2}$ , and the governing ODE becomes

$$\frac{dr_n}{dx} = \frac{-Dr_n^{3/2}}{1 - \frac{M^2}{r_n^2}} \left( \frac{1}{r_n} - \frac{1}{r_B} \right), \quad (2.30)$$

where  $r_B$  is given in terms of  $r_n$  by Equation (2.19).

#### 2.2.4.2 Frozen-in Magnetic Field

Another approach to Equation (2.27) is the so-called frozen-in condition (e.g. Warde 1990), which has been applied widely. In this approximation, ionizations and recombinations are neglected, so that for a steady flow,  $n_i v_i = \text{const.}$ , which implies  $r_i = r_B$ . This corresponds to a “frozen-in field”: the compression ratio of the magnetic field is the same as the ion flow. The governing ODE then becomes (using Equation (2.19))

$$\frac{dr_n}{dx} = \frac{-Dr_n}{1 - \frac{M^2}{r_n^2}} \left[ \frac{\sqrt{1 + \beta(r_n - 1) \left( \frac{M^2}{r_n} - 1 \right)}}{r_n} - 1 \right]. \quad (2.31)$$

One thing worth noting here is that in the frozen-in approximation, the ionization fraction in the post-shock region will be the same as in the upstream region. Since Equation (2.28) must hold far upstream and far downstream, we must choose whether to set  $x_{i,0}$  based on  $n_0$  or  $r_f n_0$ .

### 2.2.4.3 *Explicit Solution*

We can also retain all terms in the ionization-recombination equation in our numerical integration. Using  $n_i = n_0 r_n x_i$ , Equation (2.27) in steady state, for one dimension, yields

$$\frac{dx_i}{dx} = \frac{\zeta_{\text{CR}}}{v_0} r_B - \frac{\alpha_{\text{gas}} n_0}{v_0} x_i^2 r_n r_B + x_i \frac{d}{dx} \left[ \ln \left( \frac{r_B}{r_n} \right) \right], \quad (2.32)$$

Here,  $r_B$  is given in terms of  $r_n$  by Equation (2.19). By integrating Equations (2.32) and (2.23) together, we can calculate the explicit solution for the steady C shock system.

### 2.2.4.4 *Comparison of Ionization Treatments*

To compare ionization-recombination equilibrium and the explicit solution, we choose just an upstream value  $\chi_{i0}$ . For the frozen-in field case, we must also choose whether our solution will have the same upstream ionization fraction as the equilibrium case, or the same downstream value as the equilibrium case. Therefore there are four different cases for us to compare.

An example comparing the shock solutions for the four different ionization choices is shown in Fig. 2.1. Evidently, the approximation of ionization-recombination equilibrium yields a solution very close to the explicit solution. We have found that this is true for the full range of parameters of interest,  $n_0 \sim 10^2$  to  $10^3$  cm<sup>-3</sup>,  $v_0 \sim 1$  to 10 km/s,  $B_0 \sim 1$  to 15  $\mu$ G,  $\chi_{i0} \sim 1$  to 10. Henceforth, we shall adopt ionization-recombination equilibrium and use  $n_i \propto n_n^{1/2}$  so that  $r_i = r_n^{1/2}$ , and Equation (2.30)

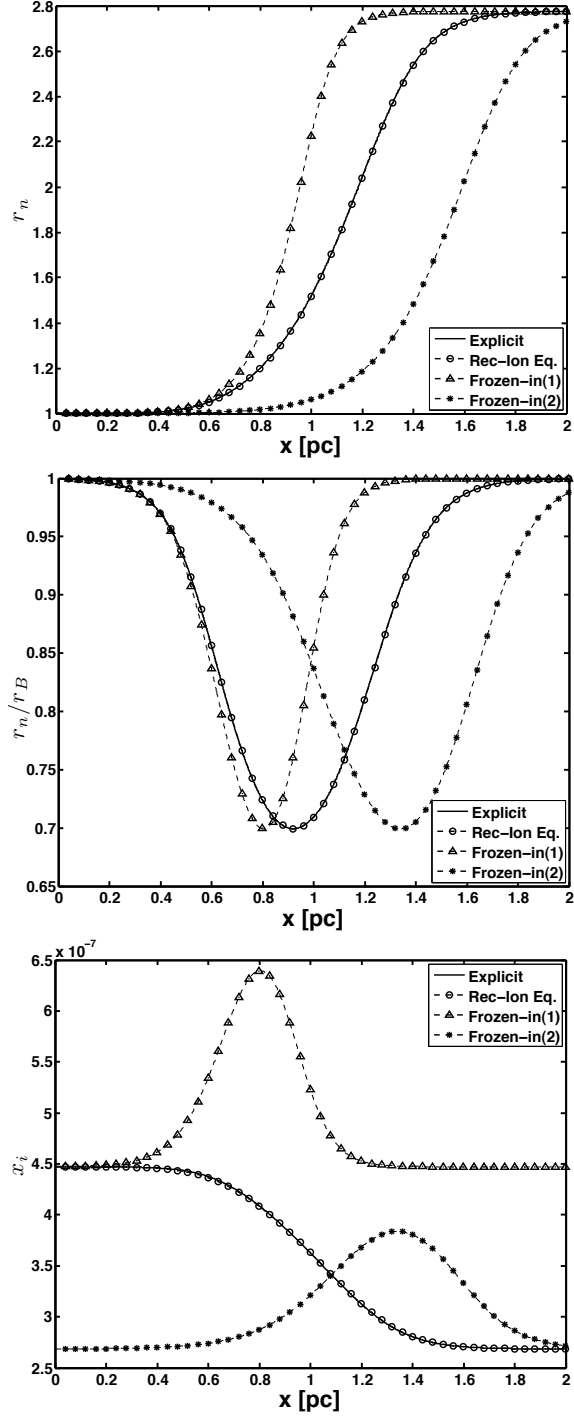


Figure 2.1: Comparison of C shock solution with different approaches to ionization. Adopted parameters are  $n_0 = 500 \text{ cm}^{-3}$ ,  $v_0 = 5 \text{ km/s}$ ,  $B_0 = 10 \mu\text{G}$ , and  $\chi_{i0} = 10$ . “Frozen-in(1)” means upstream ionization is in equilibrium, and “Frozen-in(2)” means downstream ionization is in equilibrium. Evidently, recombination-ionization equilibrium (*open circles*) is an excellent approximation to the exact solution (*solid curve*).

governs steady C shocks.

## 2.3 Steady C Shock Thickness

For any given set of parameters  $n_0$ ,  $v_0$ ,  $B_0$ , and  $\chi_{i0}$ , Equation (2.30) can be integrated to obtain a steady C shock solution. However, it is also useful to obtain estimates of the dependence of the C shock thickness on the basic flow parameters. This parameterization is potentially useful in diagnosing magnetic field strengths from observations. In addition, it provides a helpful guide to assessing the scales at which ambipolar diffusion becomes important in GMCs dominated by strong turbulence. If, by appropriate simplifications we can integrate the governing ODE of Equation (2.30) analytically, we can obtain an approximate expression for the shock thickness as a function of  $n_0$ ,  $v_0$ ,  $B_0$ , and  $\chi_{i0}$ . Note that, since the governing equations for oblique shocks are qualitatively similar to the simplified case applied here, the oblique shock thickness can be approached using the same methods discussed in this section (see Appendix A).

### 2.3.1 Exact Solution

From numerical integrations of Equation (2.30) with a range of parameters, we have found that  $r_n/r_B$  drops very quickly at the beginning, becomes flat in the central region, then increases rapidly near the other edge of the shock (see bottom panels of Fig. 2.2 and 2.3). This behavior can be used to define the thickness of C-type shocks. Since the minimum of  $r_n/r_B$  depends on the parameters (see

Equation (2.42) below), we should ensure that our thickness definition is insensitive to this value. Based on these considerations, we adopt the following definition of shock thickness for exact numerical solutions:

$$x_s \equiv x \Big|_{r_n/r_B=0.95}, \quad x_f \equiv x \Big|_{r_n/r_B=0.95}, \quad x_f > x_s; \Rightarrow \text{shock thickness } L_{\text{exact}} \equiv |x_f - x_s|. \quad (2.33)$$

Note that for some weak shocks,  $r_n/r_B$  is always larger than 0.95. Therefore this definition also provides limitations in the parameter space to exclude shocks which are not strong and thus do not satisfy our strong shock analysis.

We have integrated the shock ODE for a range of parameters, and computed the shock thickness according to the definition in Equation (2.33). This is the dataset of exact solutions of C shock thickness over a parameter grid with 10 values of  $n_0$  equally spaced between  $10^2$  and  $10^3 \text{ cm}^{-3}$ , 14 values of  $v_0$  equally spaced between 2 and 15 km/s, 14 values of  $B_0$  equally spaced between 2 and 15  $\mu\text{G}$ , and 11 values of  $\chi_{i0}$  equally spaced between 1 and 21. The range of C shock thickness is 0.1 to 20 pc in this parameter range. Note that all parts of this parameter space are not necessarily astronomically realistic. For example, low  $n_0$  and high  $v_0$  is unlikely to have low  $\chi_{i0}$ , so very large C shock thickness is not likely to be found.

Also note that even for C shock thickness  $\sim 1$  pc, in a real molecular cloud all the parameters are likely to vary within this length scale, instead of staying constant as in our models. However, our solutions still provide a useful guide to approximate shock thicknesses for parameters within a given range.

### 2.3.2 Zeroeth-order Approximation

We consider the relative magnitudes of the terms in Equations (2.19) and (2.30). First, since  $c_s \sim 0.2$  km/s whereas  $v_0 \gtrsim 1$  km/s, in general  $\mathcal{M}^2$  is a very large number, and typically  $\mathcal{M}^2 \gg r_n^2$  (see Equation (2.21)). Also, from Fig. 2.1, the ratio  $r_n/r_B$  is small in much of the shock region. If we let  $r_n/r_B \ll 1$ , a “zeroeth-order” approximation to Equation (2.30) is

$$\frac{dr_n}{dx} \approx \frac{Dr_n^{5/2}}{\mathcal{M}^2}. \quad (2.34)$$

This can be integrated analytically to yield

$$r_n(x) = \left(1 - \frac{3}{2} \frac{Dx}{\mathcal{M}^2}\right)^{-2/3}. \quad (2.35)$$

This “zeroeth-order” approximation to the shock structure using Equation (2.35) is shown in Fig. 2.2 and 2.3 for two parameter sets, in comparison to the exact solution. The zeroeth-order shock thickness  $L_{\text{zeroeth}}$  is defined as  $x$  such that  $r_n \rightarrow r_f$  in Equation (2.35), giving

$$L_{\text{zeroeth}} = \frac{2}{3} \frac{\mathcal{M}^2}{D} \left(1 - r_f^{-3/2}\right) \approx \frac{2}{3} \frac{\mathcal{M}^2}{D}, \quad (2.36)$$

where the second approximation assumes a strong shock,  $r_f \gg 1$ .

Substituting Equation (2.24) for  $D$  in Equation (2.36), we obtain a thickness estimate in terms of physical parameters

$$L_{\text{zeroeth}} = \frac{2}{3} \frac{v_0}{\alpha \rho_{i,0}} \propto \frac{v_0}{\chi_{i0} n_0^{1/2}}, \quad (2.37)$$

or in dimensional form,

$$L_{\text{zeroeth}} \approx 0.12 \text{ pc} \times \left(\frac{n_0}{100 \text{ cm}^{-3}}\right)^{-1/2} \left(\frac{v_0}{\text{km/s}}\right) \left(\frac{\chi_{i0}}{10}\right)^{-1}. \quad (2.38)$$

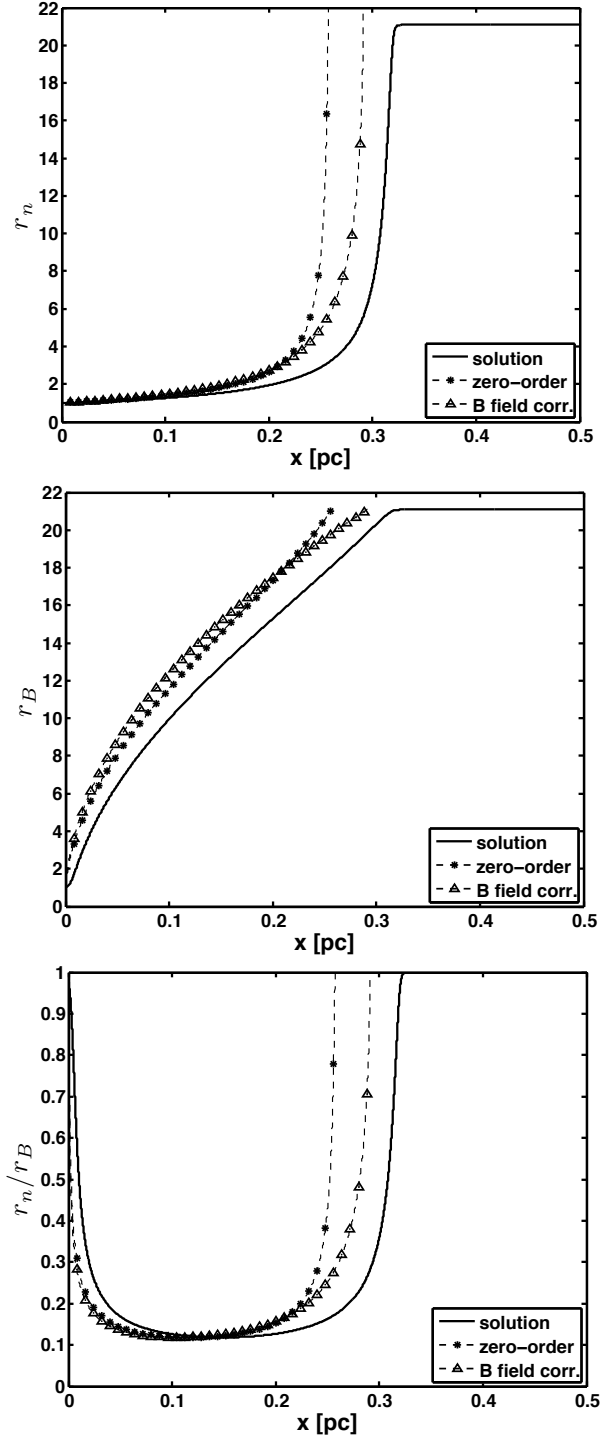


Figure 2.2: Exact C shock solution (*solid*) compared to the “zeroeth-order” estimate of Equation (2.35) (*circles*) and an improved approximation given by Equation (2.43) (*triangles*), for parameters  $n_0 = 500 \text{ cm}^{-3}$ ,  $v_0 = 5 \text{ km/s}$ ,  $B_0 = 5 \text{ } \mu\text{G}$ , and  $\chi_{i0} = 10$ .

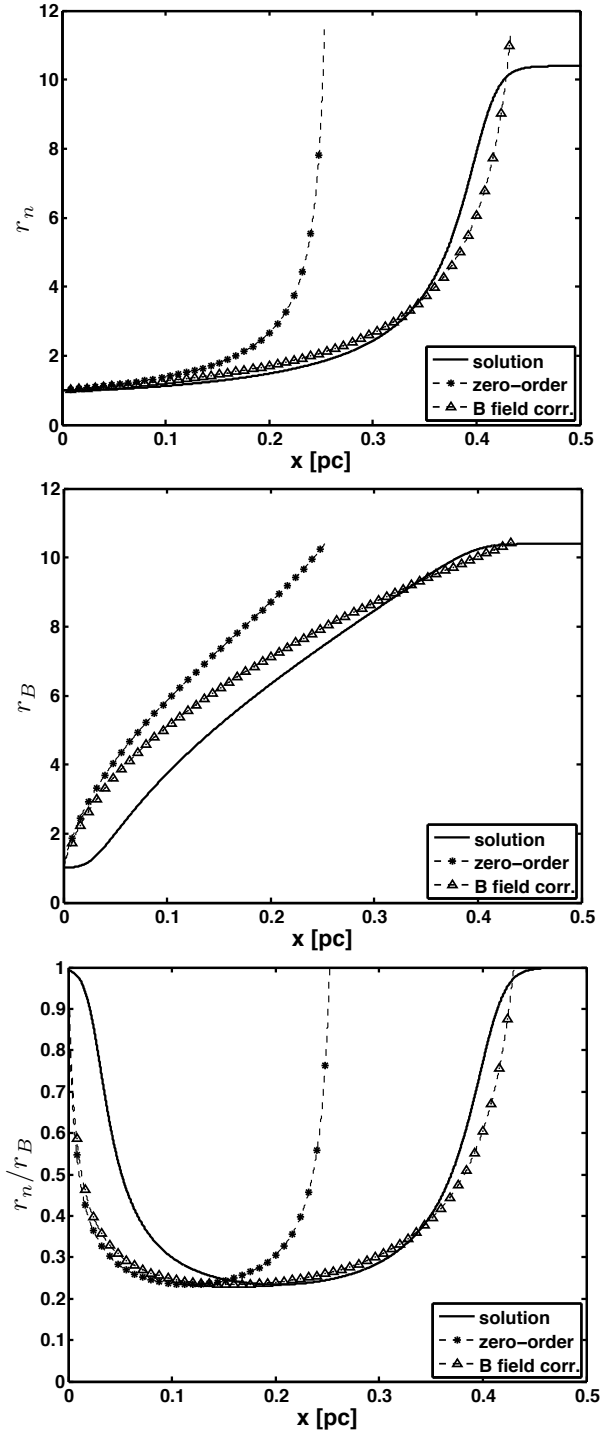


Figure 2.3: Same as Fig. 2.2, for  $n_0 = 500 \text{ cm}^{-3}$ ,  $v_0 = 5 \text{ km/s}$ ,  $B_0 = 10 \text{ } \mu\text{G}$ , and  $\chi_{i0} = 10$ .

Thus, the shock thickness increases with higher upstream velocity, and decreases with higher upstream neutral density and ionization fraction. In this “zeroeth-order” approximation the shock thickness does not depend on the upstream magnetic field strength. From the examples shown in Fig. 2.2 and 2.3, we can see that although the zeroeth-order solution follows the general behavior of C shocks, it is not accurate for strongly-magnetized cases (Fig. 2.3). Compared with the dataset of exact solutions discussed in previous section, the RMS value of  $(L_{\text{exact}} - L_{\text{zeroeth}})/L_{\text{exact}}$  is 0.355, and the range of  $(L_{\text{exact}} - L_{\text{zeroeth}})/L_{\text{exact}}$  is  $-0.8$  to  $0.28$ .

The dependence on the velocity, ion density, and collision coefficient in Equation (2.37) can be understood in terms of the drag force between ions and neutrals. The total momentum flux in neutrals entering the shock is  $\rho_0 v_0^2$ . The mean drag force per volume is  $\sim \alpha \rho_0 \rho_{i,0} v_0$ . The ratio of these quantities, which is the characteristic distance over which momentum exchange takes place, is

$$L \sim \frac{\rho_0 v_0^2}{\alpha \rho_0 \rho_{i,0} v_0} \sim \frac{v_0}{\alpha \rho_{i,0}} \propto v_0 n_0^{-1/2} \chi_{i0}^{-1}. \quad (2.39)$$

This dependence is similar to Equation (3.12) in Draine & McKee (1993) if the Alfvén speed in the fluid is similar to the upstream velocity,  $v_A \sim v_0$ . Although they obtained an estimate using different assumptions and approximations, the basic idea that the momentum transfer rate determines the shock thickness is similar.

### 2.3.3 Magnetic Field Influence

To obtain a more accurate estimate of the C shock thickness, we return to the differential equation (2.11) for neutral momentum flux, making use of Equa-

tion (2.24) and the ionization equilibrium condition  $r_i = r_n^{1/2}$ ,

$$\frac{d}{dx} \left( r_n + \frac{\mathcal{M}^2}{r_n} \right) = -Dr_n^{3/2} \left( \frac{1}{r_n} - \frac{1}{r_B} \right) = -Dr_n^{1/2} \left( 1 - \frac{r_n}{r_B} \right). \quad (2.40)$$

We integrate this equation, using constant values on the right-hand-side

$$\langle r_n^{1/2} \rangle \rightarrow \frac{1 + r_f^{1/2}}{2} \approx \frac{\sqrt{r_f}}{2}, \quad \left\langle 1 - \frac{r_n}{r_B} \right\rangle \rightarrow \left( \frac{1 - (r_n/r_B)_{\min}}{2} \right), \quad (2.41)$$

where the minimum value of  $r_n/r_B$  can be derived explicitly from Equation (2.19)

as

$$\left. \frac{r_n}{r_B} \right|_{\min} = \frac{3\sqrt{3}}{2\sqrt{\beta}\mathcal{M}}. \quad (2.42)$$

This yields a quadratic for  $r_n$  as a function of  $x$ :

$$r_n^2 - \left( \mathcal{M}^2 + 1 - D \langle r_n^{1/2} \rangle \left\langle 1 - \frac{r_n}{r_B} \right\rangle x \right) r_n + \mathcal{M}^2 = 0. \quad (2.43)$$

Solving Equation (2.43) for  $r_n(x)$  gives us another analytical approximation of the shock structure. When compared with the explicit solution and the zeroth-order approximation in Fig. 2.2 and 2.3, we can see that this correction is necessary only when the background magnetic field is strong (Fig. 2.3).

For Equation (2.43) the magnetically-corrected estimate of the shock thickness ( $x = L_{\text{est}}$  such that  $r_n = r_f$ ) can be written as

$$L_{\text{est}} = \frac{(\mathcal{M}^2 - r_f)(r_f - 1)}{D \langle r_n^{1/2} \rangle \langle 1 - r_n/r_B \rangle r_f}. \quad (2.44)$$

Assuming  $\mathcal{M}^2 \gg r_f \gg 1$  and  $(r_n/r_B)_{\min} \ll 1$ , and using Equation (2.24), we have

$$L_{\text{est}} \approx \frac{4\mathcal{M}^2}{Dr_f^{1/2}} = \frac{4v_0}{\alpha\rho_{i,0}r_f^{1/2}}. \quad (2.45)$$

Note that a similar result can be obtained for the generalized case with an oblique C shock (Equation (A.23)). See Appendix A for detailed discussion.

Taking the strong-compression limit  $r_f \approx \sqrt{2}v_0/v_{A,0}$  of Equation (2.21), we have

$$L_{\text{est}} = \frac{2^{7/4}v_0^{1/2}v_{A,0}^{1/2}}{\alpha\rho_{i,0}} \propto n_0^{-3/4}v_0^{1/2}B_0^{1/2}\chi_{i0}^{-1}, \quad (2.46)$$

or in dimensional form

$$L_{\text{est}} = 0.22 \text{ pc} \times \left(\frac{n_0}{100\text{cm}^{-3}}\right)^{-0.75} \left(\frac{v_0}{\text{km/s}}\right)^{0.5} \left(\frac{B_0}{\mu\text{G}}\right)^{0.5} \left(\frac{\chi_{i0}}{10}\right)^{-1}. \quad (2.47)$$

Compared with Equation (2.37), the shock thickness still depends positively on inflow velocity and negatively on upstream density and ionization fraction, but now a dependence on the magnetic field enters as well. Compared with the dataset of exact solutions discussed above, the RMS value of  $(L_{\text{exact}} - L_{\text{est}})/L_{\text{exact}}$  is 0.13, and the range of  $(L_{\text{exact}} - L_{\text{est}})/L_{\text{exact}}$  is  $-0.21$  to  $0.26$ . Wardle (1990) and Li et al. (2006) find  $L_{\text{shock}} \sim \sqrt{2}v_{A,0}/(\alpha\rho_{i,0})$  in the case where ions are frozen in; this is smaller than Equation (2.46) by a factor  $2^{-5/4}(v_{A,0}/v_0)^{1/2}$ .

### 2.3.4 Numerical Approach

Using the dataset of exact solutions discussed in Section 2.3.1, we construct a simultaneous linear fit for  $\log L_{\text{exact}}$  to  $\log n_0$ ,  $\log B_0$ ,  $\log v_0$ , and  $\log \chi_{i0}$ . We find

$$L_{\text{fit}} = 0.21 \text{ pc} \times \left(\frac{n_0}{100\text{cm}^{-3}}\right)^{-0.73} \left(\frac{v_0}{\text{km/s}}\right)^{0.54} \left(\frac{B_0}{\mu\text{G}}\right)^{0.46} \left(\frac{\chi_{i0}}{10}\right)^{-1}. \quad (2.48)$$

Over the parameter grid, the RMS value of  $(L_{\text{exact}} - L_{\text{fit}})/L_{\text{exact}}$  is 0.08, and the range of  $(L_{\text{exact}} - L_{\text{fit}})/L_{\text{exact}}$  is  $-0.29$  to  $0.22$ .

The result in Equation (2.48) agrees with our expectation that the shock thickness depends on the magnetic field. Also, the dependences on all parameters are

Table 2.1: Steady C shock Thickness Comparison

Model	$n_0$ ( $\text{cm}^{-3}$ )	$v_0$ (km/s)	$B_0$ ( $\mu\text{G}$ )	$\chi_{i0}$	$L_{\text{shock}}$ (pc)		
					exact eq. (2.30)	est. eq. (2.45)	fit eq. (2.48)
N01	100	5	10	5	3.03	3.15	2.89
N03	300	5	10	5	1.20	1.38	1.30
N05	500	5	10	5	0.82	0.94	0.89
N08	800	5	10	5	0.58	0.66	0.63
N10	1000	5	10	5	0.50	0.56	0.54
V04	200	4	10	5	1.41	1.68	1.54
V06	200	6	10	5	1.55	2.05	1.92
V08	200	8	10	5	1.79	2.37	2.24
V10	200	10	10	5	2.08	2.65	2.53
V12	200	12	10	5	2.38	2.90	2.79
B02	200	5	2	5	0.92	0.84	0.83
B04	200	5	4	5	1.08	1.18	1.14
B06	200	5	6	5	1.26	1.45	1.38
B08	200	5	8	5	1.46	1.68	1.57
B10	200	5	10	5	1.66	1.87	1.74
B12	200	5	12	5	1.89	2.05	1.89
B14	200	5	14	5	2.12	2.22	2.03
X01	200	5	10	1	8.32	9.37	8.71
X06	200	5	10	6	1.39	1.56	1.45
X10	200	5	10	10	0.83	0.94	0.87
X15	200	5	10	15	0.55	0.62	0.58
X20	200	5	10	20	0.42	0.47	0.44

extremely close to Equation (2.47). Table 2.1 lists a set of model parameters (to be used in time-dependent simulations) and the C shock thickness based on the analytic estimate in Equation (2.45) and the multivariate fit in Equation (2.48), in comparison with the results from explicit integration of the ODE (Equation (2.30)). Both approaches are useful to estimate the shock thickness.

## 2.4 C Shock Formation

### 2.4.1 Numerical Algorithm for Ambipolar Diffusion

To investigate how C shocks develop in time, we use a modified version of the numerical MHD code, *Athena* (Stone et al. 2008). *Athena* employs a single-step, directionally unsplit Godunov scheme to obtain conservative, second-order accurate solutions of the ideal MHD equations (Gardiner & Stone 2005).

In the strong coupling limit, the drag force  $\mathbf{f}_d = \alpha\rho_i\rho_n(\mathbf{v}_i - \mathbf{v}_n)$  is equal to the Lorentz force  $\mathbf{f}_L = [(\nabla \times \mathbf{B}) \times \mathbf{B}] / (4\pi)$ . The momentum equation for neutrals is thus identical to that in the ideal MHD limit. The mass conservation equation for neutrals is also the same as for ideal MHD. In this approximation,  $\mathbf{v}_i = \mathbf{v}_n + [(\nabla \times \mathbf{B}) \times \mathbf{B}] / (4\pi\alpha\rho_i\rho_n)$ , so that the induction equation (2.4) becomes

$$\frac{\partial \mathbf{B}}{\partial t} - \nabla \times (\mathbf{v}_n \times \mathbf{B}) = \nabla \times \left[ \frac{((\nabla \times \mathbf{B}) \times \mathbf{B}) \times \mathbf{B}}{4\pi\rho_i\rho_n\alpha} \right]. \quad (2.49)$$

With  $\mathbf{v}_d = \mathbf{v}_i - \mathbf{v}_n$  the drift velocity between ions and neutrals, we can write the correction term in Equation (2.49) in terms of a “drift” EMF,

$$\mathcal{E}_d = \mathbf{v}_d \times \mathbf{B} = \frac{[(\nabla \times \mathbf{B}) \times \mathbf{B}] \times \mathbf{B}}{4\pi\rho_i\rho_n\alpha}. \quad (2.50)$$

In our simplified 1-D problem,  $\mathbf{B} = B_y \hat{\mathbf{y}}$ ,  $\mathbf{v} = v_x \hat{\mathbf{x}}$ , and the discretized magnetic field corrected by ambipolar diffusion before each step, at interface position  $i\Delta x$  and time  $n\Delta t$ , is

$$B_y|_i^{n+1} = B_y|_i^n + \frac{\Delta t}{\Delta x} \left( \mathcal{E}_{d,z}|_{i+\frac{1}{2}}^n - \mathcal{E}_{d,z}|_{i-\frac{1}{2}}^n \right),$$

and

$$\mathcal{E}_{d,z}|_{i+\frac{1}{2}}^n = \frac{1}{4\pi\alpha} \left( \frac{B_y|_{i+1}^n - B_y|_i^n}{\Delta x} \right) \frac{B_y^2}{\rho_i \rho_n} \Big|_{i+\frac{1}{2}}^n.$$

This term is implemented in *Athena* as an operator-split update to the magnetic field. The mesh resolution is set to be 0.01 pc.

In setting the timestep, we implement the super-timestepping approach as described by Choi et al. (2009), choosing the factor  $\nu = 0.2$ , and taking the ambipolar diffusion timestep

$$\Delta t_{\text{AD}} = 2\pi\alpha (\text{CFL number}) (\Delta x)^2 \cdot \min \left[ \frac{\rho_n \rho_i}{B_y^2} \right], \quad (2.51)$$

where the CFL number is set to be 0.8 in all simulations.

For figures presenting numerical results,  $n_n \rightarrow n$  and  $\mathbf{v}_n \rightarrow \mathbf{v}$ .

## 2.4.2 Convergent Flow Test

### 2.4.2.1 Simple Convergent Flow Test

One way to produce shocks in a numerical simulation is to use a simple convergent flow, in which the initial conditions are

$$n = \text{const.}, \quad B_y = \text{const.}, \quad v_x = \begin{cases} v_{\text{inflow}}, & \text{left half} \\ -v_{\text{inflow}}, & \text{right half.} \end{cases} \quad (2.52)$$

This will evolve to a dense post-shock region in the center, with outward-propagating reverse C-type structures at the left and right (Fig. 2.4).

The C shock structures seen at  $x \approx 1.5$  and  $x \approx 3.5$  in Fig. 2.4 are the same as the steady solutions obtained by integration of Equation (2.30), as confirmed by comparing the detailed profiles (not shown). Note that the mass-to-flux ratio  $n/B_y$

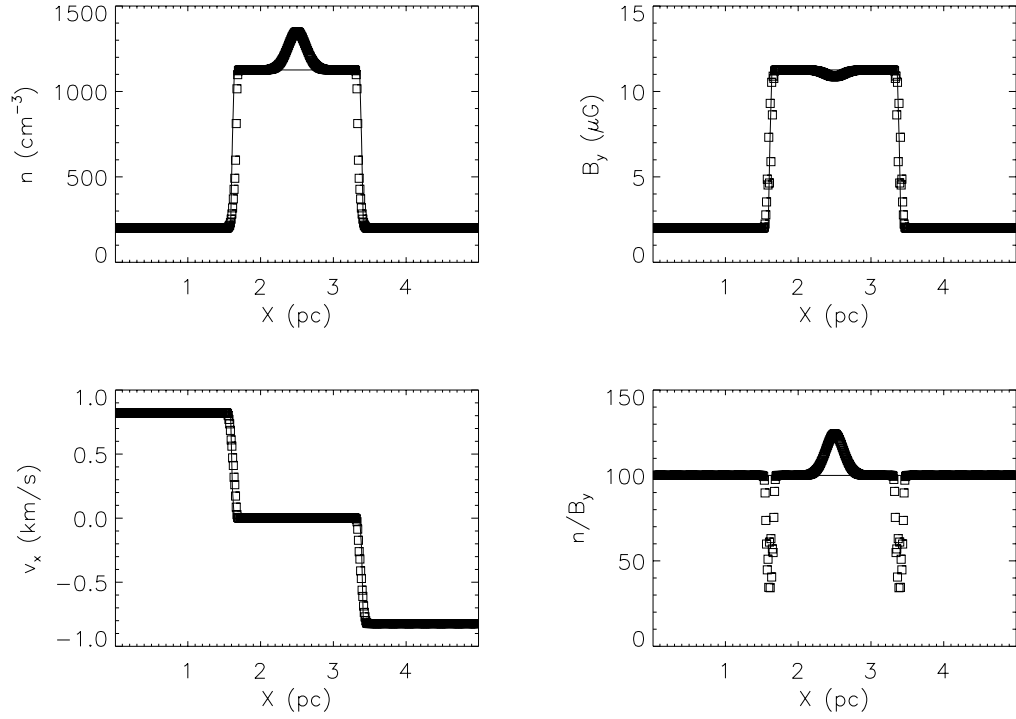


Figure 2.4: Transient C shock structure (*squares*) compared with ideal MHD shock (*thin lines*), generated from convergent flow, for parameters  $n_0 = 200 \text{ cm}^{-3}$ ,  $v_0 = 1 \text{ km/s}$ ,  $B_0 = 2 \mu\text{G}$ , and  $\chi_{i0} = 10$ . The central peak in density  $n$  and mass-to-flux ratio  $n/B_y$  is a signature of early C shock structure.

is analogous to  $r_n/r_B$  (except not normalized by upstream values). The dips in  $n/B_y$  at the C shock locations correspond to the “well” in  $r_n/r_B$  seen in Fig. 2.2 and 2.3. However, the central peaks in both neutral density  $n$  and the mass-to-flux ratio  $n/B_y$  in Fig. 2.4 are not a feature of steady C shocks. As the solution shown in Fig. 2.4 evolves further in time, these peaks disappear. Thus, these peaks are a signature of transient C shock development, as we discuss further below.

#### *2.4.2.2 Colliding Clouds*

The initial conditions for the simple converging flow are somewhat artificial, in that only the velocity is discontinuous. Thus, we would like to test whether shocks formed under more realistic conditions also show the transient peaks in  $n$  and  $n/B_y$  described above.

We consider the collision of two idealized clumps inside a large molecular cloud. We suppose that the two clumps are both denser than their surrounding, but the mass-to-flux ratios are the same throughout the whole cloud. We imagine that the large-scale turbulence in the molecular cloud imposes velocities such that the two dense clumps collide with each other, producing a shock. We simulate the scenario described, setting the background density to be 5% of the value in the dense clumps, and the initial velocity of this gas to be zero. We focus just on the collision region, so that the right and left sides of the domain are set to “clump” conditions, as in Equation (2.52).

When the two dense clumps meet each other, a strong shock forms (Fig. 2.5).

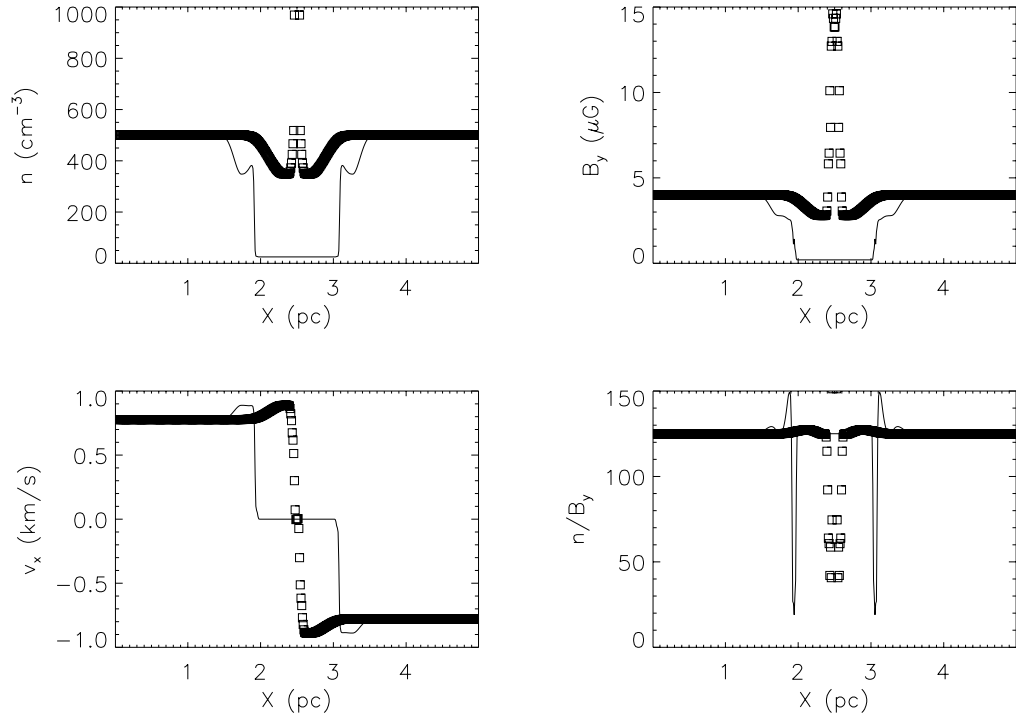


Figure 2.5: Two dense clumps collide with each other and produce a shock (*squares*). Conditions at a time 0.88 Myr prior to the collision are shown as thin lines for comparison. Parameters are  $n_0 = 500 \text{ cm}^{-3}$ ,  $v_0 = 1 \text{ km/s}$ ,  $B_0 = 4 \mu\text{G}$ , and  $\chi_{i0} = 10$ .

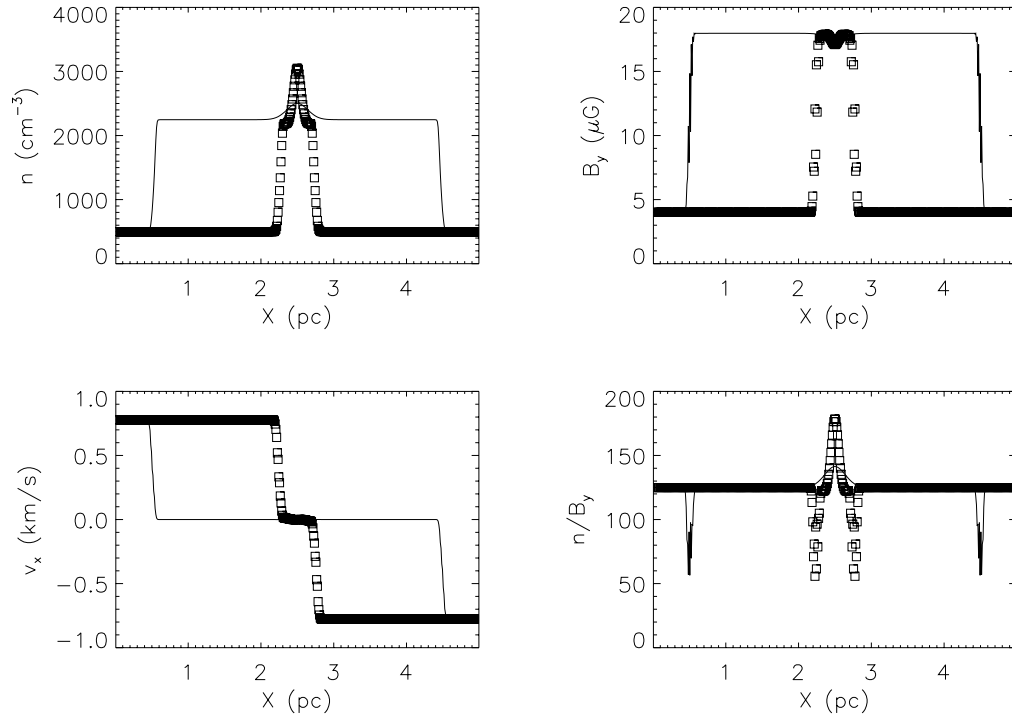


Figure 2.6: Shock structure generated from the colliding clumps (*squares*), at a time 1.08 Myr after the stage shown in Fig. 2.5. Note that the central peaks in  $n$  and  $n/B_y$  are qualitatively similar to those in Fig. 2.4. These central peaks will then expand and smooth out (thin lines show solution after an additional 7.67 Myr).

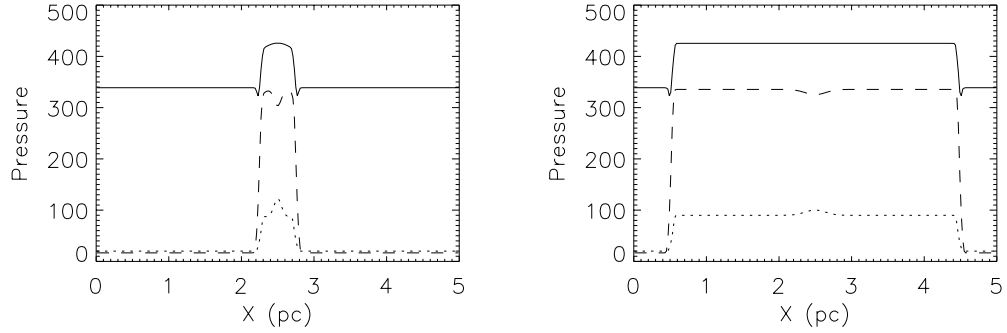


Figure 2.7:  $P_{\text{tot}}$  (*solid*),  $P_B$  (*dashed*), and  $P_{\text{gas}}$  (*dotted*) in the colliding clump simulation, corresponding to the earlier (*left*) and later (*right*) stages in Fig. 2.6. Note that the magnetic pressure dominates the post-shock region, with the central peak in thermal pressure compensated for by a reduction in the magnetic pressure. Over time, the thermal pressure peak and magnetic pressure valley decline due to diffusion within the post-shock region. In the frame of the (right- or left-ward) expanding shock fronts (not shown), the total pressure in the post-shock region is the same as the total pressure upstream. Units for pressure are  $[2.3m_{\text{H}} \text{ cm}^{-3}] [1 \text{ km s}^{-1}]^2$ .

Since all fluid variables ( $n$ ,  $B_y$ ,  $v_x$ ) are smooth and continuous prior to shock formation, the features produced are not a consequence of discontinuous initial conditions. This test case eventually evolves to profile similar to that in the simple convergent flow test (Fig. 2.6). The central peaks in density and mass-to-flux ratio show up as well. Subsequent evolution leads to a decline in the central peak in  $n$  and  $n/B_y$  (Fig. 2.6).

### 2.4.2.3 Transient C shock Development

Peaks in density above the “steady” shock solution have also been observed in other ambipolar diffusion simulations using different MHD codes (e.g. Choi et al. 2009). In addition, similar transient behavior of C shocks has been noted in

models with more complex chemistry implemented (e.g. Chieze et al. 1998; van Loo et al. 2009; Ashmore et al. 2010). Physically, we believe these peaks arise because the neutrals are effectively “unmagnetized” when the shock first forms. As a consequence, the neutrals can be very strongly compressed, forming what is seen as a central density peak in Figs. 2.4–2.6.

The magnetic field, however, does not follow the initial strong compression of the neutrals. Instead, the overly-compressed neutrals generate higher pressure in the central regions, inhibiting the magnetic flux from getting in. Fig. 2.7 shows the total pressure  $P_{\text{tot}} = \rho_n v_n^2 + P_{\text{gas}} + P_B$  of the system, where  $P_{\text{gas}} = \rho_n c_s^2$  and  $P_B = B^2/8\pi$ , with  $v_n$  measured in the “laboratory” frame. These three terms correspond to  $\mathcal{M}^2/r_n$ ,  $r_n$ , and  $r_B^2/\beta$  respectively, in Equation (2.17). Since *Athena* uses the conservative form of the momentum equation ( $\partial(\rho v)/\partial t + \partial P_{\text{tot}}/\partial x = 0$ ),  $P_{\text{tot}}$  must become constant in the post-shock region at late times. For strong shocks, the magnetic pressure term dominates at late times in the post-shock region. At early times, there is a slight depression of the magnetic field strength at the center of the shock, in order to balance the extremely high neutral gas pressure in the density peak.

Combining the strong neutral compression and slight magnetic exclusion, the mass-to-flux ratio is elevated in the center when a shock forms. The collisions between neutrals and ions will gradually slow down the incoming neutrals and compress ions and magnetic field to the center. Meanwhile, the neutrals in the central peak diffuse outward in order to balance the increasing magnetic pressure and keep the total pressure constant. Eventually, the ions and neutrals interact sufficiently that

a steady-state C shock structure develops. The post-shock  $n/B_y$  is the same as the upstream value. However, the ambipolar diffusion process takes time, and during the transient stage, a region of very strongly compressed neutrals will be present.

Our finding that there is a transient stage of very strong density compression, with an enhanced ratio of  $n/B_y$  or mass-to-magnetic flux, suggests that the very early stage of shock development in GMCs may be particularly important to star formation. The following sections examine this idea further.

## 2.5 Criticality of Clouds

### 2.5.1 Mass-to-flux Ratio

The mass-to-flux ratio is a crucial parameter defining whether the magnetic field can support a cloud against its own self-gravity. The critical value of  $M/\Phi_B$  for an uniform, spherical cloud has been derived to be  $M/\Phi_B|_{\text{crit}} = c_\Phi/\sqrt{G} \approx 0.126/\sqrt{G}$  (Mouschovias & Spitzer 1976). The numerical coefficient  $c_\Phi$  differs with the geometry of the cloud: an infinite sheet-like cloud has  $c_\Phi = 1/2\pi \approx 0.16$  (Nakano & Nakamura 1978), while Tomisaka et al. (1988) found  $c_\Phi = 0.17 - 0.18$  for clouds with various  $M/\Phi_B$  distributions (see review by McKee & Ostriker 2007). Since the value of  $c_\Phi$  varies only  $\sim 10\%$  with geometry, we choose the commonly-used  $c_\Phi = 1/2\pi$  (Kudoh & Basu 2011; Vázquez-Semadeni et al. 2011) as a reference value, while keeping in mind that core geometry is not explicitly defined for our slab system.

Practically, for magnetic field in the  $y$ -direction the ratio can be written as

$$\frac{M}{\Phi} = \frac{\int \rho dx \cdot L_y L_z}{\int B_y dx \cdot L_z} = \frac{L_y \int \rho dx}{\int B_y dx} \sim \frac{\Sigma}{\langle B_y \rangle}, \quad (2.53)$$

where we assume that if a core formed in the post-shock region, its effective length in the  $y$ -direction,  $L_y$ , would be comparable to that in the  $x$ -direction,  $L_x$ , so that  $\langle B_y \rangle = \int B_y dx / \int dx \sim \int B_y dx / L_y$ . The mass-to-flux ratio, in units of the critical value  $M/\Phi_B|_{\text{crit}} = (2\pi\sqrt{G})^{-1}$ , is

$$\Gamma \equiv \frac{2\pi\sqrt{G} \cdot \Sigma}{\langle B_y \rangle} = 3.8 \left( \frac{N(\text{H})}{10^{21} \text{cm}^{-2}} \right) \left( \frac{\langle B_y \rangle}{\mu\text{G}} \right)^{-1} \quad (2.54)$$

To convert the column of neutrals in our simulation to  $N(\text{H})$ , we use  $n = n_{\text{H}_2} + n_{\text{He}} = 0.6n_{\text{H}}$ . Note that the true value of the normalized mass-to-flux ratio would differ from Equation (2.54) by a factor  $L_y/L_x$ , which could be up to  $\sim 2$ .

If the mass-to-flux ratio of a prestellar core is larger than the critical value ( $\Gamma > 1$ ), i.e., the gravitational force exceeds the magnetic support, the core is supercritical and is eligible for collapse (subject to support by thermal pressure). In contrast, a subcritical core has a mass-to-flux ratio smaller than the critical value ( $\Gamma < 1$ ), and cannot collapse unless it loses magnetic energy in either the strong-gravity mode (the field lines diffuse outward through ambipolar diffusion while gravity holds the gas material together) in which  $\Gamma \sim 1$  is required, or the magnetic-dominated mode (neutral mass moves toward the center under the gravitational pull while ambipolar diffusion allows the magnetic field lines to remain stationary) so the mass-to-flux ratio increases.

## 2.5.2 Bonnor-Ebert Sphere

A typical low-mass prestellar core has  $\Sigma_{\text{core}} \sim 1 M_{\odot} / [(0.1 \text{ pc})^2 \pi] \approx 0.007 \text{ g} \cdot \text{cm}^{-2}$ , so that a core with  $B_{\text{initial}} \gtrsim 2\pi\sqrt{G} \cdot \Sigma_{\text{core}} \sim 10.7 \mu\text{G}$  may be subcritical.

More precisely, we consider the Bonnor-Ebert sphere radius for a core whose mean density is equal to the post-shock density  $\rho_f$ ,

$$R_{\text{BE}} = \frac{2.7c_s}{(4\pi G\rho_f)^{1/2}} \quad (2.55)$$

(e.g. Gong & Ostriker 2009), which is the largest sphere that can be supported by its own internal thermal pressure.

We note that, from Equation (2.45), the ratio of the shock thickness to the diameter of a Bonnor-Ebert sphere at the post-shock density is

$$\frac{L_{\text{est}}}{2R_{\text{BE}}} \approx \frac{0.7(4\pi G\rho_0)^{1/2}}{\alpha\rho_{i,0}} \left(\frac{v_0}{c_s}\right) \approx \frac{v_0}{\chi_{i0}c_s}. \quad (2.56)$$

A converging flow bounded by C shocks has breadth at least twice the shock thickness. Under conditions in GMCs where  $v_0/c_s \gtrsim 10$ , and  $\chi_{i0} \lesssim 10$ , this implies that shocks are sufficiently broad that Bonnor-Ebert spheres can fit within the post-shock region. Thus, if magnetic fields are weak enough, cores could grow and collapse in post-shock gas.

The mass-to-flux ratio for a sphere of radius  $R_{\text{BE}}$  in a post-shock magnetized region, without ambipolar diffusion, is

$$\left.\frac{M}{\Phi_B}\right|_{\text{BE}} = \frac{4\pi R^3 \rho_f / 3}{\pi R^2 B_f} = \frac{4}{3} R_{\text{BE}} \frac{\rho_f}{B_f}, \quad (2.57)$$

with corresponding

$$\Gamma_{\text{BE}} = \frac{M/\Phi_B|_{\text{BE}}}{M/\Phi_B|_{\text{crit}}} = \frac{8\pi\sqrt{G}}{3} R_{\text{BE}} \frac{\rho_f}{B_f} = \frac{1.8c_s}{v_{\text{A},f}} = \frac{1.8c_s}{r_f^{1/2} v_{\text{A},0}} \quad (2.58)$$

where

$$v_{\text{A},f}^2 = B_f^2 / (4\pi\rho_f) = r_f v_{\text{A},0}^2$$

using the shock jump conditions. Note that for a strong shock,  $r_f \approx \sqrt{2}v_0/v_{\text{A},0}$ , so that  $\Gamma_{\text{BE}} \approx 1.5c_s / (v_0 v_{\text{A},0})^{1/2}$ , or

$$\Gamma_{\text{BE}} \approx 0.8 \left( \frac{n_0}{100\text{cm}^{-3}} \right)^{0.25} \left( \frac{v_0}{\text{km/s}} \right)^{-0.5} \left( \frac{B_0}{\mu\text{G}} \right)^{-0.5} \left( \frac{T}{10\text{K}} \right)^{-0.5}. \quad (2.59)$$

If  $\Gamma_{\text{BE}}$  is larger than 1, a post-shock region of radius  $\sim R_{\text{BE}}$  is dense enough to gravitationally collapse whether or not there is ambipolar diffusion. Otherwise, ambipolar diffusion would be needed for a region of size  $\sim R_{\text{BE}}$  to become supercritical. For the set of shock models we are studying (see Table 2.1 for inflow parameters), calculated radii and mass-to-flux ratios for Bonnor-Ebert spheres under post-shock conditions without ambipolar diffusion are listed in Table 2.2. In all cases,  $\Gamma_{\text{BE}}$  is much smaller than 1, which means no collapse at the BE scale could happen in the post-shock region without significant ambipolar diffusion. More generally, since  $\Gamma_{\text{BE}} \sim c_s / (v_0 v_{\text{A},0})^{1/2} \ll 1$  under GMC conditions, most post-shock regions are sufficiently magnetized that gravitational collapse of low-mass cores would be prevented unless ambipolar diffusion occurs. Note that if  $\rho > r_f \rho_0$ , as is true in the candidate core material for transient C shocks,  $R_{\text{BE}}$  will be lower than the value in the table.

## 2.6 Core Forming Process

Current theoretical and observational work suggests that shocks produced by supersonic turbulence play a role in compressing gas to form prestellar cores. Our findings that the neutrals are compressed more than the magnetic field during the early stages of shock formation raise an interesting question: Is it possible for a subcritical cloud to form supercritical cores in shocks, which can then gravitationally collapse promptly?

### 2.6.1 Evolution of Overdense Regions

For a prestellar core to collapse, the region must be dense enough so that self-gravity overcomes the magnetic support. Although self-gravity is not included in the present models, we can make an initial assessment of whether transient C shocks are likely to affect the ability of cores to collapse promptly after they form.

In the context of our converging flow test, we shall define “candidate core” material to be regions where

$$\frac{n}{B_y} > 1.2 \times \left( \frac{n}{B_y} \right)_{\text{background}} ; \quad (2.60)$$

the background has uniform  $n/B_y$ , so the time evolution of this candidate core material is easily calculated. Physically, this candidate core material corresponds to that in the central peak of  $n/B_y$  as shown in e.g. Fig. 2.4 or Fig. 2.6.

For steady shocks with compression factor  $r_f$  produced by a two-sided converging flow with inflow speed  $v_{\text{inflow}}$  from both sides, the upstream speed in the

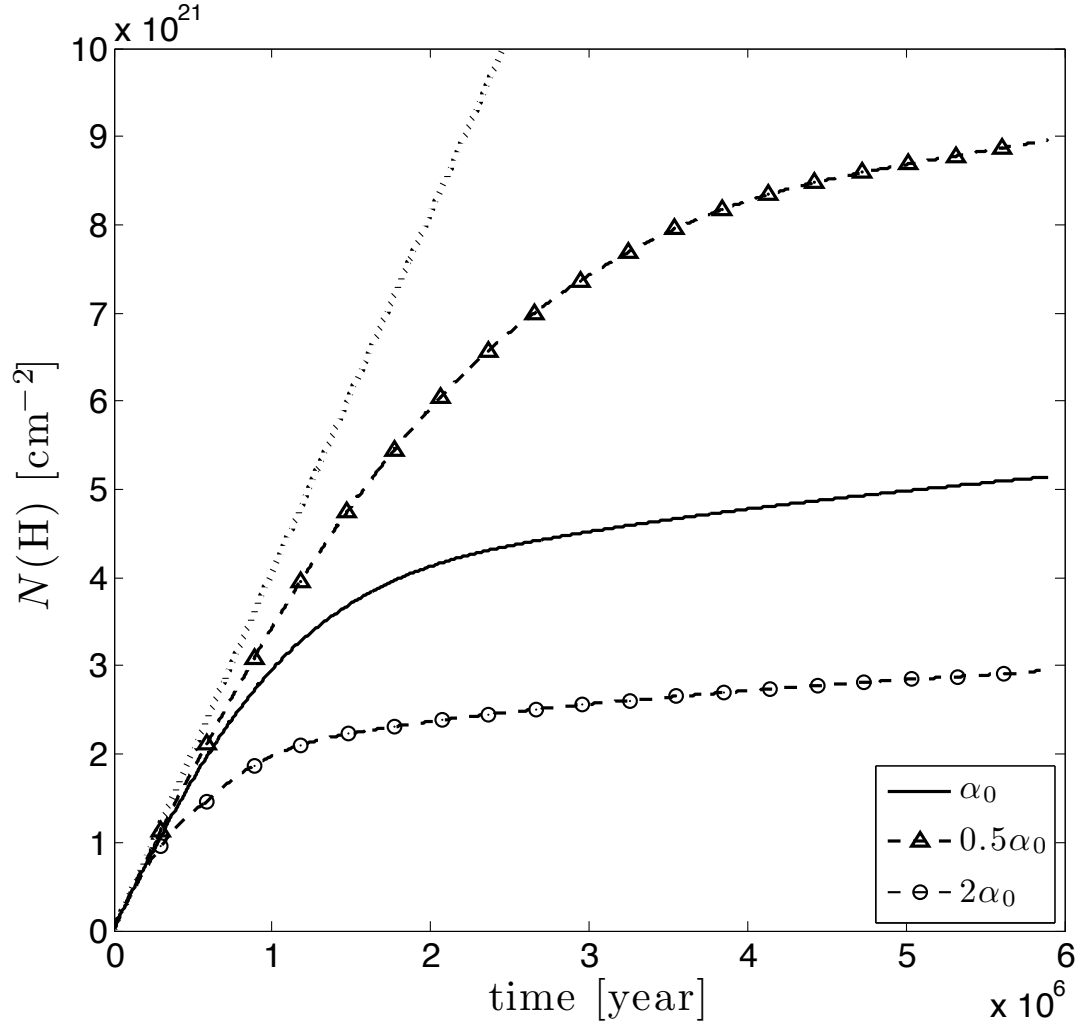


Figure 2.8: Dependence of “candidate core” material column density on the ion-neutral collisional coefficient, for  $\alpha = \alpha_0 = 3.7 \times 10^{13} \text{ cm}^3 \text{ s}^{-1} \text{ g}^{-1}$ ,  $\alpha = 0.5\alpha_0$ , and  $\alpha = 2\alpha_0$ . Also shown (*straight dotted line*) is the “kinematic” growth rate  $dN(\text{H})/dt = 2n_{\text{H}}v_{\text{inflow}}$  for a steady shock. Parameters for this model are  $n_0 = 100 \text{ cm}^{-3}$ ,  $v_0 = 5 \text{ km/s}$ ,  $B_0 = 10 \text{ } \mu\text{G}$ , and  $\chi_{i0} = 5$ .

shock frame is  $v_0 = v_{\text{inflow}} r_f / (r_f - 1)$ , and  $v_{\text{shock}} = v_{\text{inflow}} / (r_f - 1)$ . The rate at which the column density grows for a steady shock is therefore

$$\frac{\Delta N(\text{H})}{\Delta t} = 2n_{\text{H}} v_{\text{inflow}} = 1.05 \times 10^{21} \text{ cm}^{-2} \text{ Myr}^{-1} \left( \frac{n_0}{100 \text{ cm}^{-3}} \right) \left( \frac{v_{\text{inflow}}}{\text{km/s}} \right), \quad (2.61)$$

where  $n = n_{\text{H}_2} + n_{\text{He}} = 0.6n_{\text{H}}$  is assumed.

For a steady shock, the growth rate of the post-shock column is independent of  $\alpha$ , the collision coefficient between neutrals and ions. Fig. 2.8 shows evolution of the “candidate core” column density with different values of  $\alpha$ , for a model with  $n_0 = 100 \text{ cm}^{-3}$ ,  $v_{\text{inflow}} = 3.87 \text{ km/s}$ ,  $B_0 = 10 \mu\text{G}$ , and  $\chi_{i0} = 5$ . In the very beginning, all of the post-shock material has  $n/B_y$  greater than the background value, because the core grows by unimpeded motion of the neutrals which do not “see” the ions. Thus the column of “candidate core” material initially follows Equation (2.61), with slope  $\Delta N(\text{H})/\Delta t \approx 4 \times 10^{21} \text{ cm}^{-2} \text{ Myr}^{-1}$  (also shown in Fig. 2.8), independent of  $\alpha$ .

It is evident that at some point the growth rate of the “candidate core” column decreases. Physically, the growth rate decreases as ions are pushed into the column by inflowing neutrals, which causes the magnetic flux in the “candidate core” region to increase more rapidly than the neutral column, and the mass-to-flux ratio to decrease. Therefore, we might expect the growth of the demagnetized column to slow down on a timescale  $t_{\text{AD}} \sim L_{\text{shock}}/v_{\text{drift}}$ , the time for neutrals to travel across the shock front under the influence of ions. In timescales short compared to  $t_{\text{AD}}$ , neutrals which have arrived at the center were moving fully or partly free from collisions with ions. These neutrals thus contribute to the column with high mass-to-flux ratio. After  $t_{\text{AD}}$ , neutrals which have interacted strongly with ions dominate,

and the growth rate of the low-magnetization column starts to decrease.

This also corresponds to the timescale for steady C shock structure to develop, and for the fronts surrounding the shocked layer to expand. After this time, neutrals must then travel a greater distance through the condensed magnetic field and ions to stream into the “candidate core” area. From Fig. 2.8, the “saturation” time varies, roughly inversely with the collision coefficient  $\alpha$ . With Equation (2.37) or (2.45) we have  $L_{\text{shock}}$  (and hence  $t_{\text{AD}}$ )  $\propto 1/\alpha$ , consistent with our numerical results.

## 2.6.2 Time Scale and the Mass-to-flux Ratio

As discussed earlier, our simulation results indicate that during an initial transient period, the neutrals are compressed much more strongly than the magnetic field. Up to a certain time, corresponding to the ambipolar diffusion time scale, the column density of gas with elevated  $n/B$  grows. After this time, the profile transitions to that of a steady C shock, with  $n/B$  equal to the upstream value.

The ambipolar diffusion time scale should be comparable to the time it takes for neutrals to travel through the thickness of a C-type shock under the influence of ion drag. Therefore we have

$$t_{\text{AD}} \equiv \frac{L_{\text{shock}}}{\langle v_{\text{drift}} \rangle} = \frac{L_{\text{shock}}}{v_0} \left\langle \left| \frac{1}{r_n} - \frac{1}{r_B} \right|^{-1} \right\rangle, \quad (2.62)$$

where we have used  $v_{\text{drift}} = |v_i - v_n| = v_0 |r_n^{-1} - r_B^{-1}|$  (see Equations (2.8) and (2.9)).

Assuming that  $r_n \gg r_B$  over the shock region because a steady-state C shock has

not yet formed, and using  $\langle r_B \rangle \approx r_f/2$  as an average value, we obtain

$$t_{\text{AD}} \approx \langle r_B \rangle \frac{L_{\text{shock}}}{v_0} \approx \frac{r_f}{2} \frac{L_{\text{shock}}}{v_0} \quad (2.63)$$

$$\approx \frac{2r_f^{1/2}}{\alpha\rho_{i,0}} \approx \frac{2^{5/4}}{\alpha\rho_{i,0}} \left( \frac{v_0}{v_{\text{A},0}} \right)^{1/2}. \quad (2.64)$$

In the second line, we use the estimate of Equation (2.45) for the shock thickness, and Equation (2.21) for  $r_f$  in a strong shock. Note that a similar formula for more general cases with oblique shocks is given in Equation (A.24). In dimensional terms, using the analytical approximation Equation (2.47) to the C shock thickness  $L_{\text{shock}}$ , Equation (2.63) gives

$$t_{\text{AD}} \approx 1 \times 10^6 \text{ yr} \left( \frac{n_0}{100\text{cm}^{-3}} \right)^{-0.25} \left( \frac{v_0}{\text{km/s}} \right)^{0.5} \left( \frac{B_0}{\mu\text{G}} \right)^{-0.5} \left( \frac{\chi_{i0}}{10} \right)^{-1} \quad (2.65)$$

$$= 0.36 \times 10^6 \text{ yr} \left( \frac{n_0}{100\text{cm}^{-3}} \right)^{-0.5} \left( \frac{v_0}{v_{\text{A},0}} \right)^{0.5} \left( \frac{\chi_{i0}}{10} \right)^{-1}. \quad (2.66)$$

The time  $t_{\text{AD}}$  can be compared to the gravitational free fall time

$$t_{\text{ff}}(\rho) = \left( \frac{3\pi}{32G\rho} \right)^{1/2} = 3.4 \times 10^6 \text{ yr} \left( \frac{n}{100\text{cm}^{-1}} \right)^{-1/2} \quad (2.67)$$

to give

$$\frac{t_{\text{AD}}}{t_{\text{ff}}(\rho)} \approx \left( \frac{\rho}{\rho_0} \right)^{1/2} \left( \frac{v_0}{v_{\text{A},0}} \right)^{1/2} \chi_{i0}^{-1}. \quad (2.68)$$

The post-shock gas has density  $\rho_f = r_f \rho_0$  with  $r_f \approx \sqrt{2}(v_0/v_{\text{A},0})$  (see Equation (??)), which means that  $t_{\text{AD}}/t_{\text{ff}}(\rho_f) \sim (v_0/v_{\text{A},0}) \chi_{i0}^{-1}$ . During the transient stage,  $\rho_t > \rho_f$ , so  $t_{\text{ff}}(\rho_t) < t_{\text{ff}}(\rho_f)$ , implying  $t_{\text{AD}}/t_{\text{ff}}(\rho_t) > (v_0/v_{\text{A},0}) \chi_{i0}^{-1}$ . Thus, for strong shocks ( $v_0/v_{\text{A},0} \gtrsim 10$ ) and low ionization conditions ( $\chi_{i0} \lesssim 10$ ), the transient duration  $t_{\text{AD}}$  will exceed the time  $t_{\text{ff}}(\rho_t)$  for post-shock perturbations to develop into collapsing cores.

If the growth rate of the neutral column density is  $dN_{\text{H}}/dt \approx 2n_{\text{H}}v_0$  (see Equation (2.61)), the final (maximum) value of the mass-to-flux ratio should be

$$\left. \frac{M}{\Phi_B} \right|_{\text{final}} \approx \frac{1.4m_{\text{H}}dN_{\text{H}}/dt \times t_{\text{AD}}}{B_{\text{final}}} \approx \frac{2\rho_0v_0 \times L_{\text{shock}}r_f/(2v_0)}{r_fB_0} = \frac{\rho_0L_{\text{shock}}}{B_0}. \quad (2.69)$$

This estimate of the mass-to-flux ratio inside the pre-collapsing core depends only on the upstream density and magnetic field, and the steady-state C shock thickness.

This can be evaluated (using Equation (2.47)) to give  $\Gamma_{\text{final}} \equiv 2\pi\sqrt{G}(M/\Phi_B)_{\text{final}}$ :

$$\Gamma_{\text{final}} \approx 0.41 \left( \frac{n_0}{100\text{cm}^{-3}} \right)^{0.25} \left( \frac{v_0}{\text{km/s}} \right)^{0.5} \left( \frac{B_0}{\mu\text{G}} \right)^{-0.5} \left( \frac{\chi_{i0}}{10} \right)^{-1} \quad (2.70)$$

$$= 0.14 \left( \frac{v_0}{v_{\text{A},0}} \right)^{0.5} \left( \frac{\chi_{i0}}{10} \right)^{-1}. \quad (2.71)$$

Note that true  $\Gamma$  would differ by a factor  $L_y/L_x$  from Equations (2.70) and (2.71); i.e. up to factor  $\sim 2$  larger.

Combining Equations (2.64), (2.67), and (2.69), we have

$$t_{\text{AD}} = \left( \frac{32}{6\pi^2} \right)^{1/2} \Gamma_{\text{final}} t_{\text{ff}}(\rho_0) = 0.74 \Gamma_{\text{final}} t_{\text{ff}}(\rho_0). \quad (2.72)$$

Thus, shocks that are able to reach  $\Gamma_{\text{final}} \sim 1$  through transient ambipolar diffusion will do so on a timescale comparable to the gravitational time  $t_{\text{ff}}(\rho_0)$  of the large-scale cloud. Since the large-scale dynamical timescale ( $\sim t_{\text{ff}}(\rho_0)$  for a self-gravitating cloud) determines the correlation time of the flows that create shocks, this means that shocks will be sustained long enough for diffusion to occur.

If  $v_0 \gtrsim v_{\text{A},0}$  and  $\chi_{i0} \sim 1$ , from Equation (2.71) the candidate core will have  $\Gamma_{\text{final}}$  exceeding unity. In this situation, a core would be able to collapse promptly, without an extended period of ambipolar diffusion, since

$$\frac{t_{\text{AD}}}{t_{\text{ff}}(\rho_t)} \gtrsim \left( \frac{v_0}{v_{\text{A},0}} \right)^{1/2} \Gamma_{\text{final}} > \Gamma_{\text{final}}. \quad (2.73)$$

In GMCs, the ionization fraction is dependent on chemical processes, with  $\chi_{i0} \sim 1-20$  (McKee et al. 2010). The turbulent flow speed will not exceed  $\sim 10$  km/s under realistic conditions, and  $n_0 \sim 10^2 - 10^3$  cm $^{-3}$ , typically<sup>1</sup>. Therefore,  $\Gamma_{\text{final}}$  will exceed 1 (see Equation (2.70)) only if the upstream magnetic field in the direction parallel to the shock front is moderate, probably  $\lesssim 10$   $\mu\text{G}$ . The line-of-sight magnetic field strengths in molecular clouds with density  $\lesssim 10^3$  cm $^{-3}$ , however, can vary over  $\sim 5 - 25$   $\mu\text{G}$  (Crutcher 1999; Crutcher et al. 2010). If the total magnetic field strength (which is always  $\geq B_{\text{LOS}}$ ) exceeds  $\sim 20\mu\text{G}$ , then in order to reach  $\Gamma_{\text{final}}$  close to 1 so that pre-collapse cores can develop efficiently, converging flows with  $\mathbf{v}_0$  aligned  $\lesssim 30^\circ$  to  $\mathbf{B}_{\text{cloud}}$  are favored.

In addition, we note that for  $\sigma_{3\text{D, cloud}}$  and  $v_{\text{A, cloud}}$  the 3D turbulent velocity dispersion and mean-field Alfvén speed in a cloud, a gravitationally-bound (or virialized) cloud has

$$\Gamma_{\text{cloud}} \sim \frac{\sigma_{3\text{D, cloud}}}{v_{\text{A, cloud}}}, \quad (2.74)$$

so that

$$\Gamma_{\text{final}} \sim \frac{1}{\chi_{i0}} \left( \frac{v_0}{\sigma_{3\text{D, cloud}}} \right)^{1/2} \left( \frac{B_{\text{cloud}}}{B_0} \right)^{1/2} \Gamma_{\text{cloud}}^{1/2}. \quad (2.75)$$

The strongest shocks will have  $v_0 \sim \sigma_{3\text{D, cloud}}$ . These regions will be able to reach  $\Gamma_{\text{final}} \sim 1$  if the cloud is sufficiently supercritical ( $\Gamma_{\text{cloud}} \gg 1$ ), the ionization fraction is sufficiently low ( $\chi_{i0} \sim 1$ ), and/or the magnetic field parallel to the shock front is weaker than the mean field threading the cloud ( $B_{\text{cloud}}/B_0 > 1$ ). Again, with realistic  $\chi_{i0}$  and  $\Gamma_{\text{cloud}}$ , the most favorable circumstance for ambipolar diffusion to

---

<sup>1</sup> Keep in mind that some combinations of parameters are not astronomically realistic; e.g. high  $v_0$  is unlikely to have low  $\chi_{i0}$ , and high  $n_0$  is unlikely to have low  $B_0$ .

yield  $\Gamma_{\text{final}} > 1$  is if the inflow  $\mathbf{v}_0$  is aligned locally towards  $\mathbf{B}_{\text{cloud}}$  so that  $B_{\text{cloud}}/B_0 > 1$ .<sup>2</sup>

Even if post-shock regions are subcritical, transient ambipolar diffusion significantly increases the mass-to-flux ratio compared to the value that would hold in ideal MHD. A measure of the importance of this effect is the ratio between  $\Gamma_{\text{final}}$  and  $\Gamma_{\text{BE}}$  in the post-shock region. From Equations (2.70) and (2.59),

$$\frac{\Gamma_{\text{final}}}{\Gamma_{\text{BE}}} \sim 5 \left( \frac{v_0}{\text{km/s}} \right) \left( \frac{T}{10\text{K}} \right)^{-1/2} \chi_{i0}^{-1} \sim \frac{\mathcal{M}}{\chi_{i0}} \quad (2.76)$$

is predicted. The turbulent motions in clouds can achieve  $\mathcal{M} \sim 50$ . With  $\chi_{i0} \sim 1 - 20$ , a significant enhancement in the mass-to-flux ratio can be expected due to transient ambipolar diffusion.

### 2.6.3 Simulation Results

The estimates of Equations (2.65) and (2.70) can be compared to the ambipolar diffusion time and mass-to-flux ratio as measured directly from time-dependent numerical simulations. Examples showing evolution of the measured  $\Gamma$  for several different parameter values are shown in Fig. 2.9.

To read the ambipolar diffusion time scale from simulations, recall that the growth rate of the mass-to-flux ratio inside the core decreases at time  $\sim t_{\text{AD}}$ . We adopt a definition of  $t_{\text{AD}}$  as the time when the slope of the  $\Gamma$  vs. time curve drops to 25% of its maximum value. For each simulation, we measure the mass-to-flux ratio

---

<sup>2</sup>We have investigated oblique shocks with nonzero  $B_{x,0} = B_{\text{cloud}} \cos \theta = B_0 \cot \theta$  in Appendix A, where  $B_0 = B_{y,0} = B_{\text{cloud}} \sin \theta$  is the magnetic component parallel to the shock front. Equation (A.25) gives an approximation of  $\Gamma_{\text{final}}$  as a function of  $\theta$  (the angle between  $\mathbf{B}_{\text{cloud}}$  and  $\mathbf{v}_0$ ). Since there is no strong dependence of  $\Gamma_{\text{final}}$  on  $\theta$ , our 1-D results (Equations (2.70), (2.71), and (2.75)) are applicable in most cases with nonzero  $B_{x,0}$ .

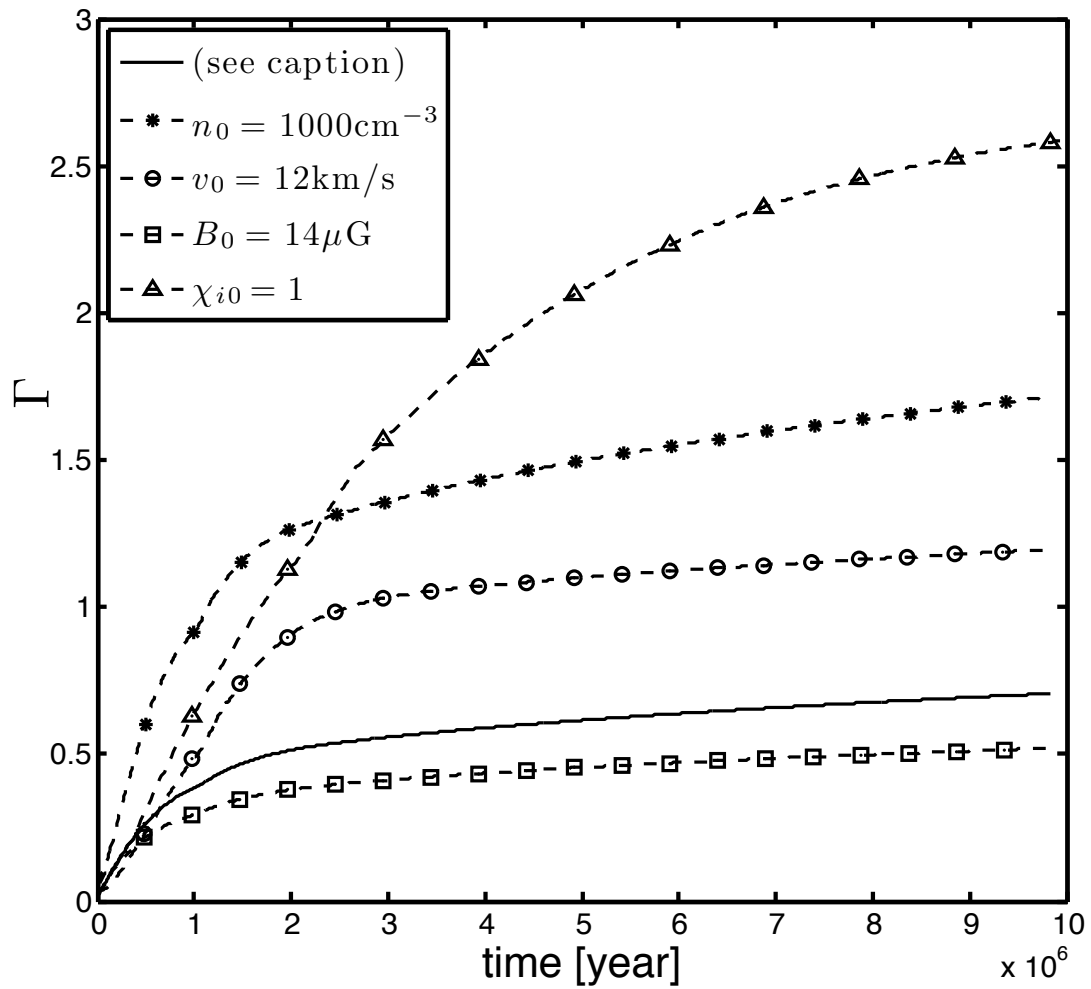


Figure 2.9: Time evolution of the normalized central mass-to-flux ratio  $\Gamma$  in the shocked gas. The parameters are  $n_0 = 200 \text{ cm}^{-3}$ ,  $v_0 = 5 \text{ km/s}$ ,  $B_0 = 10 \mu\text{G}$ , and  $\chi_{i0} = 5$  (*solid line*), with modifications as noted in the key.

Table 2.2: Results for Transient Mass-to-flux Enhancement

Model	$t_{\text{AD}}$		$\Gamma_{\text{final}}$		$L_{\text{core}}$	BE Sphere <sup>†</sup>		
	eq. (2.65) ( $10^6$ years)	result <sup>§</sup>	eq. (2.70)	$\Gamma_{2t_{\text{AD}}}$	at $2t_{\text{AD}}$ <sup>¶</sup> (pc)	$R_{\text{BE}}$ (pc)	$\Gamma_{\text{BE}}$	$\Gamma_{2t_{\text{AD}}}/\Gamma_{\text{BE}}$
N01	1.42	1.12	0.55	0.37	0.58	0.46	0.12	3.08
N03	1.10	1.11	0.74	0.64	0.34	0.20	0.15	4.27
N05	0.98	1.09	0.85	0.78	0.27	0.13	0.17	4.59
N08	0.88	1.07	0.96	0.95	0.23	0.09	0.19	5.00
N10	0.83	0.90	1.02	1.07	0.21	0.08	0.20	5.35
V04	1.07	0.94	0.59	0.44	0.40	0.31	0.16	2.75
V06	1.33	1.42	0.73	0.60	0.42	0.25	0.13	4.62
V08	1.56	1.86	0.86	0.76	0.42	0.21	0.11	6.91
V10	1.75	1.88	0.96	0.91	0.43	0.19	0.10	9.10
V12	1.94	2.13	1.06	1.06	0.43	0.17	0.09	11.78
B02	2.88	4.93	1.58	2.83	0.51	0.12	0.31	9.13
B04	1.98	2.64	1.09	1.35	0.44	0.17	0.22	6.14
B06	1.59	2.15	0.87	0.89	0.43	0.21	0.18	4.94
B08	1.36	1.58	0.75	0.66	0.42	0.24	0.15	4.40
B10	1.21	1.08	0.66	0.52	0.42	0.27	0.14	3.71
B12	1.09	0.90	0.60	0.43	0.42	0.30	0.13	3.31
B14	1.01	0.79	0.55	0.37	0.40	0.33	0.12	3.08
X01	6.03	5.78	3.32	2.63	2.03	0.27	0.14	18.79
X06	1.01	0.89	0.55	0.43	0.34	0.27	0.14	3.07
X10	0.60	0.57	0.33	0.25	0.20	0.27	0.14	2.78
X15	0.40	0.48	0.22	0.16	0.14	0.27	0.14	1.79
X20	0.30	0.45	0.17	0.12	0.12	0.27	0.14	0.86

<sup>†</sup> Computed for post-shock conditions without ambipolar diffusion (see Equations (2.55) and (2.58)).

<sup>§</sup> Defined as when the slope of the  $\Gamma$  vs. time curve drops to 20% of its maximum value.

<sup>¶</sup>  $L_{\text{core}} \equiv N/\langle n \rangle$  in “candidate core” region with enhanced  $n/B$ .

$\Sigma/\langle B_y \rangle$  at time  $t = 2t_{\text{AD}}$ , and define this mass-to-flux ratio inside the central peak (multiplied by  $2\pi\sqrt{G}$ ) as  $\Gamma_{\text{final}}$ .

Table 2.2 shows the predicted values of  $t_{\text{AD}}$  and  $\Gamma_{\text{final}}$  from Section 2.6.2, as well as the simulation results for these quantities. The measured ambipolar diffusion time scale is  $\sim 0.3 - 3$  Myr. Our model predicts the ambipolar diffusion time scale very well: the RMS value of  $(t_{\text{AD, pred}} - t_{\text{AD, sim}})/t_{\text{AD, sim}}$  is 0.19, and the range of  $(t_{\text{AD, pred}} - t_{\text{AD, sim}})/t_{\text{AD, sim}}$  is  $-0.42$  to  $0.28$ . The measured

mass-to-flux ratios deviate from predicted values somewhat more, with a range of  $(\Gamma_{\text{final, pred}} - \Gamma_{\text{final, sim}}) / \Gamma_{\text{final, sim}} -0.44$  to  $0.49$ , and RMS value  $0.28$ . The typical size  $L_{\text{core}} \equiv N / \langle n \rangle$  of the region with enhanced mass-to-flux ratio at time  $2t_{\text{AD}}$  is  $\sim 0.2 - 0.6$  pc (Table 2.2, column 6).

In most of our simulations, the mass-to-flux ratios are higher than  $0.6$  (see column 5 of Table 2.2), with some cases (N10, V12, B02, B04, and X01) reaching  $\Gamma_{2t_{\text{AD}}} > 1$ . Recall that we assumed the effective length of the system is comparable in all directions when we define  $\Gamma$  in the candidate core material (see Section 2.5.1). This means that the real mass-to-flux ratio would differ from our measured  $\Gamma_{2t_{\text{AD}}}$  by a factor  $L_y / L_x$ . Since cores may have axis ratios  $\sim 2 : 1$ , the measured  $\Gamma_{2t_{\text{AD}}}$  may be underestimated by a factor up to  $\sim 2$ . Therefore the fact that almost all models have  $\Gamma_{2t_{\text{AD}}}$  close to  $1$  shows that C shock transients may lead to supercritical cores quite frequently.

The models with  $\Gamma_{2t_{\text{AD}}} > 1$  confirm our prediction that small values of  $B_0$  are crucial for forming supercritical cores (otherwise uncommonly high neutral density/inflow speed or extremely low ionization fraction may become necessary). Given the limits on physical conditions in clumps within GMCs (see discussion in Section 2.6.2), prompt supercritical core formation would preferentially occur if the inflow direction is aligned relatively close to the magnetic field. A study of oblique shocks using similar analysis to that in the previous section is performed in Appendix A, where we show that the transient behavior of C shocks is insensitive to the component of magnetic field parallel to inflow velocity, so that our 1-D model is qualitatively applicable in cases with more general geometry.

We also list the value of  $\Gamma_{2t_{\text{AD}}}/\Gamma_{\text{BE}}$  in Table 2.2 for all our numerical models. In most cases, this ratio is greater than 2, and the average value is  $\sim 5.4$ . This means that for essentially all reasonable parameters, transient ambipolar diffusion will be important in enhancing the mass-to-flux ratio for forming cores. Since  $\Gamma_{2t_{\text{AD}}}$  is close to 1 in many situations, and  $\Gamma_{2t_{\text{AD}}}/\Gamma_{\text{BE}}$  is large, transient ambipolar diffusion during core formation clearly plays an important role in setting the stage for subsequent core evolution.

## 2.7 Summary

Ambipolar diffusion is an important phenomenon in interstellar clouds, which are strongly magnetized in the sense  $v_A \sim v_0 \gg c_s$ , but are poorly ionized. Supersonic turbulence creates shocks, but ambipolar diffusion between ions and neutrals spreads these shocks out. The thickness of C-type shocks depends on the inflow velocity, density, the magnetic field strength, and the ionization fraction. Although C shocks are normally studied in the steady-state limit, their early transient development is quite interesting. During this transient stage, the central compression of neutrals is strongly enhanced because they are effectively “unmagnetized.” The time and space scales of these transients make them important to the structure and dynamics within GMCs. The transient duration is comparable to the drift time across the C shock thickness ( $\sim 0.1 - 1$  pc), typically  $\sim 0.1 - 1$  Myr for GMC conditions.

For star formation, ambipolar diffusion is usually analyzed in the context of

slow evolution leading to gravitational collapse in magnetically-supported clouds. However, our results show that since neutrals can stream through field lines in shocks because of ambipolar diffusion, magnetically-supercritical cores may form due to C shock transients. During the transient, strong central compression of neutrals enhances  $n/B$  compared to steady-state values. If the compression and duration of the transient are sufficient, the central post-shock region may become supercritical and collapse gravitationally to make a prestellar core before it re-expands.

For both the traditional picture of supercritical core formation and the scenario we propose, the magnetic field remains relatively stationary while the neutrals move inward, within the high density regions. For the traditional picture, the inward neutral motions are due to small-scale self-gravity within the core. For shock-induced core formation, the inward motions of neutrals owes to large-scale converging supersonic flows within GMCs (which may ultimately be driven by large-scale self-gravity within the cloud).

Transient ambipolar diffusion is particularly important because without it, post-shock regions in GMCs typically have very small mass-to-magnetic flux ratios. Thus, the regions with the shortest gravitational timescales (at high density, due to shocks) would be prevented from collapsing by magnetic fields, which are also enhanced by shocks. Our numerical simulations show a peak in the mass-to-flux ratio, produced by transient ambipolar diffusion. For strong shocks ( $v_0/v_{A,0}$  sufficient) and low enough ionization fraction, our results suggest that supercritical cores can be produced.

Based on our simulation results and analyses, our main conclusions are as

follows:

1. The dominant factors determining the ionization fraction in molecular clouds are ionizing cosmic rays and gas-phase recombination. We derive steady-state equations for C shocks including ionization and recombination (Equations (2.23) and (2.32)). Analyzing the solutions of these equations (Fig. 2.1), we find that ionization-recombination equilibrium is generally an excellent approximation, and for this regime is much better than the widely-applied frozen-in condition. For equilibrium ionization,  $\rho_i \propto \rho_n^{1/2}$  (Nakano 1976, 1979) so that  $r_i = r_n^{1/2}$  in our notation, and Equation (2.30) governs steady C shocks.
  
2. We have solved the steady C shock ODE over a parameter range of upstream neutral density  $n_0 = 10^2 - 10^3 \text{ cm}^{-3}$ , inflow speed  $v_0 = 2 - 15 \text{ km/s}$ , upstream magnetic field strength  $B_0 = 2 - 15 \mu\text{G}$ , and ionization parameter  $\chi_{i0} = 1 - 21$  ( $\chi_{i0}$  is defined in Equations (2.28)–(2.29)). Using a multilinear fit, we obtain an expression for the C shock thickness (Equation (2.48)), in terms of these parameters. We also obtain an analytic expression for the C shock thickness (Equation (2.46)), which is in excellent agreement with the numerical result. The dependence  $L_{\text{shock}} \propto (v_0 v_{A,0})^{1/2} / (\alpha \rho_{i,0})$  can be understood based on the requirement for momentum transfer mediated by ion-neutral collisions. Our result for the C shock thickness is comparable to previous estimates (e.g. Draine & McKee 1993), although the parameter dependence differs from the case of “frozen-in” ions (Wardle 1990; Li et al. 2006).

3. During the transient stage of C shocks, the central column density of gas with enhanced mass-to-flux ratio initially grows kinematically (Equation (2.61)), but this slows after a time comparable to the ion-neutral drift time  $t_{\text{AD}} \approx L_{\text{shock}}/v_{\text{drift}}$  across the C shock (Fig. 2.8 and Equation (2.63)). The duration of the transient from our numerical models (see Table 2.2) is similar to our analytic estimate, 0.1 – 1 Myr for the regime we have studied (see Equations (2.65)–(2.66)). Although the present models do not include self-gravity, the duration of the transient C shock is comparable to the time needed for prestellar cores to collapse, from both observations (e.g. Ward-Thompson et al. 2007; Evans et al. 2009) and numerical simulations (e.g. Gong & Ostriker 2011).
4. Our finding of rapid initial enhancement in density and mass-to-flux ratio is consistent with the results of Kudoh & Basu (2008), for somewhat different parameter regime. Their simulations included self-gravity, and they also pointed out that with appropriate parameters, collapsing cores may form due to the initial compression. Our work helps to explain the physics behind the rapid collapse they identified, and more generally provides insight into other numerical studies of turbulence-accelerated, magnetically-regulated star formation (e.g. Li & Nakamura 2004).
5. Over the transient time  $t_{\text{AD}}$ , a column  $\sim 2n_0v_0t_{\text{AD}}$  of “candidate core” material accumulates. By taking the ratio with the post-shock magnetic field strength, we can estimate the mass-to-flux ratio of this dense material. Equation (2.70)

gives an estimate of the final dimensionless mass-to-flux estimate,  $\Gamma$ , which is similar to numerical measures of  $\Gamma_{\text{final}}$  (Table 2.2). The relatively high mass-to-flux ratios we find may explain the weak magnetic fields observed in dense cores (Troland & Crutcher 2008). Without ambipolar diffusion, the post-shock mass-to-flux ratio on the scale of a Bonnor-Ebert sphere ( $\Gamma_{\text{BE}} \approx 1.5c_s/(v_0v_{\text{A},0})^{1/2}$ ) would be much smaller than the critical value. In contrast, the mass-to-flux ratio in the candidate core material produced within transient C shocks is several times larger than  $\Gamma_{\text{BE}}$  (Table 2.2 and Equation (2.76)). This large enhancement shows the significance of ambipolar diffusion during shock-induced core formation.

6. In transient shocks that can produce  $\Gamma_{\text{final}} \gtrsim 1$ , magnetically supercritical cores can form and collapse rapidly. Shocks that can reach  $\Gamma_{\text{final}} \gtrsim 1$  have  $t_{\text{AD}}$  comparable to the gravitational free-fall time of the larger-scale cloud (Equation (2.72)). Thus, shock-induced ambipolar diffusion is rapid, wherever it occurs.
7. The most favorable conditions for forming gravitationally bound cores in cold, turbulent, magnetized clouds are strong shocks ( $v_0 \gg v_{\text{A},0}$ ) in regions with low ionization fraction ( $\chi_{i0} \sim 1$ ). Equation (A.25) in the Appendix gives the final mass-to-flux ratio for the case of oblique shocks; the result is similar to that with the same component of the magnetic field parallel to the shock front (Equation (2.70)). Considering realistic conditions in molecular clouds, converging flows with  $\mathbf{v}_{\text{inflow}} \perp \mathbf{B}_{\text{cloud}}$  will have relatively low post-shock density

and post-shock mass-to-flux ratio, and the post-shock gas layers formed will be unfavorable for star formation. Cases where  $\mathbf{v}_{\text{inflow}}$  and  $\mathbf{B}_{\text{cloud}}$  are more aligned are more favorable for reaching  $\Gamma_{\text{final}} > 1$  (Equation (2.75)). Further observations of the directions of magnetic fields relative to observed gas filaments with or without embedded cores will test whether these orientation effects are indeed important. If orientation of shocks is in fact important in producing cores that can collapse, this may help explain the observed inefficiency of star formation in GMCs.

While the present models are extremely useful for explaining the phenomenon of transient ambipolar diffusion, simulations of more generalized cases are required to support the scenario of prompt supercritical core formation in shocks. Three-dimensional simulations of systems with oblique shocks, including self-gravity of the gas, would be immediately helpful. In addition, a more realistic core-forming environment can be examined by adding nonlinear turbulence to the inflow velocity field. Further simulations along these lines, together with observations probing density and magnetic structure in filaments and cores at different stages, will improve understanding of what precipitates star formation.

# Chapter 3: Formation of Magnetized Prestellar Cores with Ambipolar Diffusion and Turbulence

## Abstract

We investigate the roles of magnetic fields and ambipolar diffusion during prestellar core formation in turbulent giant molecular clouds (GMCs), using three-dimensional numerical simulations. Our simulations focus on the shocked layer produced by a converging large-scale flow, and survey varying ionization and angle between the upstream flow and magnetic field. We also include ideal magnetohydrodynamic (MHD) and hydrodynamic models. From our simulations, we identify hundreds of self-gravitating cores that form within 1 Myr, with masses  $M \sim 0.04 - 2.5 M_{\odot}$  and sizes  $L \sim 0.015 - 0.07$  pc, consistent with observations of the peak of the core mass function (CMF). Median values are  $M = 0.47 M_{\odot}$  and  $L = 0.03$  pc. Core masses and sizes do not depend on either the ionization or upstream magnetic field direction. In contrast, the mass-to-flux ratio does increase with lower ionization, from twice to four times the critical value. The higher mass-to-flux ratio for low ionization is the result of enhanced transient ambipolar

diffusion when the shocked layer first forms. However, ambipolar diffusion is not necessary to form low-mass supercritical cores. For ideal MHD, we find similar masses to other cases. These masses are 1 – 2 orders of magnitude lower than the value  $M_{\text{mag,sph}} = 0.007 B^3 / (G^{3/2} \rho^2)$  that defines a magnetically supercritical sphere under post-shock ambient conditions. This discrepancy is the result of anisotropic contraction along field lines, which is clearly evident in both ideal MHD and diffusive simulations. We interpret our numerical findings using a simple scaling argument which suggests that gravitationally critical core masses will depend on the sound speed and mean turbulent pressure in a cloud, regardless of magnetic effects.

### 3.1 Introduction

The formation of stars begins with dense molecular cores (McKee & Ostriker 2007; André et al. 2009). These cores form through the concentration of overdense regions within turbulent, filamentary GMCs; subsequent core collapse leads to protostellar (or protobinary)/disk systems. Magnetic fields are important at all scales during this process (McKee & Ostriker 2007; Crutcher 2012): the cloud-scale magnetic field can limit compression in interstellar shocks that create dense clumps and filaments in which cores form, while the local magnetic field within individual cores can prevent collapse if it is large enough (Mestel & Spitzer 1956; Strittmatter 1966; Mouschovias & Spitzer 1976), and can help to remove angular momentum during the disk formation process if cores are successful in collapsing (Mestel 1985; Mouschovias 1991; Allen et al. 2003; Li et al. 2014). The significance of magnetic

fields in self-gravitating cores can be quantified by the ratio of mass to magnetic flux; only if the mass-to-flux ratio exceeds a critical value is gravitational collapse possible. How the mass-to-flux ratio increases from the strongly-magnetized interstellar medium to weakly-magnetized stars is a fundamental problem of star formation (Shu et al. 1987; McKee & Ostriker 2007). Here, as suggested in Chen & Ostriker (2012, hereafter Chapter 2), we consider core formation in GMCs with highly supersonic turbulence and non-ideal MHD.

Magnetic fields are coupled only to charged particles, while the gas in GMCs and their substructures is mostly neutral. The ability of magnetic fields to affect core and star formation thus depends on the collisional coupling between neutrals and ions. Ambipolar diffusion is the non-ideal MHD process that allows charged particles to drift relative to the neutrals, with a drag force proportional to the collision rate (Spitzer 1956). Ambipolar drift modifies the dynamical effect of magnetic fields on the gas, and may play a key role in the star formation.

In classical theory, quasi-static ambipolar diffusion is the main mechanism for prestellar cores to lose magnetic support and reach supercritical mass-to-flux ratios. Through ambipolar drift, the mass within dense cores can be redistributed, with the neutrals diffusing inward while the magnetic field threading the outer region is left behind (Mouschovias 1979). However, the quasi-static evolution model (e.g. Mouschovias & Ciolek 1999; Ciolek & Basu 2001) gives a prestellar core lifetime considerably longer (up to a factor of 10) than the gravitational free-fall timescale,  $t_{\text{ff}}$ , while several observational studies have shown that cores only live for  $(2 - 5) t_{\text{ff}}$  (e.g. Ward-Thompson et al. 2007; Evans et al. 2009).

The failure of the traditional picture to predict core lifetimes indicates that supercritical cores may not have formed quasi-statically through ambipolar diffusion. Indeed, it is now generally recognized that, due to pervasive supersonic flows in GMCs, core formation is not likely to be quasi-static. Realistic star formation models should take both ambipolar diffusion and large-scale supersonic turbulence into consideration. This turbulence may accelerate the ambipolar diffusion process (Heitsch et al. 2004; Li & Nakamura 2004), with an analytic estimate of the enhanced diffusion rate by a factor of 2–3 for typical conditions in GMCs (Fatuzzo & Adams 2002).

In our previous work (Chapter 2; or see Chen & Ostriker 2012), we investigated the physical mechanism driving enhanced ambipolar diffusion in one-dimensional C-type shocks. These shocks pervade GMCs, and are responsible for the initial compression of gas above ambient densities. We obtained a formula for the C-shock thickness as a function of density, magnetic field, shock velocity, and ionization fraction, and explored the dependence of shock-enhanced ambipolar diffusion on environment through a parameter study. Most importantly, we identified and characterized a transient stage of rapid ambipolar diffusion at the onset of shock compression, for one-dimensional converging flows. For an interval comparable to the neutral-ion collision time and before the neutral-ion drift reaches equilibrium, the neutrals do not experience drag forces from the ions. As a consequence, the initial shock in the neutrals is essentially unmagnetized, and the neutrals can be very strongly compressed. This transient stage, with timescale  $t_{\text{transient}} \sim 1 \text{ Myr}$  (but depending on ionization), can create dense structures with much higher  $\rho/B$

than upstream gas. Chapter 2 suggested this could help enable supercritical core formation. In Chapter 2, we also found that (1) the perpendicular component of the magnetic field is the main determinant of the shock compression, and (2) the perpendicular component of the magnetic field  $B_{\perp}$  must be weak ( $\lesssim 5 \mu\text{G}$ ) for transient ambipolar diffusion in shocks to significantly enhance  $\rho/B_{\perp}$ .

Observations of nearby clouds provide direct constraints on the role of magnetic fields, as well as other properties of prestellar cores. The typical mean mass-to-flux ratio of dark cloud cores is  $\Gamma \sim 2$  (in units of critical value; see Equation (3.16)) from Zeeman studies (Falgarone et al. 2008; Troland & Crutcher 2008). Due to the instrumental limitations, magnetic field observations in solar-mass and smaller scale regions are relatively lacking compared with observations of larger scales (see review in Crutcher 2012), however. Surveys in nearby clouds have found that prestellar cores have masses between  $\sim 0.1 - 10 M_{\odot}$  and sizes  $\sim 0.01 - 1$  pc (Motte et al. 2001; Ikeda et al. 2009; Rathborne et al. 2009; Kirk et al. 2013). In addition, a mass-size relation has been proposed as a power law  $M \propto R^k$ , with  $k = 1.2 - 2.4$  dependent on various molecule tracers (e.g. Elmegreen & Falgarone 1996; Curtis & Richer 2010; Roman-Duval et al. 2010; Kirk et al. 2013).

The magnetic field strength within prestellar cores is important for late evolution during core collapse, since disk formation may be suppressed by magnetic braking (for recent simulations see Allen et al. 2003; Hennebelle & Fromang 2008; Mellon & Li 2008; Hennebelle et al. 2011; or see review in Li et al. 2014). However, many circumstellar disks and planetary systems have been detected (e.g. Haisch et al. 2001; Maury et al. 2010), suggesting that the magnetic braking “catastro-

phe” seen in many simulations does not occur in nature. The proposed solutions include the misalignment between the magnetic and rotation axes (Hennebelle & Ciardi 2009; Ciardi & Hennebelle 2010; Joos et al. 2012; Krumholz et al. 2013), turbulent reconnection and other turbulent processes during the rotating collapse (e.g. Santos-Lima et al. 2012; Seifried et al. 2012, 2013), and non-ideal MHD effects including ambipolar diffusion, Hall effect, and Ohmic dissipation (e.g. Krasnopolsky et al. 2010; Li et al. 2011; Machida et al. 2011; Dapp et al. 2012; Tomida et al. 2013). If prestellar cores have sufficiently weak magnetic fields, however, braking would not be a problem during disk formation (e.g. Mellon & Li 2008; Li et al. 2013, 2014). Therefore, the magnetic field (and mass-to-flux ratio) within a prestellar core is important not just for the ability of the core to collapse, but also of a disk to form.

Fragmentation of sheetlike magnetized clouds induced by small-amplitude perturbation and regulated by ambipolar diffusion has been widely studied (e.g. Indebetouw & Zweibel 2000; Basu & Ciolek 2004; Boss 2005; Ciolek & Basu 2006; Basu et al. 2009a). Analogous fully three-dimensional simulations have also been conducted (e.g. Kudoh et al. 2007). Supercritical cores formed in the flattened layer have masses  $\sim 0.1 - 10 M_{\odot}$  (e.g. Indebetouw & Zweibel 2000; Basu et al. 2009a), at timescales  $\sim 1 - 10$  Myr dependent on the initial mass-to-flux ratio of the cloud (e.g. Indebetouw & Zweibel 2000; Kudoh et al. 2007; Basu et al. 2009a). The above cited simulations start from relatively high densities ( $\sim 10^4 \text{ cm}^{-3}$ ; e.g. Kudoh et al. 2007) and included only the low-amplitude perturbations. Alternatively, Li & Nakamura (2004) and Nakamura & Li (2005) took the formation of these overdense regions into consideration by including a direct treatment of the

large-scale supersonic turbulence. They demonstrated that ambipolar diffusion can be sped up locally by the supersonic turbulence, forming cores with masses  $\sim 0.5 M_{\odot}$  and sizes  $\sim 0.1$  pc within  $\sim 2$  Myr, while the strong magnetic field keeps the star formation efficiency low (1 – 10%). Similarly, Basu et al. (2009b) found that turbulence-accelerated, magnetically-regulated core formation timescales are  $\sim 1$  Myr in two-dimensional simulations of magnetized sheet-like clouds, with corresponding three-dimensional simulations showing comparable results (Kudoh & Basu 2008, 2011). In addition, Nakamura & Li (2008) measured the core properties in their three-dimensional simulations to find  $L_{\text{core}} \sim 0.04 - 0.14$  pc,  $\Gamma_{\text{core}} \sim 0.3 - 1.5$ , and  $M_{\text{core}} \sim 0.15 - 12.5 M_{\odot}$ , while Basu et al. (2009b) found a broader core mass distribution  $M_{\text{core}} \sim 0.04 - 25 M_{\odot}$  in their parameter study using thin-sheet approximation.

Supersonic turbulence within GMCs extends over a wide range of spatial scales (Mac Low & Klessen 2004; Ballesteros-Paredes et al. 2007). Although turbulence contains sheared, diverging, and converging regions in all combinations, regions in which there is a large-scale convergence in the velocity field will strongly compress gas, creating favorable conditions for the birth of prestellar cores. Gong & Ostriker (2011) investigated core formation in an idealized model containing both a large-scale converging flow and multi-scale turbulence. These simulations showed that the time until the first core collapses depends on inflow Mach number  $\mathcal{M}$  as  $t_{\text{collapse}} \propto \mathcal{M}^{-1/2}$ . With a parameter range  $\mathcal{M} = 1.1$  to 9, cores formed in the Gong & Ostriker (2011) simulations had masses  $0.05 - 50 M_{\odot}$ . Following similar velocity power spectrum but including ideal MHD effects, Myers et al. (2014) performed

simulations with sink particle, radiative transfer, and protostellar outflows to follow the protostar formation in turbulent massive clump. They demonstrated that the median stellar mass in the simulated star cluster can be doubled by the magnetic field, from  $0.05 M_{\odot}$  (unmagnetized case) to  $0.12 M_{\odot}$  (star cluster with initial mass-to-flux ratio  $\Gamma = 2$ ). This is qualitatively consistent with the conclusion in Inoue & Fukui (2013), that the mass of the cores formed in the post-shock regions created by cloud-cloud collision is positively related to (and dominated by) the strong magnetic field in the shocked layer. Note that, though the main focus of Inoue & Fukui (2013) is the cloud’s ability to form massive cores ( $\sim 20 - 200 M_{\odot}$  in their simulations), the idea of cloud-cloud collision is very similar to the converging flows setup adopted in Gong & Ostriker (2011) and this study.

In this chapter, we combine the methods of Chapter 2 for modeling ambipolar diffusion with the methods of Gong & Ostriker (2011) for studying self-gravitating structure formation in turbulent converging flows. Our numerical parameter study focuses on the level of ambipolar diffusion (controlled by the ionization fraction of the cloud) and the obliquity of the shock (controlled by the angle between the magnetic field and the upstream flow). We show that filamentary structures similar to those seen in observations (see review in André et al. 2014) develop within shocked gas layers, and that cores form within these filaments. We measure core properties to test their dependence on these parameters. As we shall show, our models demonstrate that low-mass supercritical cores can form for all magnetic obliquities and all levels of ionization, including ideal MHD. However, our models also show that ambipolar diffusion affects the magnetization of dynamically-formed cores.

The outline of this chapter is as follows. We provide a theoretical analysis of oblique MHD shocks in Section 3.2, pointing out that a quasi-hydrodynamic compression ratio (which is  $\sim 5$  times stronger than in *fast* MHD shocks for the parameters we study) can exist when the converging flow is nearly parallel to the magnetic field. We also show that shock compression cannot increase the mass-to-flux ratio except in the nearly-parallel case or with ambipolar diffusion. Section 3.3 describes methods used in our numerical simulations and data analysis, including our model parameter set and method for measuring magnetic flux within cores. The evolution of gas structure (including development of filaments) and magnetic fields for varying parameters is compared in Section 3.4. In Section 3.5 we provide quantitative results for masses, sizes, magnetizations, and other physical properties of the bound cores identified from our simulations. Implications of these results for core formation is discussed in Section 3.6, where we argue that the similarity of core masses and sizes among models with different magnetizations and ionizations can be explained by anisotropic condensation preferentially along the magnetic field. Section 3.7 summarizes our conclusions.

## **3.2 Theoretical Analysis**

### **3.2.1 Oblique MHD Shock**

Chapter 2 describes a one-dimensional simplified MHD shock system with velocity and magnetic field perpendicular to each other, including a short discussion of oblique shocks. Here we review the oblique shock equations and write them in a

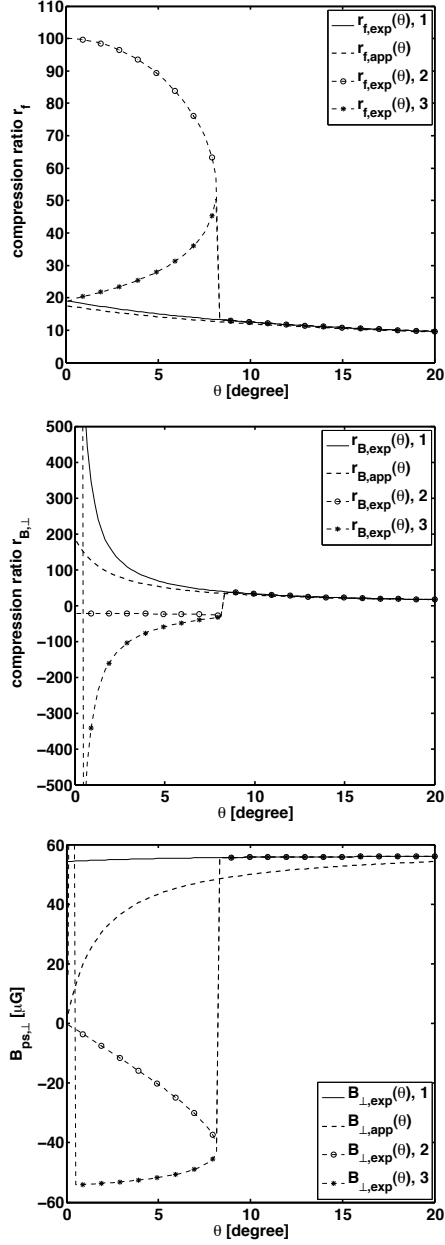


Figure 3.1: Multiple solutions for Equation (3.3) at varying  $\cos \theta = \hat{\mathbf{B}} \cdot \hat{\mathbf{v}}$  with the following parameters:  $\mathcal{M} = 10$ ,  $B_0 = 10 \mu\text{G}$ ,  $\rho_0 = \mu_n \cdot 1000 \text{ cm}^{-3}$  where  $\mu_n = 2.3 m_H$ . *Top:* Compression ratio for neutrals. Equation (3.5) works as a good analytical approximation to  $r_{f,\text{exp}}(\theta), 1$ . *Middle:* Compression ratio for the perpendicular component (with respect to the inflow direction) of the magnetic field. The analytical approximation  $r_{B,\text{app}}(\theta)$  is calculated from Equation (3.4), using Equation (3.5) for  $r_f(\theta)$ . *Bottom:* The corresponding post-shock magnetic field component that is perpendicular to the inflow (parallel to the shock front).

more general form to give detailed jump conditions.

We shall consider a plane-parallel shock with uniform pre-shock neutral density  $\rho_0$  and ionization-recombination equilibrium everywhere. The shock front is in the  $x$ - $y$  plane, the upstream flow is along the  $z$ -direction ( $\mathbf{v}_0 = v_0 \hat{\mathbf{z}}$ ), and the upstream magnetic field is in the  $x$ - $z$  plane, at an angle  $\theta$  to the inflow ( $\mathbf{B}_0 = B_0 \sin \theta \hat{\mathbf{x}} + B_0 \cos \theta \hat{\mathbf{z}}$ ) such that  $B_x = B_0 \sin \theta$  is the upstream component perpendicular to the flow. The parameters  $\mathcal{M}$  and  $\beta$  (upstream value of the Mach number and plasma parameter) defined in Chapter 2 therefore become

$$\mathcal{M} \equiv \mathcal{M}_z = \frac{v_0}{c_s}, \quad \frac{1}{\beta_0} \equiv \frac{B_0^2}{8\pi\rho_0 c_s^2} = \frac{1}{\beta_x} \frac{1}{\sin^2 \theta}. \quad (3.1)$$

The jump conditions of MHD shocks are described by compression ratios of density and magnetic field:

$$r_f \equiv \frac{\rho_{n, \text{downstream}}}{\rho_{n, \text{upstream}}}, \quad r_{B_\perp} \equiv \frac{B_{\perp, \text{downstream}}}{B_{\perp, \text{upstream}}}. \quad (3.2)$$

From Equations (A.14) and (A.18) in Appendix A, we have

$$\frac{\sin^2 \theta r_f^2}{\beta_0} \left( 1 - \frac{2 \cos^2 \theta}{\beta_0 \mathcal{M}^2} \right)^2 = \left( \mathcal{M}^2 + 1 + \frac{\sin^2 \theta}{\beta_0} - \frac{\mathcal{M}^2}{r_f} - r_f \right) \left( 1 - \frac{2r_f \cos^2 \theta}{\beta_0 \mathcal{M}^2} \right)^2, \quad (3.3)$$

which can be solved numerically to obtain explicit solution(s)  $r_{f, \text{exp}}(\theta)$ . The compression ratio for the magnetic field perpendicular to the inflow is

$$r_{B_\perp}(\theta) = r_f(\theta) \frac{1 - \frac{2 \cos^2 \theta}{\beta_0 \mathcal{M}^2}}{1 - \frac{2r_f(\theta) \cos^2 \theta}{\beta_0 \mathcal{M}^2}}. \quad (3.4)$$

Equation (A.21) of Appendix A gives an analytical approximation to  $r_f(\theta)$ :

$$r_{f, \text{app}}(\theta) = \frac{\sqrt{\beta_0} \mathcal{M}}{\sin \theta} \left[ \frac{2 \sin \theta}{\sqrt{\beta_0} \mathcal{M} \tan^2 \theta} + \frac{\sqrt{\beta_0}}{2 \mathcal{M} \sin \theta} + 1 \right]^{-1}. \quad (3.5)$$

Since Equation (3.3) is a quartic function of  $\theta$ , there are four possible roots of  $r_f$  for each angle, and  $r_f(\theta) = \text{const.} = 1$  (no-shock solution) is always a solution. When  $\theta$  is large, Equation (3.3) has one simple root ( $r_f = 1$ ) and a multiple root with multiplicity = 3. When  $\theta$  drops below a critical value,  $\theta_{\text{crit}}$ , Equation (3.3) has four simple roots, which give us four different values of  $r_{B\perp}$ . Figure 3.1 shows the three explicit solutions for  $r_f$  and  $r_{B\perp}$  ( $r_{f,\text{exp}}(\theta)$  and  $r_{B,\text{exp}}(\theta)$ ) as well as the approximations ( $r_{f,\text{app}}(\theta)$  and  $r_{B,\text{app}}(\theta)$ ) that employ Equation (3.5).

The fact that there are multiple solutions for post-shock properties is the consequence of the non-unique Riemann problem in ideal MHD (see discussions in e.g. Torrilhon 2003; Delmont & Keppens 2011; Takahashi & Yamada 2013), and whether all solutions are physically real is still controversial. The first set of solutions  $r_{f,\text{exp}}(\theta), 1$  and  $r_{B,\text{exp}}(\theta), 1$  shown in Figure 3.1 gives positive  $r_f$  and  $r_{B\perp}$ , classified as *fast* MHD shocks (Shu 1992; Draine & McKee 1993), and is the principal oblique shock solution referred to in this contribution<sup>3</sup>. The other two solutions for post-shock magnetic field,  $r_{B,\text{exp}}(\theta), 2$  and  $r_{B,\text{exp}}(\theta), 3$ , both become negative when  $\theta < \theta_{\text{crit}}$ , indicating that the tangential component of the magnetic field to the shock plane is reversed in the post-shock region. These two solutions are commonly specified as *intermediate* shocks (e.g. Wu 1987; Karimabadi 1995; Inoue & Inutsuka 2007). Among these two field-reversal solutions, we notice that  $r_{f,\text{exp}}(\theta), 2$  approaches the hydrodynamic jump condition ( $r_{f,\text{hydro}} = \mathcal{M}^2$ ) when  $\theta \rightarrow 0$ , and  $r_{B,\text{exp}}(\theta), 2$  is smaller in magnitude than other solutions when  $\theta < \theta_{\text{crit}}$ . Thus, we classify this set of solutions  $r_{f,\text{exp}}(\theta), 2$  and  $r_{B,\text{exp}}(\theta), 2$  as the *quasi-hydrodynamic*

---

<sup>3</sup>We use Equation (3.5) as analytical approximation for  $r_f(\theta)$ , if necessary.

shock. This quasi-hydrodynamic solution can create gas compression much stronger than the regularly-applied *fast* shock condition, and may be the reason that when  $\theta < \theta_{\text{crit}}$ , even ideal MHD simulations can generate shocked layers with relatively high mass-to-flux ratio (see Sections 3.4 and 3.5 for more details).

The definition of  $\theta_{\text{crit}}$  can be derived from Equation (3.4), which turns negative when  $1 - \frac{2\cos^2\theta}{\beta_0\mathcal{M}^2} > 0$  and  $1 - \frac{2r_f(\theta)\cos^2\theta}{\beta_0\mathcal{M}^2} < 0$ :

$$\cos^2\theta > \cos^2\theta_{\text{crit}} = \frac{\beta_0\mathcal{M}^2}{2r_f(\theta_{\text{crit}})}. \quad (3.6)$$

Using Equation (3.5) and considering only the terms  $\sim \mathcal{M}$ , this becomes

$$\frac{\cos^2\theta_{\text{crit}}}{\sin\theta_{\text{crit}}} \approx \frac{\sqrt{\beta_0}\mathcal{M}}{2}, \quad (3.7)$$

or

$$\sin^2\theta_{\text{crit}} + \frac{\sqrt{\beta_0}\mathcal{M}}{2}\sin\theta_{\text{crit}} - 1 = 0. \quad (3.8)$$

Assuming  $\theta_{\text{crit}} \ll 1$ , this gives

$$\theta_{\text{crit}} \sim \frac{2}{\sqrt{\beta_0}\mathcal{M}} = \sqrt{2}\frac{v_{A,0}}{v_0}, \quad (3.9)$$

where  $v_{A,0} \equiv B_0/\sqrt{4\pi\rho_0}$  is the Alfvén speed in the cloud. Therefore, the criterion to have multiple solutions,  $\theta < \theta_{\text{crit}}$ , is approximately equivalent to

$$v_{\perp} = v_0 \sin\theta \lesssim v_0 \cdot \sqrt{2}\frac{v_{A,0}}{v_0} \sim v_{A,0} \quad (3.10)$$

where  $v_{\perp}$  is the component of the inflow perpendicular to the magnetic field. Though Equation (3.9) only provides a qualitative approximation<sup>4</sup> for  $\theta_{\text{crit}}$ , Equation (3.10) suggests that when  $v_{\perp}/v_{A,0}$  is sufficiently small, high-compression *quasi-hydrodynamic* shocks are possible.

---

<sup>4</sup>For parameters used in Figure 3.1, Equation (3.9) gives  $\theta_{\text{crit}} = 18^\circ$ , approximately 2 times larger than the exact solution.

### 3.2.2 Gravitational Critical Scales in Spherical Symmetry

For a core to collapse gravitationally, its self-gravity must overcome both the thermal and magnetic energy. For a given ambient density  $\rho \equiv \mu_n n$  and assuming spherical symmetry, the mass necessary for gravity to exceed the thermal pressure support (with edge pressure  $\rho c_s^2$ ) is the mass of the critical Bonnor-Ebert sphere (see e.g. Gong & Ostriker 2009):

$$M_{\text{th,sph}} = 4.18 \frac{c_s^3}{\sqrt{4\pi G^3 \rho}} = 4.4 M_\odot \left( \frac{T}{10 \text{ K}} \right)^{3/2} \left( \frac{n}{1000 \text{ cm}^{-3}} \right)^{-1/2} \quad (3.11)$$

(see Section 3.3.2 for discussion about the value of  $\mu_n$ ). The corresponding length scale at the original ambient density is

$$R_{\text{th,sph}} \equiv \left( \frac{3M_{\text{th,sph}}}{4\pi\rho} \right)^{1/3} = 2.3 \frac{c_s}{\sqrt{4\pi G\rho}} = 0.26 \text{ pc} \left( \frac{T}{10 \text{ K}} \right)^{1/2} \left( \frac{n}{1000 \text{ cm}^{-3}} \right)^{-1/2}, \quad (3.12)$$

although the radius of a Bonnor-Ebert sphere with mass given by Equation (3.11) would be smaller than Equation (3.12) by 25%, due to internal stratification.

In a magnetized medium with magnetic field  $B$ , the ratio of mass to magnetic flux for a region to be magnetically supercritical<sup>5</sup> can be written as

$$\left. \frac{M}{\Phi_B} \right|_{\text{mag,crit}} \equiv \frac{1}{2\pi\sqrt{G}}. \quad (3.13)$$

With  $M = 4\pi R^3 \rho/3$  and  $\Phi_B = \pi R^2 B$  for a spherical volume at ambient density  $\rho$ , this gives

$$M_{\text{mag,sph}} = \frac{9}{128\pi^2 G^{3/2}} \frac{B^3}{\rho^2} = 14 M_\odot \left( \frac{B}{10 \mu\text{G}} \right)^3 \left( \frac{n}{1000 \text{ cm}^{-3}} \right)^{-2}. \quad (3.14)$$

---

<sup>5</sup>See Section 3.3.3 for more detailed discussion about the critical value of  $M/\Phi_B$ .

and

$$R_{\text{mag,sph}} = \frac{3}{8\pi\sqrt{G}} \frac{B}{\rho} = 0.4 \text{ pc} \left( \frac{B}{10 \mu\text{G}} \right) \left( \frac{n}{1000 \text{ cm}^{-3}} \right)^{-1}, \quad (3.15)$$

A spherical region must have  $M > M_{\text{th,sph}}$  as well as  $M > M_{\text{mag,sph}}$  to be able to collapse. In the cloud environment (the pre-shock region),  $B \sim 10 \mu\text{G}$  and  $n \sim 1000 \text{ cm}^{-3}$  are typical. Comparing Equation (3.11) and (3.14), the magnetic condition is more strict than the thermal condition; if cores formed from a spherical volume, the mass would have to exceed  $\sim 10 M_{\odot}$  in order to collapse. This value is much larger than the typical core mass ( $\sim 1 M_{\odot}$ ) identified in observations. This discrepancy is the reason why traditionally ambipolar diffusion is invoked to explain how low-mass cores become supercritical.

We can examine the ability for magnetically supercritical cores to form isotropically in a post-shock layer. The normalized mass-to-flux ratio

$$\Gamma \equiv \frac{M}{\Phi_B} \cdot 2\pi\sqrt{G} \quad (3.16)$$

of a spherical volume with density  $\rho$ , magnetic field  $B$ , and mass  $M$  is

$$\begin{aligned} \Gamma_{\text{sph}} &= \frac{8\pi\sqrt{G}}{3} \left( \frac{3}{4\pi} \right)^{1/3} M^{1/3} \rho^{2/3} B^{-1} \\ &= 0.4 \left( \frac{M}{M_{\odot}} \right)^{1/3} \left( \frac{n}{1000 \text{ cm}^{-3}} \right)^{2/3} \left( \frac{B}{10 \mu\text{G}} \right)^{-1}. \end{aligned} \quad (3.17)$$

Or, with  $\Sigma = 4R\rho/3 \equiv \mu_n N_n$  for a sphere, we have

$$\Gamma_{\text{sph}} = 2\pi\sqrt{G} \cdot \frac{\Sigma}{B} = 0.6 \left( \frac{N_n}{10^{21} \text{ cm}^{-2}} \right) \left( \frac{B}{10 \mu\text{G}} \right)^{-1}. \quad (3.18)$$

Considering the cloud parameters from Figure 3.1 ( $\mathcal{M} = 10$ ,  $B_0 = 10 \mu\text{G}$ ,  $n_0 = 1000 \text{ cm}^{-3}$ ), the post-shock density and magnetic field are approximately  $n_{\text{ps}} \sim$

$10^4 \text{ cm}^{-3}$  and  $B_{\text{ps}} \sim 50 \text{ } \mu\text{G}$  when  $\theta > \theta_{\text{crit}}$ . A solar-mass spherical region in this shocked layer will have  $\Gamma_{\text{ps,sph}} \approx 0.37$ ; spherical contraction induced by gravity would be suppressed by magnetic fields. Thus, typical post-shock conditions are unfavorable for forming low-mass cores by spherical contraction in ideal MHD.

Furthermore, using  $r_f$  and  $r_{B_\perp}$  defined in Section 3.2.1, we can compare  $\Gamma_{\text{ps,sph}}$  and the pre-shock value  $\Gamma_{\text{pre,sph}}$  for spherical post-shock and pre-shock regions:

$$\frac{\Gamma_{\text{ps,sph}}}{\Gamma_{\text{pre,sph}}} = \left(\frac{M_{\text{ps}}}{M_{\text{pre}}}\right)^{1/3} \left(\frac{\rho_{\text{ps}}}{\rho_{\text{pre}}}\right)^{2/3} \left(\frac{B_{\text{ps}}}{B_{\text{pre}}}\right)^{-1} \approx \left(\frac{M_{\text{ps}}}{M_{\text{pre}}}\right)^{1/3} r_f^{2/3} r_{B_\perp}^{-1}. \quad (3.19)$$

Considering volumes containing similar mass,  $M_{\text{ps}} \sim M_{\text{pre}}$ , the ratio between the post-shock and pre-shock  $\Gamma_{\text{sph}}$  is smaller than unity when  $\theta > \theta_{\text{crit}}$ , because Equation (3.4) shows that  $r_{B_\perp}$  is larger than  $r_f$ . Thus, provided  $\theta > \theta_{\text{crit}}$ , the post-shock layer will actually have stronger magnetic support than the pre-shock region for a given spherical mass.

Based on the above considerations, formation of low-mass supercritical cores appears difficult in ideal MHD. Adapting classical ideas, one might imagine that low-mass subcritical cores form quasi-statically within the post-shock layer, then gradually lose magnetic support via ambipolar diffusion to become magnetically supercritical in a timescale  $\sim 1 - 10 \text{ Myr}$ . A process of this kind would, however, give prestellar core lifetimes longer than observed, and most cores would have  $\Gamma < 1$  (inconsistent with observations).

Two alternative scenarios could lead to supercritical core formation in a turbulent magnetized medium. First, the dynamic effects during a turbulence-induced shock (including rapid, transient ambipolar diffusion and the quasi-hydrodynamic

compression when  $\theta < \theta_{\text{crit}}$ ) may increase the compression ratio of neutrals, creating  $r_f \gg r_{B_\perp}$  and  $\Gamma_{\text{ps,sph}} > 1$ , enabling low-mass supercritical cores to form. Second, even if the post-shock region is strongly magnetized, mass can accumulate through anisotropic condensation along the magnetic field until both the thermal and magnetic criteria are simultaneously satisfied. In this study, we carefully investigate these two scenarios, showing that both effects contribute to the formation of low-mass supercritical cores within timescale  $\lesssim 0.6$  Myr, regardless of ionization or magnetic obliquity.

### 3.3 Numerical Methods and Models

#### 3.3.1 Simulation Setup and Equations

To examine core formation in shocked layers of partially-ionized gas, we employ a three-dimensional convergent flow model with ambipolar diffusion, self-gravity, and a perturbed turbulent velocity field. We conducted our numerical simulations using the *Athena* MHD code (Stone et al. 2008) with Roe’s Riemann solver. To avoid negative densities if the second-order solution fails, we instead use first-order fluxes for bad zones. The self-gravity of the domain, with an open boundary in one direction and periodic boundaries in the other two, is calculated using the fast Fourier transformation (FFT) method developed by Koyama & Ostriker (2009). Ambipolar diffusion is treated in the strong coupling approximation, as described in Bai & Stone (2011), with super time-stepping (Choi et al. 2009) to accelerate the evolution.

The equations we solve are:

$$\frac{\partial \rho_n}{\partial t} + \nabla \cdot (\rho_n \mathbf{v}) = 0, \quad (3.20)$$

$$\frac{\partial \rho_n \mathbf{v}}{\partial t} + \nabla \cdot \left( \rho_n \mathbf{v} \mathbf{v} - \frac{\mathbf{B} \mathbf{B}}{4\pi} \right) + \nabla P^* = 0, \quad (3.21)$$

$$\frac{\partial \mathbf{B}}{\partial t} + \nabla \times (\mathbf{B} \times \mathbf{v}) = \nabla \times \left[ \frac{((\nabla \times \mathbf{B}) \times \mathbf{B}) \times \mathbf{B}}{4\pi \rho_i \rho_n \alpha} \right], \quad (3.22)$$

where  $P^* = P + B^2/(8\pi)$ . For simplicity, we adopt an isothermal equation of state  $P = \rho c_s^2$ . The numerical setup for inflow and turbulence is similar to that adopted by Gong & Ostriker (2011). For both the whole simulation box initially and the inflowing gas subsequently, we apply perturbations following a Gaussian random distribution with a Fourier power spectrum as described in Gong & Ostriker (2011).

The scaling law for supersonic turbulence in GMCs obeys the relation

$$\frac{\delta v_{1D}(\ell)}{\sigma_{v,\text{cloud}}} = \left( \frac{\ell}{2R_{\text{cloud}}} \right)^{1/2}, \quad (3.23)$$

where  $\delta v_{1D}(\ell)$  represents the one-dimensional velocity dispersion at scale  $\ell$ , and  $\sigma_{v,\text{cloud}}$  is the cloud-scale one-dimensional velocity dispersion. In terms of the virial parameter  $\alpha_{\text{vir}} \equiv 5\sigma_v^2 R_{\text{cloud}}/(GM_{\text{cloud}})$  with  $M_{\text{cloud}} \equiv 4\pi\rho_0 R_{\text{cloud}}^3/3$ , and for the inflow Mach number  $\mathcal{M}$  comparable to  $\sigma_v/c_s$  of the whole cloud, the three-dimensional velocity dispersion  $\delta v = \sqrt{3} \cdot \delta v_{1D}$  at the scale of the simulation box would be

$$\delta v(L_{\text{box}}) = \sqrt{3} \left( \frac{\pi G \alpha_{\text{vir}}}{15} \right)^{1/4} \mathcal{M}^{1/2} c_s^{1/2} \rho_0^{1/4} L_{\text{box}}^{1/2}. \quad (3.24)$$

To emphasize the influence of the cloud magnetization instead of the perturbation field, our simulations are conducted with 10% of the value  $\delta v(L_{\text{box}})$ , or  $\delta v = 0.14$  km/s with  $\alpha_{\text{vir}} = 2$ . With larger  $\delta v(L_{\text{box}})$ , simulations can still form cores,

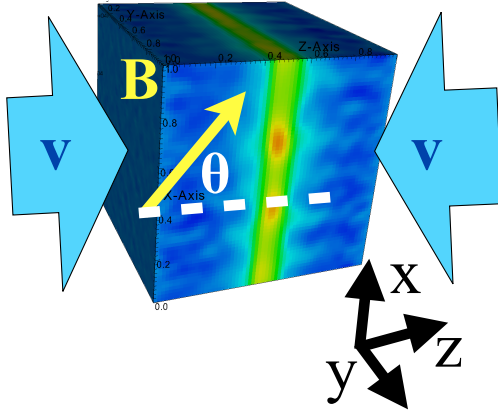


Figure 3.2: The schematic configuration for our simulations.

but because non-self-gravitating clumps can easily be destroyed by strong velocity perturbations and no core can form before the turbulent energy dissipates, it takes much longer, with corresponding higher computational expense.

### 3.3.2 Model Parameters

A schematic showing our model set-up is shown in Figure 3.2. Our simulation box is 1 pc on each side and represents a region within a GMC where a large-scale supersonic converging flow with velocity  $\mathbf{v}_0$  and  $-\mathbf{v}_0$  (i.e. in the center-of-momentum frame) collides. The  $z$ -direction is the large-scale inflow direction, and we adopt periodic boundary conditions in the  $x$ - and  $y$ -directions. We initialize the background magnetic field in the cloud,  $\mathbf{B}_0$ , in the  $x$ - $z$  plane, with an angle  $\theta$  with respect to the convergent flow. For simplicity, we treat the gas as isothermal at temperature  $T = 10$  K, such that the sound speed is  $c_s = 0.2$  km/s. The neutral density within the cloud,  $\rho_0$ , is set to be uniform in the initial conditions and in the

upstream converging flow.

It has been shown that ionization-recombination equilibrium generally provides a good approximation to the ionization fraction within GMCs for the regime under investigation (Chapter 2). Thus, the number density of ions in our model can be written as

$$n_i = \frac{\rho_i}{\mu_i} = 10^{-6} \chi_{i0} \left( \frac{\rho_n}{\mu_n} \right)^{1/2}, \quad (3.25)$$

with

$$\chi_{i0} \equiv 10^6 \times \sqrt{\frac{\zeta_{\text{CR}}}{\alpha_{\text{gas}}}} \quad (3.26)$$

determined by the cosmic-ray ionization rate ( $\zeta_{\text{CR}}$ ) and the gas-phase recombination rate ( $\alpha_{\text{gas}}$ ). The ionization coefficient,  $\chi_{i0}$ , has values  $\sim 1 - 20$  (McKee et al., 2010), and is the model parameter that controls ambipolar diffusion effects in our simulations, following Chapter 2. We use typical values of the mean neutral and ion molecular weight  $\mu_n$  and  $\mu_i$  of  $2.3m_{\text{H}}$  and  $30m_{\text{H}}$ , respectively, which give the collision coefficient (see Equation (3.22)) between neutrals and ions  $\alpha = 3.7 \times 10^{13} \text{ cm}^3 \text{ s}^{-1} \text{ g}^{-1}$ .

The physical parameters defining each model are  $\rho_0$ ,  $v_0 = |\mathbf{v}_0|$ ,  $B_0 = |\mathbf{B}_0|$ ,  $\theta$ , and  $\chi_{i0}$ . We set the upstream neutral number density to be  $n_0 = \rho_0/\mu_n = 1000 \text{ cm}^{-3}$  in all simulations, consistent with typical mean molecular densities within GMCs<sup>6</sup> (e.g. Larson 1981; Williams et al. 2000; Bot et al. 2007; Bolatto et al. 2008). We choose the upstream  $B_0 = 10 \mu\text{G}$  as typical of GMC values (Goodman et al. 1989; Crutcher et al. 1993; Heiles & Crutcher 2005; Heiles & Troland 2005) for all our simulations. To keep the total number of simulations practical, we set the large-

---

<sup>6</sup>Note that the upstream neutral number density we adopted here is  $n_0 = n_{\text{neutral},0} \equiv n_{\text{H}_2} + n_{\text{He}} = 0.6n_{\text{H}} = 1.2n_{\text{H}_2}$ , with GMC observations giving  $n_{\text{H}_2} \sim 10^2 - 10^3 \text{ cm}^{-3}$ . Also note that  $\mu_n \equiv \rho_n/n_n = (\rho_{\text{H}_2} + \rho_{\text{He}})/(n_{\text{H}_2} + n_{\text{He}}) = (0.5n_{\text{H}} \times 2m_{\text{H}} + 0.1n_{\text{H}} \times 4m_{\text{H}})/(0.5n_{\text{H}} + 0.1n_{\text{H}}) = 2.3m_{\text{H}}$ .

scale inflow Mach number to  $\mathcal{M} = 10$  for all models. Exploration of the dependence on Mach number of ambipolar diffusion and of core formation has been studied in previous simulations (Chapter 2 and Gong & Ostriker (2011), respectively). For our parameter survey, we choose  $\theta = 5, 20,$  and  $45$  degrees to represent small ( $\theta < \theta_{\text{crit}}$ ), intermediate ( $\theta > \theta_{\text{crit}}$ ), and large ( $\theta \gg \theta_{\text{crit}}$ ) angles between the inflow velocity and cloud magnetic field. For each  $\theta$ , we conduct simulations with  $\chi_{i0} = 3, 10,$  and ideal MHD to cover situations with strong, weak, and no ambipolar diffusion. We also run corresponding hydrodynamic simulations with same  $\rho_0$  and  $v_0$  for comparison.

A full list of models is contained in Table 3.1. Table 3.1 also lists the steady-state post-shock properties, as described in Section 3.2.1. Solutions for all three types of shocks are listed for the  $\theta = 5^\circ$  (A5) case. For the  $\theta = 20^\circ$  and  $\theta = 45^\circ$  cases, there is only one shock solution. Also included in Table 3.1 are the nominal values of critical mass and radius for spherically symmetric volumes to be self-gravitating under these steady-state post-shock condition, as discussed in Section 3.2.2 (see Equations (3.11), (3.12), (3.14) and (3.15)). Both “thermal” and “magnetic” critical masses are listed. In most models,  $M_{\text{mag,sph}} > M_{\text{th,sph}}$  and  $M_{\text{mag,sph}} \gg M_\odot$ , indicating the post-shock regions are dominated by magnetic support, and either ambipolar diffusion or anisotropic condensation would be needed to form low-mass supercritical cores, as discussed in Section 3.2.2. On the other hand, the *quasi-hydrodynamic* shock solution for models with  $\theta < \theta_{\text{crit}}$  (i.e. A5 cases) has  $M_{\text{mag,sph}} < M_{\text{th,sph}} < M_\odot$  downstream. If this shock solution could be sustained, then in principle low-mass supercritical cores could form by spherical condensation of post-shock gas.

Table 3.1: Summary of the simulation model parameters.

Model	model settings <sup>^</sup>		steady-state post-shock solutions		gravitational critical scales <sup>§</sup>				
	$\theta$ (deg)	$\chi_{i0}$ $B_{\perp}$ ( $\mu\text{G}$ )	$n_{\text{ps}}$ ( $10^4 \text{ cm}^{-3}$ )	$B_{\perp}$ ( $\mu\text{G}$ )	$B_{\text{tot}}$ ( $\mu\text{G}$ )	$M_{\text{th,sph}}$ ( $M_{\odot}$ )	$R_{\text{th,sph}}$ (pc)	$M_{\text{mag,sph}}$ ( $M_{\odot}$ )	$R_{\text{mag,sph}}$ (pc)
HD <sup>¶</sup>	—	—	10.0	—	—	0.44	0.03	—	—
A5X3	5	3 0.87							
A5X10	5	10 0.87							
A5ID <sup>*†</sup>	5	—* 0.87	1.51 8.93 <sup>†</sup> 2.79	55.3 -20.2 <sup>†</sup> -51.8	56.2 22.5 <sup>†</sup> 52.7	1.14 0.47 <sup>†</sup> 0.84	0.07 0.03 <sup>†</sup> 0.05	11 0.01 <sup>†</sup> 2.6	0.15 0.01 <sup>†</sup> 0.07
A20X3	20	3 3.42							
A20X10	20	10 3.42							
A20ID <sup>*</sup>	20	—* 3.42	0.96	56.0	56.7	1.43	0.08	28	0.23
A45X3	45	3 7.07							
A45X10	45	10 7.07							
A45ID <sup>*</sup>	45	—* 7.07	0.69	57.9	58.3	1.68	0.10	59	0.33

<sup>^</sup>In the model settings,  $\theta$  is the angle between inflow velocity and the magnetic field, and  $B_{\perp}$  is the upstream magnetic field perpendicular to the shock front.

<sup>§</sup>The critical masses and sizes for a spherical core at ambient post-shock conditions to have gravity exceed thermal or magnetic forces, calculated from Equations (3.11), (3.12), (3.14), and (3.15).

<sup>¶</sup>Hydrodynamics; no magnetic field, or  $\chi_{i0} = 0$ .

<sup>\*</sup>Ideal MHD; neutrals and ions are perfectly coupled.

<sup>†</sup>The A5 model satisfies  $\theta < \theta_{\text{crit}}$  and has three shock solutions (see Section 3.2.1). We list all three. The post-shock conditions in simulations may be a combination of these possible solutions.

<sup>‡</sup>The quasi-hydrodynamic solution.

In order to collect sufficient statistical information on the core properties from simulations, we repeat each parameter set 6 times with different random realizations of the same perturbation power spectrum for the turbulence. The resolution is  $256^3$  for all simulations such that  $\Delta x \approx 0.004$  pc, or  $\sim 800$  AU. We tested this setup with two times of this resolution ( $\Delta x \approx 0.002$  pc), and the resulting dense structures are highly similar. Though the individual core properties vary around  $\pm 50\%$ , the median values (which are more important in our statistical study) only change within  $\pm 10 - 30\%$ . Thus, our simulations with  $\Delta x \approx 0.004$  pc are well-resolved for investigations of core properties.

### 3.3.3 Analysis of Core Properties

To measure the physical properties of the cores formed in our simulations, we apply the *GRID* core-finding method developed by Gong & Ostriker (2011), which uses gravitational potential isosurfaces to identify cores. In this approach, the largest closed potential contour around a single local minimum of the gravitational potential defines the material eligible to be part of a core. We define the bound core region as all the material within the largest closed contour that has the sum of gravitational, magnetic, and thermal energy negative.<sup>7</sup> All of our cores are, by definition, self-gravitating.

The essential quantity to measure the significance of magnetic fields in self-

---

<sup>7</sup>The gravitational, thermal, and magnetic energy density in each zone are  $u_g = -\rho\Delta\Phi_g$ ,  $u_{\text{th}} = 3nkT/2$ , and  $u_B = B^2/8\pi$ , respectively, where  $\Delta\Phi_g$  is the difference in gravitational potential relative to the largest closed contour, and  $n$  is the neutral number density defined as  $n = \rho/\mu_n$ . The self-gravitating core consists of all zones with  $u_g + u_{\text{th}} + u_B < 0$ .

gravitating cores is the ratio of mass to magnetic flux (Mestel & Spitzer 1956; Mouschovias & Spitzer 1976). From Gauss’s law the net flux of the magnetic field through a closed surface is always zero. As a result, to measure the magnetic flux within a core, we need firstly to define a cross-section of the core, and then measure the net magnetic flux through the surface of the core defined by this cross-section (which is the same as the flux through the cross-section itself).

To define the cross-section through a core, we use the plane perpendicular to the average magnetic field that also includes the minimum of the core’s gravitational potential. This choice ensures that we measure the magnetic flux through the part of the core with strongest gravity. After defining this plane, we separate the core into an upper half and a lower half, and measure the magnetic flux  $\Phi_B$  through one of the halves. In practice, we compute this by firstly finding all zones that contain at least one face which is on the core surface, and assign normal vectors  $\hat{\mathbf{n}}$  (pointing outwards) to those faces. From these, we select only those in the upper “hemisphere” of the core. After we have a complete set of those grid-faces that are on the upper half of the core surface, we sum up their  $\mathbf{B} \cdot \hat{\mathbf{n}}$  to get the net magnetic flux of the core. This method is tested in spherical and rectangular ‘cores’ with magnetic fields in arbitrary directions. Note that this method works best when the core is approximately spherical (without corners).

After we have the measurement of magnetic flux  $\Phi_B$ , we can calculate the mass-to-flux ratio of the core,  $M/\Phi_B$ . This determines whether the magnetic field can support a cloud against its own self-gravity. The critical value of  $M/\Phi_B$  differs with the geometry of the cloud, but the value varies only within  $\sim 10\%$  (e.g. Mouschovias

& Spitzer 1976; Nakano & Nakamura 1978; Tomisaka et al. 1988, or see review in McKee & Ostriker 2007). We therefore choose the commonly used value  $(2\pi\sqrt{G})^{-1}$  (e.g. Kudoh & Basu 2011; Vázquez-Semadeni et al. 2011; Chapter 2) as a reference value, and define the normalized mass-to-flux ratio as  $\Gamma \equiv 2\pi\sqrt{G} \cdot M/\Phi_B$  (see Equation (3.16)). For a prestellar core with  $\Gamma > 1$ , the gravitational force exceeds the magnetic support and the core is magnetically supercritical. A subcritical core has  $\Gamma < 1$  and is ineligible for wholesale collapse unless magnetic fields diffuse out.

### 3.4 Sample Evolution of Structure

Figure 3.3 shows typical evolution of column density and magnetic field<sup>8</sup> in our numerical simulations. The simulations start with uniform density and constant magnetic field. When compressed by the supersonic converging flows, the magnetic fields perpendicular to the converging flows are amplified in the post-shock dense region. Seeded by turbulent velocity perturbations, dense structures form within the compressed layer.

The post-shock structure can be very different for different model parameters. Figure 3.4 and 3.5 provide examples with weak (small  $\theta$  and/or small  $\chi_{i0}$ ) and strong (large  $\theta$  and/or large  $\chi_{i0}$ ) magnetic effects in the shocked gas. The thickness of the post-shock layer is very different for these two extreme cases. Especially at early

---

<sup>8</sup>The magnetic field lines shown in left panels of Figure 3.3, 3.4, and 3.5 are contours of the absolute value of the magnetic vector potential  $\Psi$  in the direction perpendicular to the plane plotted. By definition,  $\mathbf{B} = \nabla \times \Psi$ , and therefore  $B_x = d\Psi_z/dy$ ,  $B_y = -d\Psi_z/dx$ . If we start with  $\Psi_z = 0$  in the lower-left corner ( $x = y = 0$ ), we can compute  $\Psi_z(0, y) = \int_0^y B_x(0, y') dy'$ , and  $\Psi_z(x, y) = \Psi_z(0, y) - \int_0^x B_y(x', y) dx'$ . After we have  $\Psi_z$  everywhere, we make contours to show the magnetic field structures, with fixed spacing so  $\delta\Psi = \text{constant}$ .

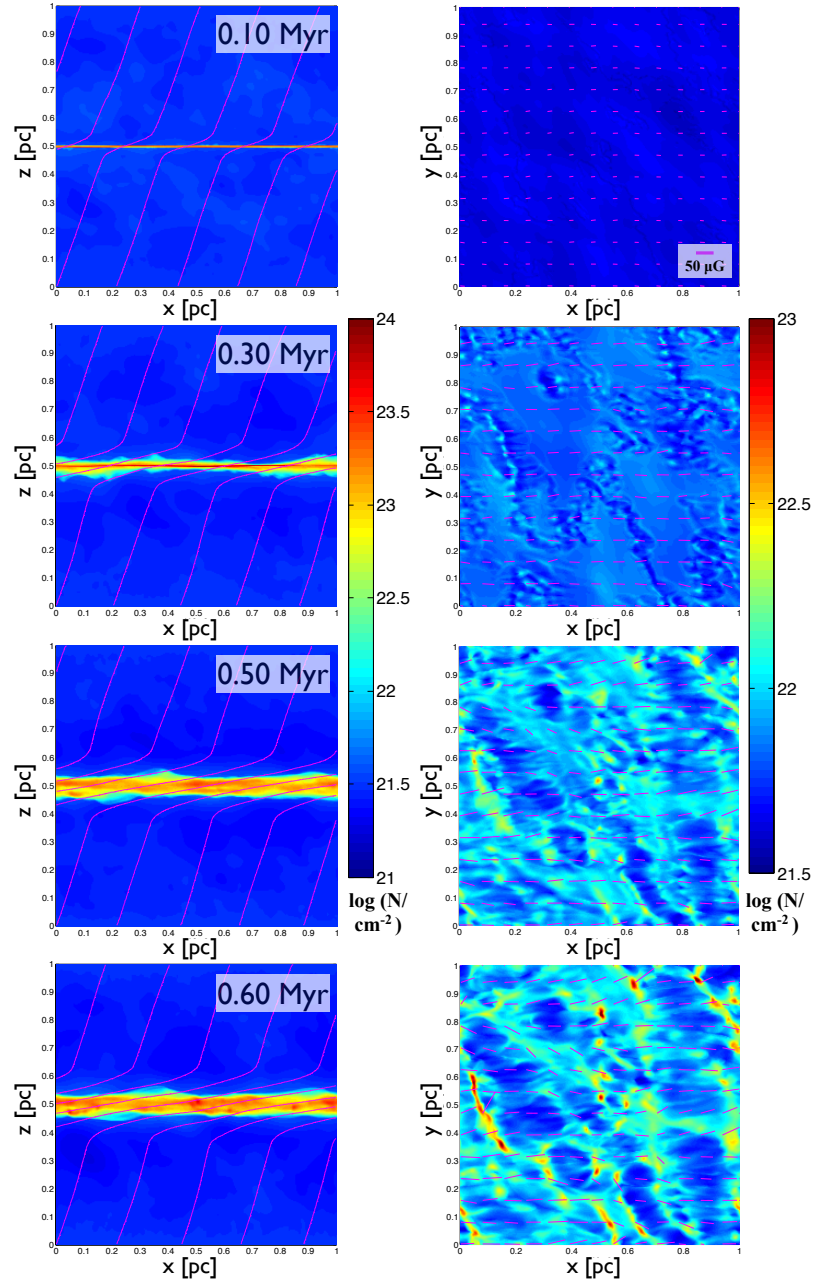


Figure 3.3: An example of the evolution of the column density (colormap) and magnetic field structures (pink lines on left and segments on right) projected to the  $x$ - $z$  plane (*left panel*) and  $x$ - $y$  plane (*right panel*), for model A20X10. Magnetic fields (integrated over the whole box) bend through the shocked gas layer, as seen on left. Right panel shows  $x$ - $y$  projections (with segment lengths indicating strength) of the magnetic field, which points primarily from left to right. The box size is  $(1\text{pc})^3$ .

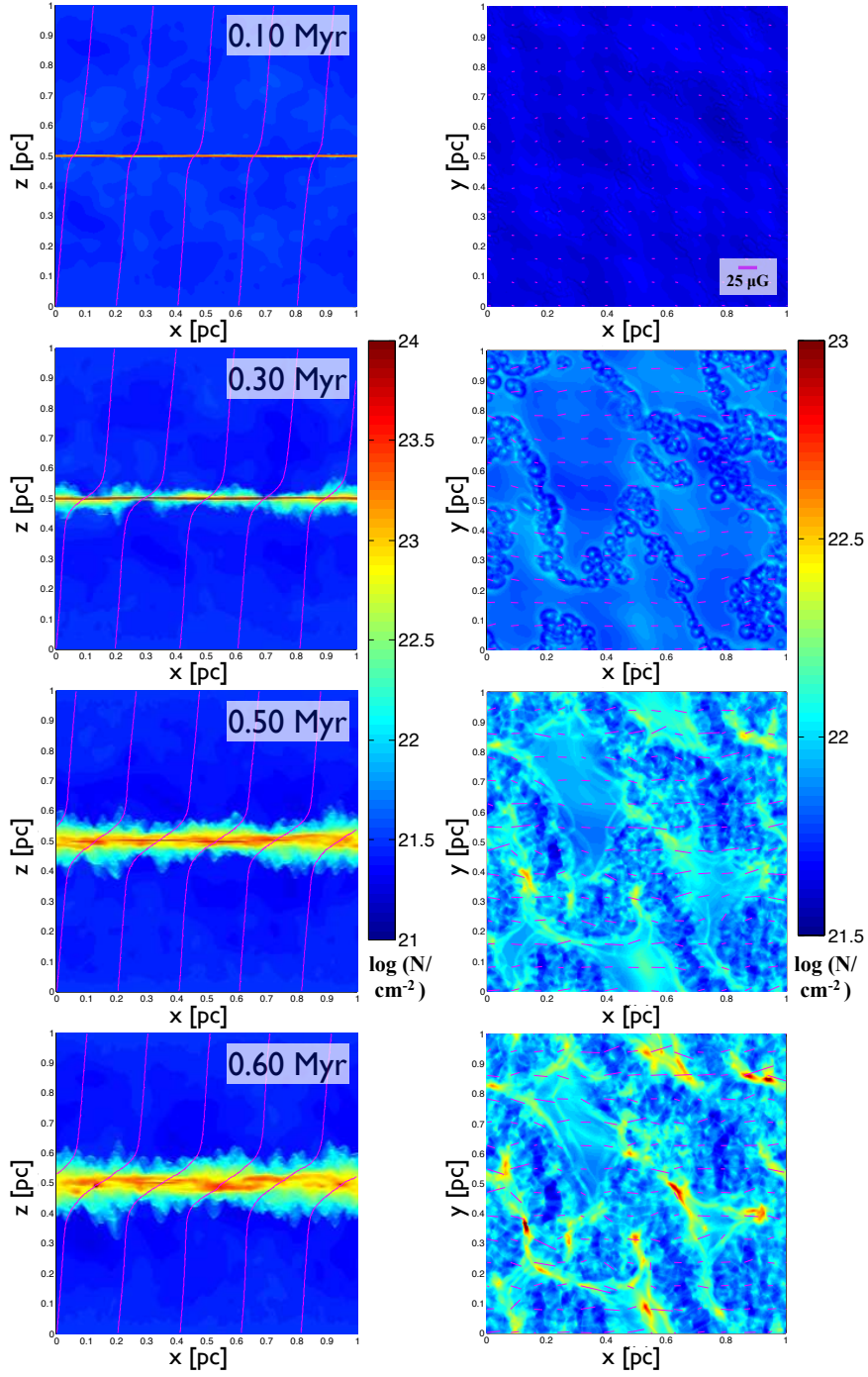


Figure 3.4: Similar to Figure 3.3, but for model A5X3 with upstream magnetic field nearly parallel to the inflow ( $\theta = 5^\circ$ ), and low ionization fraction ( $\chi_{i0} = 3$ ).

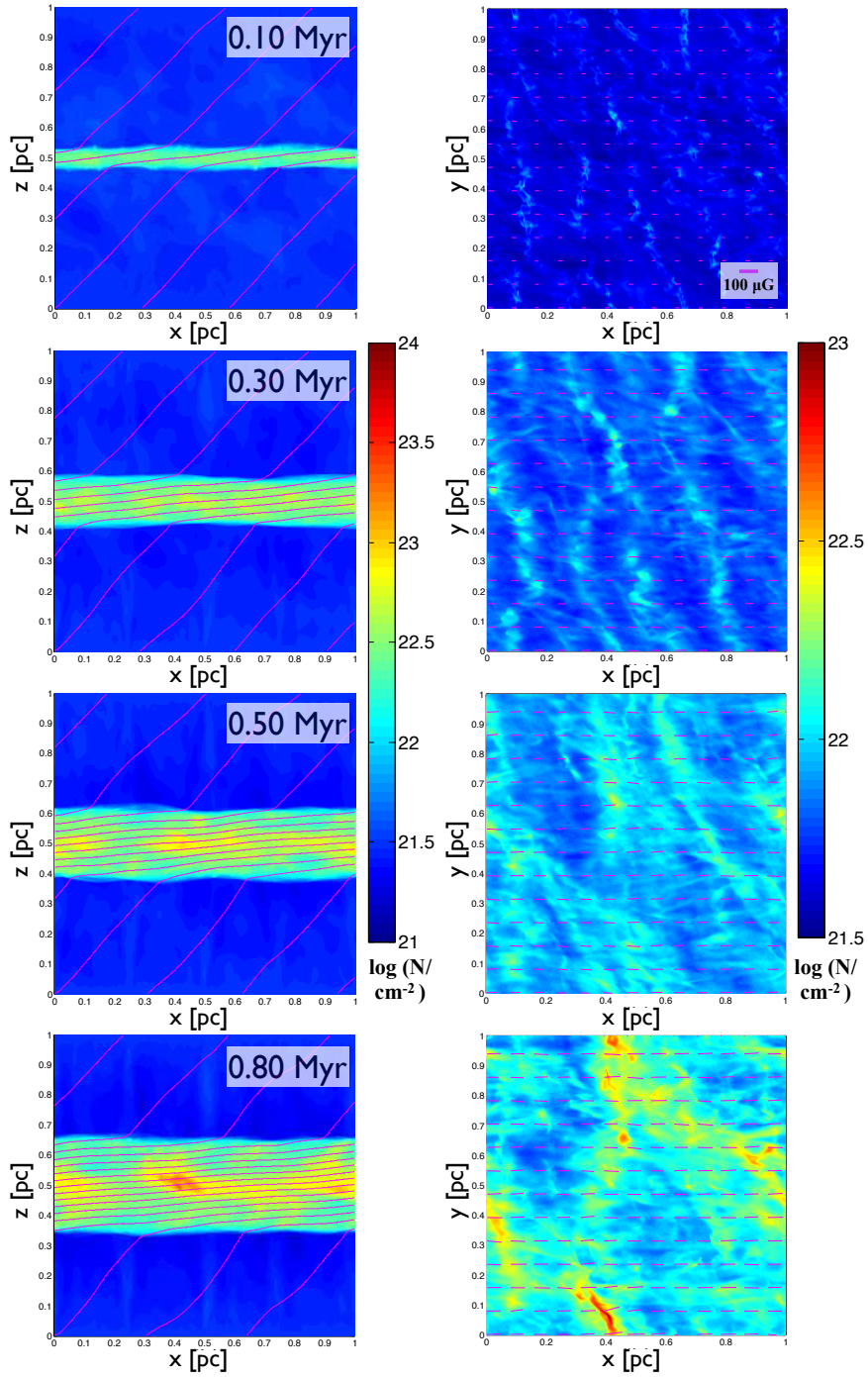


Figure 3.5: Similar to Figure 3.3, but for model A451D, with  $45^\circ$  angle between upstream  $\mathbf{v}$  and  $\mathbf{B}$ , and ideal MHD.

time (0.3 Myr), structure is also different in these two cases, with stronger magnetic effects producing filaments perpendicular to the magnetic field. The timescale at which compressed layers become gravitationally unstable and start to form cores also differ. Note that in the cases with ambipolar diffusion (Figure 3.3 and 3.4), a highly-compressed layer forms in the center of the post-shock region. Quantitatively, we measured the average density within the  $z = 0.5 \text{ pc} \pm \Delta x$  layer at  $t = 0.3 \text{ Myr}$  for model A5X3, and found this overdense layer has  $\bar{n} \approx 1.4 \times 10^5 \text{ cm}^{-3}$ , which exceeds the steady-MHD shock jump condition predicted in Table 3.1 even for the *quasi-hydrodynamic* solution. This is a direct evidence of the existence of transient stage of ambipolar diffusion (Chapter 2).

Table 3.2 lists the physical properties of the post-shock layers measured at  $t = 0.2 \text{ Myr}$  as well as the corresponding values of the critical mass and size of a spherical region under these ambient conditions. Generally, models with upstream magnetic field almost parallel to the inflow (A5 models) have weaker post-shock magnetic field than that for a *fast* shock (see Table 3.1) even with ideal MHD (A5ID), indicating that the *quasi-hydrodynamic* shock mode discussed in Section 3.2 plays a role. Also, models with stronger transient ambipolar diffusion effect (smaller  $\chi_{i0}$ ) have higher density and weaker magnetic field in the post-shock layer, and thus it would be easier to form self-gravitating cores promptly (small  $M_{\text{th,sph}}$  and  $M_{\text{mag,sph}}$  values).

The difference in post-shock magnetic field among models with same upstream magnetic obliquity but various ionization levels can be explained by varying transient ambipolar diffusion. From Equation (2.64) in Chapter 2, the timescale before the

shock profile transitions to that of a steady C-shock is

$$t_{\text{transient}} \approx \frac{2r_f^{1/2}}{\alpha\rho_{i,0}} = 0.34 \text{ Myr} \left(\frac{r_f}{10}\right)^{1/2} \left(\frac{\chi_{i0}}{10}\right)^{-1} \left(\frac{n_0}{1000 \text{ cm}^{-3}}\right)^{-1/2}. \quad (3.27)$$

Therefore, while the late-time (ideal MHD) value of  $r_f$  is the same for models with same  $\theta$  value, it will take 3.33 times longer for the X3 models to reach steady-state post-shock values than the X10 models. Correspondingly, the compression rate of the magnetic field in X3 models is 0.3 times slower than in X10 models, and thus the magnetic field within the post-shock layer is weaker in X3 models than in X10 or ideal MHD models at a given time. This tendency is clearly shown in Table 3.2; note that since  $r_f$  might be larger because of the transient ambipolar diffusion effect, the difference in post-shock magnetic field is further enhanced (smaller  $\chi_{i0}$  causes higher  $r_f$ , resulting in longer  $t_{\text{transient}}$  and weaker  $B_{\text{ps}}$ ).

Figure 3.6 compares the density structures formed under different physical conditions, at the timescale when  $n_{\text{max}} \geq 10^7 \text{ cm}^{-3}$  in each simulation. With low ionization (strong ambipolar diffusion), the clumps are relatively more isolated and randomly distributed, following the initial perturbation pattern. Models with high ionization (weak or no ambipolar diffusion) show well-ordered large-scale filament structures. Structures are also at larger scales for models with larger magnetic field parallel to the shock front (large  $\theta$ ). The filaments are around 0.05 pc wide, consistent with the observed characteristic width of filaments ( $\sim 0.1$  pc, Arzoumanian et al. 2011; or see review in André et al. 2014). Note that the filaments are not necessary perpendicular to the magnetic field as indicated in Inoue & Fukui (2013) because the initial velocity field in our simulations is not homogeneous.

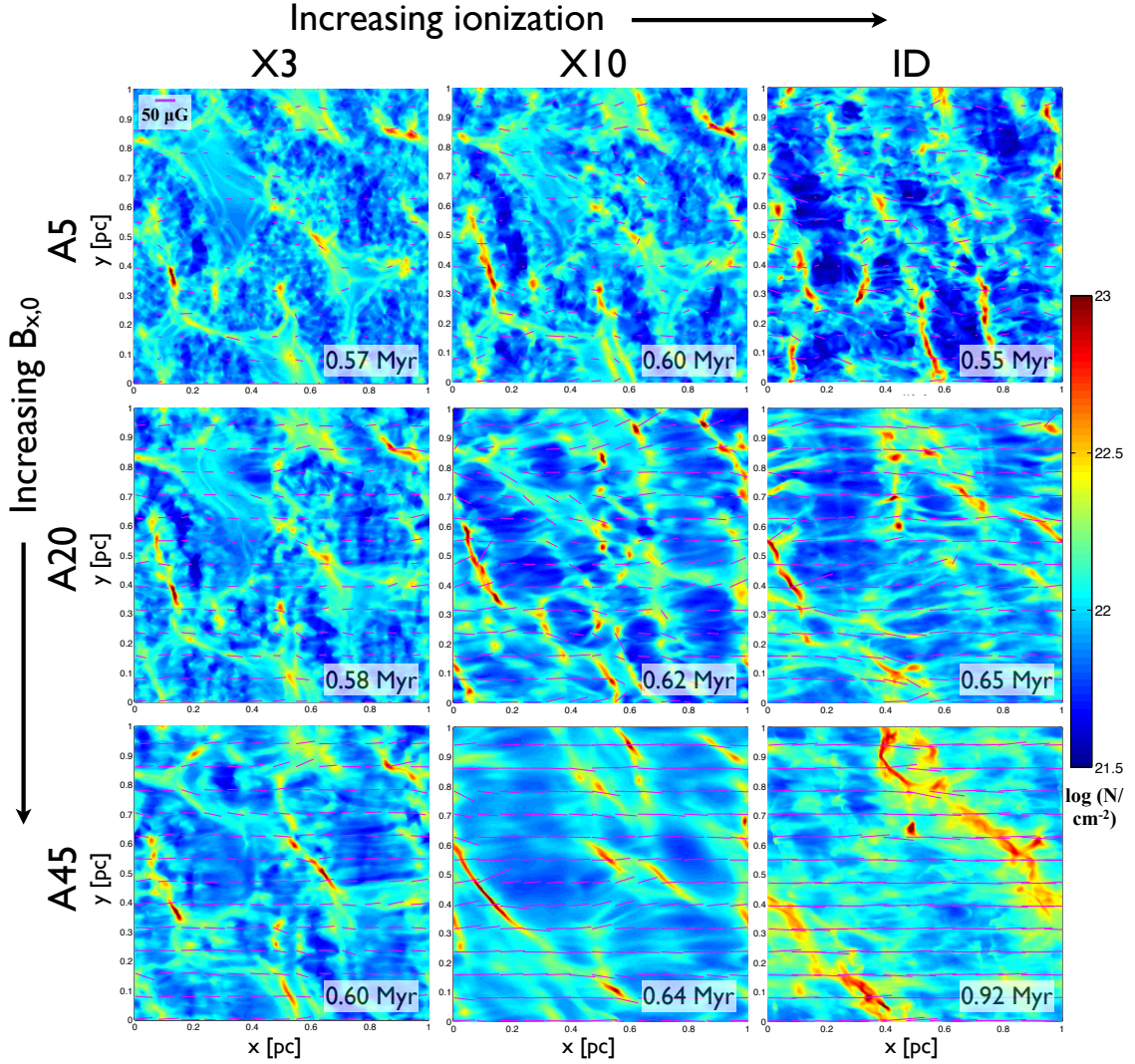


Figure 3.6: The “spectrum” of column density (color map) and magnetic field (pink segments) structure in the shocked gas layer for varying magnetic field parallel to the shock and ionization, at the time that maximum density reaches  $10^7 \text{ cm}^{-3}$ . Model parameters are given in Table 3.1.

Table 3.2: Summary of the post-shock properties measured from simulations.

Model	post-shock properties <sup>§</sup>			gravitational critical scales			
	$\bar{n}_{\text{ps}}$ ( $10^4 \text{ cm}^{-3}$ )	$\bar{B}_{\text{ps}}$ ( $\mu\text{G}$ )	$\bar{\beta}_{\text{ps}}$	$M_{\text{th,sph}}$ ( $M_{\odot}$ )	$R_{\text{th,sph}}$ (pc)	$M_{\text{mag,sph}}$ ( $M_{\odot}$ )	$R_{\text{mag,sph}}$ (pc)
HD	5.5	—	—	0.60	0.04	—	—
A5X3	5.3	26	3.0	0.61	0.04	0.09	0.02
A5X10	5.3	40	1.3	0.60	0.04	0.31	0.03
A5ID	2.4	47	0.43	0.90	0.05	2.4	0.08
A20X3	5.3	45	1.02	0.61	0.04	0.45	0.03
A20X10	3.6	68	0.30	0.74	0.04	3.4	0.07
A20ID	1.4	78	0.09	1.2	0.07	33	0.22
A45X3	4.2	60	0.45	0.69	0.04	1.7	0.06
A45X10	2.7	86	0.14	0.85	0.05	12	0.13
A45ID	0.91	96	0.04	1.5	0.09	151	0.41

<sup>§</sup>Post-shock properties are measured at  $t = 0.2$  Myr in each model, averaged over the whole post-shock layer. The timescale is chosen so the downstream properties are measured before the post-shock layer becomes strongly self-gravitating.

In addition, models with moderately strong magnetization have a network of small sub-filaments aligned parallel to the magnetic field (A20X10, A20ID, A45X10, and A45ID models in Figure 3.6). These features are very similar to the striations identified in  $^{12}\text{CO}$  emission map of the Taurus molecular cloud (Goldsmith et al. 2008), subsequently observed in other clouds (Sugitani et al. 2011; Hennemann et al. 2012; Palmeirim et al. 2013; or see review in André et al. 2014). This filament pattern is likely due to the anisotropy of turbulence at small scales in a magnetized medium (Goldreich & Sridhar 1995), which tends to have more power for wavenumbers  $\hat{k} \perp \mathbf{B}$ . This leads to the formation of threads/striations/sub-filaments with small separations aligned parallel to the magnetic field in molecular clouds if the magnetic field is sufficiently strong. Vestuto et al. (2003) and Heyer et al. (2008)

found that in order to have significant turbulent anisotropy, the plasma  $\beta$  must satisfy  $\beta \lesssim 0.2$ , which agrees with our results for when these striations are seen (see  $\bar{\beta}_{\text{ps}}$  values listed in Table 3.2).

### 3.5 Survey of Core Properties

We define the timescale used in Figure 3.6 (at which  $n_{\text{max}} \geq 10^7 \text{ cm}^{-3}$ ) as the moment  $t_{\text{collapse}}$  when the most evolved core starts to collapse, and measure the physical properties of all cores formed at this time. We identified hundreds of gravitationally bound cores from our 60 simulations (6 runs for each parameter set), with examples illustrated in Figure 3.7. The simulation results are summarized in Table 3.3, including the following core properties: mean density  $\bar{n}$ , size  $L$ , mass  $M$ , mean magnetic field  $\bar{B}$ , and normalized mass-to-flux ratio  $\Gamma$ . To ensure the measured core properties are only for resolved structures, we omit cores with less than 27 zones, or  $L_{\text{core}}$  smaller than  $\sim 0.015$  pc. Table 3.3 also shows for each parameter set the mean value of time  $t_{\text{collapse}}$  (at which the core properties are measured). These cores have masses, sizes, and mass-to-flux ratios similar to observed values (e.g. Falgarone et al. 2008; Troland & Crutcher 2008; Rathborne et al. 2009; Kirk et al. 2013).

Our results show that low-mass supercritical cores form at  $t < 1$  Myr in all models: with converging velocity either nearly aligned with the magnetic field (small  $\theta$ ) or highly oblique (large  $\theta$ ), and for all levels of ambipolar diffusion. We also calculated the core formation efficiency (CFE) from our simulations:

$$\text{CFE} \equiv \frac{\text{mass in cores}}{\text{mass of the shocked layer}} = \frac{\sum_i M_{\text{core},i}}{2\rho_0 v_0 t_{\text{collapse}} \cdot L_x L_y} \approx 3.1\%. \quad (3.28)$$

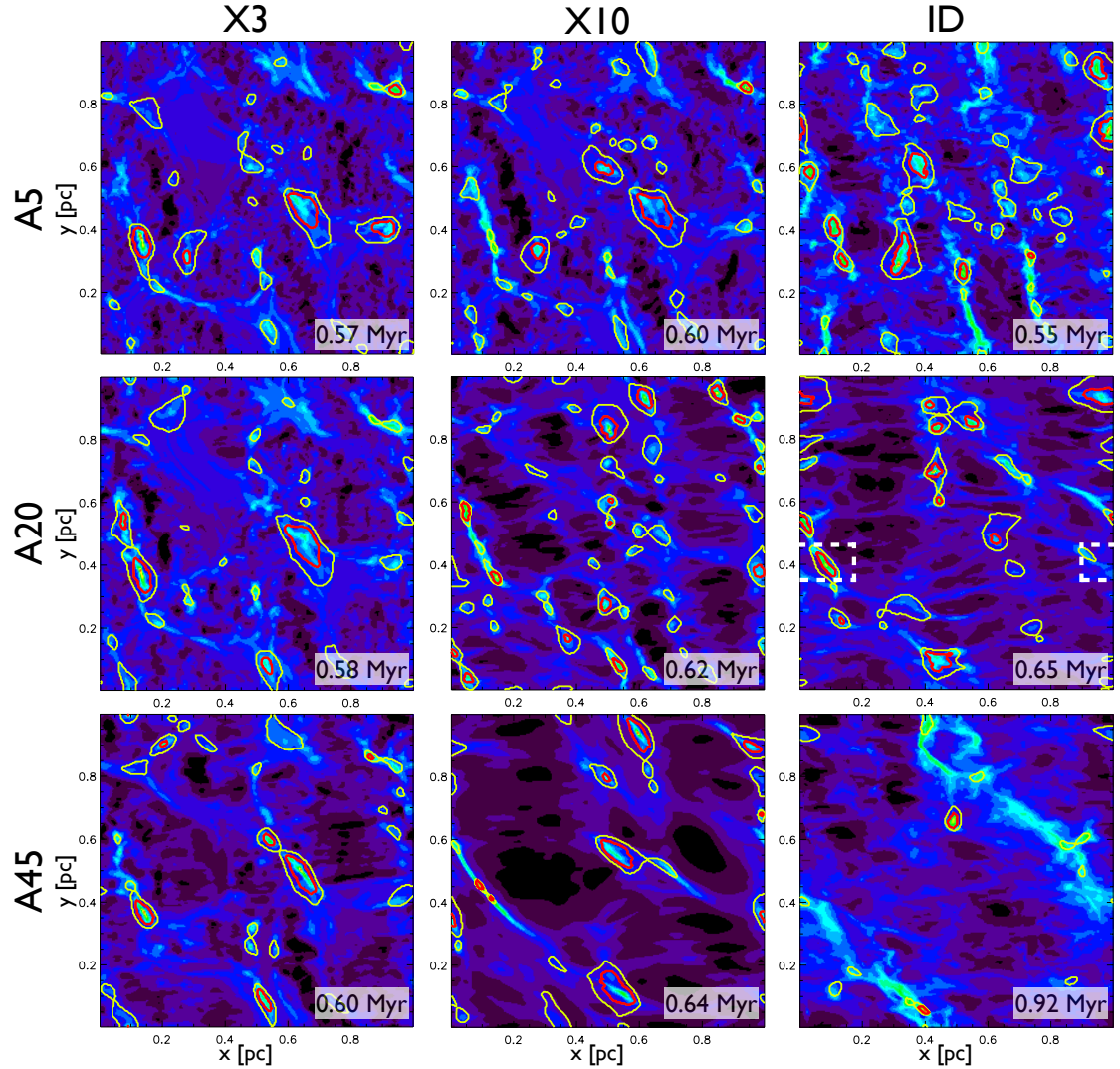


Figure 3.7: An illustration, using one simulation for each set of model parameters, of the cores identified at the time  $t_{\text{collapse}}$  when the maximum density reaches  $10^7 \text{ cm}^{-3}$ . Candidate core regions are identified using the modified *GRID* core-finding method (*yellow contours*), and we only consider the gravitationally bound sub-regions (*red contours*). The white dashed-line box in A20ID model is the zoomed-in region shown in Figure 3.13 (note that the simulation box is periodic in  $x$ - and  $y$ -directions).

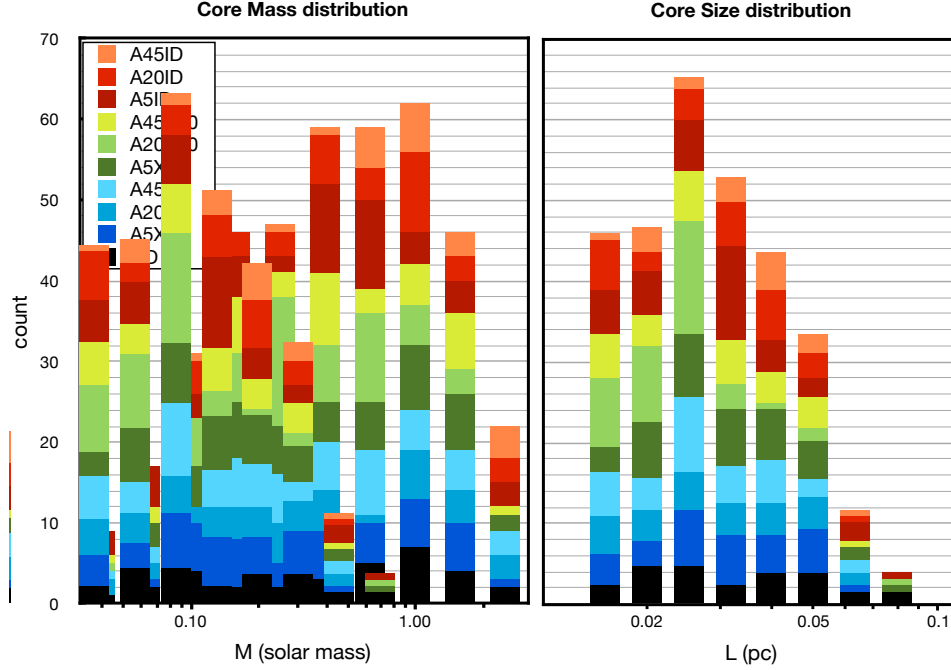


Figure 3.8: The statistical distribution of core mass (*left*) and size (*right*) from all models combined.

This is similar to the observed star formation efficiency (SFE), which is around 1 – 10% (e.g. Myers et al. 1986; Evans et al. 2009; Lada et al. 2010). Note that, though the core formation timescale is slightly different from model to model (see Figure 3.6), the CFE does not vary significantly between models; the variance in CFE among all models is only  $\sim 10\%$ .

### 3.5.1 Mass and Size

Figure 3.8 shows the distribution of mass and size of cores for all model parameters. The masses range between 0.04 to  $2.5 M_{\odot}$ , with peak around  $\sim 0.6 M_{\odot}$ ; the core sizes are between 0.015 – 0.07 pc, with peak around  $\sim 0.03$  pc. These

Table 3.3: Results from identified cores measured at  $t = t_{\text{collapse}}$ .

Model	# Cores Identified*	CFE <sup>¶</sup> (%)	$t_{\text{collapse}}^{\S}$ (Myr)	$\bar{n}_{\text{core}}$ ( $10^5 \text{ cm}^{-3}$ )	$L_{\text{core}}^{\dagger}$ (pc)	$M_{\text{core}}$ ( $M_{\odot}$ )	$\bar{B}_{\text{core}}$ ( $\mu\text{G}$ )	$\Gamma_{\text{core}}$ (normalized)
HD	32	3.1	0.56	5.8	0.036	0.75	—	—
A5X3	40	3.1	0.58	5.5	0.032	0.63	42	4.4
A5X10	49	3.7	0.61	6.6	0.031	0.65	64	3.7
A5ID	51	3.9	0.54	5.6	0.030	0.58	67	2.6
A20X3	34	3.0	0.59	5.6	0.032	0.72	60	3.9
A20X10	54	3.1	0.60	9.7	0.025	0.47	79	3.3
A20ID	36	3.3	0.62	9.5	0.031	0.78	90	2.7
A45X3	42	3.7	0.60	8.9	0.031	0.73	83	3.7
A45X10	38	3.2	0.60	9.2	0.030	0.70	82	3.0
A45ID	21	1.9	0.90	11	0.035	1.12	137	2.1

\*We only consider gravitationally bound cores with  $E_{\text{grav}} + E_{\text{thermal}} + E_{\text{B}} < 0$ .

<sup>¶</sup>CFE is the ratio of the total mass in cores to the total mass in the shocked layer at  $t_{\text{collapse}}$ .

<sup>†</sup>Columns (5)–(9) are averaged over all cores for each parameter set (6 simulation runs).

<sup>§</sup>Collapse is defined as the time when  $n_{\text{max}} = 10^7 \text{ cm}^{-3}$  in each simulation. The  $t_{\text{collapse}}$  shown here is the mean value over all 6 runs for each parameter set.

<sup>‡</sup> $L_{\text{core}}$  is calculated from the total number of zones  $N$  within a core, for an equivalent spherical volume:  $L_{\text{core}} = 2 \times (3N/(4\pi))^{1/3} \Delta x$ , where  $\Delta x = 1/256 \text{ pc}$  is the grid size.

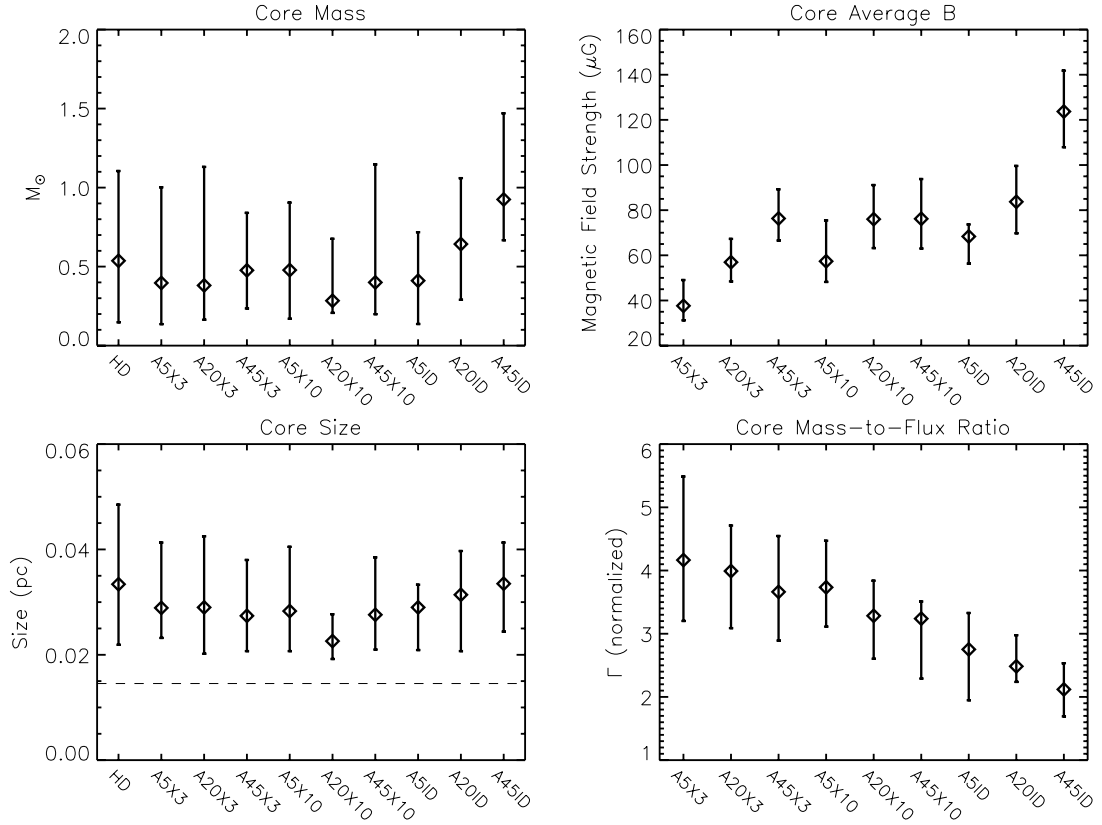


Figure 3.9: Median (*diamond*) and  $\pm 25\%$  values (*vertical bars*) of core mass, size, average magnetic field, and normalized mass-to-flux ratio for different model parameters. In each figure from left to right, higher X corresponds to increasing ionization, and larger A corresponds to larger angle  $\theta$ , or increasing pre-shock (upstream) magnetic field  $B_x = B_0 \sin \theta$  parallel to the shock front. The dashed line in the core size plot (*bottom left*) indicates the lower limit (0.015 pc) of resolved core size; for our simulations,  $0.015 \text{ pc} \approx 3\Delta x$ .

are consistent with observational results (e.g. Motte et al. 2001; Ikeda et al. 2009; Rathborne et al. 2009; Kirk et al. 2013). Also, the distribution of the core mass shows a similar shape to the observed core mass function (CMF) (e.g. Simpson et al. 2008; Rathborne et al. 2009; Könyves et al. 2010). Interestingly, the peak in the distribution is close to value given by Equation (7) from Gong & Ostriker (2011):

$$M_{\text{BE, ps}} = 1.2 \frac{c_s^4}{\sqrt{G^3 P_{\text{ps}}}} = 1.2 \frac{c_s^3}{\sqrt{G^3 \rho_0}} \frac{1}{\mathcal{M}} \rightarrow 0.45 M_{\odot}. \quad (3.29)$$

This mass is characteristic of what is expected for collapse of a thermally-supported core that is confined by an ambient medium with pressure equal to the post-shock value<sup>9</sup>, where the numerical figure uses values for the mean cloud density and large-scale Mach number equal to those of the converging flow in our simulations,  $n_0 = 1000 \text{ cm}^{-3}$  and  $\mathcal{M} = 10$ . Correspondingly, since the critical ratio of mass and radius is  $M_{\text{BE}}/R_{\text{BE}} = 2.4c_s^2/G$  (Bonnor 1956), the characteristic size expected for a collapsing core formed in a post-shock region when the Mach number of the large-scale converging flow is  $\mathcal{M}$  and the mean cloud density is  $\rho_0$ , is

$$L_{\text{BE}} = 2R_{\text{BE}} = \frac{c_s}{\sqrt{G\rho_0}} \frac{1}{\mathcal{M}} \rightarrow 0.04 \text{ pc}. \quad (3.30)$$

This is again comparable to the peak value of the core size distribution in Figure 3.8.

We also separately explore the dependence of core mass, size, magnetic field strength, and mass-to-flux ratio on model parameters, as shown in Figure 3.9. Our results show that the core mass is relatively insensitive to both the ionization (i.e. ambipolar diffusion effect) and obliquity of the upstream magnetic field (Figure 3.9,

---

<sup>9</sup>The post-shock total pressure (whether for an unmagnetized medium, as considered by Gong & Ostriker (2011), or for a magnetized medium as considered here) will be comparable to the momentum flux of the converging flow,  $P_{\text{ps}} \approx \rho_0 v_0^2 = \rho_0 c_s^2 \mathcal{M}^2$ .

top left). The median masses are within a factor 2.4 of the mean of the whole distribution,  $0.68 M_{\odot}$ , or a factor 2 of the median of all core masses ( $0.47 M_{\odot}$ ). Similarly, median core sizes vary only between 0.022 pc and 0.034 pc for the various parameter sets, with a median of 0.03 pc. Note that we chose to compare median values between different parameter sets in Figure 3.9 instead of mean values used in Table 3.3, because an average can be affected by any single value being high or low relative to the other samples. The median value, on the other hand, represents the central tendency better, and with the  $\pm 25\%$  values we can have a better understanding of the sample distribution.

We note in particular that for the  $\theta = 20^{\circ}$  and  $\theta = 45^{\circ}$  ideal MHD cases, the masses in Figure 3.8 and 3.9 are more than an order of magnitude lower than the limits for a spherical region at post-shock conditions to be magnetically supercritical, as listed in Table 3.1 and 3.2. This implies that the low-mass bound cores found in the simulations did not form isotropically. We discuss this further in Section 3.6.

To further investigate the relationship between core masses and sizes, we binned the data set by  $\log L_{\text{core}}$  and calculate the average core mass and mean density for different model parameters. The results are shown in Figure 3.10, where we chose four models with different magnetization and ionization levels to compare: HD (hydrodynamics; no magnetization), A5X3 (low ionization, weak upstream magnetic field parallel to the shock), A20X10 (moderate ionization and magnetic field), and A45ID (ideal MHD, strong magnetic field). In both the mass-size and density-size plots, the differences among models are small, and all four curves have similar shape. In fact, from all resolved cores identified in our simulations, we found a

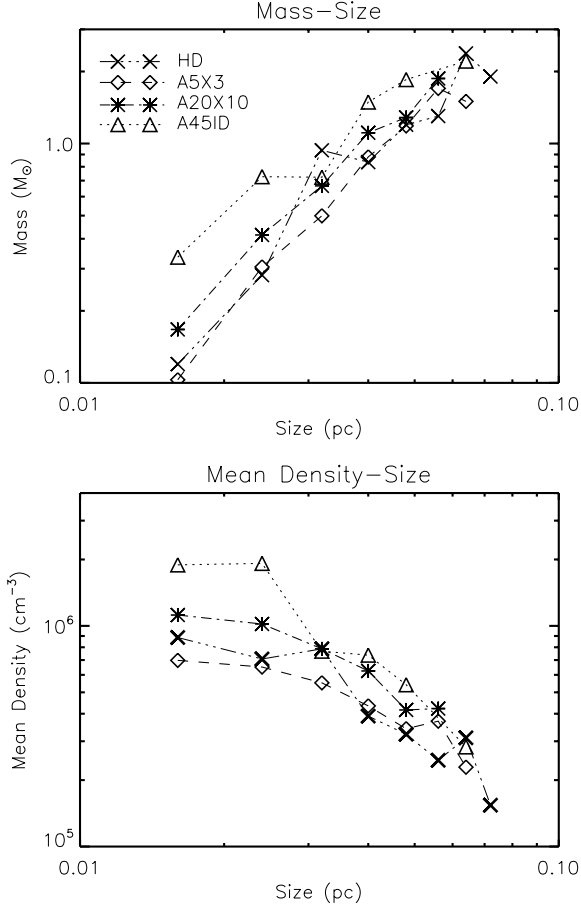


Figure 3.10: The mass-size plot (*top*) and density-size plot (*bottom*) for cores identified in selected models with different magnetization and ionization levels: HD (*cross*), A5X3 (*diamonds*), A20X10 (*asterisks*), and A45ID (*triangles*).

power-law relationship between the core mass and size,  $M \propto L^k$ , with best-fitted value  $k = 2.28$ . This is consistent with many core-property surveys towards different molecular clouds (e.g. Elmegreen & Falgarone 1996; Curtis & Richer 2010; Roman-Duval et al. 2010; Kirk et al. 2013), in which  $k = 1.2 - 2.4$  with various molecule tracers (for more details, see Figure 7 and corresponding discussions in Kirk et al. 2013).

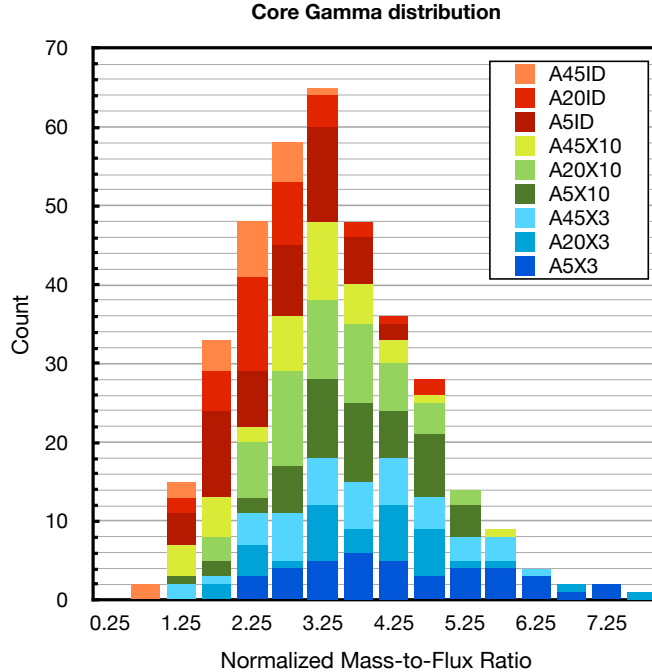


Figure 3.11: The statistical distribution of normalized core mass-to-flux ratio  $\Gamma$  from all simulations combined. Models with low ionization (*blue*) preferentially have higher  $\Gamma$ , whereas models with ideal MHD (*red*) have lower  $\Gamma$ .

### 3.5.2 Magnetization

Figure 3.11 shows the distribution of core mass-to-flux ratio, a roughly normal distribution with peak at  $\Gamma \sim 3$ . This range of  $\Gamma$  is quite similar to observational results ( $\Gamma \sim 1 - 4$ ; Falgarone et al. 2008; Troland & Crutcher 2008). In addition, the color-coded histogram in Figure 3.11 shows how the mass-to-flux ratio depends on magnetization: the high-end region ( $\Gamma \gtrsim 5$ ) is comprised of blue-green pieces (which represent models with lower ionization), while the low-end tail is mostly red and orange (highly ionized models). Note that essentially all of the cores in our simulations are magnetically supercritical ( $\Gamma > 1$ ), which is self-consistent with our

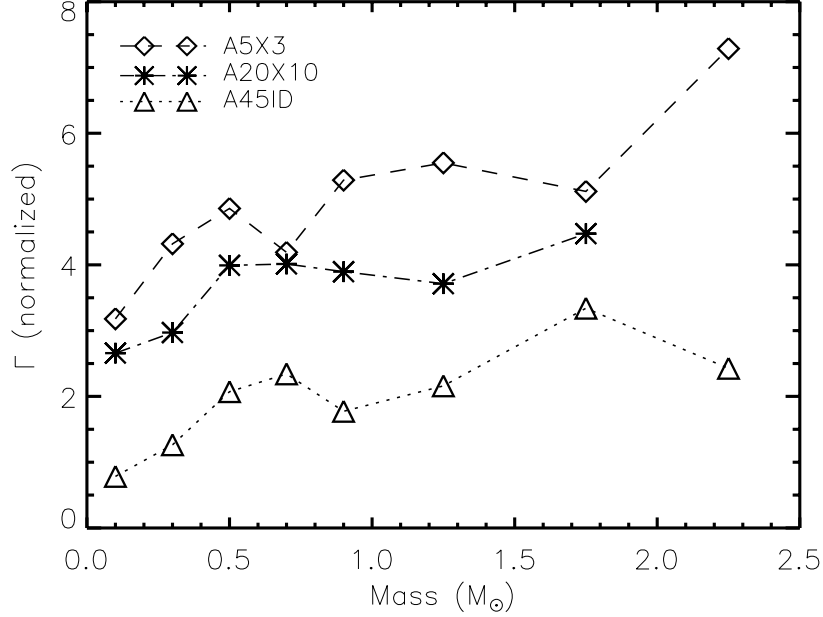


Figure 3.12: Core mass-to-flux ratio versus core mass for sample sets of parameters. The value of  $\Gamma$  tends to increase with ionization, and to a lesser extent also increases with mass.

core-finding criterion (gravitationally bound;  $E_g + E_{\text{th}} + E_B < 0$ ).

The tendency of models with lower ionization to form cores with higher mass-to-flux ratio is very clearly seen in Figure 3.9 (*bottom right*). The median value of the core mass-to-flux ratio also decreases with increasing  $\theta$  as the value of the upstream  $B_x = B_0 \sin \theta$  increases. Also from Figure 3.9 (*top right*), the average core magnetic fields show a similar tendency as in post-shock magnetic field (see Table 3.2), which decrease at lower ionization fractions for models with same pre-shock magnetic field structure (same  $\theta$ ). The larger and more systematic variation of  $\bar{B}$  than  $M$  with model parameters suggests that the core mass-to-flux ratio is not decided by the core mass, but by the core magnetic field. This is also shown in Figure 3.12, where we binned the data by  $M_{\text{core}}$  and calculated the average core mass-to-flux ratio in

each bin for different models. For cores with similar mass, the mass-to-flux ratios of cores formed in environments with low ionization and magnetization are much higher than those with stronger and better coupled magnetic fields.

The fact that the median value of magnetic field strength within the core depends on pre-shock magnetic obliquity and ionization is consistent with our discussions in Section 3.4 that magnetic fields are lower in shocked regions that have longer transient timescales. Since lower ionization fraction leads to stronger ambipolar diffusion and a longer transient stage<sup>10</sup>, it is logical to expect the cores formed in weakly-ionized clouds have lower magnetic field than those formed with higher ionization fraction (or strongly-coupled ions and neutrals).

In addition, Figure 3.9 (*top right*) shows that cores formed in models with small  $\theta$  (A5 cases) have weaker magnetic fields inside even with higher ionization fraction or ideal MHD, which indicates that the magnetic field is less compressed by the shock when the inflow is almost parallel to the upstream magnetic field. This is consistent with the discussion in Section 3.2: when  $\theta < \theta_{\text{crit}}$ , the MHD shock becomes a composite compounded of the regular (*fast*) mode and the *quasi-hydrodynamic* mode, which has relatively small magnetic field compression ratio. Thus, the magnetic obliquity relative to the shock has a similar effect to the cloud ionization fraction in determining field strengths in prestellar cores.

Based on the results shown in Section 3.5.1 and 3.5.2, we conclude that magnetic effects do not appear to control core mass and size. This suggests that once a

---

<sup>10</sup>From Chapter 2 and Equation (3.27), the predicted duration of the transient stage is 0.3 – 1.4 Myr for  $\chi_{i0} = 3$  to 10 and our range of model parameters, assuming  $r_f = r_{f, \text{ideal MHD}}$ .

core becomes strongly gravitationally bound, magnetic effects are relatively unimportant to its internal structure. However, the formation process of gravitationally bound cores is highly dependent on magnetic effects. As noted above, Figure 3.6 shows clear differences in the large-scale structures from which cores condense; we discuss core formation further in Section 3.6. Also, cores are born with either lower or higher magnetic field, depending on the magnetic field structure and the ambipolar diffusion in their surrounding environment.

## 3.6 Anisotropic Core Formation

### 3.6.1 Examples of Simulation Evolution

The fact that gravitationally supercritical low-mass cores (with  $M \ll M_{\text{mag,sph}}$ ) can form in the highly magnetized post-shock medium even without ambipolar diffusion suggests that these cores did not contract isotropically. Figure 3.13 provides a close-up view of the core forming process in highly magnetized environment with ideal MHD, from model A20ID. At stages earlier than shown, the directions of the perturbed magnetic field and gas velocity are determined randomly by the local turbulence. The magnetic field is compressed by the shock (similar to Figures 3.3–3.5), such that in the post-shock layer it is nearly parallel to the shock front (along  $\hat{\mathbf{x}}$ ). When the magnetic field strength increases, the velocity is forced to become increasingly aligned parallel to the flow, as shown in Figure 3.13. By the time  $t = 0.65$  Myr, a very dense core has formed by gathering material preferentially along the magnetic field lines. After the core becomes sufficiently massive, its self-gravity will distort

the magnetic field and drag material inward even in the direction perpendicular to the magnetic field lines ( $t = 0.77$  Myr, Figure 3.13). This collapsing process with a preferential direction is similar to the post-shock focusing flows found in previous studies (e.g. Inoue & Fukui 2013; Vaidya et al. 2013) where the gas is confined by the strong magnetic field in the shock-compressed region.

In fact, anisotropic condensation is key to core formation not only with ideal MHD, but for all cases. Figure 3.14 shows space-time diagrams of all three velocity components ( $v_x, v_y, v_z$ ) around collapsing cores in different parameter sets. Though models with stronger post-shock magnetic fields (larger  $\theta$ , larger  $\chi_{i0}$ , or ideal MHD) have more dominant  $v_x$  (bluer/redder in the colormap), there is a general preference to condense preferentially along the magnetic field lines (in the  $x$ -direction) among all models, regardless of upstream magnetic obliquity and the ambipolar diffusion level. Figure 3.14 also shows that there are flows perpendicular to the mean magnetic field (along  $\hat{\mathbf{y}}$  or  $\hat{\mathbf{z}}$ ) in the final  $\sim 0.1$  Myr of the simulations, indicating the stage of core collapse. The prominent gas movement along  $\hat{\mathbf{x}}$  long before each core starts to collapse shows that cores acquire masses anisotropically along the magnetic field lines, and thus anisotropic condensation is important for all models.

### 3.6.2 Theoretical Scalings

We have shown in Section 3.2.2 quantitatively that isotropic formation of low-mass supercritical cores is not possible for oblique shocks with ideal MHD, because the minimum mass for a spherical volume to become magnetically supercritical is

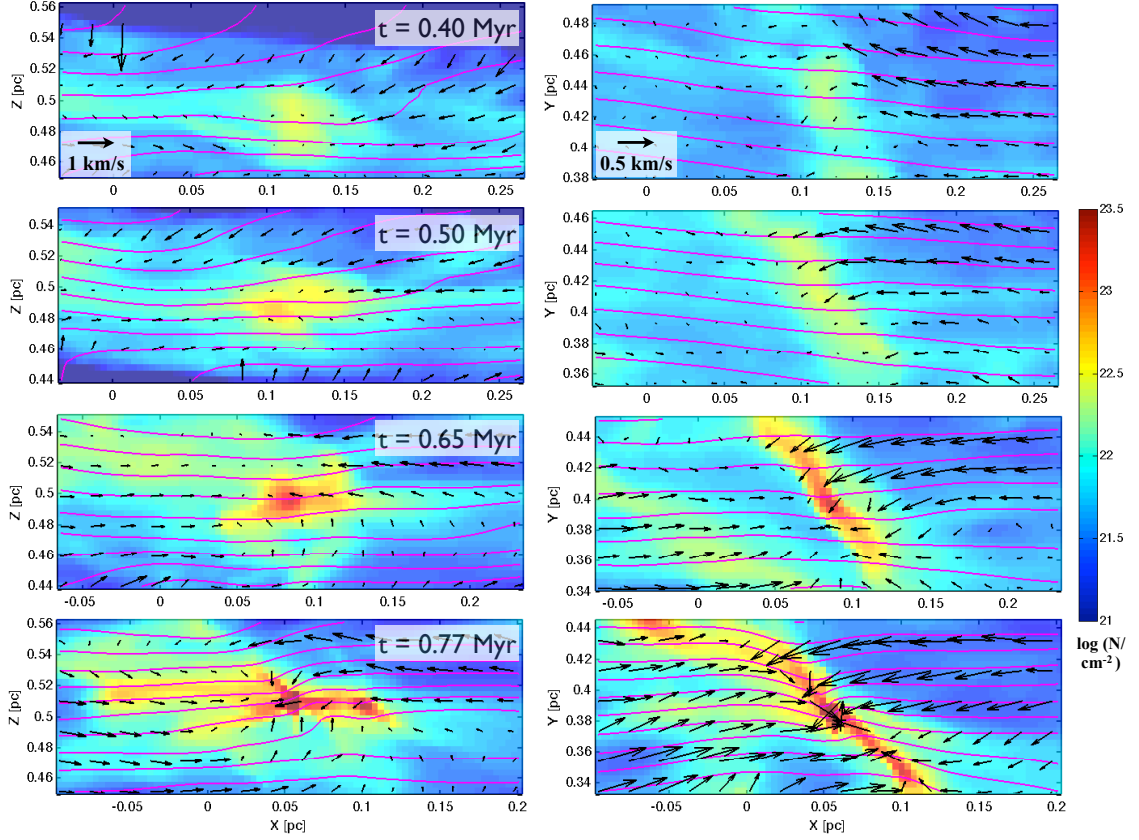


Figure 3.13: A close-up view of magnetic field (*pink lines*) and gas velocity (*black arrows*) over column density (*color map*) projected to the  $x$ - $z$  plane (*left panel*) and  $x$ - $y$  plane (*right panel*) around a forming core at different times, from model A20ID. The region shown here is indicated by the white dashed box in Figure 3.7. The size of the box  $N_x \times N_y \times N_z$  is  $L_{\text{mag,cyl}} \times 4R_{\text{th,sp}} \times 4R_{\text{th,sp}}$ , where  $L_{\text{mag,cyl}}$  and  $R_{\text{th,sp}}$  are calculated using Equation (3.33) and (3.38), respectively. The velocity vectors are density-weighted averages over the box; i.e.  $v_{2D}(i, j) = \sum_k (v_{3D}(i, j, k) \rho(i, j, k)) / \sum_k \rho(i, j, k)$ . We used the same method as in the left panel in Figure 3.3 to draw the magnetic field lines. The magnetic field line spacing and the length of the velocity vectors both indicate strength. Note that the vector scale in the right panel is 2 times larger than in the left panel in order to better show the gas movement. The pre-shock supersonic inflows along the  $z$ -direction in the earlier stages (first two plots in left panel) are omitted here to focus on the post-shock dynamics.

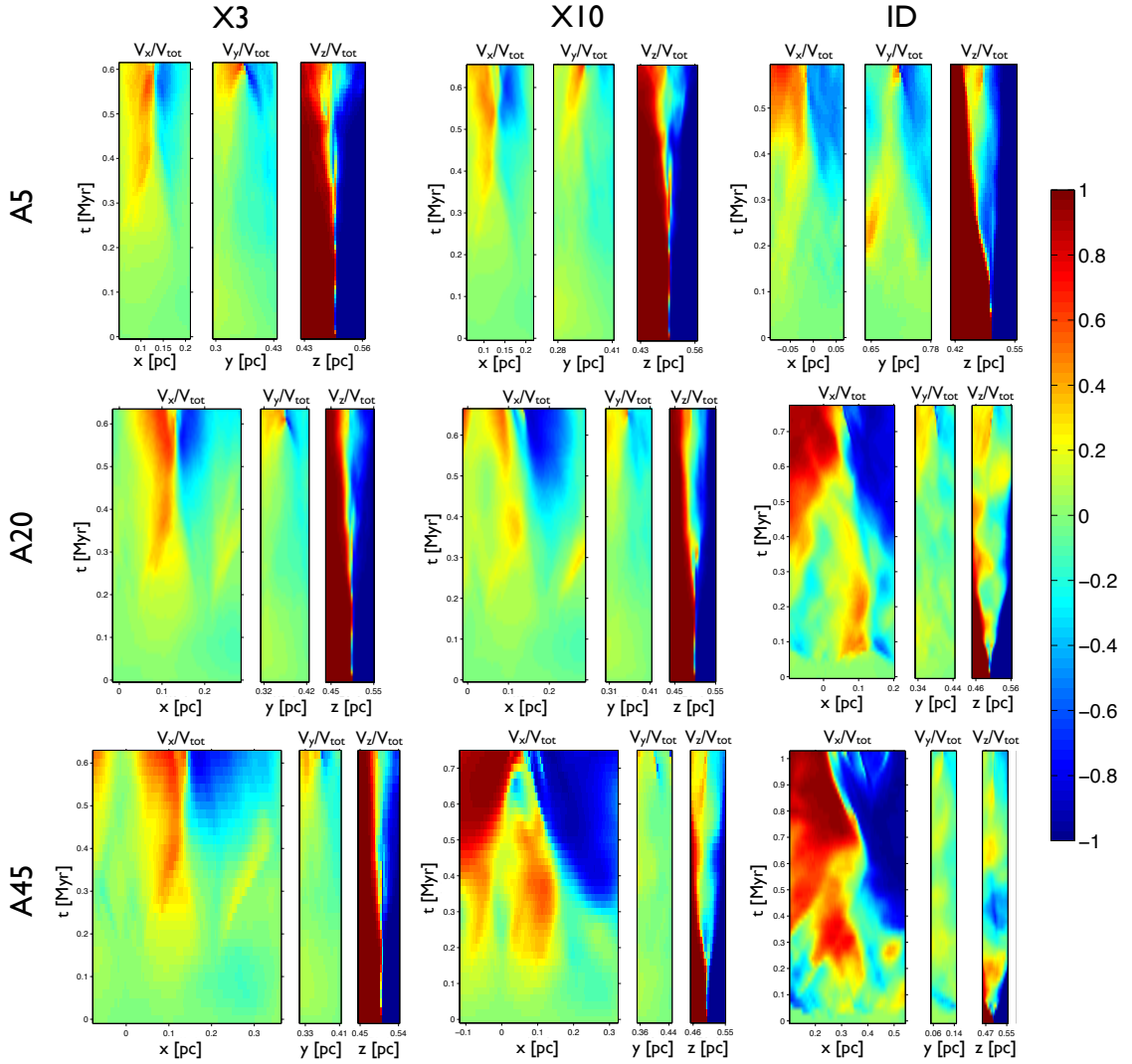


Figure 3.14: The space-time diagrams for varying magnetic obliquity and ionization, showing the  $x$ - (*left panels*),  $y$ - (*middle panels*), and  $z$ - (*right panels*) compressive components of the gas velocity averaged around a collapsing core in each model, normalized by the total velocity  $v_{\text{tot}} = \sqrt{v_x^2 + v_y^2 + v_z^2}$ . The definition of box size is the same as in Figure 3.13. It is evident that anisotropic condensation along the magnetic field ( $x$ -direction) initiates core formation in all cases.

$\geq 10 M_\odot$  (see Equation (3.14) and the  $M_{\text{mag,sph}}$  entries in Table 3.1 and 3.2 for cases A20ID and A45ID), much larger than the typical core mass ( $\sim 1 M_\odot$ ). However, non-spherical regions may have smaller critical mass. Consider, for example, a core that originates as a prolate spheroid with semi-major axis  $R_1$  along the magnetic field and semi-minor axis  $R_2$  perpendicular. The mass-to-flux ratio is then

$$\left. \frac{M}{\Phi_B} \right|_{\text{prolate}} = \frac{4\pi R_1 R_2^2 \rho / 3}{\pi R_2^2 B} = \frac{4 R_1 \rho}{3 B}. \quad (3.31)$$

The critical value for  $R_1$  would be the same as given in Equation (3.15), but the critical mass would be lower than that in Equation (3.14) by a factor  $(R_2/R_1)^2$ . For  $R_1/R_2 \sim 3 - 4$ , the critical mass will be similar to that found in the simulations.

Here we provide a physical picture for core formation via initial flow along the magnetic field, as illustrated in Figure 3.13 and 3.14. Consider a post-shock layer with density  $\rho_{\text{ps}}$  and magnetic field  $B_{\text{ps}}$ . For a cylinder with length  $L$  along the magnetic field and radius  $R$ , the normalized mass-to-flux ratio is

$$\Gamma_{\text{cyl}} = \frac{\pi R^2 L \rho_{\text{ps}}}{\pi R^2 B_{\text{ps}}} \cdot 2\pi \sqrt{G}, \quad (3.32)$$

and the critical length along the magnetic field for it to be supercritical is

$$L_{\text{mag,cyl}} = \frac{B_{\text{ps}}}{\rho_{\text{ps}}} \frac{1}{2\pi \sqrt{G}} \quad (3.33)$$

(note that up to a factor 3/4, this is the same as Equation (3.15)). The critical mass

$M_{\text{mag,cyl}} = \pi R^2 L_{\text{mag,cyl}} \rho_{\text{ps}}$  can then be written as

$$M_{\text{mag,cyl}} = \frac{R^2 B_{\text{ps}}}{2\sqrt{G}} = 1.2 M_\odot \left( \frac{R}{0.05 \text{ pc}} \right)^2 \left( \frac{B_{\text{ps}}}{50 \mu\text{G}} \right). \quad (3.34)$$

This cylinder is gravitationally stable to transverse contraction unless  $L \lesssim 2R$  (Mestel & Spitzer 1956). However, contraction along the length of the cylinder is unim-

peded by the magnetic field, and will be able to overcome pressure forces provided  $L_{\text{mag,cyl}}$  exceeds the thermal Jeans length, which is true in general for oblique shocks in typical conditions under consideration. The longitudinal contraction will produce an approximately isotropic core of radius  $R$  when the density has increased by a factor

$$\frac{\rho'}{\rho_{\text{ps}}} = \frac{L_{\text{mag,cyl}}}{2R}, \quad (3.35)$$

and at this point transverse contraction would no longer be magnetically impeded. For the core to have sufficient self-gravity to overcome thermal pressure at this point, the radius would have to be comparable to  $R_{\text{th,sph}}$  (see Equation (3.12)):

$$R \sim R_{\text{th,sph}} = 2.3 \frac{c_s}{\sqrt{4\pi G \rho'}}. \quad (3.36)$$

Combining Equations (3.33), (3.35), and (3.36) yields

$$\rho' = 0.19 \frac{B_{\text{ps}}^2}{4\pi c_s^2}, \quad (3.37)$$

and

$$R = 5.3 \frac{c_s^2}{\sqrt{G} B_{\text{ps}}} = 0.05 \text{ pc} \left( \frac{B_{\text{ps}}}{50 \mu\text{G}} \right)^{-1} \left( \frac{T}{10 \text{ K}} \right). \quad (3.38)$$

Substituting Equation (3.38) in Equation (3.34), the minimum mass that will be both magnetically and thermally supercritical, allowing for anisotropic condensation along  $\mathbf{B}$ , will be

$$M_{\text{crit}} = 14 \frac{c_s^4}{G^{3/2} B_{\text{ps}}} = 1.3 M_{\odot} \left( \frac{B_{\text{ps}}}{50 \mu\text{G}} \right)^{-1} \left( \frac{T}{10 \text{ K}} \right)^2. \quad (3.39)$$

Thus, anisotropic contraction can lead to low-mass supercritical cores, with values comparable to those formed in our simulations.<sup>11</sup>

---

<sup>11</sup>Note that up to factors of order unity, Equations (3.37) to (3.39) can equivalently be ob-

In addition, anisotropic condensation also helps explain why the core masses are quite similar for HD and MHD models, and independent of the angle between upstream magnetic field and converging flow. Note that Equation (3.39) only depends on the post-shock magnetic field strength. For a magnetized shock, the post-shock magnetic pressure must balance the pre-shock momentum flux:  $B_{\text{ps}}^2/8\pi \sim \rho_0 v_0^2$ . Therefore, Equation (3.39) can be expressed as

$$M_{\text{crit}} = 2.8 \frac{c_s^4}{\sqrt{G^3 \rho_0 v_0^2}} = 2.1 M_{\odot} \left( \frac{n_0}{1000 \text{ cm}^{-3}} \right)^{-1/2} \left( \frac{v_0}{1 \text{ km/s}} \right)^{-1} \left( \frac{T}{10 \text{ K}} \right)^2. \quad (3.40)$$

This is equivalent to Equation (24) of Gong & Ostriker (2011) with  $\psi = 2.8$ . Gong & Ostriker (2011) also pointed out that  $\rho_0 v_0^2$  will be proportional to  $G\Sigma_{\text{GMC}}^2$  for a gravitationally-bound turbulence-supported GMC. Thus, using Equation (28) of Gong & Ostriker (2011) in a cloud with virial parameter  $\alpha_{\text{vir}}$ , Equation (3.40) would become

$$M_{\text{crit}} = 2.8 M_{\odot} \left( \frac{T}{10 \text{ K}} \right)^2 \left( \frac{\Sigma_{\text{GMC}}}{100 M_{\odot} \text{ pc}^{-2}} \right)^{-1} \alpha_{\text{vir}}^{-1/2}. \quad (3.41)$$

Equations (3.40) and (3.41) suggest that  $M_{\text{crit}}$  is not just independent of magnetic field direction upstream, it is also independent of magnetic field strength upstream. That is, when cores form in post-shock regions (assuming the GMC is magnetically supercritical at large scales), the critical mass is determined by the dynamical pressure in the cloud, independent of the cloud's magnetization. The models studied here all have the same dynamical pressure  $\rho_0 v_0^2$ , and same upstream  $B_0$ . It will be very interesting to test whether for varying  $B_0$  the core masses remain the same, and whether the scaling proposed in Equation (3.40) holds for varying total dynamic

---

tained by taking  $B = B_{\text{ps}}$  and requiring that the density  $\rho \rightarrow \rho'$  in Equations (3.11)–(3.12) and (3.14)–(3.15) is such that  $R_{\text{th,sph}} \sim R_{\text{mag,sph}}$  and  $M_{\text{th,sph}} \sim M_{\text{mag,sph}}$ .

pressure.

### 3.7 Summary

In this work, we have used numerical simulations to study core formation in magnetized, highly dynamic environments, including the effect of ambipolar diffusion. Our simulations are fully three-dimensional, including a large-scale convergent flow, local turbulence, and self-gravity, and allow for varying ambipolar diffusion levels (parameterized by the ionization fraction coefficient  $\chi_{i0}$ ) and shock obliquity (parameterized by the angle  $\theta$  between the converging inflow and the global magnetic field). Filaments and then cores form in post-shock dense layers, with dense structures very similar to those found in observations.

In all of our models (with or without ambipolar diffusion), magnetically supercritical cores form with physical properties similar to those found in observations. However, our parameter survey suggests that the transient ambipolar diffusion timescale and *quasi-hydrodynamic* shocks are crucial in setting the magnetization of cores formed in post-shock regions. In addition, we demonstrate and quantitatively explain how low-mass supercritical cores form in strongly-magnetized regions, via anisotropic condensation along the magnetic field.

Our main conclusions are as follows:

1. Under typical GMC conditions, isotropic formation of low-mass supercritical cores is forbidden under ideal MHD by the relatively strong magnetic support (Equation (3.14)). This is true even downstream from strong MHD shocks

where gas density is enhanced, because the magnetic field is compressed as well. In fact, for a spherical volume of given mass, the mass-to-flux ratio is generally larger for pre-shock conditions than post-shock conditions (Equation (3.19); except for the special case described in #2 below). For typical conditions, the minimum post-shock critical mass for a spherical volume exceeds  $10 M_{\odot}$  when ideal MHD applies (Tables 3.1, 3.2). This suggests that either transient ambipolar diffusion in shocks must be taken into consideration, or that core formation is not spherically symmetric.

2. When the incoming flows are almost parallel to the background magnetic field, MHD shocks will have compound post-shock conditions, including the regular *fast* mode (Shu 1992) and the *quasi-hydrodynamic* mode in which gas is compressed more strongly (Figure 3.1). This happens when the angle  $\theta$  between the inflow and the magnetic field is smaller than a critical value,  $\theta_{\text{crit}}$  (Equation (3.8)). For small  $\theta$ , the post-shock layer will have relatively high gas density and weak magnetic field compared to *fast-mode* MHD shocks (Table 3.2).
3. Our three-dimensional simulations demonstrate the effect of transient ambipolar diffusion, as earlier identified and explained in Chapter 2. During the earliest stage of shock formation ( $t \lesssim 0.3$  Myr), a thin but extremely dense layer appears in the middle of the shocked region in models with ambipolar diffusion (Figure 3.3 and 3.4), just like the central dense peak in the one-dimensional shocks analyzed in Chapter 2. Consequently, post-shock densities are gener-

ally higher in models with lower ionizations (smaller  $\chi_{i0}$ ; see Table 3.2), which correspond to stronger ambipolar diffusion as predicted in Chapter 2.

4. The ionization fraction is the main parameter controlling the transient ambipolar diffusion timescale needed for the gas to reach steady post-shock conditions ( $t_{\text{transient}}$ ). Models with smaller  $\chi_{i0}$  have longer transient timescales (Equation (3.27)), indicating lower growth rate of the post-shock magnetic field and more weakly magnetized post-shock layers (Table 3.2). Therefore, transient ambipolar diffusion is crucial in reducing the magnetic support in the post-shock regions (see  $M_{\text{mag,sph}}$  and  $R_{\text{mag,sph}}$  in Table 3.2).
5. The filament network in more strongly magnetized post-shock cases is similar to those found in observations: in addition to large-scale main filaments, there are many thinner, less-prominent sub-filaments parallel to the magnetic field (Goldsmith et al. 2008; Sugitani et al. 2011; Hennemann et al. 2012; Palmeirim et al. 2013; André et al. 2014). Dense cores form within the large-scale main filaments for all models.
6. In our simulations, magnetically supercritical cores are able to form in the shock-compressed dense layers in all models, and the first collapse occurs at  $t \lesssim 0.6$  Myr in most cases. Cores formed in our simulations have masses  $\sim 0.04 - 2.5 M_{\odot}$  and sizes  $\sim 0.015 - 0.07$  pc (Table 3.3 and Figure 3.8), similar to the values obtained in observations (e.g. Motte et al. 2001; Ikeda et al. 2009; Rathborne et al. 2009; Kirk et al. 2013). The medians from the distributions are  $0.47 M_{\odot}$  and  $0.03$  pc. The mass-size relationship derived

from our cores,  $M \propto L^{2.3}$ , also agrees with observations (e.g. Elmegreen & Falgarone 1996; Curtis & Richer 2010; Roman-Duval et al. 2010; Kirk et al. 2013).

7. Our results show that the core mass and size are relatively independent of both the ambipolar diffusion and the upstream magnetic obliquity (Figure 3.9). Hydrodynamic and ideal MHD models also have very similar core masses and sizes. The core masses for ideal MHD cases with oblique shocks are more than an order of magnitude lower than the magnetic critical mass for a spherical region in the post-shock environment. Thus, simple estimates of the form in Equation (3.14) should not be used in predicting magnetically supercritical core masses from ambient environmental conditions in a GMC.
8. The magnetic field of cores follows the same trends as the post-shock magnetization, in terms of variation with the upstream magnetic obliquity and ionization (Tables 3.2, 3.3). This indicates that further ambipolar diffusion is limited during the core building phase, and instead cores form by anisotropic self-gravitating contraction as described in Section 3.6. The mass-to-flux ratio in cores secularly increases with decreasing ionization (Figure 3.9), ranging from  $\Gamma \sim 0.5$  to 7.5 (Figure 3.11). From all models combined, the median mass-to-flux ratio within cores is  $\Gamma \sim 3$  (Figure 3.11), agreeing with the observed range of  $\Gamma$  ( $\Gamma \sim 1 - 4$ ; Falgarone et al. 2008; Troland & Crutcher 2008).
9. Anisotropic self-gravitating condensation is likely the dominant mechanism

for supercritical core formation in magnetized environments, regardless the magnetization strength and ionization fraction. Figures 3.13 and 3.14 clearly show how gas preferentially flows along the magnetic field lines in all models, creating dense cores that are both magnetically and thermally supercritical. The theoretical analysis of Section 3.6.2 shows that the characteristic mass expected from anisotropic contraction (Equation (3.39)) is similar to the median core mass obtained from our simulations (Figure 3.8). For anisotropic core formation in a post-shock region, the critical mass is expected to depend only on the momentum flux entering the shock. We believe this explains why core masses in our simulations are similar regardless of the ionization level, whether the converging flow is nearly parallel to or highly oblique to the upstream magnetic field, or indeed whether the medium is even magnetized at all.

# Chapter 4: Anisotropic Formation of Magnetized Cores in Turbulent Clouds

## Abstract

In giant molecular clouds (GMCs), shocks driven by turbulent flows create high-density, strongly-magnetized regions that are locally sheetlike. In previous work, we showed that within these layers, dense filaments and embedded self-gravitating cores form by gathering material along the magnetic field lines. Here, we extend the parameter space of our three-dimensional, turbulent MHD core formation simulations. We confirm the anisotropic core formation model we previously proposed, and quantify the dependence of median core properties on the pre-shock inflow velocity and upstream magnetic field strength. Our results suggest that bound core properties are set by the total dynamic pressure (dominated by large-scale turbulence) and thermal sound speed in GMCs, independent of magnetic field strength. For models with Mach number between 5 and 20, the median core masses and radii are comparable to the critical Bonnor-Ebert mass and radius defined using the dynamic pressure for  $P_{\text{ext}}$ . We find cores and filaments form simultaneously, and filament column densities are a factor  $\sim 2$  greater than the surrounding cloud when

cores first collapse. We also show that cores identified in our simulations have physical properties comparable to those observed in the Perseus cloud. Superthermal cores in our models are generally also magnetically supercritical, suggesting that the same may be true in observed clouds.

## 4.1 Introduction

Prestellar core formation in giant molecular clouds (GMCs) is an important issue in theoretical studies of star formation, because these cores are the immediate precursors of protostars (Shu et al. 1987; McKee & Ostriker 2007; André et al. 2014). It is believed that the magnetic field and supersonic turbulence may both play important roles in core formation and subsequent evolution. In GMCs, simulations show that overdense structures generated by supersonic turbulence may collapse gravitationally to form protostellar systems, while also attracting material from their surroundings (e.g. Ballesteros-Paredes et al. 1999; Ostriker et al. 1999; Klessen et al. 2000; Padoan et al. 2001; Bate et al. 2003). Magnetic fields limit compression in large-scale turbulence-induced shocks, channel material toward forming filaments, provide support for cores as they grow, and remove angular momentum in collapsing cores (Mestel & Spitzer 1956; Strittmatter 1966; Mouschovias & Spitzer 1976; Mestel 1985; Mouschovias 1991; Allen et al. 2003; Basu et al. 2009b; Li et al. 2010, 2014).

Because GMCs are only lightly ionized, and magnetic fields are only coupled to charged particles, magnetic stresses are mediated by ion-neutral collisions, and are affected by the level of ambipolar diffusion. Analytic studies and numerical simu-

lations have shown that supersonic motions accelerate ambipolar diffusion (Fatuzzo & Adams 2002; Heitsch et al. 2004; Li & Nakamura 2004). Similar simulations with both strong turbulence and ambipolar diffusion have also demonstrated core evolution times, efficiency of star formation, and core structure similar to observations (Nakamura & Li 2005, 2008; Kudoh & Basu 2008, 2011; Basu et al. 2009b). More recently, Chen & Ostriker (2012, also see Chapter 2) studied the one-dimensional C-type shocks and identified a transient stage of turbulence-accelerated ambipolar diffusion. This transient stage, with timescale  $t_{\text{transient}} \sim 0.1 - 1$  Myr (depending on ionization), can explain the enhanced diffusion rate and affect the magnetization of cores that form.

In Chapter 3 (also see Chen & Ostriker 2014), we applied three-dimensional numerical simulations to study the roles of magnetic fields and ambipolar diffusion during prestellar core formation in turbulent cloud environments. Our simulations adopted the model framework of Gong & Ostriker (2011) to focus on the shocked layer produced by turbulent converging flows, and surveyed varying ionization and angle between the upstream flow and magnetic field. In simulations, we found hundreds of self-gravitating cores with masses  $M \sim 0.04 - 2.5 M_{\odot}$  and sizes  $L \sim 0.015 - 0.07$  pc, all formed within 1 Myr.

In Chapter 3, we also found that core masses and sizes do not depend on either the ionization or upstream magnetic field direction, and ambipolar diffusion is in fact not necessary to form low-mass supercritical cores. Our analysis showed that this is the result of anisotropic contraction along field lines, which can be clearly seen in our simulations, with or without ambipolar diffusion. In the anisotropic core

formation model, low-mass magnetically supercritical cores form rapidly even in a strongly magnetized medium with high ionization. This explains the prevalence of magnetically supercritical cores in observations (Crutcher 2012).

Using a simple scaling argument, we suggested in Chapter 3 that the characteristic core mass may be set by the mean turbulent pressure in a GMC, regardless of magnetic effects. The predicted core mass is a factor  $\sim \mathcal{M}^{-1}$  lower than the thermal Bonnor-Ebert mass at the mean density in the cloud, where  $\mathcal{M}$  is the turbulent Mach number. Previously, Gong & Ostriker (2011) proposed a similar formula based on the preferred scale for gravitational fragmentation of post-shock layers, for the purely hydrodynamic case. Padoan et al. (1997) also argued for a similar characteristic mass, based on statistics of turbulent flows. Although the analyses of Gong & Ostriker (2011) and Padoan et al. (1997) neglect magnetic fields, the end result is similar to the prediction of Chapter 3 that incorporates magnetic effects, with the turbulent pressure in a cloud setting the characteristic core mass.

Here, following Chapter 3, we continue our study of anisotropic core formation in turbulent molecular clouds. We extend our previous numerical study to explore how the turbulent and magnetic pressures of the pre-shock gas can affect core formation in the compressed region. We demonstrate that the dependence of core properties on pre-shock parameters are similar to those predicted by the anisotropic core formation model of Chapter 3. We also compare our results with observations, showing that the mass-size relationship and ratio of mass to critical value of our simulations is comparable to that seen in Perseus and other star-forming regions (Sadavoy et al. 2010a; Kirk et al. 2013).

The outline of this chapter is as follows. We review the anisotropic core formation model in Section 4.2, outlining the successive dynamical stages and associated parameter dependence expected. Section 4.3 describes the equations solved in our numerical simulations, and specifies the model parameter set we shall consider. The post-shock gas structure for varying parameters is analyzed in Section 4.4, including physical properties of the compressed layer (Section 4.4.1), and development of filaments within it (Section 4.4.2). In Section 4.5 we provide quantitative results for masses, sizes, magnetizations, and other physical properties of the bound cores identified from our simulations, and compare to predictions from Chapter 3. We also compare these results with observations (Section 4.6), focusing on interpreting the physical state of super-Jeans mass cores and mass-size relationships. Section 4.7 summarizes our conclusions.

## 4.2 Anisotropic Core Formation: Review

Here we briefly review the anisotropic condensation model of core formation proposed in Chapter 3. We consider a strongly-magnetized post-shock region created by a large-scale converging turbulent flow within a cloud. As shown in Figure 4.1 (top left), the magnetic field will lie primarily parallel to the shock front in the layer, with density  $\rho_{\text{ps}}$  and magnetic field strength  $B_{\text{ps}}$ . For a cylinder with radius  $R$  and length  $L$  along the magnetic field (Figure 4.1, *top right*), if  $2R \lesssim L \lesssim L_{\text{mag,crit}}$  (see Equation (3.33) of Chapter 3) for

$$L_{\text{mag,crit}} = \frac{B_{\text{ps}}}{\rho_{\text{ps}}} \frac{1}{2\pi\sqrt{G}}, \quad (4.1)$$

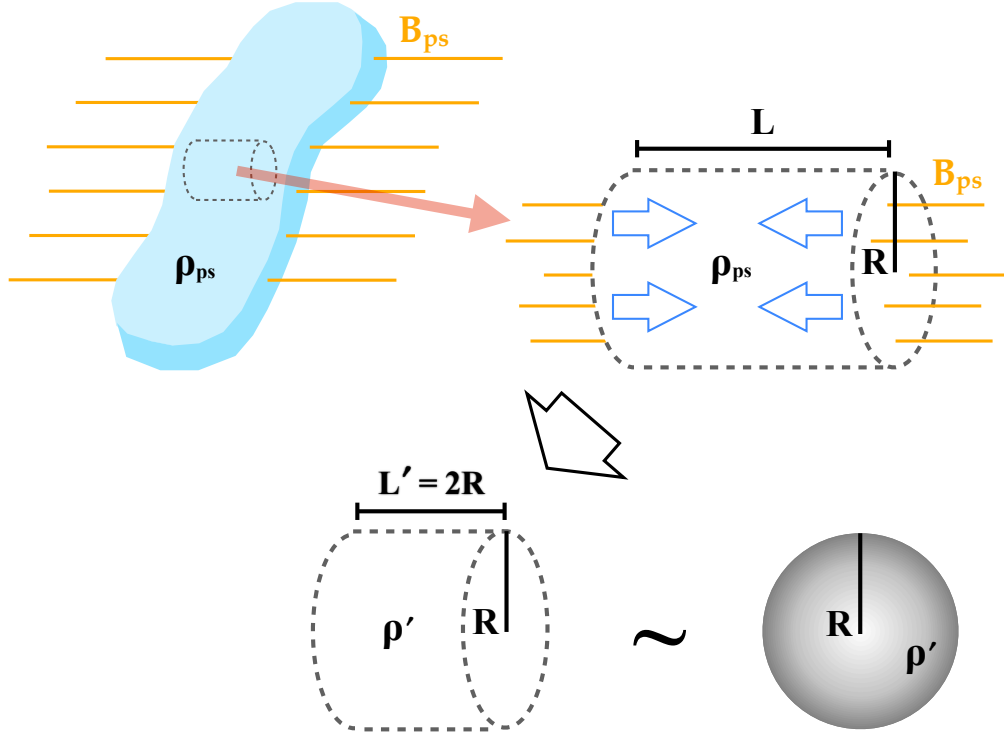


Figure 4.1: The anisotropic condensation process of a magnetically-critical cylinder, initiated by longitudinal contraction along the magnetic field. When the length of the cylinder has shrunk to satisfy  $L' \sim 2R$ , it can be treated as an isotropic sphere with radius  $R$ , which will collapse if the self-gravity overcomes thermal pressure.

it is gravitationally stable to transverse contraction across the magnetic field (Mestel & Spitzer 1956). However, the magnetic field does not prohibit contraction along the length of the cylinder, and gravity will be able to overcome pressure forces if  $L$  exceeds the thermal Jeans length within the post-shock layer,  $L_{J,2D} \equiv c_s^2/G\Sigma_{ps}$  or  $L_{J,3D} \equiv c_s(\pi/G\rho_{ps})^{1/2}$ . Here,  $\Sigma_{ps}$  is the total surface density of the post-shock layer. In this situation, longitudinal contraction can reduce the length until an approximately isotropic core with  $L' \sim 2R$  is produced (Figure 4.1, *bottom*), with

density

$$\rho' = \frac{L}{2R}\rho_{\text{ps}}. \quad (4.2)$$

At this point, transverse contraction is no longer impeded by the magnetic field provided the original  $L \sim L_{\text{mag,crit}}$  so the core is magnetically supercritical (note that the mass-to-magnetic flux ratio remains the same during the longitudinal contraction). The core will also have sufficient gravity to overcome thermal pressure support provided its mass is comparable to that of a critical Bonnor-Ebert sphere at ambient density  $\rho'$ , which corresponds to radius (prior to central concentration)

$$R \sim R_{\text{th,sph}} = 2.3 \frac{c_s}{\sqrt{4\pi G \rho'}}. \quad (4.3)$$

Combining  $L \sim L_{\text{mag,crit}}$  with Equations (4.1)-(4.3), this yields

$$\rho' = 0.19 \frac{B_{\text{ps}}^2}{4\pi c_s^2} \approx 0.38 \frac{\rho_0 v_0^2}{c_s^2}. \quad (4.4)$$

In Equation (4.4), we have assumed a strong magnetized isothermal shock with downstream magnetic pressure balanced by upstream ram pressure ( $B_{\text{ps}}^2 / (8\pi) \approx \rho_0 v_0^2$ ) so that

$$B_{\text{ps}} = 31.04 \mu\text{G} \left( \frac{v_0}{1 \text{ km/s}} \right) \left( \frac{n_0}{10^3 \text{ cm}^{-3}} \right)^{1/2}, \quad (4.5)$$

where  $\rho_0$ ,  $v_0$  are the density and inflow velocity of the shock, respectively, and  $n_0 = \rho_0 / \mu_n$  for  $\mu_n = 2.3m_{\text{H}}$  the mean molecular weight. We can then solve for the critical radius and mass that allows an anisotropically formed core to be both magnetically and thermally supercritical:

$$\begin{aligned} R_{\text{crit}} &= 5.3 \frac{c_s^2}{\sqrt{G} B_{\text{ps}}} = 1.06 \frac{c_s^2}{\sqrt{G} \rho_0 v_0^2} \\ &= 0.09 \text{ pc} \left( \frac{n_0}{1000 \text{ cm}^{-3}} \right)^{-1/2} \left( \frac{v_0}{1 \text{ km/s}} \right)^{-1} \left( \frac{c_s}{0.2 \text{ km/s}} \right)^2, \end{aligned} \quad (4.6)$$

and

$$\begin{aligned}
M_{\text{crit}} &= 14 \frac{c_s^4}{G^{3/2} B_{\text{ps}}} = 2.8 \frac{c_s^4}{\sqrt{G^3 \rho_0 v_0^2}} \\
&= 2.1 M_{\odot} \left( \frac{n_0}{1000 \text{ cm}^{-3}} \right)^{-1/2} \left( \frac{v_0}{1 \text{ km/s}} \right)^{-1} \left( \frac{c_s}{0.2 \text{ km/s}} \right)^4. \quad (4.7)
\end{aligned}$$

Equation (4.7) uses  $M_{\text{crit}} = \pi R_{\text{crit}}^2 L_{\text{mag,crit}} \rho_{\text{ps}} = R_{\text{crit}}^2 B_{\text{ps}} / (2\sqrt{G})$ . Equations (4.6) and (4.7) suggest that the characteristic mass of prestellar cores formed in post-shock regions in magnetized GMCs is determined by the dynamical pressure in the cloud, independent of the cloud's magnetization, when anisotropic condensation along the magnetic field is taken into account. We already showed in Chapter 3 that models with varying upstream magnetic field directions have similar values of the median core mass and radius. Here, we extend our previous investigation to consider variation in the inflow velocities and background magnetic field strength.

### 4.3 Numerical Methods and Models

The simulation setup is similar to the one discussed in Chapter 3, and is summarized here. We employ a three-dimensional ideal MHD model with convergent flow, self-gravity, and a perturbed turbulent velocity field (Gong & Ostriker 2011). These numerical simulations are conducted using the *Athena* MHD code (Stone et al. 2008) with the Roe Riemann solver. As we found in Chapter 3 that ambipolar diffusion plays a secondary role in core formation, here we consider ideal MHD. The

equations we solve are:

$$\frac{\partial \rho}{\partial t} + \nabla \cdot (\rho \mathbf{v}) = 0, \quad (4.8)$$

$$\frac{\partial \rho \mathbf{v}}{\partial t} + \nabla \cdot \left( \rho \mathbf{v} \mathbf{v} - \frac{\mathbf{B} \mathbf{B}}{4\pi} \right) + \nabla P^* = 0, \quad (4.9)$$

$$\frac{\partial \mathbf{B}}{\partial t} + \nabla \times (\mathbf{B} \times \mathbf{v}) = 0, \quad (4.10)$$

where  $P^* = P + B^2/(8\pi)$ . For simplicity, we adopt an isothermal equation of state  $P = \rho c_s^2$  with  $c_s = 0.2$  km/s. For both the whole simulation box initially and the inflowing gas subsequently, we apply perturbations following a Gaussian random distribution with a Fourier power spectrum  $v^2(k) \propto k^{-4}$  (Gong & Ostriker 2011, or see Equations (3.23) and (3.24) in Chapter 3). We use H-correction (Sanders et al. 1998) to suppress the carbuncle instability, and, when needed, first order flux correction (Lemaster & Stone 2009).

Our simulation box is 1 pc on each side, representing a region within a GMC where a large-scale supersonic converging flow with velocity  $\mathbf{v}_0 = v_0 \hat{\mathbf{z}}$  and  $-\mathbf{v}_0$  (i.e. in the center-of-momentum frame) collides. The  $z$ -direction is the large-scale inflow direction, and we adopt periodic boundary conditions in the  $x$ - and  $y$ -directions. We initialize the background magnetic field in the cloud,  $B_0$ , in the  $x$ - $z$  plane, with an angle  $\theta = 20^\circ$  with respect to the convergent flow. The number density of the neutrals, defined as  $n \equiv \rho/\mu_n$ , is set to  $n_0 = 1000 \text{ cm}^{-3}$  in the initial conditions and in the upstream converging flow. The physical parameters defining each model are then the inflow Mach number and upstream magnetic field strength  $\mathcal{M} \equiv v_0/c_s$  and  $B_0$ . We choose  $\mathcal{M} = 5, 10, \text{ and } 20$  to look at the dependence of core mass/size on the inflow velocity, and  $B_0 = 5, 10, \text{ and } 20 \text{ } \mu\text{G}$  to test whether the initial magnetization

of the cloud can affect the core properties (see Table 4.1).

Similar to our previous work, we repeat each model 6 times with different random realizations of the same turbulent power spectrum to collect sufficient statistical information. Note that the resolution adopted in Chapter 3 ( $\Delta x = 1/256$  pc) is not high enough to resolve strong shocks generated by high inflow velocity, especially  $\mathcal{M} = 20$  cases. Therefore, we increased our resolution to  $512^3$  for all models in this work, such that  $\Delta x \approx 0.002$  pc.

From each simulation, we apply the *GRID* core-finding method (Gong & Ostriker 2011), which uses the largest closed gravitational potential contours around single local minimums as core boundaries. We then select the gravitationally bound cores as those with negative total energy (sum of gravitational, magnetic, and thermal energy). It is then straightforward to measure the mass and size for each identified core. For the magnetic flux within a core, we first find the plane that includes the minimum of the core's gravitational potential and is perpendicular to the average magnetic field direction within the core. This plane separates the core into an upper half and a lower half, and we can measure the magnetic flux  $\Phi_B$  through the core by summing up  $\mathbf{B} \cdot \hat{\mathbf{n}}$  in either the upper or lower half of the core surface (see Chapter 3). The normalized mass-to-magnetic flux ratio of the core is therefore  $\Gamma \equiv M/\Phi_B \cdot 2\pi\sqrt{G}$ .

Table 4.1: Summary of the post-shock properties measured and derived from simulations.

Model	cloud conditions		simulated post-shock properties*				corresponding physical scales†				
	$v_0$ (km/s)	$B_0$ ( $\mu\text{G}$ )	$\bar{n}_{\text{ps}}$ ( $10^3 \text{ cm}^{-3}$ )	$\bar{B}_{\text{ps}}$ ( $\mu\text{G}$ )	$\beta_{\text{ps}}$	$v_{\text{rms}}$ (km/s)	$M_{\text{mag,sph}}$ (pc)	$R_{\text{mag,sph}}$ (pc)	$M_{\text{th,sph}}$ (pc)	$R_{\text{th,sph}}$ (pc)	$L_{\text{mag,crit}}$ (pc)
M5B10	1	10	12.1	43.0	0.25	0.44	7.64	0.14	1.26	0.07	0.19
M10B10	2	10	18.7	66.8	0.16	0.57	12.0	0.14	1.02	0.06	0.18
M20B10	4	10	32.6	121	0.09	0.79	23.5	0.14	0.77	0.05	0.19
M10B5	2	5	31.8	59.3	0.35	0.41	2.90	0.07	0.78	0.05	0.10
M10B10	2	10	18.7	66.8	0.16	0.57	12.0	0.14	1.02	0.06	0.18
M10B20	2	20	9.89	70.9	0.08	0.98	51.3	0.28	1.40	0.08	0.37

\*Post-shock properties are measured at  $t = 0.2$  Myr in each model, averaged over the whole post-shock layer. The timescale is chosen so the downstream properties are measured before the post-shock layer becomes strongly self-gravitating.

†See Equations (4.1) and (4.13)-(4.16) for definitions of physical scales.

## 4.4 Post-shock Environment and Structure Formation

### 4.4.1 Post-shock Layer

The post-shock results from our simulations are summarized in Table 4.1. Similar to our work in Chapter 3, we measured the post-shock properties at  $t = 0.2$  Myr, a timescale that is short enough that no cores have formed, yet long enough for the post-shock region to reach a steady-state solution. In fact, the timescale  $t_{\text{sg}}$  necessary for the post-shock layer to become self-gravitating can be derived by considering when the gravitational weight,

$$\frac{\pi G \Sigma_{\text{ps}}^2}{2} = \frac{\pi G (2\rho_0 v_0 t_{\text{sg}})^2}{2}, \quad (4.11)$$

exceeds the post-shock pressure  $B_{\text{ps}}^2/8\pi \approx \rho_0 v_0^2$ . The result is

$$t_{\text{sg}} = \frac{1}{\sqrt{2\pi G \rho_0}} = 0.79 \text{ Myr} \left( \frac{n_0}{1000 \text{ cm}^{-3}} \right)^{-1/2}. \quad (4.12)$$

This justifies our choice of measuring post-shock properties at  $t = 0.2$  Myr.

As explained in Chapter 3, there are two different length scales (and corresponding characteristic masses) for spherical cores in the post-shock region at a given ambient density  $\rho$ : one that is supported by thermal pressure (a critical Bonnor-Ebert sphere)

$$R_{\text{th,sph}} = 2.3 \frac{c_s}{\sqrt{4\pi G \rho}}, \quad (4.13)$$

$$M_{\text{th,sph}} = 4.18 \frac{c_s^3}{\sqrt{4\pi G^3 \rho}}, \quad (4.14)$$

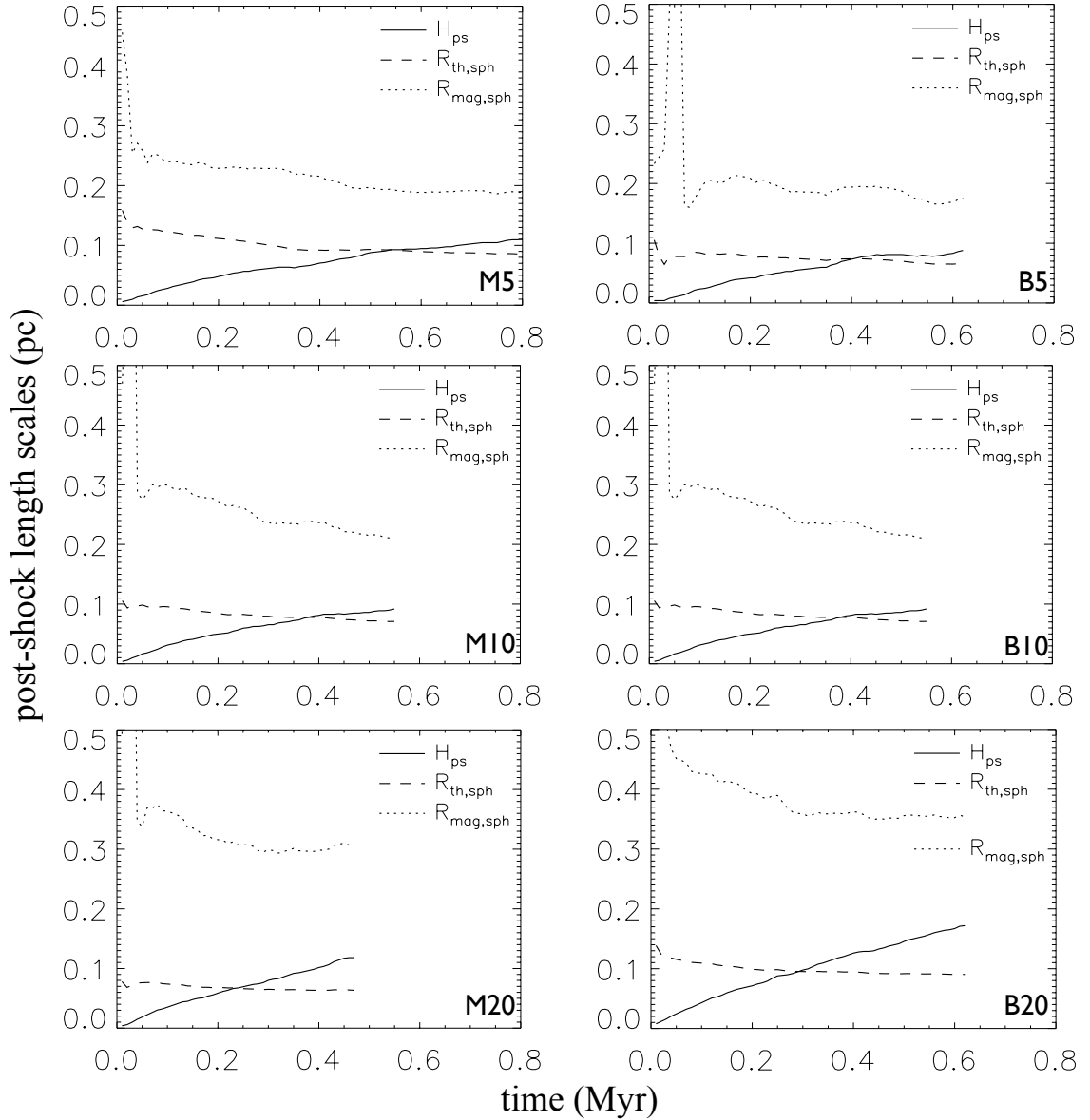


Figure 4.2: The post-shock layer thickness  $H_{ps}$  in different models measured from simulations (*solid*), compared to possible mass-gathering scales,  $R_{th,sph}$  from Equation (4.13) (*dashed*) and  $R_{mag,sph}$  from Equation (4.15) (*dotted*) within the post-shock layer. Since the post-shock layer is strongly magnetized with  $R_{mag,sph}$  much larger than  $H_{ps}$  during the core building phase ( $\sim 0.5$  Myr), cores cannot collect mass along the direction perpendicular to the layer.

and one that is supported by magnetic stresses (defined from  $4R/3 = L_{\text{mag,crit}}$ )

$$R_{\text{mag,sph}} = \frac{3}{8\pi\sqrt{G}} \frac{B}{\rho}, \quad (4.15)$$

$$M_{\text{mag,sph}} = \frac{9}{128\pi^2 G^{3/2}} \frac{B^3}{\rho^2} \quad (4.16)$$

(see Equations (3.11)–(3.12) and (3.14)–(3.15) in Chapter 3). Figure 4.2 shows the measured post-shock layer thickness in each model, compared with these two possible mass-gathering scales in the post-shock environment,  $R_{\text{th,sph}}$  and  $R_{\text{mag,sph}}$ . It is obvious from Figure 4.2 that  $R_{\text{mag,sph}}$  is much larger than the post-shock thickness during the entire core-building phase, and thus magnetically supercritical cores cannot form spherical symmetrically within the post-shock layer. Quantitatively, since the post-shock layer thickness is  $H_{\text{ps}} = \Sigma_{\text{ps}} / (2\bar{\rho}_{\text{ps}})$ , we have

$$\begin{aligned} \frac{R_{\text{mag,sph}}}{H_{\text{ps}}} &= \frac{3}{4\pi\sqrt{G}} \frac{B_{\text{ps}}}{\Sigma_{\text{ps}}} \approx \frac{3}{4\pi\sqrt{G}} \frac{\sqrt{8\pi\rho_0 v_0^2}}{2\rho_0 v_0 t} \\ &= \frac{3}{\sqrt{8\pi G \rho_0} t} = 1.2 \left( \frac{n_0}{1000 \text{ cm}^{-3}} \right)^{-1/2} \left( \frac{t}{\text{Myr}} \right)^{-1}. \end{aligned} \quad (4.17)$$

Since the core formation timescales in our models all satisfy  $t \lesssim 1$  Myr, Equation (4.17) suggests  $R_{\text{mag,sph}} > H_{\text{ps}}$  when cores formed. This means that gravity-induced mass collection in the direction perpendicular to the shocked layer is prevented by magnetic forces, and in-plane mass collection is required for core formation in post-shock regions.

#### 4.4.2 Structure Formation

Figure 4.3 shows examples of structures formed within the post-shock layers, at the time that the most evolved core collapses ( $t_{\text{coll}}$ ; see Section 4.5). We have

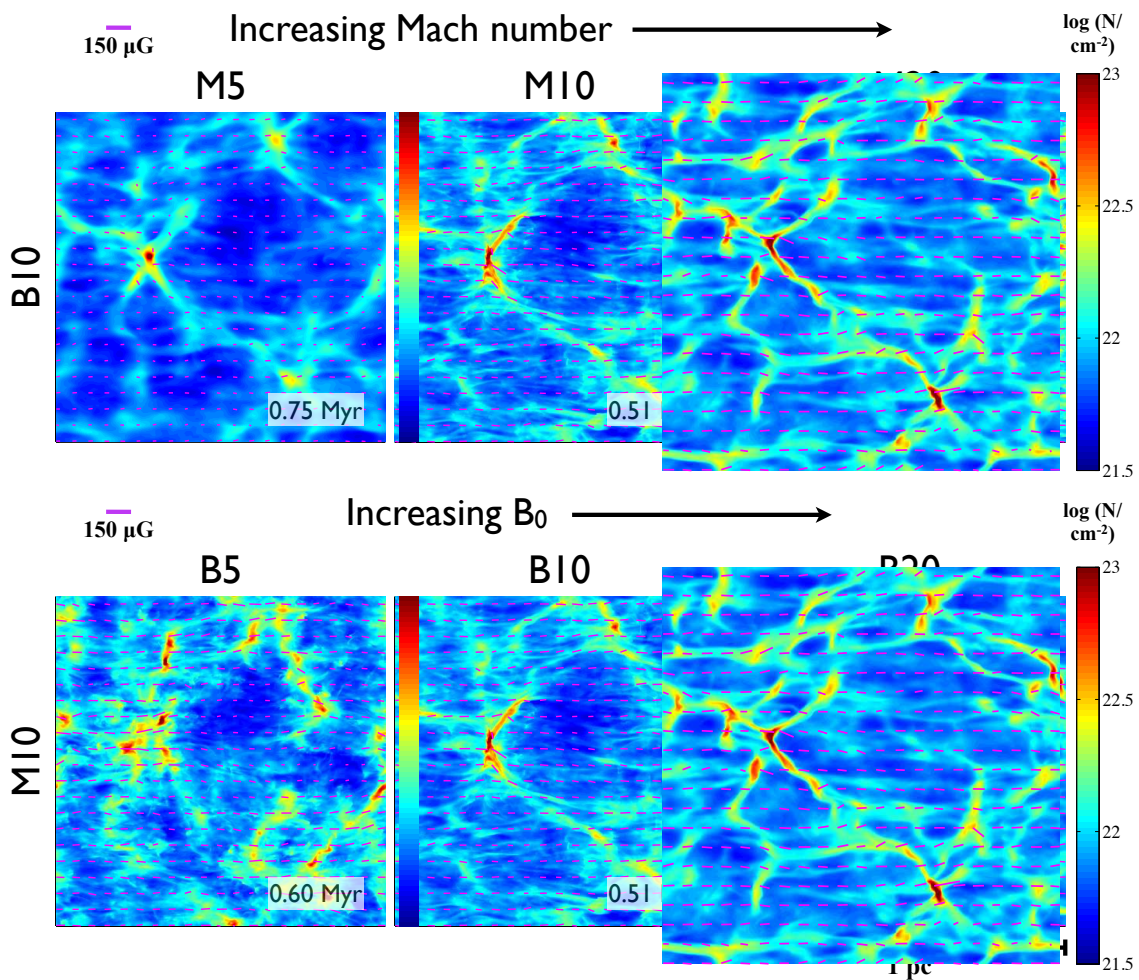


Figure 4.3: The structure formed in the post-shock layer (in column density; *color map*) for models with different inflow Mach numbers and background magnetic fields. Magnetic field directions in the post-shock layer are also shown (*pink segments*).

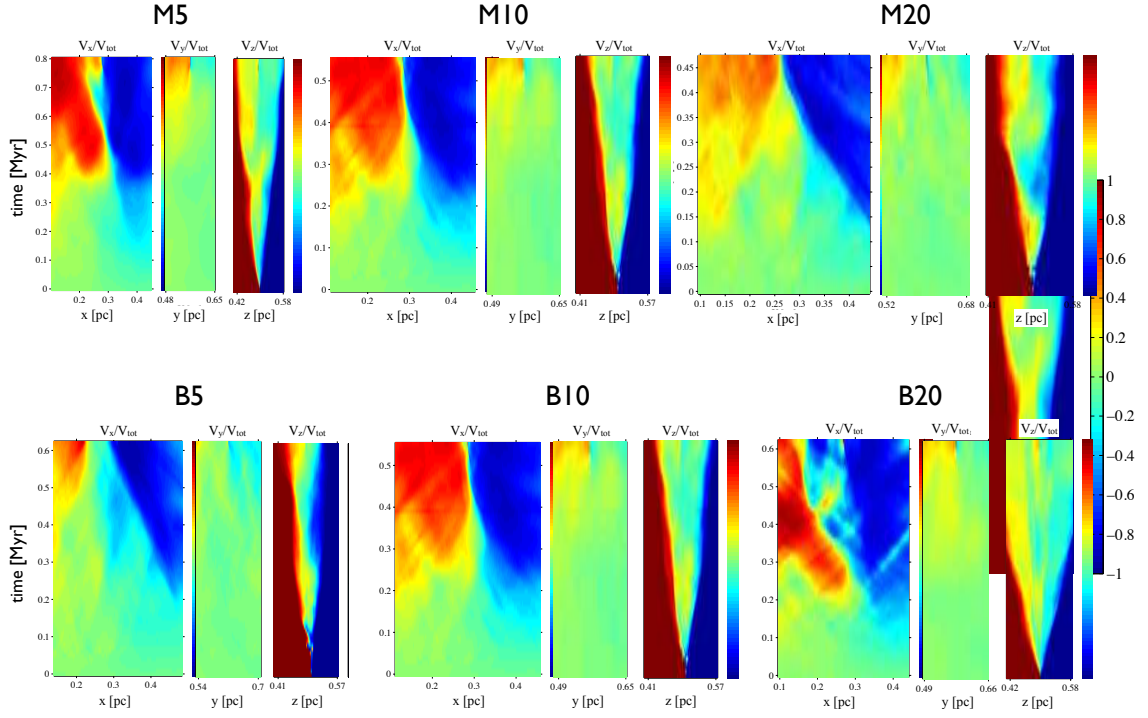


Figure 4.4: The space-time diagrams of  $v_x$ ,  $v_y$ ,  $v_z$  around the most evolved core in each model, normalized by the total velocity  $v_{\text{tot}} = (v_x^2 + v_y^2 + v_z^2)^{1/2}$  at each zone. In all models,  $v_z$  dominates in the beginning of the simulation because of the convergent flow setup, but  $v_x$  (along the magnetic field lines) soon becomes the strongest component around the forming core.

selected models with identical initial turbulence realization, which is responsible for seeding the structures that subsequently grow. Filamentary structures are obviously seen in all models with width  $\sim 0.05$  pc, similar to those found in observations (see review in André et al. 2014). Also, note that the filaments are not necessary perpendicular to the magnetic field, because the locations of nulls in the velocity field are independent of each other on each magnetic field line.

In addition, we see networks of small sub-filaments or striations parallel to the magnetic field in some models. Similar features have been observed in multiple molecular clouds (Goldsmith et al. 2008; Sugitani et al. 2011; Hennemann et al. 2012; André et al. 2014), and are consistent with the theoretical expectation of anisotropy of magnetized turbulence (Goldreich & Sridhar 1995). Quantitatively, computational studies suggest  $\beta \lesssim 0.2$  is required to have significant anisotropy at Mach number = 5 (Vestuto et al. 2003; Heyer et al. 2008), and the critical value of  $\beta$  may become smaller for higher Mach numbers (Heyer et al. 2008). This roughly agrees with our results in Figure 4.3: striations parallel to the magnetic field direction (not necessarily perpendicular to the main filaments) are evident in models with low Mach numbers or strong magnetic fields (M5, M10/B10, B20). Otherwise, the high velocity turbulence (M20) or the weak magnetization (B5, see Table 4.1) may have destroyed the anisotropy.

Similar to our work in Chapter 3, we use space-time diagrams of different velocity components to demonstrate the anisotropic process of core formation (Figure 4.4). We consider the region with size  $L_x \times L_y \times L_z = L_{\text{mag,crit}} \times 2R_{\text{th,sph}} \times 2R_{\text{th,sph}}$  centered around the most-evolved core at  $t_{\text{coll}}$  of each model, and plot the averaged

Table 4.2: Results from filaments measured at  $t = t_{\text{coll}}$ , averaged over all 6 runs for each parameter set.

Model	$t_{\text{coll}}^{\S}$ (Myr)	FFE $_{1.0}^{\dagger}$	FFE $_{1.5}^{\dagger}$	$A_{\text{fila},1.0}$ (pc $^2$ )	$A_{\text{fila},1.5}$ (pc $^2$ )	$L_{\text{mag,crit}}$ (pc)	$L_{\text{acc}}^{\ddagger}$ (pc)	$\lambda_m^{\ddagger}$ (pc)
M5B10	0.83	0.65	0.31	0.34	0.11	0.19	0.51	0.39
M10B10	0.53	0.57	0.27	0.34	0.11	0.18	0.49	0.28
M20B10	0.43	0.59	0.31	0.35	0.13	0.19	0.51	0.20
M10B5	0.58	0.61	0.33	0.34	0.13	0.10	0.27	0.28
M10B10	0.53	0.57	0.27	0.34	0.11	0.18	0.49	0.28
M10B20	0.63	0.53	0.36	0.30	0.15	0.37	1.00	0.28

$^{\S}$ Collapse is defined as the time when  $n_{\text{max}} = 10^7 \text{ cm}^{-3}$  in each simulation.

$^{\dagger}$ FFE (filament formation efficiency) is the ratio of the total mass in filamentary structures to the total mass in the shocked layer at  $t_{\text{coll}}$ , as defined in Equation (4.19).

$^{\ddagger}$ See Section 4.5.

$v_x, v_y, v_z$  along  $x$ -,  $y$ -,  $z$ -directions in the unit of the total velocity  $v_{\text{tot}}$ . Anisotropic gas flows along the  $x$ -direction are obvious in all models, and appear much earlier than the core collapse (when all three velocity components show convergent flow). Note that, from Figure 4.4 we can see that Model B5 has less prominent convergent flow along the  $x$ -direction than the other models, indicating that anisotropy is not as strong in this model (see Section 4.5).

Quantitatively, if we define overdense (filamentary) structures as those with surface density contrast higher than a certain value, say,  $\Sigma > X \cdot \bar{\Sigma}_{\text{ps}}$ , then we can measure the mean surface density of filaments,  $\bar{\Sigma}_{\text{fila}}$ , as the ratio of total mass inside filamentary structures,

$$M_{\text{fila}} \equiv \int \Sigma_{\text{fila}}(x, y) \cdot dx \cdot dy, \quad (4.18)$$

to total area ( $A_{\text{fila}}$ ) of the same structures. The filament formation efficiency (FFE) is defined by:

$$\text{FFE} = \frac{M_{\text{fila}}}{M_{\text{ps}}} = \frac{M_{\text{fila}}}{2\rho_0 v_0 t}. \quad (4.19)$$

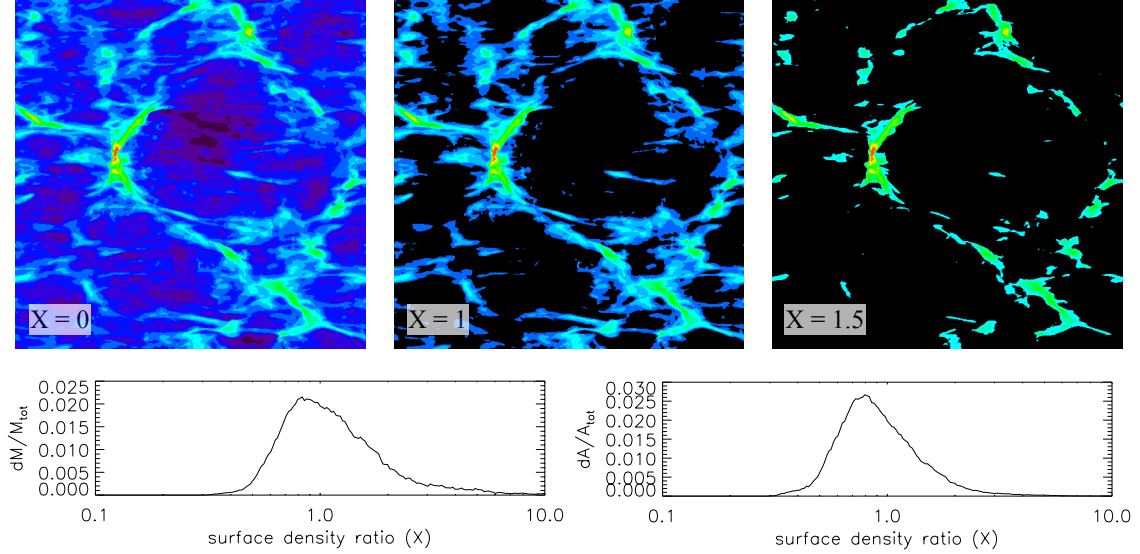


Figure 4.5: Comparison between filamentary structures above different cut-off  $X$  values in the criterion  $\Sigma > X \cdot \Sigma_{\text{ps}}$  (*top*), and the fraction of filament mass (*bottom left*) and the fraction of filament area (*bottom right*) as functions of  $X$ , from model M10B10.

Table 4.2 lists the measured FFE and total area of filaments using  $X = 1.0$  and  $X = 1.5$ , as well as three mass-accreting scales  $L_{\text{mag,crit}}$  (see Equation (4.1)),  $L_{\text{acc}}$ , and  $\lambda_m$  (see discussion in Section 4.5). Though the core collapse timescale varies with inflow Mach number, the filament formation efficiency and the total area of filaments do not seem to have strong dependence on either the inflow Mach number or the pre-shock magnetic field. This is in contrast to the core formation efficiency (CFE), which varies with  $t_{\text{coll}}$  (see Table 4.3 and discussion in Section 4.5).

Note that there is some arbitrariness in the choice of  $X$ . Figure 4.5 compares the post-shock structures under different cutoff values in surface density, and shows the differential PDFs of filament mass and area as functions of the surface density ratio  $X \equiv \Sigma/\bar{\Sigma}_{\text{ps}}$ . Since there is no “break” in the differential PDF at any particular

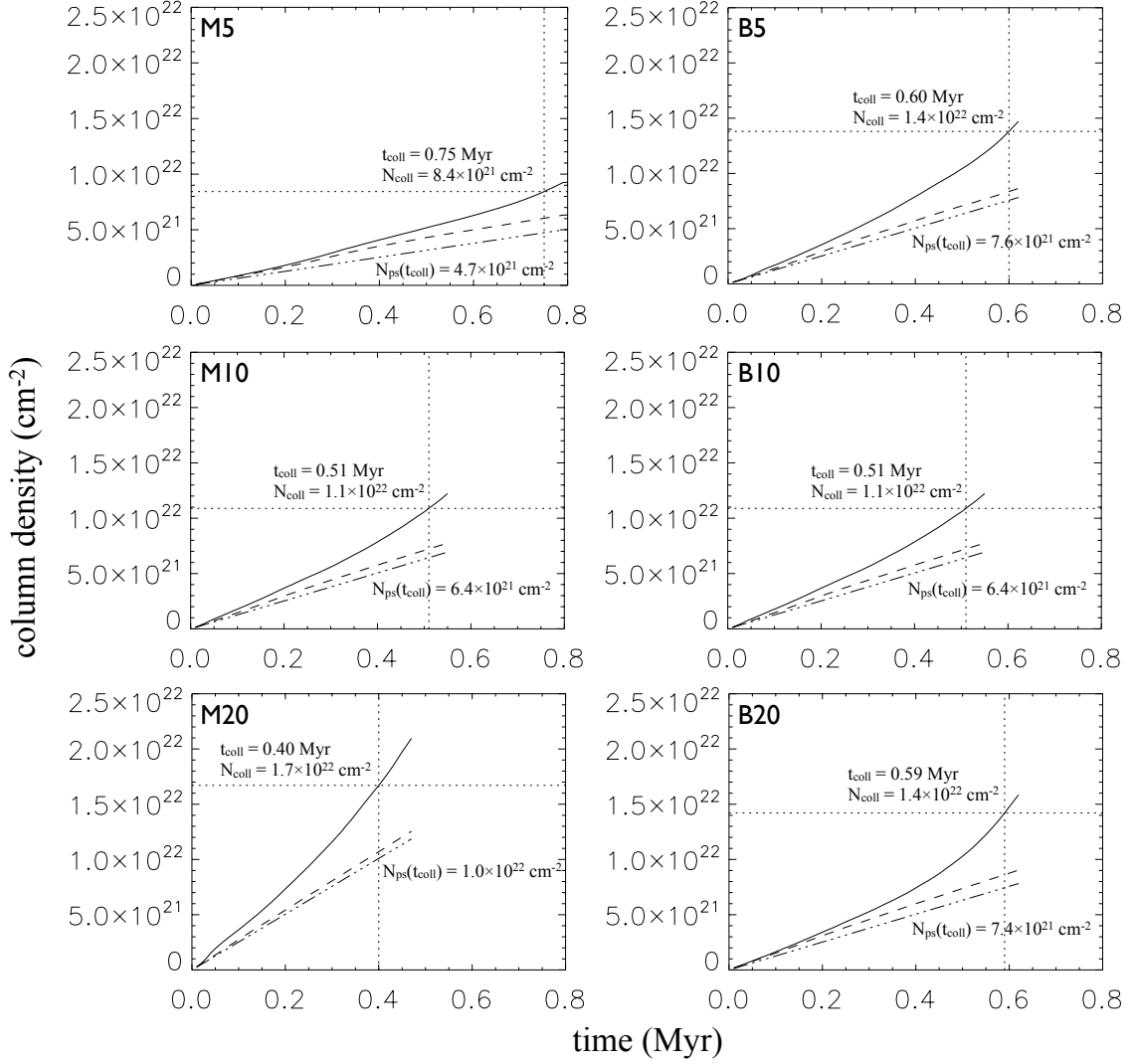


Figure 4.6: The average column density of the overdense ‘‘filament’’ structures (*solid*), post-shock layer (*dashed*), and theoretical value for the post-shock layer (*dash-dotted*) defined as  $N_{\text{ps}} \equiv 2n_0v_0t$ . The core collapse time is labeled with dotted lines, with corresponding  $N_{\text{coll}} \equiv N_{\text{fila}}(t_{\text{coll}})$ .

value of  $X$ , there is not an obvious value of  $X$  to use as a lower limit for filament gas. Using  $X = 1.0$ , Figure 4.6 shows the average column density of the post-shock layer,  $\bar{N}_{\text{ps}} = \bar{\Sigma}_{\text{ps}}/\mu_n$ , and  $N_{\text{fila}}$  for each model, as functions of time. We also measured the filament column density at  $t_{\text{coll}}$ ; in all models,  $N_{\text{coll}} \equiv N_{\text{fila}}(t_{\text{coll}}) \sim 10^{22} \text{ cm}^{-2}$ , comparable to the observed “critical column density” for filaments with active core formation (see review in André et al. 2014). In detail, we find that for  $X = 1$ ,  $N_{\text{coll}}/\bar{N}_{\text{ps}} \approx 1.8$  (see Figure 4.6).

As we shall show below (see Equation (4.27)), the expected post-shock column density at the collapse time is  $\bar{N}_{\text{ps}} \propto (n_0 v_0)^{1/2}$ . When  $\Sigma/\bar{\Sigma}_{\text{ps}} > X = 1$  is used to define filaments,  $N_{\text{coll}}/\bar{N}_{\text{ps}} \approx 1.8$  for all models (see Figure 4.6), implying the same dependence of filament column density on  $v_0$  as mean post-shock column density.

## 4.5 Statistical Core Properties

Similar to Chapter 3, we define the timescale at which  $n_{\text{max}} \geq 10^7 \text{ cm}^{-3}$  as the moment  $t_{\text{coll}}$  when the most evolved core collapses, then identify cores formed at this time and investigate their physical properties (see Section 4.3). Figures 4.7 and 4.8 show the statistical distributions of core mass, size, mean magnetic field, and mass-to-flux ratio measured from our simulations, normalized by total number of cores identified for each parameter set. The normalized mass-to-magnetic flux ratio is defined as

$$\Gamma \equiv \frac{M}{\Phi_B} \cdot 2\pi\sqrt{G}. \quad (4.20)$$

Cores with  $\Gamma > 1$  are magnetically supercritical, and have self-gravity strong enough to overcome the magnetic support and collapse.

Cores identified in our simulations have masses  $M_{\text{core}} \sim 0.002 - 10 M_{\odot}$ , sizes  $R_{\text{core}} \sim 0.004 - 0.05$  pc, and normalized mass-to-flux ratio  $\Gamma \sim 0.4 - 4.5$ , consistent with observations (e.g. Troland & Crutcher 2008; Sadavoy et al. 2010a; Kirk et al. 2013). We also included the normalized mass distribution of starless cores in the Perseus molecular cloud (adopted from Sadavoy et al. 2010a) in Figure 4.7 as a comparison (see Section 4.6 for more discussion). The median values of core properties are summarized in Table 4.3, as well as the averaged core formation efficiency (CFE) and core collapse time  $t_{\text{coll}}$ . In Figure 4.9 we show that the CFE is positively related to the core collapse time,  $t_{\text{coll}}$ . This is because more structures in the post-shock region have become nonlinear at later  $t_{\text{coll}}$ .

Note that though the mean core density,  $\bar{n}_{\text{core}}$ , is  $\sim 10$  times larger than the ambient density in the post-shock layer, the magnetic field within cores ( $\bar{B}_{\text{core}}$ ) is not significantly different from the post-shock region (see  $\bar{n}_{\text{ps}}$  and  $\bar{B}_{\text{ps}}$  in Table 4.1). This is additional evidence of anisotropic core formation: cores gather material along the magnetic field and become more massive without significantly compressing the field and enhancing the magnetic support.

In the anisotropic condensation model (Section 4.2), core properties are expected to depend on the inflow Mach number. In particular, Equations (4.6) and (4.7) suggest that  $R_{\text{core}}$  and  $M_{\text{core}}$  should decrease with increasing  $\mathcal{M}$ , while varying  $B_0$  should not have significant effect on these core properties. Furthermore, the core field is expected to be comparable to the post-shock value given in Equation (4.5),

Table 4.3: Results from identified cores measured at  $t = t_{\text{coll}}$ .

Model	# Cores Identified*	CFE <sup>¶</sup> (%)	$t_{\text{coll}}^{\S}$ (Myr)	$\bar{n}_{\text{core}}$ ( $10^5 \text{ cm}^{-3}$ )	$R_{\text{core}}^{\ddagger}$ (pc)	$M_{\text{core}}$ ( $M_{\odot}$ )	$\bar{B}_{\text{core}}$ ( $\mu\text{G}$ )	$\Gamma_{\text{core}}$	$M_{\text{core}}/M_{\text{BE}}$
M5B10	34	6.55	0.83	2.7	0.022	0.81	49	2.3	2.13
M10B10	30	3.65	0.53	4.9	0.014	0.45	69	2.1	2.46
M20B10	28	0.81	0.43	11	0.009	0.23	156	1.2	1.17
M10B5	46	1.18	0.58	7.7	0.011	0.25	89	2.1	0.95
M10B10	30	3.65	0.53	4.9	0.014	0.45	69	2.1	2.46
M10B20	59	3.90	0.63	6.9	0.015	0.55	103	1.7	2.66

\*We only consider gravitationally bound cores with  $E_{\text{grav}} + E_{\text{thermal}} + E_{\text{B}} < 0$ .

¶CFE is the ratio of the total mass in cores to the total mass in the shocked layer at  $t_{\text{coll}}$  (see Equation (3.28) in Chapter 3).

§Collapse is defined as the time when  $n_{\text{max}} = 10^7 \text{ cm}^{-3}$  in each simulation. The  $t_{\text{coll}}$  shown here is the mean value over all 6 runs for each parameter set.

†Columns (5)–(10) are median values over all cores for each parameter set (6 simulation runs).

‡ $R_{\text{core}}$  is calculated from the total number of zones  $N$  within a core, for an equivalent spherical volume:  $R_{\text{core}} = (3N/(4\pi))^{1/3}\Delta x$ , where  $\Delta x = 1/512 \text{ pc}$  is the grid size.

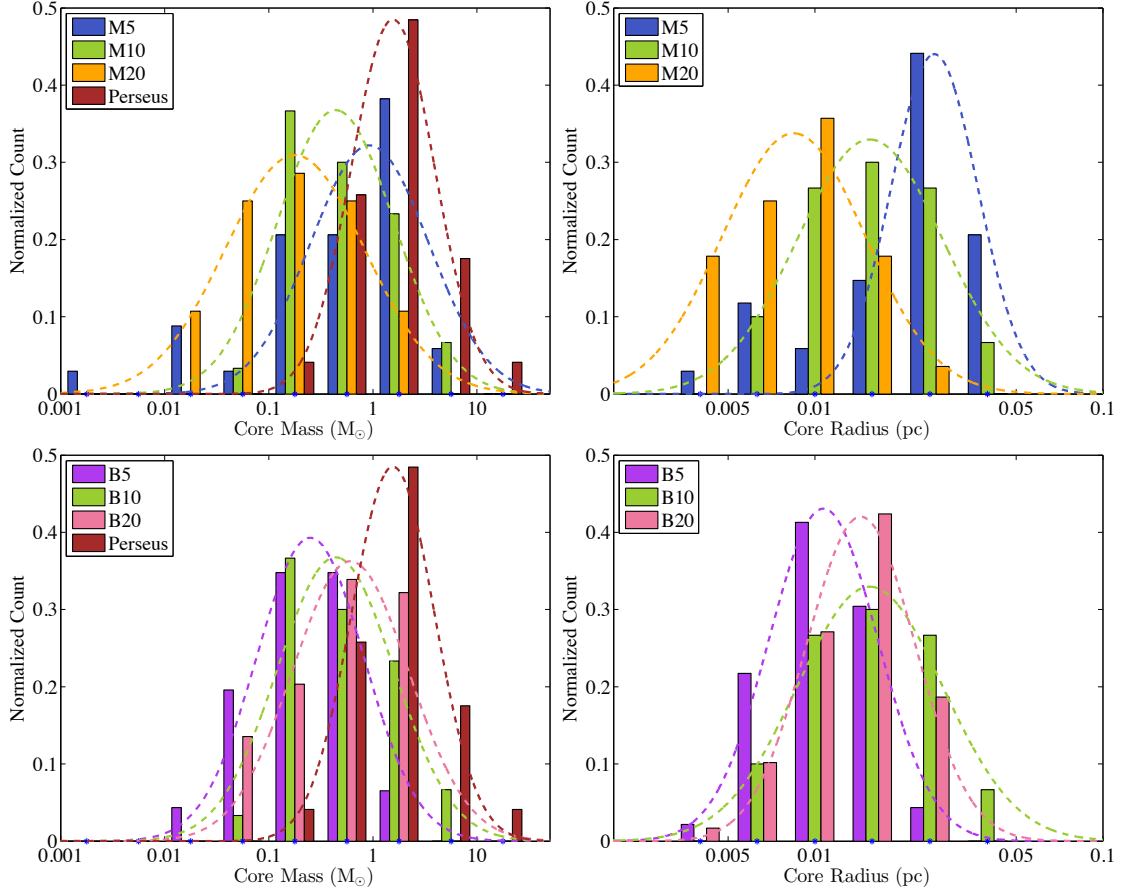


Figure 4.7: Statistical distribution of core mass (*left panel*) and size (*right panel*) for models with different inflow Mach numbers (*top row*) and cloud magnetic fields (*bottom row*).

so that it increases with  $\mathcal{M}$  and is insensitive to  $B_0$ . Our results in Table 4.3 and Figures 4.7 and 4.8 generally agree with these theoretical predictions.

Quantitatively, we plot the median values of core mass, size, and mean magnetic field as well as the average core collapse time in Figure 4.10, as functions of initial Mach number (*top row*) and pre-shock cloud magnetic field (*bottom row*). We also include theoretical models (*dotted lines*) with  $M_{\text{core}} \propto \mathcal{M}^{-1}$  (according to Equation (4.7)),  $R_{\text{core}} \propto \mathcal{M}^{-1}$  (according to Equation (4.6)),  $B_{\text{core}} \propto \mathcal{M}$  (according

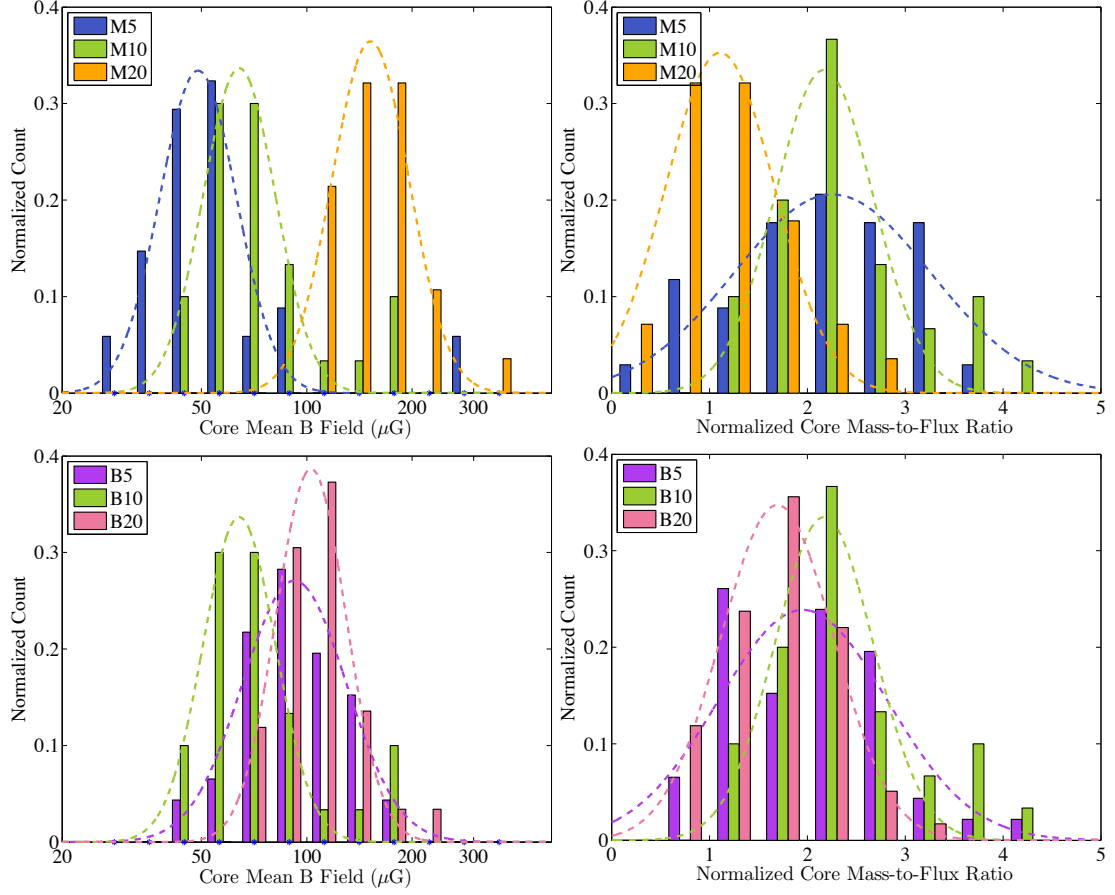


Figure 4.8: Statistical distribution of core mean magnetic field (*left panel*) and mass-to-flux ratio (*right panel*) for models with different inflow Mach numbers (*top row*) and cloud magnetic fields (*bottom row*).

to Equation (4.5)), and  $t_{\text{coll}} \propto \mathcal{M}^{-1/2}$  (see Equation (4.25) below). For each theoretical comparison, we adopt the predicted scaling and obtain a best-fit coefficient. All simulated results fit the theoretical predictions very well, providing quantitative support for the anisotropic core formation model. The fit coefficients we find for radius and mass are  $M_{\text{core}} = 4.4 M_{\odot} \mathcal{M}^{-1}$  and  $R_{\text{core}} = 0.14 \text{ pc } \mathcal{M}^{-1}$ ; these are shown in Figure 4.10.

The Bonnor-Ebert critical radius and mass for an external pressure  $P_{\text{ext}}$  are

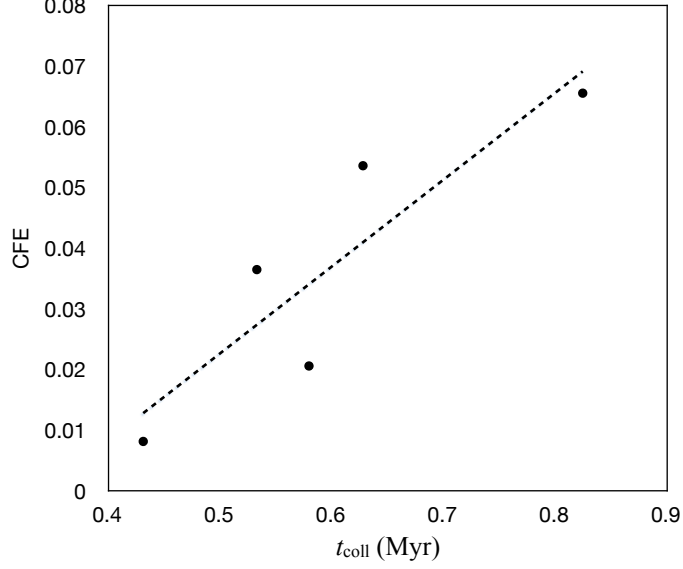


Figure 4.9: The core formation efficiency (CFE) vs. core collapse timescale. Each point represents one model parameter set (M5, M10B10, etc.).

given by  $R_{\text{BE}} = 0.485 c_s^2 (GP_{\text{ext}})^{-1/2}$  and  $M_{\text{BE}} = 1.2 c_s^4 (G^3 P_{\text{ext}})^{-1/2}$ . If we take  $P_{\text{ext}} \rightarrow \rho_0 v_0^2$  and normalize to  $n_0 = 1000 \text{ cm}^{-3}$ ,  $c_s = 0.2 \text{ km/s}$  as in our simulations, the result is

$$\begin{aligned}
 R_{\text{BE,dyn}} &= 0.196 \text{ pc} \left( \frac{n_0}{1000 \text{ cm}^{-3}} \right)^{-1/2} \left( \frac{c_s}{0.2 \text{ km/s}} \right) \mathcal{M}^{-1}, \\
 M_{\text{BE,dyn}} &= 4.43 M_{\odot} \left( \frac{n_0}{1000 \text{ cm}^{-3}} \right)^{-1/2} \left( \frac{c_s}{0.2 \text{ km/s}} \right)^3 \mathcal{M}^{-1}.
 \end{aligned} \tag{4.21}$$

Comparing to our fitted core radius and mass expressions, we have

$$R_{\text{core}} = 0.71 R_{\text{BE,dyn}}, \quad M_{\text{core}} = 0.99 M_{\text{BE,dyn}}. \tag{4.22}$$

Therefore, our results suggest that bound core properties are well described by critical Bonnor-Ebert spheres defined by the dynamical pressure of the environment. This supports the key conclusion predicted in our anisotropic core formation

model.<sup>12</sup>

Equations (4.6) and (4.7) were derived assuming that the accumulation length along the magnetic field is  $L_{\text{mag,crit}}$  (Equation (4.1)). If, however, we instead assume an accumulation length  $L_{\text{acc}}$  and follow the same steps as before, Equations (4.6) and (4.7) would have an additional factor  $(L_{\text{acc}}/L_{\text{mag,crit}})^{-1}$ , i.e.

$$R_{\text{core}} = 0.43 \text{ pc} \left( \frac{n_0}{1000 \text{ cm}^{-3}} \right)^{-1/2} \left( \frac{c_s}{0.2 \text{ km/s}} \right) \mathcal{M}^{-1} \left( \frac{L_{\text{acc}}}{L_{\text{mag,crit}}} \right)^{-1} \quad (4.23)$$

and

$$M_{\text{core}} = 10.5 M_{\odot} \left( \frac{n_0}{1000 \text{ cm}^{-3}} \right)^{-1/2} \left( \frac{c_s}{0.2 \text{ km/s}} \right)^3 \mathcal{M}^{-1} \left( \frac{L_{\text{acc}}}{L_{\text{mag,crit}}} \right)^{-1}. \quad (4.24)$$

Comparing to our fits, this implies  $L_{\text{acc}}/L_{\text{mag,crit}} = 2.4$  or  $3.2$  for the mass or radius fit, respectively. This suggests that cores actually need to gather material along the magnetic field lines from a length scale  $L_{\text{acc}} > L_{\text{mag,crit}}$ . Since  $L_{\text{mag,crit}}$  represents the critical (minimum) length scale for cores to be magnetically supercritical, our finding of  $L_{\text{acc}} > L_{\text{mag,crit}}$  is consistent with the anisotropic core formation model. Table 4.2 includes the value (in pc) of  $L_{\text{acc}} = 2.7 L_{\text{mag,crit}}$  in each model that would be required for the median core mass and radius to match Equations (4.24) and (4.23).

We also use the best-fit coefficients found in  $\mathcal{M}$ -models (Figure 4.10, *top row*) to derive the predicted values (*dotted lines*) of core mass, size, magnetic field strength, and collapse time for  $B$ -models (Figure 4.10, *bottom row*). Most of the theoretical predictions are in good agreement with the simulation results, except the

---

<sup>12</sup>Note that  $R_{\text{BE,dyn}}$  and  $M_{\text{BE,dyn}}$  are respectively factors 0.46 and 0.43 smaller than the radius and mass given in Equations (4.6) and (4.7).

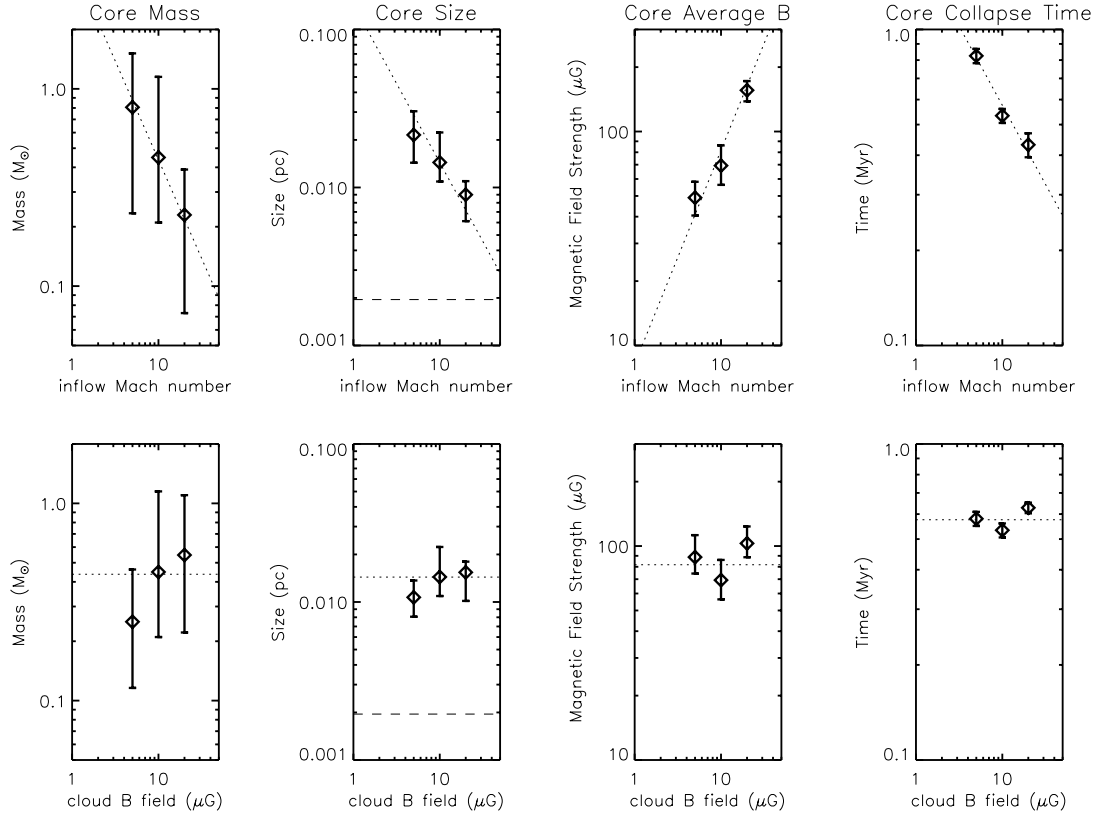


Figure 4.10: Summary of simulated core statistical properties for models with different inflow Mach numbers (*top row*) and cloud magnetic fields (*bottom row*), with theoretical predictions (*dotted lines*). The dashed lines in the core size plots (*second column*) indicate the resolution of our simulations;  $\Delta x \approx 0.002$  pc.

core mass in the B5 model. This is because the B5 model has very strong post-shock density compression but only moderate post-shock magnetic field (see Table 4.1), and supercritical cores may form isotropically. This tendency can also be seen in Figures 4.3 and 4.4, that the structures formed in the B5 model are more randomly distributed compared to other models, the anisotropic gas flow is less prominent, and there is less large-scale structure in the B5 model.

Figure 4.10 shows that the core collapse time follows the relationship  $t_{\text{coll}} \propto \mathcal{M}^{-1/2}$  very well, as predicted in Equation (29) of Gong & Ostriker (2011). The best-fit coefficient gives

$$t_{\text{coll}} = 1.82 \text{ Myr } \mathcal{M}^{-1/2} \quad (4.25)$$

If we compare with Equation (29) of Gong & Ostriker (2011) (with  $n_0 = 1000 \text{ cm}^{-3}$  and  $c_s = 0.2 \text{ km/s}$ ), this would imply a maximum amplification in the post-shock region of  $\ln(\delta\Sigma/\delta\Sigma_0)_{\text{max}} = 2.29$ . The corresponding length scale of the most-amplified mode (see Equation (30) of Gong & Ostriker (2011)) is then

$$\begin{aligned} \lambda_m &= \left( \frac{2\sqrt{3}\pi}{2.29} \right)^{1/2} \frac{c_s}{(G\rho_0)^{1/2}} \frac{1}{\mathcal{M}^{1/2}} \\ &= 0.39 \text{ pc} \left( \frac{n_0}{1000 \text{ cm}^{-3}} \right)^{-1/2} \left( \frac{v_0}{1 \text{ km/s}} \right)^{-1/2}. \end{aligned} \quad (4.26)$$

In most of our models,  $\lambda_m > L_{\text{mag,crit}}$  (see Table 4.2), which means the most-amplified mode would be able to form gravitationally bound cores and collapse. In fact, the amplification is similar for a range of modes with similar wavelengths (see Equation (26) of Gong & Ostriker (2011)), so it is not surprising that  $L_{\text{acc}}$  differs from  $\lambda_m$  (see Table 4.2).

Using the fitted coefficient of Equation (4.25) combined with the expectation  $t_{\text{coll}} \propto n_0^{-1/2}$ , the predicted post-shock surface density at the time of collapse is  $\Sigma_{\text{ps}}(t_{\text{coll}}) = 2\rho_0 v_0 t_{\text{coll}}$ , corresponding to column density

$$N_{\text{ps}}(t_{\text{coll}}) = 5.4 \times 10^{21} \text{ cm}^{-2} \left( \frac{n_0}{1000 \text{ cm}^{-3}} \right)^{1/2} \left( \frac{v_0}{1 \text{ km/s}} \right)^{1/2}. \quad (4.27)$$

This is in good agreement with measured values, as shown in Figure 4.6. Considering Equation (4.27) and the fact that  $N_{\text{fila}}(t_{\text{coll}})/\bar{N}_{\text{ps}} \approx 1.8$  in all models (see Figure 4.6),

this suggests that the filament column density at the core collapse time may have the same dependence on inflow density and velocity as the post-shock column density, i.e.  $N_{\text{fila}}(t_{\text{coll}}) \propto (n_0 v_0)^{1/2}$ .

## 4.6 Comparison to the Perseus Molecular Cloud

### 4.6.1 Cloud Environment

The dark cloud in Perseus is an active star forming region approximately 250 pc away, with a total mass of about  $10^4 M_{\odot}$  over a region about  $8 \times 25$  pc (see review in Bally et al. 2008). Dense gas tracers and dust emission have revealed filamentary structures and a wealth of dense cores in this region (e.g. Enoch et al. 2006; Kirk et al. 2006). In addition, since the Perseus molecular cloud has been observed in  $^{12}\text{CO}$  and  $^{13}\text{CO}$  emission lines (e.g. Ridge et al. 2006), the cloud density should be  $\gtrsim 10^3 \text{ cm}^{-3}$ , similar to the value adopted in our simulations. The Perseus molecular cloud thus represents a good case to compare with our simulation results.

However, the Perseus molecular cloud shows large velocity differences across the region (Bally et al. 2008). The observed CO linewidth is about 5 km/s over the whole cloud (Ridge et al. 2006). Though numerical simulations with rms Mach number  $\mathcal{M} = 6 - 8$  have shown agreement with observational data on linewidth and cloud structures (Padoan et al. 1999, 2006), there is still uncertainty in the actual value of  $\sigma_v$  in the Perseus molecular cloud because of the possibility of superposition of multiple clouds (Bally et al. 2008).

For our comparisons, we adopted the observed properties of starless cores in

the Perseus molecular cloud from Sadavoy et al. (2010a). The core mass distribution of Perseus is included in Figure 4.7 as a comparison to simulations. As discussed in Section 4.5, the Gaussian-fit peaks of the core mass functions from our simulations shift with the inflow Mach number, or equivalently, the velocity dispersion in the cloud. From Figure 4.7, the CMF of Perseus has a peak core mass similar to that of the M5 model, suggesting that Perseus may be a relatively quiescent star-forming environment with converging flow velocities only of order  $\sim 1$  km/s.

#### 4.6.2 Bonnor-Ebert Mass

One interesting feature of the Perseus cloud is the existence of “super-Jeans mass cores” (Sadavoy et al. 2010b). These massive cores have relatively strong self-gravity compared to their internal thermal pressure, but still remain starless. An interesting possibility is that these and similar cores may be partially magnetically supported. Our models are useful for addressing this question, because we can measure the fraction of super-Jeans mass cores under different environments in our simulations, and we also can measure magnetic support.

For consistency with theoretical work, we will consider the critical Bonnor-Ebert mass instead of the Jeans mass. We thus convert from the  $M/M_J$  ratios in Sadavoy et al. (2010b) to  $M/M_{BE}$ , making use of the core mass and effective radius published in Sadavoy et al. (2010a), and using Equation (19) in Gong & Ostriker

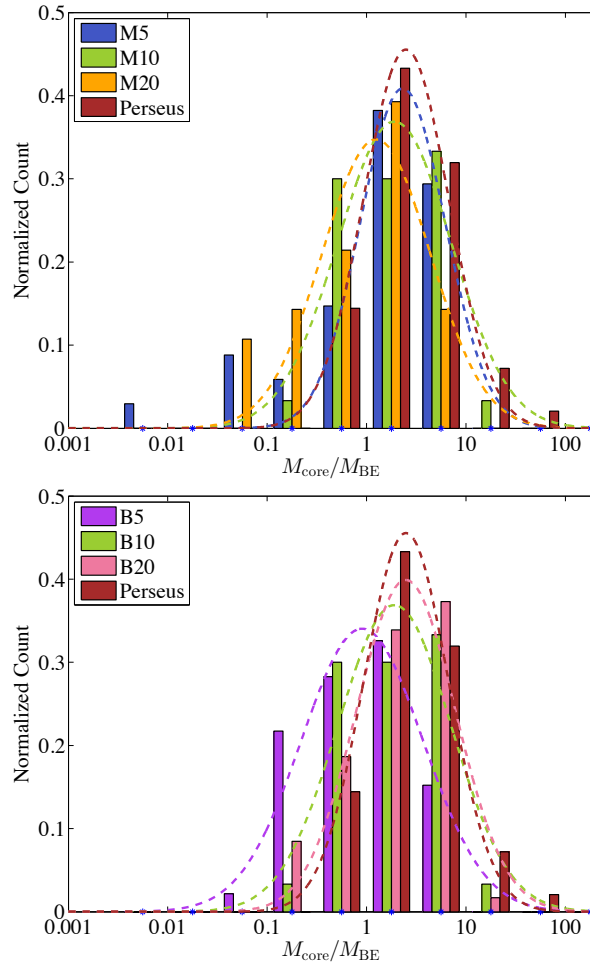


Figure 4.11: Statistical distribution of the ratio between core mass and theoretical Bonnor-Ebert mass, compared with the observed values in Perseus, for cores formed in the M-models (*top*) and B-models (*bottom*).

(2009):

$$\begin{aligned}
M_{\text{BE}} &= 1.18 \frac{c_s^4}{\sqrt{G^3 P_{\text{edge}}}} = 1.85 \frac{c_s^4}{\sqrt{G^3 P_{\text{mean}}}} \\
&= 1.85 \frac{c_s^3}{\sqrt{G^3 \rho_{\text{mean}}}} = 3.8 \frac{c_s^3}{G^{3/2}} \frac{R^{3/2}}{M^{1/2}}.
\end{aligned} \tag{4.28}$$

For a core at mass  $M$ , radius  $R$ , and density  $\rho_{\text{mean}}$  that is pressure confined at its surface, the thermal pressure is insufficient to prevent gravitational collapse if  $M > M_{\text{BE}}$ . For each core identified in our simulations, we calculated the value of the Bonnor-Ebert mass using the core's mass and radius.

Figure 4.11 shows the statistical distribution of  $M_{\text{core}}/M_{\text{BE}}$  from both our simulations and Perseus; in addition to the binned counts, we also show best fit log-normal functions for each model. The distributions for all models and for Perseus are similar. Figure 4.11 shows that although the median core mass is close to  $M_{\text{BE}}$ , the majority of our gravitationally-bound cores have  $M_{\text{core}}/M_{\text{BE}} > 1$ , naïvely consistent with the fact that these cores are magnetized. However, these super-BE mass cores do not in fact seem to be supported primarily by the magnetic field. Figure 4.12 shows the mass-to-flux ratio  $\Gamma$  versus  $M/M_{\text{BE}}$  for all cores from our simulations. Evidently, most cores with high  $M/M_{\text{BE}}$  ( $\gtrsim 3$ ) are also strongly magnetically supercritical ( $\Gamma \gtrsim 2$ ). This suggests that the super-BE mass cores observed in Perseus may be strongly self-gravitating and on their way to collapse, rather than being magnetically supported. In fact, in our model, cores with  $M_{\text{core}}/M_{\text{BE}} \gtrsim 7$  all have  $n_{\text{max}} \gtrsim 10^7 \text{ cm}^{-3}$ , which means they are the most-evolved collapsing cores in individual simulation runs.

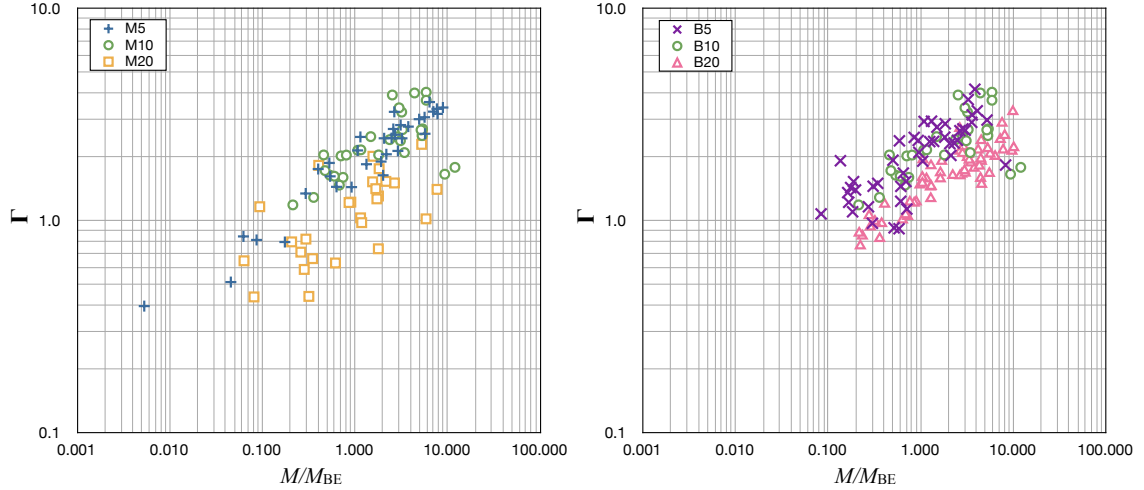


Figure 4.12: Scatter plot of core mass-to-flux ratio vs.  $M/M_{\text{BE}}$  in different models. Each point represents one core formed in the corresponding model.

### 4.6.3 Mass-radius Relation

Several observations have found that there is a power-law relationship between the core mass and its size,  $M \propto R^k$ , with  $k \sim 2$  (Kirk et al. 2013). Figure 4.13 is the binned mass-size plot from all identified cores in our simulations, compared to the observed cores found in the Perseus molecular cloud (reported in Sadavoy et al. 2010a). Similar to the observations, the binned data from our simulations show  $k \sim 2$  for the power-law relationship between core mass and radius. At a given radius, our cores have slightly higher mass than those in Perseus.

A relationship  $M_{\text{core}} \propto R_{\text{core}}^2$  would suggest that the core surface density  $\Sigma_{\text{core}} \equiv M_{\text{core}}/(\pi R_{\text{core}}^2)$  is constant for cores regardless of their masses and sizes. Figure 4.14 shows the scatter plot of the core column density ( $N_{\text{core}} \equiv \Sigma_{\text{core}}/\mu_n$ ) versus core mass for all cores formed in our simulations. Although core mass varies

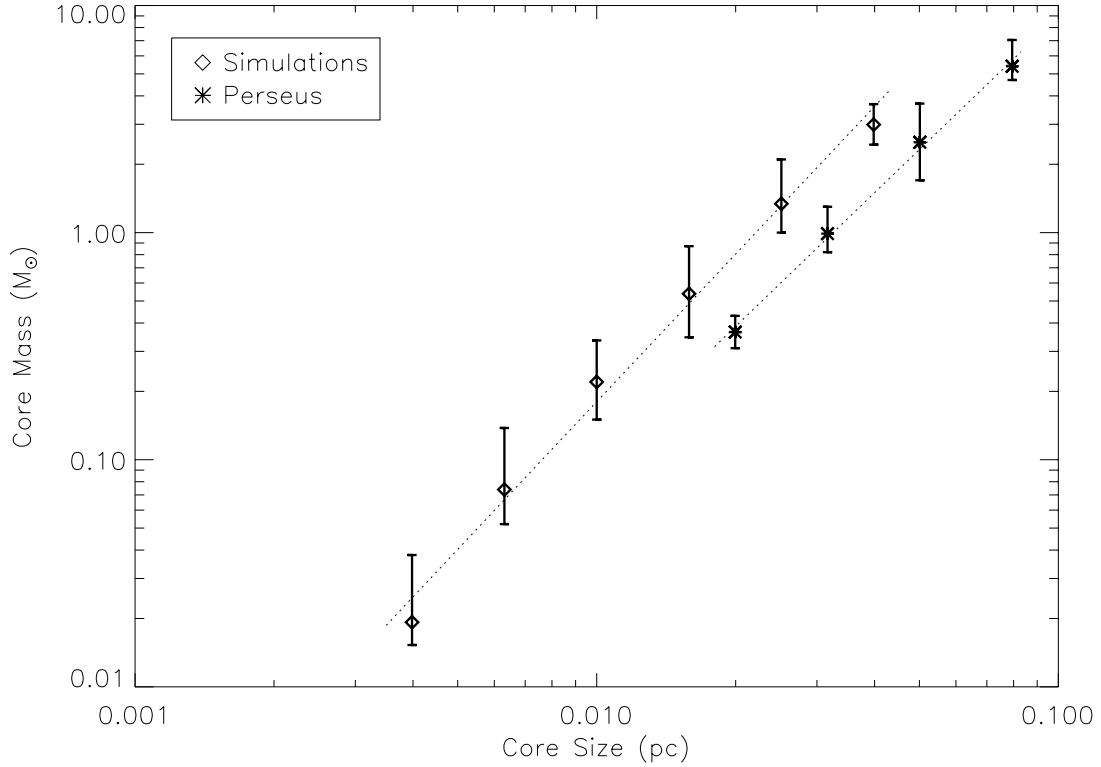


Figure 4.13: The mass-radius relationship measured from our simulations (*diamonds*) compared with the observation results from Perseus (*asterisks*), using the median values of the binned counts. For both the simulations and observations, the vertical bars represent the  $\pm 25\%$  values in each bin. The best-fit power laws (*dotted lines*) are  $M \propto R^{1.96}$  for Perseus, and  $M \propto R^{2.16}$  for our simulations.

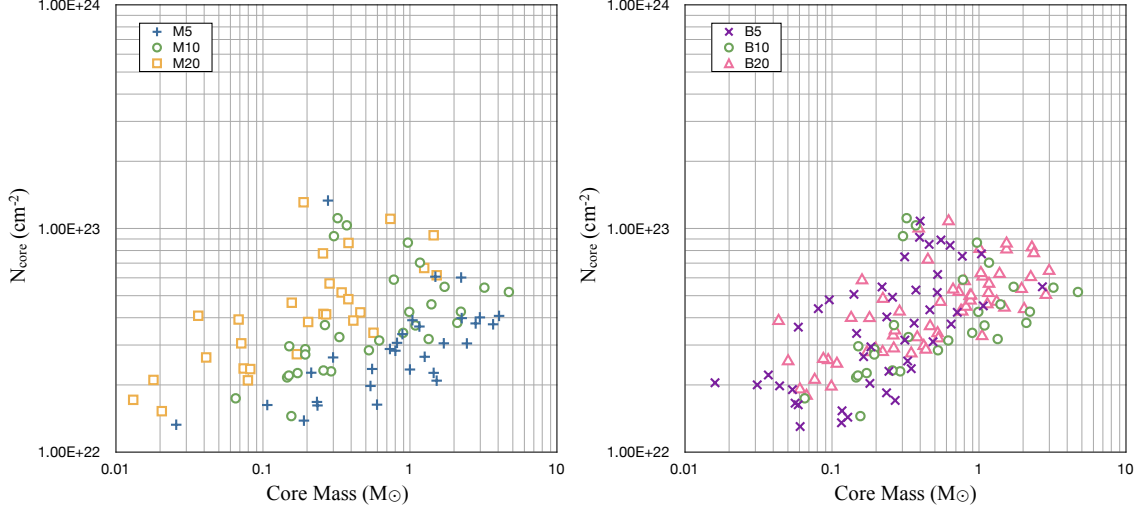


Figure 4.14: Scatter plot of  $N_{\text{core}}$  vs.  $M_{\text{core}}$  in different models. Each point represents one core formed in the corresponding model.

over nearly three orders of magnitude ( $\sim 0.01 - 10 M_{\odot}$ ),  $N_{\text{core}}$  is within a factor of 10. The mean value is  $N_{\text{core}} = 3.7 \times 10^{22} \text{ cm}^{-2}$ . By comparison, we found in Section 4.4.2 that the overdense filamentary structures have column density  $N_{\text{fila}} \sim 10^{22} \text{ cm}^{-2}$  at the time of collapse. Thus, the typical core column density  $N_{\text{core}} \sim 4 N_{\text{fila}}$ .

However, any  $k > 2$  value indicates that  $N_{\text{core}}$  increases with  $M_{\text{core}}$  or  $R_{\text{core}}$ , and this trend is evident in Figure 4.14, for different models. Figure 4.15 shows the mass-radius relations for individual models in our simulations as well as the fitted  $M_{\text{core}} \propto R_{\text{core}}^k$  power-law (the complete fitting coefficients are listed in Table 4.4). We found that the fitted  $k$  values are generally higher than 2, implying that  $N_{\text{core}}$  is not a constant over cores with different masses and sizes.<sup>13</sup> This means that it is possible that there is no “universal” core column density, but simply a weak

<sup>13</sup>Composite distribution of cores from different models show a smaller value of  $k$ , and more dispersion, than individual models.

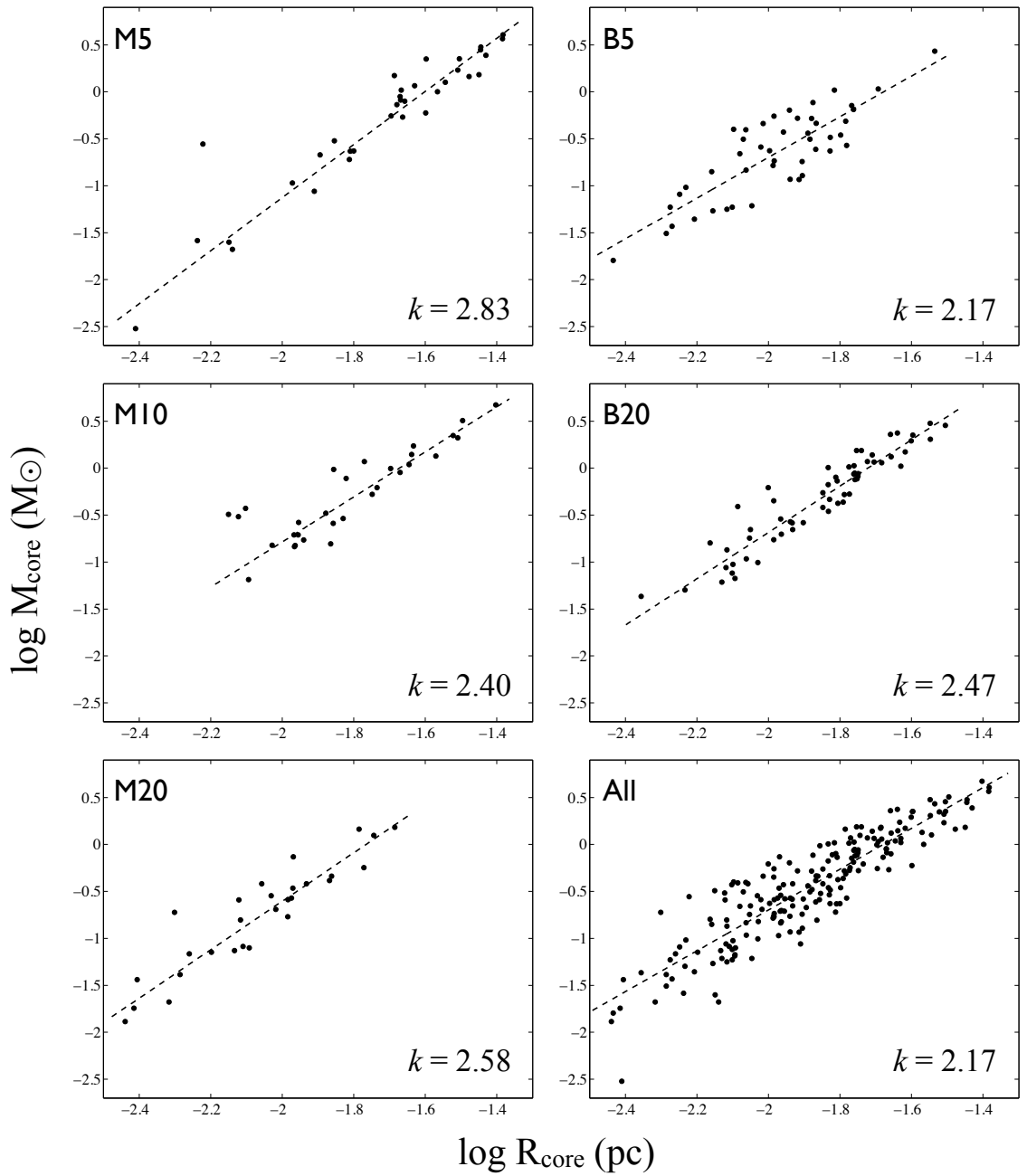


Figure 4.15: Scatter plot of  $M_{\text{core}}$  vs.  $R_{\text{core}}$  in different models (each point represents one core formed in corresponding model), as well as the fitted power-law relationship  $M \propto R^k$  (*dashed lines*) with the  $k$  values listed on the bottom right of each panel.

Table 4.4: The fitted Mass-size relationship from our simulations,  $M_{\text{core}}/M_{\odot} = A(R_{\text{core}}/\text{pc})^k$ .

Model	$A (\times 10^3)$	$k$	R-square*
M5	33.57	2.83	0.94
M10	10.28	2.40	0.82
M20	36.14	2.58	0.86
B5	4.31	2.17	0.64
B20	17.66	2.47	0.88
All	4.45	2.17	0.81

\*R-square is the coefficient of determination that indicates the goodness of fit. R-square = 1 means the regression line perfectly fits the data.

dependence of  $N_{\text{core}}$  on parameters, which is difficult to identify from the present models. For example, the post-shock column density at the time of core collapse varies as  $N_{\text{ps}} \propto (n_0 v_0)^{1/2}$  (see Equation (4.27)), and filament column densities appear to follow a similar trend. If the mean core column density is also a multiple of this, then it would vary by only a factor two for our models, which all have  $n_0 = 1000 \text{ cm}^{-3}$  and have  $v_0$  varying by a factor four. We do indeed find a higher mean  $N_{\text{core}}$  for  $v_0 = 4 \text{ km/s}$  ( $4.8 \times 10^{22} \text{ cm}^{-2}$ ) compared to  $v_0 = 1 \text{ km/s}$  ( $3.0 \times 10^{22} \text{ cm}^{-2}$ ). Further investigations, both observational and computational, are needed to reach a clearer conclusion.

## 4.7 Summary

In this chapter, we extended the investigation of Chapter 3 to further examine the anisotropic core formation model and test the theoretical scalings of core

properties over a larger parameter space. We carried out fully three-dimensional ideal MHD simulations with self-gravitating gas, including supersonic convergent flows with local turbulence. Our models allow for varying inflow Mach number and magnetic field strength of the background cloud. Our simulation results demonstrate that the ram pressure of the converging flow ( $\rho_0 v_0^2$ ) is the dominant factor controlling the physical properties of cores formed in the shocked layer. These core properties are consistent with the predictions of the anisotropic core formation theory. Although the post-shock layer is strongly magnetized in all cases, core properties are insensitive to the pre-shock magnetic field strength. We also compared cores formed in our simulations with those observed in the Perseus molecular cloud, and found very similar core mass distribution, super-Bonnor-Ebert mass ratio, and mass-size relation.

Our main conclusions are as follows:

1. Considering typical GMC conditions, spherically symmetric core formation is impossible in the magnetized post-shock region, because the required mass gathering scales are much larger than the thickness of the shocked layer (Table 4.1 and Figure 4.2). Quantitatively, it takes  $\gtrsim 1$  Myr for the post-shock layer thickness to be comparable with the magnetic critical length under post-shock conditions (Equation (4.17)), much longer than typical core formation timescale in our simulations.
2. Filamentary structures formed in the post-shock regions are similar to those found in observations, with dense cores embedded within filaments (Figure 4.3).

We measured the filament formation efficiency (FFE) to be around 50% (dependent on the choice of column density threshold of filament; Table 4.2), independent of the pre-shock conditions. We also found that the filament column density at the time when cores start to collapse is proportional to the mean post-shock column density;  $N_{\text{fila}}(t_{\text{coll}}) \approx 1.8\bar{N}_{\text{ps}}$  (Figure 4.6).

3. Our velocity space-time diagrams (Figure 4.4) show clear evidence that the mass-gathering flows that create cores and filaments are highly anisotropic. Until late times, flow along the magnetic field is much stronger than in the two perpendicular directions. However, our simulations also show that the “seeds” of cores are present even at early times. This suggests that core and filament formation is simultaneous, instead of the commonly-assumed picture that cores form only after filaments do.
4. Magnetically supercritical cores form within the post-shock layers in all of our simulations, with masses  $\sim 0.002 - 10 M_{\odot}$ , sizes  $\sim 0.004 - 0.05$  pc, and normalized mass-to-flux ratio  $\sim 0.4 - 4.5$  (Table 4.3). The core formation timescale is  $t_{\text{coll}} \sim 0.4 - 0.9$  Myr, and the core formation efficiency is positively-related to the core collapse time (Figure 4.9).
5. The statistical distributions of core mass, size, mean magnetic field, and mass-to-flux ratio clearly show that median core properties depend on the pre-shock inflow Mach number  $\mathcal{M} = v_0/c_s$  but not the upstream magnetic field strength  $B_0$  (Figures 4.7 and 4.8). The theoretical scalings predicted in the anisotropic core formation model are  $M_{\text{core}} \propto \mathcal{M}^{-1}$ ,  $R_{\text{core}} \propto \mathcal{M}^{-1}$ , and  $B_{\text{core}} \sim B_{\text{ps}} \propto \mathcal{M}$

(Equations (4.5)-(4.7)), which agree with our simulation results very well (Figure 4.10). Furthermore, the core collapse timescale in our MHD simulations generally follow the relationship  $t_{\text{coll}} \propto \mathcal{M}^{-1/2}$ . The  $t_{\text{coll}}$  scaling is consistent with the prediction of Gong & Ostriker (2011) based on hydrodynamic analysis, because the flows in the post-shock layer are primarily parallel to the magnetic field. This also gives the post-shock column density at  $t_{\text{coll}}$  to be  $N_{\text{ps}}(t_{\text{coll}}) \propto \mathcal{M}^{1/2}$  (Equation (4.27)).

6. Quantitatively, the median core mass and radius depend on inflow velocity as  $M_{\text{core}} = 0.88 M_{\odot} (v_0 / (\text{km/s}))^{-1}$  and  $R_{\text{core}} = 0.028 \text{ pc} (v_0 / (\text{km/s}))^{-1}$ . This suggests that the core mass and radius will be, respectively, a factor 0.99 and 0.71 lower than the Bonnor-Ebert critical mass and radius computed using the sound speed and total dynamical pressure ( $\rho_0 v_0^2$ ) in the cloud (Equations (4.21) and (4.22)). This result is similar to the scaling for characteristic mass proposed by Padoan et al. (1997), but our coefficient is higher by a factor  $\sim 2$ .
7. Cores identified in our simulations have physical properties very similar to those observed in Perseus (Sadavoy et al. 2010a). In addition, we found similar statistical distributions of  $M_{\text{core}}/M_{\text{BE}}$  in simulations and observations (Figure 4.11). We suggest that the “super-Bonnor-Ebert mass cores” identified in Sadavoy et al. (2010b) are probably not supported by magnetic pressure and will collapse gravitationally, since most cores with high  $M_{\text{core}}/M_{\text{BE}}$  in our simulations also have high  $\Gamma$  values, indicating that these cores are magnetically

supercritical (Figure 4.12).

8. We find (Figure 4.13) a composite mass-radius relation for our simulated prestellar cores comparable to that seen in observations,  $M_{\text{core}} \propto R_{\text{core}}^2$  (e.g. Kirk et al. 2013). Although the observed relation is sometimes interpreted as implying a “universal” core surface density, our results suggest that there might be a weak dependence of the core surface density  $\Sigma_{\text{core}} \equiv M_{\text{core}}/(\pi R_{\text{core}}^2)$  on core mass or radius (Figure 4.14). We also find that the exponent  $k$  in the mass-size relation  $M \propto R^k$  is larger for individual models with consistent shock conditions than the composite from heterogeneous environments (Figure 4.15).

To conclude, the success of the anisotropic core formation model for explaining idealized converging turbulent magnetized flows is very encouraging, and provides strong motivation for testing these ideas in global MHD simulations of star-forming molecular clouds. Further investigations considering more extreme conditions of GMCs would also be interesting to examine the properties of core-forming filaments, and potential variations in the core mass-size relationship.

We are grateful to Sarah Sadavoy for providing a table of core properties in Perseus.

## Chapter 5: Summary and Future Work

Understanding prestellar core formation is an important step in developing a complete theory of stellar evolution, as needed to explain the lives of stars, the building blocks of the universe seen by human eyes. The process for dense cores to form within diffuse ISM involves physics, chemistry, and dynamics over a large range of spatial scales. The complexity makes the overall problem challenging, but we have made considerable progress by breaking it down to several focused investigations.

### 5.1 Summary of Thesis Study

Before I started my thesis research, it had been generally recognized that magnetic fields and supersonic turbulence are the two keys of core formation within GMCs, but it was not well understood exactly how these interact or the role played by ion-neutral drift. We therefore began our study with a combined analytic and numerical investigation of MHD shocks, focusing on the behavior of turbulence-accelerated ambipolar diffusion (Chapter 2). We found an analytic estimate of the C-type shock thickness as a function of the pre-shock density, inflow velocity, background magnetic field, and gas ionization fraction (Equation (2.47)). We also derived an expression for the ambipolar diffusion timescale,  $t_{\text{AD}} \approx L_{\text{shock}}/v_{\text{drift}}$

(Equation (2.65)), which can be applied to determine the duration of the transient stage in GMCs, before neutrals and ions are well coupled.

The transient stage of turbulence-enhanced ambipolar diffusion is the most important discovery in our one-dimensional study, during which the post-shock gas is strongly compressed as in pure hydrodynamic shocks (Figures 2.4 and 2.8). The existence of this transient diffusion effect increases the mass-to-flux ratio downstream (Equation (2.76)), creating a favorable circumstance for prestellar cores to form. Our results help to explain why ambipolar diffusion that drives core formation can be accelerated by turbulence, because the transient behavior happens promptly at the beginning of the shock compression.

In addition, in our analysis of one-dimensional oblique C-type shocks (Appendix A), we concluded that regions with large-scale velocity more aligned to the cloud magnetic field are more favorable for magnetically supercritical cores to form (Equation (A.25)).

To study how transient ambipolar diffusion and shock obliquity can affect core formation within real turbulent clouds, we conducted fully three-dimensional simulations to follow structure (filaments, clumps, and cores) formation with converging flows and magnetic effects, ideal and non-ideal (Chapter 3). We used the ionization fraction coefficient (see Equation (2.29) or (3.26)) as the main parameter controlling ambipolar diffusion, and varied the angle between the inflow and the cloud magnetic field to achieve different shock obliquity (see Equations (3.4) and (3.5)).

To provide context for our simulations, we analyzed MHD shock compression with varying obliquity. We found that shocks that have inflows almost parallel to

the magnetic field can create post-shock compression in neutrals as strong as in hydrodynamic shocks, making the magnetization level relatively weak (see Table 3.1). This effect is in addition to transient ambipolar diffusion. We showed that, except for these quasi-hydrodynamic cases, without non-ideal MHD effects, the formation of low-mass, magnetically-supercritical cores by spherical contraction is forbidden under typical GMC conditions, because the minimum scale for a spherical region to be magnetically supercritical corresponds to a large mass (see Section 3.2.2).

From our three-dimensional, self-gravitating, turbulent converging flow simulations, we identified gravitationally bound cores within the post-shock dense layer using the gravitational potential of the neutral gas (Figure 3.7). These cores are physically similar to those observed in GMCs in terms of mass, size, magnetization, and formation timescale (Table 3.3). However, though the magnetization level within cores (or the core mass-to-flux ratio) depends on transient ambipolar diffusion and the upstream magnetic obliquity (Figures 3.11 and 3.12), the core mass and size are relatively independent of both effects (Figures 3.8 and 3.9).

Close-up views of the gas dynamics around forming cores suggest that material flows primarily along the magnetic field lines into the forming core regions (Figures 3.13 and 3.14), which explains why the magnetic field of cores follows the same trends as the post-shock magnetization (Tables 3.2 and 3.3). Motivated by this evidence, we proposed that anisotropic self-gravitating condensation may be the dominant mechanism for low-mass, magnetically-supercritical cores to form within GMCs, regardless of the ambipolar diffusion strength or magnetization level in the ambient environment. Anisotropy would explain how low-mass cores are able to

form even with ideal MHD, given that the strong magnetic fields forbid spherical contraction of low-mass condensations.

To further test the anisotropic core formation model, we extended our numerical study to a larger parameter survey, allowing for varying inflow velocities and cloud magnetic fields (Chapter 4). Our simulation results strengthened the idea that it is impossible for cores to form isotropically in the magnetized post-shock layer under reasonable cloud conditions (Figure 4.2 and Table 4.1). In addition, we demonstrated that the momentum flux (or ram pressure) of the converging flow is the dominant parameter controlling the physical properties of cores formed in the post-shock region, while the primary role played by the magnetic field is to enforce anisotropic core formation (Figure 4.10).

In addition, we compared our results with the observed properties of starless cores in the Perseus molecular cloud, using data published in Sadavoy et al. (2010a). We found very similar core mass distributions (Figure 4.7) and mass-size relationship (Figure 4.13) between cores formed in our simulations and identified in Perseus. More importantly, the range of  $M_{\text{core}}/M_{\text{BE}}$  values in our simulations agrees with that derived from Sadavoy et al. (2010a) and Sadavoy et al. (2010b), approximately  $\sim 0.01 - 100$  (Figure 4.11). For both our simulations and in Perseus, most cores have  $M_{\text{core}}/M_{\text{BE}} > 1$  (i.e. they are “super-BE” in mass), indicating that their internal thermal pressure is relatively weak compared to the self-gravity. However, we also showed that most cores in our simulations with high  $M_{\text{core}}/M_{\text{BE}}$  values are also magnetically supercritical (Figure 4.12). This suggests that the observed super-BE mass cores may not be supported by the magnetic field, and will in fact collapse

gravitationally.

To conclude, this thesis work provides answers to some longstanding and fundamental problems in star formation, including how dense cores form from more diffuse gas and what role cloud magnetic fields play during this process. We now know that ambipolar diffusion is important at the very beginning of core formation, because the shock-induced transient ambipolar diffusion sets the magnetization level of the post-shock region and of the cores that form within that region. However, ambipolar diffusion is not necessary in order to form low-mass, magnetically-supercritical cores. Through anisotropic mass collection along the magnetic field lines, candidate cores can gather enough material to overcome magnetic support and collapse gravitationally to form protostellar systems. Cores formed via this anisotropic mechanism in our simulations strongly resemble observed cores in their masses, sizes, and magnetizations.

## 5.2 Future Work

### 5.2.1 From Local to Global Simulations

Our core-forming simulations with converging flows showed great success in explaining the magnetohydrodynamics of prestellar core formation, characterizing their physical properties, and connecting them to the GMC environment. However, this idealized setup has limitations. For example, our simulations did not include turbulence corresponding to the scales between the size of the simulation box (1 pc) and the size of the cloud ( $\sim 10$  pc). In addition, we applied somewhat reduced tur-

bulent amplitudes compared to observations, due to constraints of the local model. Also, the real converging flows in GMCs may not be perfectly aligned up to 1 pc wide as assumed in our model, and thus the pc-size post-shock dense layer formed in our simulations may be too artificial as a core-forming site.

Therefore, it is necessary to test under what circumstances the conditions in the local model actually apply within realistic turbulent clouds, and how the less idealized converging-flow conditions within a global simulation may affect core formation. By running larger-scale adaptive mesh refinement (AMR) simulations with box size covering the whole cloud (e.g.  $L_{\text{box}} = 20 - 30$  pc) and including multi-scale turbulence following the observed power spectrum ( $|\sigma_v(k)| \propto k^{-2}$ ), one can investigate the shocked regions as they form within a more natural environment. The shape, kinematic structure, and lifetime of these dense post-shock “layers,” together with the user-controlled cloud parameters like density and turbulence amplitude, will reveal under what circumstances our idealized converging flow model can be considered to represent local regions in the real GMCs.

## 5.2.2 Potential Future Projects

The magnetization level within prestellar cores is not only important for the ability of the core to collapse, but also for late evolutionary stages during protostellar disk formation and subsequent planet formation. One major challenge in understanding the evolution from prestellar cores to protostellar systems is the magnetic braking problem (McKee & Ostriker 2007; Li et al. 2014). In contrast to the

unmagnetized situation in which disks form naturally from angular momentum conservation during core collapse, the magnetic field removes angular momentum from the inner parts of the collapsing core and thus suppresses disk formation (Allen et al. 2003; Hennebelle & Fromang 2008; Mellon & Li 2008; Hennebelle et al. 2011). Numerical simulations show that the formation of large-scale rotationally supported disks (RSDs) (as are needed to form observed planetary systems) is suppressed by powerful magnetic braking unless the dense cores are weakly magnetized to an unrealistic level (Allen et al. 2003; Hennebelle & Fromang 2008; Mellon & Li 2008; Hennebelle et al. 2011).

One potential solution is that non-ideal MHD effects, which break the flux-freezing condition, may alter the evolution sufficiently to avert the “catastrophe” (Li et al. 2011; Machida et al. 2011; Dapp et al. 2012; Tomida et al. 2013, 2015). With observational evidence for a random distribution of the angle between the magnetic field and the bipolar outflow axis (Hull et al. 2013), some theoretical models have also suggested that a reduction in the magnetic braking efficiency is induced by large-enough field-rotation misalignment, and RSDs may form in moderately-magnetized dense cores (Hennebelle & Ciardi 2009; Ciardi & Hennebelle 2010; Joos et al. 2012; Krumholz et al. 2013; Li et al. 2013). In addition, simulations of turbulent core collapse demonstrated a beneficial effect of turbulence on RSD formation because of the turbulence-induced magnetic flux loss and tangling of field lines (Santos-Lima et al. 2012; Seifried et al. 2012, 2013; Joos et al. 2013), though it is possible that limited grid resolution enhances the magnetic reconnection (Li et al. 2014).

The above work shows promise for solving the magnetic braking catastrophe.

However, it all shares a common numerical weakness: making artificial assumptions for idealized initial conditions. By following evolution of cores similar to those found in our previous simulations (Chapters 3 and 4), one can investigate the formation of protostellar systems with realistic turbulent levels and magnetic field strengths. Note that to follow disk formation, AMR is required to increase numerical resolution locally, because our previous simulations ( $\Delta x = 400 - 800$  AU) do not have enough resolution for disk-scale structures. From our previous results, one can systematically choose a sample of cores with different angular momentum, magnetic field strength, turbulence level, and field-rotation misalignment. By importing these cores as initial conditions into three-dimensional MHD simulations with AMR, it may be possible to understand better the environmental requirements of circumstellar disk formation, as well as details of the processes involved. This kind of study will be extremely helpful for understanding what physical mechanism is responsible for reducing the efficiency of magnetic braking during prestellar core collapse.

## Appendix A: Oblique C shocks

The main text in Chapter 2 considers a 1-D system with velocities and magnetic fields perpendicular to each other, for simplicity. We expect that our results will qualitatively hold for more general geometry. Here, we show that under certain conditions, our results can quantitatively be applied to oblique C-type shocks.

In the following, we shall consider a plane-parallel shock in the standard shock frame, using the same coordinate system as before. The shock front is in the  $y$ - $z$  plane, the upstream flow is along the  $x$ -direction ( $\mathbf{v}_0 = v_0\hat{\mathbf{x}}$ ), and the upstream magnetic field is now in the  $x$ - $y$  plane ( $\mathbf{B}_{\text{cloud}} = B_{x,0}\hat{\mathbf{x}} + B_{y,0}\hat{\mathbf{y}}$ ), at an angle  $\theta$  to the inflow ( $B_{y,0}/B_{x,0} = \tan \theta$ ).

For steady, plane-parallel shocks,  $\partial_t = \partial_y = \partial_z = 0$ . From the mass and momentum conservation equations for neutrals (Equations (2.1)–(2.2)), we have

$$\frac{d}{dx}(\rho_n v_{n,x}) = 0, \quad (\text{A.1})$$

$$\frac{d}{dx}(\rho_n v_{n,x}^2 + c_s^2 \rho_n) = \alpha \rho_i \rho_n (v_{i,x} - v_{n,x}), \quad (\text{A.2})$$

$$\frac{d}{dx}(\rho_n v_{n,x} v_{n,y}) = \alpha \rho_i \rho_n (v_{i,y} - v_{n,y}). \quad (\text{A.3})$$

Similarly, the momentum equation for ions and the magnetic induction equation

(Equations (2.3)–(2.4)) are (with the strong coupling approximation)

$$\frac{1}{8\pi} \frac{d}{dx} B_y^2 = \alpha \rho_i \rho_n (v_{n,x} - v_{i,x}), \quad (\text{A.4})$$

$$\frac{B_x}{4\pi} \frac{d}{dx} B_y = -\alpha \rho_i \rho_n (v_{n,y} - v_{i,y}), \quad (\text{A.5})$$

$$v_{i,x} B_y - v_{i,y} B_x = \text{const.} = v_0 B_{y,0}. \quad (\text{A.6})$$

Note that  $B_x = \text{const.} = B_{x,0}$  in plane-parallel shocks, since  $\nabla \cdot \mathbf{B} = 0$ .

By defining our parameters as

$$r_n \equiv \frac{\rho_n}{\rho_0} = \frac{v_0}{v_{n,x}}, \quad r_{ix} \equiv \frac{v_0}{v_{i,x}}, \quad r_B \equiv r_{B_y} = \frac{B_y}{B_{y,0}}, \quad (\text{A.7})$$

and

$$\mathcal{M} \equiv \mathcal{M}_x = \frac{v_0}{c_s}, \quad \frac{1}{\beta_y} \equiv \frac{B_{y,0}^2}{8\pi \rho_0 c_s^2} = \frac{1}{2} \left( \frac{v_{Ay,0}}{c_s} \right)^2, \quad (\text{A.8})$$

and applying the ionization-recombination equilibrium ( $\rho_i \propto \rho_n^{1/2}$ ), Equations (2.15) and (2.16) become

$$\frac{d}{dx} r_B^2 = -\beta_y \frac{\alpha \rho_{i,0}}{v_0} \mathcal{M}^2 r_n^{3/2} \left( \frac{1}{r_{ix}} - \frac{1}{r_n} \right) \quad (\text{A.9})$$

$$\frac{d}{dx} \left( \frac{\mathcal{M}^2}{r_n} \right) + \frac{d}{dx} (r_n) = -\frac{1}{\beta_y} \frac{d}{dx} r_B^2. \quad (\text{A.10})$$

Since Equation (A.10) is the same as Equation (2.16) with  $\beta \rightarrow \beta_y$ , the  $r_B$  vs.  $r_n$  relation for oblique shocks is the same as in shocks with  $B_x = 0$  (Equation (2.19)).

In addition, in the post-shock regime,  $r_{n,f} = r_{ix,f}$ . From Equations (A.3) and (A.5), the neutral velocity parallel to the front is given by

$$\frac{v_{n,y}}{v_0} = \frac{1}{\tan \theta} \left( \frac{v_{Ay,0}}{v_0} \right)^2 (r_B - 1). \quad (\text{A.11})$$

The governing equation in the direction perpendicular to the shock front now becomes

$$\frac{d}{dx}r_n = \frac{-Dr_n^{3/2}}{1 - \mathcal{M}^2/r_n^2} \left( \frac{1}{r_n} - \frac{1}{r_{ix}} \right). \quad (\text{A.12})$$

This approaches Equation (2.30) only if  $r_{ix} \approx r_B$ .

It is straightforward to show (Wardle 1991) that

$$\frac{1}{r_{ix}} = \frac{1}{r_B} \frac{\tan^2 \theta + (r_n r_B)^{-1} + 2(r_B - 1)(\beta_y \mathcal{M}^2)^{-1}}{\tan^2 \theta + r_B^{-2}}; \quad (\text{A.13})$$

evidently  $r_{ix} \approx r_B$  for  $\theta \rightarrow \pi/2$ . By substituting for  $r_B$  in terms of  $r_n$  using Equation (2.19), Equation (A.13) gives  $r_{ix}$  in terms of  $r_n$ . Using this, Equation (A.12) may be integrated. Fig. A.1 shows an example of the C shock structure with varying  $\theta$  values. For sufficiently large  $\theta$ , the shock is changed little with respect to the  $\theta = \pi/2$  case. For smaller  $\theta$ , the structure is quantitatively different, but qualitatively similar.

The final magnetic compression ratio  $r_{B,f}$  is obtained from Equation (A.13) using  $r_f(\theta) \equiv r_{n,f} = r_{ix,f}$ :

$$r_{B,f} = \frac{r_f(\theta) \left( \tan^2 \theta - \frac{2}{\beta_y \mathcal{M}^2} \right)}{\tan^2 \theta - \frac{2r_f(\theta)}{\beta_y \mathcal{M}^2}}. \quad (\text{A.14})$$

From the exact solutions, we know that  $r_f(\theta) \leq r_f(\pi/2) \equiv r_{f,90}$ , Equation (A.14) therefore suggests that for each model, there is a minimum angle between  $\mathbf{B}_0$  and  $\mathbf{v}_0$ :

$$\theta_{\min} \approx \tan^{-1} \left( \sqrt{\frac{2r_{f,90}}{\beta_y \mathcal{M}^2}} \right) \approx \tan^{-1} \left[ \left( \frac{2}{\sqrt{\beta_y \mathcal{M}^2}} \right)^{1/2} \right]. \quad (\text{A.15})$$

Since, for a given  $B_{y,0}$  (or  $\beta_y$ ), small  $\theta$  corresponds to large upstream magnetic field strength, a shock is not possible for very small  $\theta$ . More practically, this can also be

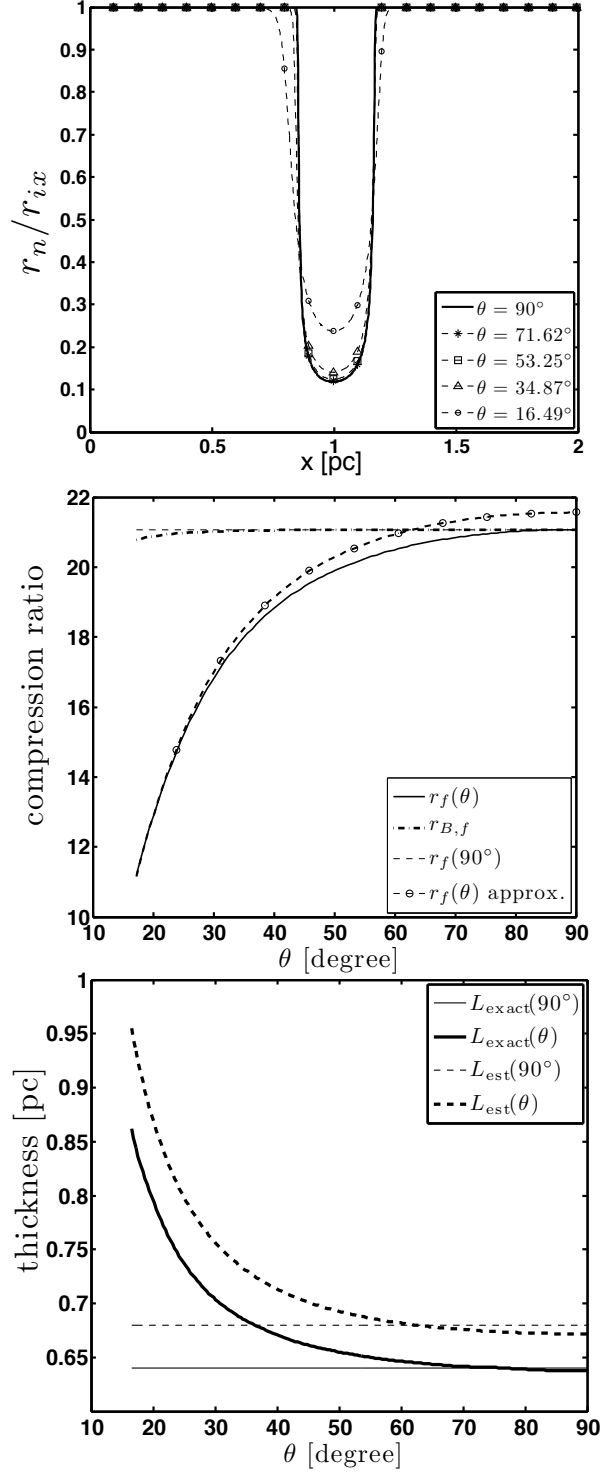


Figure A.1: The structure, the final compression ratio, and the shock thickness of an oblique C shock with  $n_0 = 500 \text{ cm}^{-3}$ ,  $B_{y,0} = 5 \text{ } \mu\text{G}$ ,  $v_0 = 5 \text{ km/s}$ , and  $\chi_{i0} = 5$ , as functions of the angle  $\theta$  between  $\mathbf{B}_0$  and  $\mathbf{v}_0$  from  $\theta = \theta_{\min} = 16.49^\circ$  to  $\theta = 90^\circ$ . The analytical approximations, Equations (A.20) and (A.23), provide good estimates to the exact solutions.

written as

$$v_0 \gtrsim \sqrt{2}v_{A,\text{cloud}} \frac{1 - \sin^2 \theta}{\sin \theta}, \quad (\text{A.16})$$

or  $\theta > \theta_{\min}$  (assuming  $\sin \theta_{\min} \ll 1/\sin \theta_{\min}$ ) for

$$\sin \theta_{\min} \sim \sqrt{2} \frac{v_{A,\text{cloud}}}{v_0}, \quad (\text{A.17})$$

where  $v_{A,\text{cloud}} = B_{\text{cloud}}/\sqrt{4\pi\rho_0}$ . The reason for the condition  $\theta > \theta_{\min}$  is to ensure that the inflow is strong enough to produce shocks in the magnetized gas.

To obtain  $r_f(\theta)$ , we need to simultaneously solve

$$\frac{\mathcal{M}^2}{r_f(\theta)} + r_f(\theta) + \frac{r_{B,f}^2}{\beta_y} = \mathcal{M}^2 + 1 + \frac{1}{\beta_y} \quad (\text{A.18})$$

and Equation (A.14), which can only be done numerically. Alternatively, we can also use Equation (A.18) to write (assuming  $\mathcal{M}^2 \gg r_f(\theta) \gg 1$ )

$$r_{B,f} \approx \sqrt{\beta_y [\mathcal{M}^2 - r_f(\theta)]} \approx \sqrt{\beta_y} \mathcal{M} \left( 1 - \frac{r_f(\theta)}{2\mathcal{M}^2} \right). \quad (\text{A.19})$$

Substituting Equation (A.19) into Equation (A.14) gives us a quadratic equation for  $r_f(\theta)$ :

$$\frac{r_f^2(\theta)}{\sqrt{\beta_y} \mathcal{M}^3 \tan^2 \theta} + \left[ \frac{2}{\beta_y \mathcal{M}^2 \tan^2 \theta} \left( 1 - \sqrt{\beta_y} \mathcal{M} \right) - 1 - \frac{\sqrt{\beta_y}}{2\mathcal{M}} \right] r_f(\theta) + \sqrt{\beta_y} \mathcal{M} = 0. \quad (\text{A.20})$$

Since  $\mathcal{M} \gg 1$ , keeping only  $\mathcal{M}^{-1}$  terms gives

$$r_f(\theta) \approx \sqrt{\beta_y} \mathcal{M} \left[ \frac{2}{\sqrt{\beta_y} \mathcal{M} \tan^2 \theta} + \frac{\sqrt{\beta_y}}{2\mathcal{M}} + 1 \right]^{-1}. \quad (\text{A.21})$$

This is an analytical approximation for  $r_f(\theta)$  (see Fig. A.1). The compression factor  $r_{f,90}$  for the case with magnetic field parallel to the shock front ( $\tan \theta \rightarrow \infty$ ) is

$r_{f,90} \approx \sqrt{\beta_y} \mathcal{M}$  (see Equation (2.21)). Note that for  $\tan \theta \gtrsim [2/(\sqrt{\beta_y} \mathcal{M})]^{1/2}$ ,  $r_f(\theta) \sim r_{f,90}$ . Thus, for all but the smallest angles, oblique shocks have similar compression factor to the 90° case with the same  $B_{y,0}$ .

Since  $r_n/r_{ix}$  is small through most of the shock just like  $r_n/r_B$ , we can follow the derivation in Section 2.3.3 to get the formula for the C shock thickness with different  $r_f(\theta)$ . Equation (A.12) for the shock structure is

$$\frac{d}{dx} \left( r_n + \frac{\mathcal{M}^2}{r_n} \right) = -Dr_n^{1/2} \left( 1 - \frac{r_n}{r_{ix}} \right), \quad (\text{A.22})$$

similar to Equation (2.40). Therefore, as for Equation (2.45), the oblique C shock thickness can be written as

$$L_{\text{est}}(\theta) \approx \frac{4\mathcal{M}^2}{D [r_f(\theta)]^{1/2}} = \frac{4v_0}{\alpha \rho_{i,0} [r_f(\theta)]^{1/2}}. \quad (\text{A.23})$$

An example comparing the approximation Equation (A.23) (using  $r_f(\theta)$  from Equation (A.21)) with the exact solution is shown in Fig. A.1.

Regarding the time-dependent behavior of oblique C shocks, we use convergent flow to produce shocks in numerical simulations. To see how the component of magnetic field parallel to the inflow direction ( $B_x$ ) can affect the evolution of the candidate core material, we fix the values of  $n_0$ ,  $v_0$ ,  $B_{y,0}$ ,  $\chi_{i0}$ , and choose different values of  $\theta$  so that  $B_x = B_{y,0} \cot \theta$ . Based on our theory, the growth rate of column density  $dN(\text{H})/dt$  is proportional to  $v_{\text{inflow}}(\theta) = v_0 [r_f(\theta) - 1]/r_f(\theta)$ , which should be almost the same for different  $\theta$ , since  $r_f(\theta) \gg 1$ . The ambipolar diffusion timescale  $t_{\text{AD}}$  and the final mass-to-flux ratio  $\Gamma_{\text{final}}$ , however, should decrease slightly for smaller  $\theta$  because of their dependence on  $r_f(\theta)$ . The generalizations of

Equations (2.64) and (2.69) are:

$$t_{\text{AD}}(\theta) \approx \frac{2[r_f(\theta)]^{1/2}}{\alpha\rho_{i,0}} = t_{\text{AD},90} \left[ \frac{r_f(\theta)}{r_{f,90}} \right]^{1/2}, \quad (\text{A.24})$$

$$\Gamma_{\text{final}}(\theta) \approx 2\pi\sqrt{G} \cdot \frac{2\rho_0 v_0 \times t_{\text{AD}}(\theta)}{r_{B,f} B_0} \approx \Gamma_{\text{final},90} \left[ \frac{r_f(\theta)}{r_{f,90}} \right]^{1/2} \quad (\text{A.25})$$

where we apply  $r_{B,f} \approx r_{f,90}$  to get the second equation, and Equation (2.70) gives  $\Gamma_{\text{final},90}$ . Since  $r_f(\theta)/r_{f,90}$  is order-unity unless  $\theta$  is extremely small,  $\Gamma_{\text{final}}(\theta)$  is close to  $\Gamma_{\text{final},90}$  in most cases.

The simulation results shown in Fig. A.2 agree with our expectation. The column density grows at an identical rate in all cases (though the shape of the central peak differs from one to another), and the transition happens slightly earlier for smaller  $\theta$ . There is no obvious difference between the final mass-to-flux ratios in each case, however, since  $r_{B,f}$  actually decreases for smaller  $\theta$  and makes  $\Gamma_{\text{final}}(\theta)$  slightly larger, thus cancels part of the effect from  $r_f(\theta)$ .

In conclusion, these tests show that the evolution of C shock transients to make candidate prestellar cores is not significantly affected by the component of magnetic field parallel to the inflow velocity.

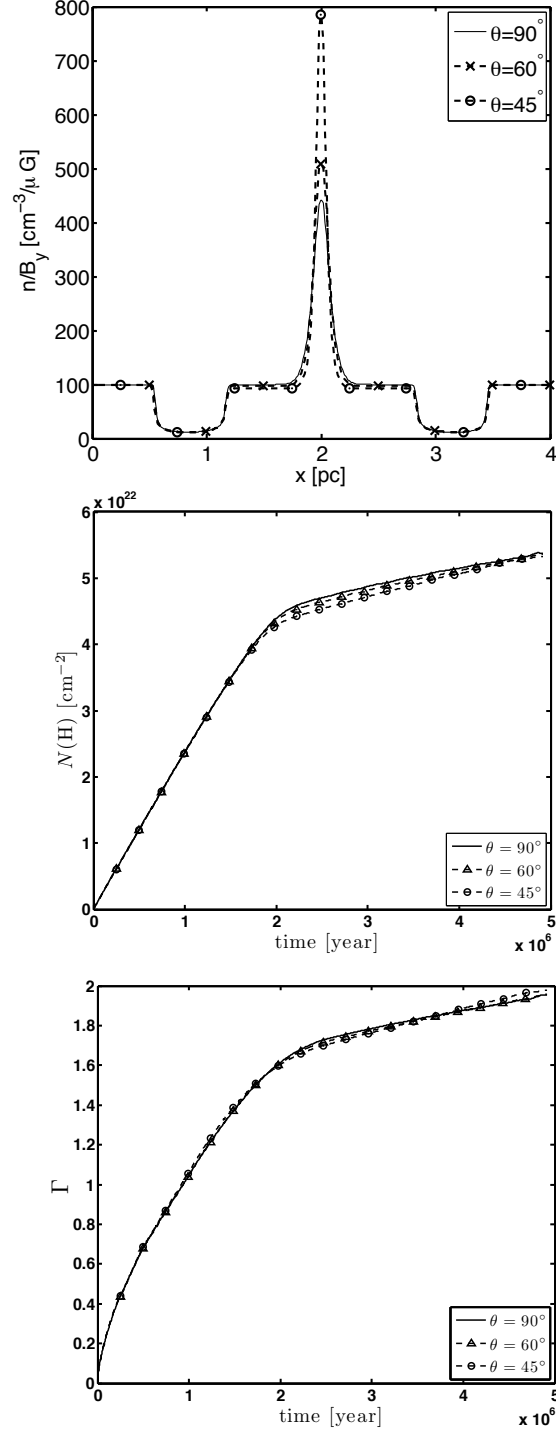


Figure A.2: The transient behavior and time evolution of the column density and normalized central mass-to-flux ratio in the post-shock gas of oblique C shocks with  $n_0 = 500 \text{ cm}^{-3}$ ,  $B_{y,0} = 5 \mu\text{G}$ ,  $v_0 = 5 \text{ km/s}$ , and  $\chi_{i0} = 5$ . Though the profile of transient central core differs, the growth rate and the final value of  $\Gamma$  are very similar in each case.

## Bibliography

- Allen, A., Li, Z.-Y., & Shu, F. H. 2003, *Astrophysical Journal*, 599, 363
- Alves, J. F., Lada, C. J., & Lada, E. A. 2001, *Nature*, 409, 159
- Alves, J., Lombardi, M., & Lada, C. J. 2007, *Astronomy and Astrophysics*, 462, L17
- André, P., Basu, S., & Inutsuka, S. 2009, *Structure Formation in Astrophysics*, 254
- Andre, P., Ward-Thompson, D., & Barsony, M. 2000, *Protostars and Planets IV*, 59
- André, P., Men'shchikov, A., Bontemps, S., et al. 2010, *Astronomy and Astrophysics*, 518, LL102
- André, P., Di Francesco, J., Ward-Thompson, D., et al. 2014, *Protostars and Planets VI*, 27
- Ashmore, I., van Loo, S., Caselli, P., Falle, S. A. E. G., & Hartquist, T. W. 2010, *Astronomy and Astrophysics*, 511, A41
- Arzoumanian, D., André, P., Didelon, P., et al. 2011, *Astronomy and Astrophysics*, 529, L6
- Bacmann, A., André, P., Puget, J.-L., et al. 2000, *Astronomy and Astrophysics*, 361, 555
- Bai, X.-N., & Stone, J. M. 2011, *Astrophysical Journal*, 736, 144

- Ballesteros-Paredes, J., Hartmann, L., & Vázquez-Semadeni, E. 1999, *Astrophysical Journal*, 527, 285
- Ballesteros-Paredes, J., Klessen, R. S., Mac Low, M.-M., & Vazquez-Semadeni, E. 2007, *Protostars and Planets V*, 63
- Bally, J., Langer, W. D., Stark, A. A., & Wilson, R. W. 1987, *Astrophysical Journal Letters*, 312, L45
- Bally, J., Walawender, J., Johnstone, D., Kirk, H., & Goodman, A. 2008, *Handbook of Star Forming Regions*, Volume I, 308
- Basu, S., & Ciolek, G. E. 2004, *Astrophysical Journal Letters*, 607, L39
- Basu, S., Ciolek, G. E., & Wurster, J. 2009b, *New Astronomy*, 14, 221
- Basu, S., Ciolek, G. E., Dapp, W. B., & Wurster, J. 2009a, *New Astronomy*, 14, 483
- Bate, M. R., Bonnell, I. A., & Bromm, V. 2003, *Monthly Notices of the Royal Astronomical Society*, 339, 577
- Bigiel, F., Leroy, A., Walter, F., et al. 2008, *Astronomical Journal*, 136, 2846
- Blitz, L. 1993, *Protostars and Planets III*, 125
- Bolatto, A. D., Leroy, A. K., Rosolowsky, E., Walter, F., & Blitz, L. 2008, *Astrophysical Journal*, 686, 948
- Bolatto, A. D., Wolfire, M., & Leroy, A. K. 2013, *Annual Review of Astronomy and Astrophysics*, 51, 207
- Bonnell, I. A., & Bate, M. R. 2006, *Monthly Notices of the Royal Astronomical Society*, 370, 488
- Bonnor, W. B. 1956, *Monthly Notices of the Royal Astronomical Society*, 116, 351
- Bourke, T. L., Myers, P. C., Robinson, G., & Hyland, A. R. 2001, *Astrophysical Journal*, 554, 916

- Boss, A. P. 1997, *Astrophysical Journal*, 483, 309
- Boss, A. P. 2005, *Astrophysical Journal*, 622, 393
- Bot, C., Boulanger, F., Rubio, M., & Rantakyro, F. 2007, *Astronomy and Astrophysics*, 471, 103
- Brunt, C. M., & Heyer, M. H. 2002, *Astrophysical Journal*, 566, 276
- Caselli, P., Benson, P. J., Myers, P. C., & Tafalla, M. 2002, *Astrophysical Journal*, 572, 238
- Chabrier, G. 2005, *The Initial Mass Function 50 Years Later*, 327, 41
- Chandrasekhar, S., & Fermi, E. 1953, *Astrophysical Journal*, 118, 113
- Chapman, N. L., Goldsmith, P. F., Pineda, J. L., et al. 2011, *Astrophysical Journal*, 741, 21
- Chen, C.-Y., & Ostriker, E. C. 2012, *Astrophysical Journal*, 744, 124
- Chen, C.-Y., & Ostriker, E. C. 2014, *Astrophysical Journal*, 785, 69
- Chieze, J.-P., Pineau des Forets, G., & Flower, D. R. 1998, *Monthly Notices of the Royal Astronomical Society*, 295, 672
- Chini, R., Reipurth, B., Ward-Thompson, D., et al. 1997, *Astrophysical Journal Letters*, 474, L135
- Choi, E., Kim, J., & Wiita, P. J. 2009, *Astrophysical Journal Supplement*, 181, 413
- Ciardi, A., & Hennebelle, P. 2010, *Monthly Notices of the Royal Astronomical Society*, 409, L39
- Ciolek, G. E., & Basu, S. 2001, *Astrophysical Journal*, 547, 272
- Ciolek, G. E., & Basu, S. 2006, *Astrophysical Journal*, 652, 442

- Combes, F. 1991, *Annual Review of Astronomy and Astrophysics*, 29, 195
- Crutcher, R. M. 1999, *Astrophysical Journal*, 520, 706
- Crutcher, R. M. 2012, *Annual Review of Astronomy and Astrophysics*, 50, 29
- Crutcher, R. M., Troland, T. H., Goodman, A. A., et al. 1993, *Astrophysical Journal*, 407, 175
- Crutcher, R. M., Wandelt, B., Heiles, C., Falgarone, E., & Troland, T. H. 2010, *Astrophysical Journal*, 725, 466
- Curtis, E. I., & Richer, J. S. 2010, *Monthly Notices of the Royal Astronomical Society*, 402, 603
- Dame, T. M., Hartmann, D., & Thaddeus, P. 2001, *Astrophysical Journal*, 547, 792
- Dapp, W. B., Basu, S., & Kunz, M. W. 2012, *Astronomy and Astrophysics*, 541, AA35
- Delmont, P., & Keppens, R. 2011, *Journal of Plasma Physics*, 77, 207
- Dickman, R. L. 1978, *Astrophysical Journal Supplement*, 37, 407
- di Francesco, J., Evans, N. J., II, Caselli, P., et al. 2007, *Protostars and Planets V*, 17
- Dobbs, C. L., Krumholz, M. R., Ballesteros-Paredes, J., et al. 2014, *Protostars and Planets VI*, 3
- Draine, B. T. 1980, *Astrophysical Journal*, 241, 1021
- Draine, B. T., & McKee, C. F. 1993, *Annual Review of Astronomy and Astrophysics*, 31, 373
- Draine, B. T., Roberge, W. G., & Dalgarno, A. 1983, *Astrophysical Journal*, 264, 485

- Elmegreen, B. G. 1993, *Astrophysical Journal Letters*, 419, L29
- Elmegreen, B. G., & Falgarone, E. 1996, *Astrophysical Journal*, 471, 816
- Enoch, M. L., Young, K. E., Glenn, J., et al. 2006, *Astrophysical Journal*, 638, 293
- Evans, N. J., II, Dunham, M. M., Jørgensen, J. K., et al. 2009, *Astrophysical Journal Supplement*, 181, 321
- Falgarone, E., Troland, T. H., Crutcher, R. M., & Paubert, G. 2008, *Astronomy and Astrophysics*, 487, 247
- Fatuzzo, M., & Adams, F. C. 2002, *Astrophysical Journal*, 570, 210
- Federrath, C., Klessen, R. S., & Schmidt, W. 2008, *Astrophysical Journal Letters*, 688, L79
- Frerking, M. A., Langer, W. D., & Wilson, R. W. 1982, *Astrophysical Journal*, 262, 590
- Fukui, Y., Mizuno, N., Yamaguchi, R., et al. 1999, *Publications of the Astronomical Society of Japan*, 51, 745
- Gardiner, T. A., & Stone, J. M. 2005, *Journal of Computational Physics*, 205, 509
- Gillis, J., Mestel, L., & Paris, R. B. 1979, *Monthly Notices of the Royal Astronomical Society*, 187, 311
- Goldreich, P., & Sridhar, S. 1995, *Astrophysical Journal*, 438, 763
- Goldsmith, P. F., Heyer, M., Narayanan, G., et al. 2008, *Astrophysical Journal*, 680, 428
- Gong, H., & Ostriker, E. C. 2009, *Astrophysical Journal*, 699, 230
- Gong, H., & Ostriker, E. C. 2011, *Astrophysical Journal*, 729, 120

- Goodman, A. A., Crutcher, R. M., Heiles, C., Myers, P. C., & Troland, T. H. 1989, *Astrophysical Journal Letters*, 338, L61
- Goodman, A. A., Bastien, P., Menard, F., & Myers, P. C. 1990, *Astrophysical Journal*, 359, 363
- Hacar, A., & Tafalla, M. 2011, *Astronomy and Astrophysics*, 533, AA34
- Hacar, A., Tafalla, M., Kauffmann, J., & Kovács, A. 2013, *Astronomy and Astrophysics*, 554, AA55
- Haisch, K. E., Jr., Lada, E. A., & Lada, C. J. 2001, *Astrophysical Journal Letters*, 553, L153
- Heiderman, A., Evans, N. J., II, Allen, L. E., Huard, T., & Heyer, M. 2010, *Astrophysical Journal*, 723, 1019
- Heiles, C., & Crutcher, R. 2005, *Cosmic Magnetic Fields*, 664, 137
- Heiles, C., Goodman, A. A., McKee, C. F., & Zweibel, E. G. 1993, *Protostars and Planets III*, 279
- Heiles, C., & Troland, T. H. 2005, *Astrophysical Journal*, 624, 773
- Heitsch, F., Zweibel, E. G., Slyz, A. D., & Devriendt, J. E. G. 2004, *Astrophysical Journal*, 603, 165
- Hennebelle, P., & Chabrier, G. 2008, *Astrophysical Journal*, 684, 395
- Hennebelle, P., & Ciardi, A. 2009, *Astronomy and Astrophysics*, 506, L29
- Hennebelle, P., Commerçon, B., Joos, M., et al. 2011, *Astronomy and Astrophysics*, 528, AA72
- Hennebelle, P., & Fromang, S. 2008, *Astronomy and Astrophysics*, 477, 9
- Hennemann, M., Motte, F., Schneider, N., et al. 2012, *Astronomy and Astrophysics*, 543, L3

- Heyer, M. H., Brunt, C., Snell, R. L., et al. 1998, *Astrophysical Journal Supplement*, 115, 241
- Heyer, M. H., & Brunt, C. M. 2004, *Astrophysical Journal Letters*, 615, L45
- Heyer, M., Gong, H., Ostriker, E., & Brunt, C. 2008, *Astrophysical Journal*, 680, 420
- Heyer, M., Krawczyk, C., Duval, J., & Jackson, J. M. 2009, *Astrophysical Journal*, 699, 1092
- Heyer, M. H., Vrba, F. J., Snell, R. L., et al. 1987, *Astrophysical Journal*, 321, 855
- Hiltner, W. A. 1949, *Astrophysical Journal*, 109, 471
- Hiltner, W. A. 1951, *Astrophysical Journal*, 114, 241
- Hopkins, P. F. 2012, *Monthly Notices of the Royal Astronomical Society*, 423, 2037
- Hosking, J. G., & Whitworth, A. P. 2004, *Monthly Notices of the Royal Astronomical Society*, 347, 1001
- Hull, C. L. H., Plambeck, R. L., Bolatto, A. D., et al. 2013, *Astrophysical Journal*, 768, 159
- Ikeda, N., Kitamura, Y., & Sunada, K. 2009, *Astrophysical Journal*, 691, 1560
- Indebetouw, R., & Zweibel, E. G. 2000, *Astrophysical Journal*, 532, 361
- Inoue, T., & Fukui, Y. 2013, *Astrophysical Journal Letters*, 774, L31
- Inoue, T., & Inutsuka, S. 2007, *Progress of Theoretical Physics*, 118, 47
- Jappsen, A.-K., Klessen, R. S., Larson, R. B., Li, Y., & Mac Low, M.-M. 2005, *Astronomy and Astrophysics*, 435, 611
- Jijina, J., Myers, P. C., & Adams, F. C. 1999, *Astrophysical Journal Supplement*, 125, 161

- Johnstone, D., & Bally, J. 1999, *Astrophysical Journal Letters*, 510, L49
- Joos, M., Hennebelle, P., & Ciardi, A. 2012, *Astronomy and Astrophysics*, 543, AA128
- Joos, M., Hennebelle, P., Ciardi, A., & Fromang, S. 2013, *Astronomy and Astrophysics*, 554, AA17
- Kandori, R., Nakajima, Y., Tamura, M., et al. 2005, *Astronomical Journal*, 130, 2166
- Karimabadi, H. 1995, *Advances in Space Research*, 15, 507
- Kennicutt, R. C., Jr. 1998, *Astrophysical Journal*, 498, 541
- Kirk, J. M., Ward-Thompson, D., & André, P. 2005, *Monthly Notices of the Royal Astronomical Society*, 360, 1506
- Kirk, H., Johnstone, D., & Di Francesco, J. 2006, *Astrophysical Journal*, 646, 1009
- Kirk, J. M., Ward-Thompson, D., Palmeirim, P., et al. 2013, *Monthly Notices of the Royal Astronomical Society*, 432, 1424
- Klessen, R. S. 2000, *Astrophysical Journal*, 535, 869
- Klessen, R. S., Heitsch, F., & Mac Low, M.-M. 2000, *Astrophysical Journal*, 535, 887
- Klessen, R. S. 2001, *Astrophysical Journal*, 556, 837
- Könyves, V., André, P., Men'shchikov, A., et al. 2010, *Astronomy and Astrophysics*, 518, LL106
- Koyama, H., & Ostriker, E. C. 2009, *Astrophysical Journal*, 693, 1316
- Kroupa, P. 2001, *Monthly Notices of the Royal Astronomical Society*, 322, 231
- Krasnopolsky, R., Li, Z.-Y., & Shang, H. 2010, *Astrophysical Journal*, 716, 1541

- Kroupa, P., Weidner, C., Pflamm-Altenburg, J., et al. 2013, *Planets, Stars and Stellar Systems. Volume 5: Galactic Structure and Stellar Populations*, 115
- Krumholz, M. R., Crutcher, R. M., & Hull, C. L. H. 2013, *Astrophysical Journal Letters*, 767, LL11
- Krumholz, M. R., Klein, R. I., & McKee, C. F. 2012, *Astrophysical Journal*, 754, 71
- Kudoh, T., & Basu, S. 2008, *Astrophysical Journal Letters*, 679, L97
- Kudoh, T., & Basu, S. 2011, *Astrophysical Journal Letters*, 728, 123
- Kudoh, T., Basu, S., Ogata, Y., & Yabe, T. 2007, *Monthly Notices of the Royal Astronomical Society*, 380, 499
- Lada, C. J. 1976, *Astrophysical Journal Supplement*, 32, 603
- Lada, C. J., Lombardi, M., & Alves, J. F. 2010, *Astrophysical Journal*, 724, 687
- Larson, R. B. 1981, *Monthly Notices of the Royal Astronomical Society*, 194, 809
- Lee, C. W., & Myers, P. C. 1999, *Astrophysical Journal Supplement*, 123, 233
- Lee, C. W., Myers, P. C., & Tafalla, M. 1999, *Astrophysical Journal*, 526, 788
- Lee, K. I., Fernández-López, M., Storm, S., et al. 2014, *Astrophysical Journal*, 797, 76
- Lemaster, M. N., & Stone, J. M. 2009, *Astrophysical Journal*, 691, 1092
- Li, P. S., McKee, C. F., & Klein, R. I. 2006, *Astrophysical Journal*, 653, 1280
- Li, P. S., Norman, M. L., Mac Low, M.-M., & Heitsch, F. 2004, *Astrophysical Journal*, 605, 800
- Li, Z.-Y., Banerjee, R., Pudritz, R. E., et al. 2014, *Protostars and Planets VI*, 173

- Li, Z.-Y., Krasnopolsky, R., & Shang, H. 2011, *Astrophysical Journal*, 738, 180
- Li, Z.-Y., Krasnopolsky, R., & Shang, H. 2013, *Astrophysical Journal*, 774, 82
- Li, Z.-Y., & Nakamura, F. 2004, *Astrophysical Journal Letters*, 609, L83
- Li, Z.-Y., Wang, P., Abel, T., & Nakamura, F. 2010, *Astrophysical Journal Letters*, 720, L26
- Lizano, S., & Shu, F. H. 1989, *Astrophysical Journal*, 342, 834
- Machida, M. N., Inutsuka, S.-I., & Matsumoto, T. 2011, *Publications of the Astronomical Society of Japan*, 63, 555
- Mac Low, M.-M., & Klessen, R. S. 2004, *Reviews of Modern Physics*, 76, 125
- Mac Low, M.-M., Norman, M. L., Konigl, A., & Wardle, M. 1995, *Astrophysical Journal*, 442, 726
- Maury, A. J., André, P., Hennebelle, P., et al. 2010, *Astronomy and Astrophysics*, 512, A40
- McKee, C. F., Li, P. S., & Klein, R. I. 2010, *Astrophysical Journal*, 720, 1612
- McKee, C. F., & Ostriker, E. C. 2007, *Annual Review of Astronomy and Astrophysics*, 45, 565
- Mellon, R. R., & Li, Z.-Y. 2008, *Astrophysical Journal*, 681, 1356
- Mestel, L. 1985, *Protostars and Planets II*, 320
- Mestel, L., & Spitzer, L., Jr. 1956, *Monthly Notices of the Royal Astronomical Society*, 116, 503
- Molinari, S., Bally, J., Glover, S., et al. 2014, *Protostars and Planets VI*, 125
- Moneti, A., Pipher, J. L., Helfer, H. L., McMillan, R. S., & Perry, M. L. 1984, *Astrophysical Journal*, 282, 508

- Motte, F., André, P., Ward-Thompson, D., & Bontemps, S. 2001, *Astronomy and Astrophysics*, 372, L41
- Mouschovias, T. C. 1978, *IAU Colloq. 52: Protostars and Planets*, 209
- Mouschovias, T. C. 1979, *Astrophysical Journal*, 228, 475
- Mouschovias, T. C. 1991, *Astrophysical Journal*, 373, 169
- Mouschovias, T. C. 1995, *The Physics of the Interstellar Medium and Intergalactic Medium*, 80, 184
- Mouschovias, T. C., & Ciolek, G. E. 1999, *NATO ASIC Proc. 540: The Origin of Stars and Planetary Systems*, 305
- Mouschovias, T. C., & Spitzer, L., Jr. 1976, *Astrophysical Journal*, 210, 326
- Myers, P. C. 1983, *Astrophysical Journal*, 270, 105
- Myers, P. C., & Benson, P. J. 1983, *Astrophysical Journal*, 266, 309
- Myers, P. C., Dame, T. M., Thaddeus, P., et al. 1986, *Astrophysical Journal*, 301, 398
- Myers, A. T., Klein, R. I., Krumholz, M. R., & McKee, C. F. 2014, *Monthly Notices of the Royal Astronomical Society*, 439, 3420
- Myers, P. C., Linke, R. A., & Benson, P. J. 1983, *Astrophysical Journal*, 264, 517
- Nakamura, F., & Li, Z.-Y. 2005, *Astrophysical Journal*, 631, 411
- Nakamura, F., & Li, Z.-Y. 2008, *Astrophysical Journal*, 687, 354
- Nakano, T. 1976, *Publications of the Astronomical Society of Japan*, 28, 355
- Nakano, T. 1979, *Publications of the Astronomical Society of Japan*, 31, 697

- Nakano, T., & Nakamura, T. 1978, *Publications of the Astronomical Society of Japan*, 30, 671
- Nutter, D., & Ward-Thompson, D. 2007, *Monthly Notices of the Royal Astronomical Society*, 374, 1413
- Offner, S. S. R., Clark, P. C., Hennebelle, P., et al. 2014, *Protostars and Planets VI*, 53
- Onishi, T., Mizuno, A., Kawamura, A., Tachihara, K., & Fukui, Y. 2002, *Astrophysical Journal*, 575, 950
- Ostriker, E. C., Gammie, C. F., & Stone, J. M. 1999, *Astrophysical Journal*, 513, 259
- Ostriker, E. C., Stone, J. M., & Gammie, C. F. 2001, *Astrophysical Journal*, 546, 980
- Padoan, P., Nordlund, A., & Jones, B. J. T. 1997, *Monthly Notices of the Royal Astronomical Society*, 288, 145
- Padoan, P., Bally, J., Billawala, Y., Juvela, M., & Nordlund, Å. 1999, *Astrophysical Journal*, 525, 318
- Padoan, P., Juvela, M., Goodman, A. A., & Nordlund, Å. 2001, *Astrophysical Journal*, 553, 227
- Padoan, P., Juvela, M., Kritsuk, A., & Norman, M. L. 2006, *Astrophysical Journal Letters*, 653, L125
- Padoan, P., & Nordlund, Å. 2002, *Astrophysical Journal*, 576, 870
- Palmeirim, P., André, P., Kirk, J., et al. 2013, *Astronomy and Astrophysics*, 550, A38
- Passot, T., Pouquet, A., & Woodward, P. 1988, *Astronomy and Astrophysics*, 197, 228

- Pineau des Forets, G., Flower, D. R., & Chieze, J.-P. 1997, *Herbig-Haro Flows and the Birth of Stars*, 182, 199
- Rathborne, J. M., Lada, C. J., Muench, A. A., et al. 2009, *Astrophysical Journal*, 699, 742
- Ridge, N. A., Di Francesco, J., Kirk, H., et al. 2006, *Astronomical Journal*, 131, 2921
- Roberge, W. G., & Ciolek, G. E. 2007, *Monthly Notices of the Royal Astronomical Society*, 382, 717
- Roman-Duval, J., Jackson, J. M., Heyer, M., Rathborne, J., & Simon, R. 2010, *Astrophysical Journal*, 723, 492
- Sadavoy, S. I., Di Francesco, J., Bontemps, S., et al. 2010, *Astrophysical Journal*, 710, 1247
- Sadavoy, S. I., Di Francesco, J., & Johnstone, D. 2010, *Astrophysical Journal Letters*, 718, L32
- Sadavoy, S. I., Di Francesco, J., André, P., et al. 2014, *Astrophysical Journal Letters*, 787, L18
- Sanders, D. B., Solomon, P. M., & Scoville, N. Z. 1984, *Astrophysical Journal*, 276, 182
- Sanders, R., Morano, E., & Druguet, M. C. 1998, *Journal of Computational Physics*, 145, 511
- Santos-Lima, R., de Gouveia Dal Pino, E. M., & Lazarian, A. 2012, *Astrophysical Journal*, 747, 21
- Scalo, J. M. 1985, *Protostars and Planets II*, 201
- Scoville, N. Z., & Solomon, P. M. 1975, *Astrophysical Journal Letters*, 199, L105
- Seifried, D., Banerjee, R., Pudritz, R. E., & Klessen, R. S. 2012, *Monthly Notices of the Royal Astronomical Society*, 423, L40

- Seifried, D., Banerjee, R., Pudritz, R. E., & Klessen, R. S. 2013, *Monthly Notices of the Royal Astronomical Society*, 432, 3320
- Shetty, R., Glover, S. C., Dullemond, C. P., & Klessen, R. S. 2011, *Monthly Notices of the Royal Astronomical Society*, 412, 1686
- Shu, F. H. 1992, *Physics of Astrophysics, Vol. II*, by Frank H. Shu. Published by University Science Books, ISBN 0-935702-65-2, 476pp, 1992.,
- Shu, F. H., Adams, F. C., & Lizano, S. 1987, *Annual Review of Astronomy and Astrophysics*, 25, 23
- Simpson, R. J., Nutter, D., & Ward-Thompson, D. 2008, *Monthly Notices of the Royal Astronomical Society*, 391, 205
- Smith, M. D., & Mac Low, M.-M. 1997, *Astronomy and Astrophysics*, 326, 801
- Snell, R. L., Mundy, L. G., Goldsmith, P. F., Evans, N. J., II, & Erickson, N. R. 1984, *Astrophysical Journal*, 276, 625
- Solomon, P. M., Rivolo, A. R., Barrett, J., & Yahil, A. 1987, *Astrophysical Journal*, 319, 730
- Spitzer, L., Jr. 1942, *Astrophysical Journal*, 95, 329
- Spitzer, L. 1956, *Physics of Fully Ionized Gases*, New York: Interscience Publishers, 1956,
- Stone, J. M. 1997, *Astrophysical Journal*, 487, 271
- Stone, J. M., Gardiner, T. A., Teuben, P., Hawley, J. F., & Simon, J. B. 2008, *Astrophysical Journal Supplement*, 178, 137
- Strittmatter, P. A. 1966, *Monthly Notices of the Royal Astronomical Society*, 132, 359
- Sugitani, K., Nakamura, F., Watanabe, M., et al. 2011, *Astrophysical Journal*, 734, 63

- Takahashi, K., & Yamada, S. 2013, *Journal of Plasma Physics*, 79, 335
- Tamura, M., Nagata, T., Sato, S., & Tanaka, M. 1987, *Monthly Notices of the Royal Astronomical Society*, 224, 413
- Tielens, A. G. G. M. 2005, *The Physics and Chemistry of the Interstellar Medium*, by A. G. G. M. Tielens, pp. . ISBN 0521826349. Cambridge, UK: Cambridge University Press, 2005.,
- Tomida, K., Okuzumi, S., & Machida, M. N. 2015, *Astrophysical Journal*, 801, 117
- Tomida, K., Tomisaka, K., Matsumoto, T., et al. 2013, *Astrophysical Journal*, 763, 6
- Tomisaka, K., Ikeuchi, S., & Nakamura, T. 1988, *Astrophysical Journal*, 335, 239
- Torrilhon, M. 2003, *Journal of Plasma Physics*, 69, 253
- Troland, T. H., & Crutcher, R. M. 2008, *Astrophysical Journal*, 680, 457
- Vaidya, B., Hartquist, T. W., & Falle, S. A. E. G. 2013, *Monthly Notices of the Royal Astronomical Society*, 433, 1258
- van Loo, S., Ashmore, I., Caselli, P., Falle, S. A. E. G., & Hartquist, T. W. 2009, *Monthly Notices of the Royal Astronomical Society*, 395, 319
- Vázquez-Semadeni, E., Banerjee, R., Gómez, G. C., Hennebelle, P., Duffin, D., & Klessen, R. S. 2011, *Monthly Notices of the Royal Astronomical Society*, 414, 2511
- Vázquez-Semadeni, E., Kim, J., Shadmehri, M., & Ballesteros-Paredes, J. 2005, *Astrophysical Journal*, 618, 344
- Vázquez-Semadeni, E., Passot, T., & Pouquet, A. 1995, *Astrophysical Journal*, 441, 702
- Vestuto, J. G., Ostriker, E. C., & Stone, J. M. 2003, *Astrophysical Journal*, 590, 858
- Vrba, F. J., Strom, S. E., & Strom, K. M. 1976, *Astronomical Journal*, 81, 958

- Ward-Thompson, D., André, P., & Kirk, J. M. 2002, *Monthly Notices of the Royal Astronomical Society*, 329, 257
- Ward-Thompson, D., André, P., Crutcher, R., Johnstone, D., Onishi, T., & Wilson, C. 2007, *Protostars and Planets V*, 33
- Wardle, M. 1990, *Monthly Notices of the Royal Astronomical Society*, 246, 98
- Wardle, M. 1991, *Monthly Notices of the Royal Astronomical Society*, 251, 119
- Weingartner, J. C., & Draine, B. T. 2001, *Astrophysical Journal*, 563, 842
- Williams, J. P., Blitz, L., & McKee, C. F. 2000, *Protostars and Planets IV*, 97
- Wu, C. C. 1987, *Geophysical Research Letters*, 14, 668